SUSTAINABLE SYNTHESIS OF MULTIFUNCTIONAL MIXED METAL OXIDE NANOPARTICLES VIA PLANT-MEDIATED GREEN CHEMISTRY

Thesis submitted in partial fulfilment

for the Award of Degree

Doctor of Philosophy

by

SHALU YADAV

RAJIV GANDHI INSTITUTE OF PETROLEUM TECHNOLOGY
JAIS, INDIA – 229304

20BS0009 **2025**

CERTIFICATE

It is certified that the work contained in the thesis titled ***"SUSTAINABLE SYNTHESIS OF MULTIFUNCTIONAL MIXED METAL OXIDE NANOPARTICLES VIA PLANT-MEDIATED GREEN CHEMISTRY"*** by ***"SHALU YADAV"*** has been carried out under my supervision and that this work has not been submitted elsewhere for a degree.

It is further certified that the student has fulfilled all the requirements of Comprehensive, Candidacy and SOTA.

Prof. Abhay Kumar Choubey
Department of Energy and Human Sciences
Rajiv Gandhi Institute of Petroleum Technology
Jais-229304, U.P., India

DECLARATION BY THE CANDIDATE

I, *"SHALU YADAV"*, certify that the work embodied in this thesis is my own bona fide work and was carried out by me under the supervision of *"Prof. ABHAY KUMAR CHOUBEY"* from *"AUGUST, 2020"* to "*OCTOBER, 2025*," at the Rajiv Gandhi Institute of Petroleum Technology, Jais. The matter embodied in this thesis has not been submitted for the award of any other degree. I declare that I have faithfully acknowledged and given credit to the research workers wherever their works have been cited in my work in this thesis. I further declare that I have not wilfully copied any other's work, paragraphs, text, data, results, *etc*., reported in journals, books, magazines, reports, dissertations, theses, *etc*., or available at websites and have not included them in this thesis and have not cited as my own work.

Date :

Place: SHALU YADAV

CERTIFICATE BY THE SUPERVISOR

It is certified that the above statement made by the student is correct to the best of my/our knowledge.

Prof. Abhay Kumar Choubey
Department of Energy and Human Sciences
Rajiv Gandhi Institute of Petroleum Technology
Jais-229304, U.P., India

Head of Department
Energy and Human Sciences

CERTIFICATE

CERTIFIED that the work contained in the thesis titled "***Sustainable Synthesis of Multifunctional Mixed Metal Oxide Nanoparticles via Plant-Mediated Green Chemistry***" by **Ms. Shalu Yadav** has been carried out under my supervision. It is also certified that she fulfilled the mandatory requirement for TWO quality publications that arose out of her thesis work.

It is further certified that the two publications (copies enclosed) of the aforesaid **Ms. Shalu Yadav** have been published in the Journals indexed by –

(a) SCI
(b) SCI Extended
(c) SCOPUS

Prof. Abhay Kumar Choubey
Supervisor

Dr. Omvir Singh
Convener, DPGC

COPYRIGHT TRANSFER CERTIFICATE

Title of the Thesis: Sustainable Synthesis of Multifunctional Mixed Metal Oxide Nanoparticles via Plant-Mediated Green Chemistry

Name of the Student: SHALU YADAV

Copyright Transfer

The undersigned hereby assigns to the Rajiv Gandhi Institute of Petroleum Technology, Jais, India, all rights under copyright that may exist in and for the above thesis submitted for the award of the "Doctor of Philosophy"**.**

Date :
Place: SHALU YADAV

Note: However, the author may reproduce or authorize others to reproduce material extracted verbatim from the thesis or derivative of the thesis for author's personal use provided that the source and the Institute's copyright notice are indicated.

Acknowledgements

My first vote of thanks is dedicated wholeheartedly to Almighty God, whose blessings and strength have sustained me throughout this journey, guiding me through challenges and inspiring perseverance in every step. This journey has been a transformative experience of my life, filled with moments of triumph and trials alike, each leaving a lasting impact and contributing significantly to my growth, resilience, and understanding.

I would like to express my sincere gratitude to my thesis supervisor, Prof. Abhay Kumar Choubey, for his formal guidance and for providing me with the opportunity to pursue this research under his supervision. His role as my advisor has been significant in shaping the direction of this work, and I remain thankful for his support throughout my academic journey. I would also like to express my gratitude to Dr. Arshad Aijaz and Dr. Gunjan Kumar Agrahari for their valuable teachings, suggestions, inputs, and continued support during this time. I would also like to offer my sincere thanks to Dr. Praveen Kumar Srivastava, who has been not just a collaborator but an inspiring person whose hard work, support, and encouragement have been invaluable time and again. I would also like to thank the Head of Department, Prof. Atul Sharma. I am truly thankful to Prof. A. S. K. Sinha for the support and kind gestures I received during his tenure at RGIPT as the director. I also appreciate the support received from RGIPT for the fellowship and providing analytical facilities that allowed me to devote myself entirely to my research. I would also like to acknowledge IIT Roorkee for providing research facilities. Thanks to Dr. Shailendra Tripathi, Dr. Deepanshu Rana, Dr. Kesari Nandan, and Dr. Anuj for all their help.

To my dear family, whose endless love, support, care, and understanding have been my foundation, I am profoundly thankful. For my parents, Smt. Gyan Kumari and Shri. Shatrughan Kumar Yadav, your constant support and encouragement and faith in me were the source of my strength. I also extend my gratitude to my lovely sisters, Anokhi and Vaishali, for their continuous support and empathy. Your presence has always been a stress buster.

A special thank you goes to my sweet juniors, Rahul, Vaibhav, Shani, Shashank, Aparajita, and Mohit; my dear friends, Ajeet, Arpan, Amit, Diksha, Anand, Sher, Prince, and Sumanth; my seniors at RGIPT, Akanksha, Divyanshi, Gargi, Niharika, and Abhishek; and my dear lab mates, Amrendra, Bhupendra, Ankit, Pooja and Sachin. The laughter we shared, countless tea breaks, and thoughtful discussions made this journey both enriching and memorable, leaving me with moments I will always cherish.

I would like to extend a special and heartfelt thanks to my dearest friend, Akash, whose unwavering support and quiet strength have been a constant source of encouragement. Your belief in me, shared laughter, and companionship lightened challenges and made every milestone more meaningful. Your friendship is a rare and treasured gift that will stay with me well beyond this thesis.

Finally, I extend my gratitude to everyone who, in different ways, offered help, advice, or encouragement throughout this journey. Your support has been essential to completing this work.

~ Shalu

Dedicated To

The Almighty
My Family and Friends

For their endless blessings, support, and love

Table of Contents

Acknowledgements ix

List of Abbreviations xxi

List of Figures xxiii

List of Tables xxvii

List of Equations xxix

Preface xxxi

CHAPTER 1 1

Introduction and Literature Survey 1

1.1 Background and Significance of Nanotechnology *1*

1.1.1 Definition and Fundamental Concepts 1

1.1.2 Importance of Nanotechnology 1

1.2 Historical Roots and Thermochemical Evolution of Green Nanotechnology *2*

1.2.1 Traditional Metallurgy as a Precursor to Modern Nanoscience 2

1.2.2 Mechanistic Bridging from Ancient Processing to Modern Green Nanoscience 5

1.3 Methods of Nanoparticles Synthesis *7*

1.4 The Need for Green Synthesis *7*

1.5 Role of Phytochemicals in Plant Mediated Nanoparticle Synthesis *9*

1.5.1 Major Phytochemical Classes 9

1.5.2 Theoretical Background and Mechanistic Insights 12

1.5.2.1 Classical Nucleation Theory (CNT) 12
1.5.2.2 LaMer Model: Burst Nucleation and Controlled Growth Mechanism 13
1.5.2.3 Oriented Attachment and Ostwald Ripening Mechanism 13
1.5.2.4 Role of Metal ion-Phytochemical Interaction 14
1.5.3 Major Phytochemical Classes Involved in Plant-Mediated Nanoparticle Synthesis 15
1.5.3.1 Flavonoids 15
1.5.3.2 Phenolic Acids 16
1.5.3.3 Tannins 16
1.5.3.4 Alkaloids 17
1.5.3.5 Terpenoids 17
1.5.3.6 Saponins 17
1.5.3.7 Synergistic Role of Phytochemicals 18
1.6 Classification of Nanomaterials *18*
1.6.1 Classification by Dimensionality 18
1.6.2 Classification by Origin 19
1.6.3 Classification by Composition 19
1.6.4 Classification by Morphology 19
1.7 Literature Review *20*
1.7.1 Reported Synthesis and Applications of Mixed Metal Oxide Nanoparticles 21
1.7.1.1 Nanoparticles for Environmental Applications 22
1.7.1.2 Magnetic and Structural Properties 23
1.7.1.3 Pharmaceutical and Biomedical Applications 24
1.8 Motivation and Research Gaps *26*
1.8.1 Research Gaps 26

1.8.2 Thesis Objectives 27

1.9 Conclusions *28*

CHAPTER 2 ..... **31**

Materials and Methods **31**

2.1 Materials *31*

2.2 Selection of plant (Moringa oleifera) for biosynthesis *32*

2.3 Preparation of Moringa oleifera Leaves Extract *33*

2.4 Phytochemical Profiling of Moringa oleifera Extract *34*

2.4.1 Qualitative screening of *Moringa oleifera* Leaves Extract 34

2.4.2 Gas Chromatography-Mass Spectrometry (GC–MS/MS) Analysis 34

2.4.2.1 Instrumentation and Sample Preparation 34

2.4.2.2 Analysis of GC-MS Profile 35

2.4.3 Ultra-Performance Liquid Chromatography (UPLC) Analysis 37

2.4.3.1 Instrumentation and Sample Preparation 37

2.4.3.2 Analysis of chromatographic Profile 37

2.5 Synthesis Methodologies *39*

2.5.1 Biosynthesis of Cu/Ni/Co Oxide Nanoparticles 41

2.5.2 Biosynthesis of CuO/NiO Nanoparticles 41

2.6 Experimental Techniques for Nanoparticle Characterization *43*

2.6.1 Fourier Transform Infrared Spectroscopy (FTIR) 43

2.6.2 Ultraviolet–Visible Spectroscopy (UV-Vis) 44

2.6.3 Diffuse Reflectance Spectroscopy (DRS) 45

2.6.4 X-Ray Diffraction (XRD) 46

2.6.5 X-Ray Photoelectron Spectroscopy (XPS) 47

2.6.6 Transmission Electron Microscopy (TEM) 47

2.6.7 Field Emission Scanning Electron Microscopy (FESEM) and Energy-Dispersive X-ray Analysis (EDAX) 48

2.6.8 Inductively Coupled Plasma Optical Emission Spectroscopy (ICP-OES) 49

2.6.9 BET (Brunauer-Emmett-Teller) Surface Area Analysis 50

2.6.10 Vibrating Sample Magnetometer (VSM) 52

2.7 Statistical Analysis *53*

2.8 Experimental Design and Methodology *53*

2.8.1 Production of Nano-Organic Vermicompost 53

2.8.1.1 Feedstock Formulation and Composting Setup 53

2.8.2 Evaluation of Plant Growth Parameters in *Abelmoschus esculentus* 54

2.8.2.1 Seed Germination Assay 54

2.8.2.2 Growth Indices and Calculations 54

2.8.3 Earthworm (Eisenia fetida) Survival Assay for Toxicity Assessment *55*

2.8.4 Sample Digestion and Preparation for ICP-OES analysis (metal toxicity) 55

2.8.5 Computational Screening for Drug-Likeness 56

2.8.6 Antimicrobial Assay 56

2.8.7 Molecular Docking Analysis of NPs Against *E. coli* and *F. oxysporum* 57

2.8.8 Spectrophotometric Quantification of Antimicrobial Activity 57

2.9 Concluding Remarks *58*

CHAPTER 3 ..... **59**

Synergistic effects of biogenic Cu/Ni/Co oxide nanoparticles on the agronomic performance of *Abelmoschus esculentus* (L.) in conjunction with organic compost amendments **59**

3.1. Introduction *59*

3.2 Results *63*

3.2.1 FTIR Analysis 63

3.2.2 XRD Analysis 63

3.2.3 XPS Analysis 64

3.2.4 EDAX and TEM Analysis 65

3.2.5 Physicochemical Properties, Nutrient Composition, And Surface Analysis of Vermicompost 67

3.2.6 Toxicological Evaluation of Biogenic CuO/NiO/CoO Nanoparticles on Earthworms 69

3.2.7 Toxicological Evaluation of Heavy Metals (Cu/Ni/Co) in Soil and Leaves of Okra Plant 70

3.2.8 Evaluation of Growth Performance of *A. esculentus* 71

3.2.8.1 The Seed Vigour Index (SVI) 73

3.2.8.2 The Mean Germination Time (MGT) 73

3.2.8.3 The Coefficient Velocity of Germination (CVG) 73

3.3 Discussion *75*

3.3.1 Evaluation of Agro-Waste Derived Vermicompost Maturity 75

3.3.2 Influence of *TmONs*-Enriched Vermicompost on Okra Growth Performance 76

3.3.3 Impact and Interaction of Biogenic Cu/Ni/Co Oxide Nanoparticles with Soil Health, Biodiversity, and Soil Biota 79

3.3.4 Physiochemical and Biochemical Roles of Cu, Ni, And Co in Plant Growth and Stress Tolerance 80

3.3.4.1 Role of Cu in Germination and Antifungal Activity 81

3.3.4.2 Role of Ni in Nitrogen Metabolism and ROS Signalling 81

3.3.4.3 Role of Co in Chlorophyll Synthesis, Metal Transport and Root Development 82

3.3.5 Mechanism of *TmONs* Uptake and Metal Ion Transport in Plants 84

3.3.6 Comparison of Agro-Waste Derived Vermicompost with Chemical Fertilizers 86

3.3.7 Potential Regulatory Challenges Associated with the Use of Nanoparticles 87

3.3.8 Leaching and Bioaccumulation of Cu, Ni, And Co Metals 87

3.4 Conclusions *88*

3.5 Limitations and Future Research Directions *89*

CHAPTER 4 ..... **91**

Influence of compositional variation on the structural, morphological, optical and magnetic properties of CuO/NiO NPs synthesized using *Moringa oleifera* leaves extract **91**

4.1 Introduction *91*

4.2 Results and Discussion *94*

4.2.1 Characterization of Synthesized Nanoparticles 94

4.2.2.1 Structural and Functional Analysis 94

4.2.2.2 Morphological and Surface Analysis 99

4.2.2.3 Optical Properties 104

4.2.2.4 Magnetic Properties and Size-Dependent Behaviour of CuO/NiO Biogenic Nanoparticles 106

4.3 Conclusions.....*110*

CHAPTER 5.....**113**

Evaluation of broad-spectrum antimicrobial efficacy of biogenic NiO/CuO nanocomposite: In vitro, in silico, and molecular docking approach.....**113**

5.1 Introduction.....*113*

5.2 Results and Discussion.....*117*

5.2.1 *In Silico* Drug-Likeness study of *M. oleifera*.....117

5.2.2 Characterizations of Biogenic NiO/CuO NPs.....119

5.2.2.1 FTIR Analysis.....119

5.2.2.2 UV-DRS Analysis.....121

5.2.2.3 PXRD Analysis.....122

5.2.2.4 FE-SEM and TEM Analysis.....123

5.2.3 Antimicrobial Efficacy of Biogenic NiO/CuO Nanoparticles.....124

5.2.3.1 Antibacterial Activity.....124

5.2.3.2 Antifungal Activity.....127

5.2.3.3 Evaluation of Time-Dependent and Species-Specific Microbial Inhibition..129

5.2.4 Molecular Docking and Interaction Analysis.....132

5.2.4.1 Enzymatic Mechanisms of Action: FabH & Chitin Synthase.....135

5.3 Conclusion and Future Perspectives.....*137*

CHAPTER 6.....**141**

Conclusions and Future Horizons.....**141**

6.1 Summary of Key Findings.....*141*

6.1.1 Green Synthesis as a Sustainable Route.....141

6.1.2 Comprehensive Physicochemical Characterization 142
6.1.3 Agricultural Applications and Soil Reclamation 142
6.1.4 Structure-Property Relationships 142
6.1.5 Broad Spectrum Antimicrobial Efficacy 143
6.1.6 Eco-toxicological and Regulatory Awareness 144
6.2 Future Horizons *144*
6.2.1 Functional Modifications 144
6.2.2 Use of AI–ML for Predictive Nanotechnology 144
6.2.3 Advancement in Agriculture 145
6.2.4 In Vivo and Clinical Validation 145
6.2.5 Molecular Level Mechanistic Studies 145
6.2.6 Policy, Regulation, and Commercialization Pathways 146
Appendix A **147**
References: *159*
List of Publications and Attended Conferences *181*
List of publications arising directly from thesis 181
List of attended conferences 181
List of attended workshops 182

List of Abbreviations

ABC - ATP-Binding Cassette
ADME - Absorption, Distribution, Metabolism, and Excretion
AMR - Antimicrobial Resistance
ANOVA - Analysis of Variance
ATR - Attenuated Total Reflectance
BBB - Blood-Brain Barrier
BET - Brunauer-Emmett-Teller
CD - Cow Dung
CGR - Cumulative Germination Rate
CNS - Central Nervous System
CVG - Coefficient Velocity of Germination
DRS - Diffuse Reflectance Spectroscopy
EC - Electrical Conductivity
EDAX - Energy-Dispersive X-ray Analysis
FabH - β-Kßetoacyl-acyl carrier protein synthase III
FESEM - Field Emission Scanning Electron Microscopy
FTIR - Fourier Transform Infrared Spectroscopy
FWHM - Full Width at Half Maximum
G% - Germination Percentage
HRTEM - High-Resolution Transmission Electron Microscopy
ICP-OES - Inductively Coupled Plasma Optical Emission Spectroscopy
IRT1 - Iron-Regulated Transporter 1
IUPAC - International Union of Pure and Applied Chemistry
LoD - Limit of Detection
MDR - Multidrug-Resistant
MGT - Mean Germination Time
MHA - Mueller Hinton Agar
MMONs - Mixed Metal Oxide Nanoparticles
MRI - Magnetic Resonance Imaging
MRSA - Methicillin-Resistant Staphylococcus aureus
MTCC - Microbial Type Culture Collection
NRAMP - Natural Resistance-Associated Macrophage Protein
NPK - Nitrogen, Phosphorus, Potassium
NPs - Nanoparticles
PDA - Photodiode Array
PM - Pressmud
PXRD - Powder X-ray Diffraction
ROS - Reactive Oxygen Species
RS - Rice Straw
SAED - Selected Area Electron Diffraction
SEM - Scanning Electron Microscopy
SMILES - Simplified Molecular Input Line Entry System
SSA - Specific Surface Area
SVI - Seedling Vigor Index
TEM - Transmission Electron Microscopy
TmONs - Trimetallic Oxide Nanoparticles
TOC - Total Organic Carbon

TPSA - Total Polar Surface Area
UPLC - Ultra-Performance Liquid Chromatography
UV-Vis - Ultraviolet-Visible Spectroscopy
VSM - Vibrating Sample Magnetometer
WHO - World Health Organization
XPS - X-ray Photoelectron Spectroscopy
XRD - X-ray Diffraction
ZFC - Zero Field Cooling
FC - Field Cooling

List of Figures

Figure 1.1: Comparative schematic of Bhasma preparation and nanomaterial synthesis.……3

Figure 1.2: Flow chart illustrating the steps involved in plant mediated synthesis of nanoparticles……..21

Figure 1.3: Major applications of nanomaterials in biomedical, agricultural, energy, and industrial sectors……25

Figure 2.1: Qualitative assays for phytoconstituent screening of *Moringa oleifera* extract……34

Figure 2.2: UPLC-PDA spectrogram of bioactive molecules of *Moringa oleifera* leaves extract……38

Figure 2.3: Schematic representation of *Moringa oleifera* assisted synthesis of Cu/Ni/Co oxide nanoparticles (*TmONs)* using green solution combustion method……...41

Figure 2.4: Schematic representation of *Moringa oleifera* assisted synthesis of CuO/NiO nanoparticles……..42

Figure 3.1: (A) FTIR spectrum and (B) XRD patterns of biogenic Cu/Ni/Co oxide nanoparticles synthesized using *M. oleifera* leaves extract…….……..….63

Figure 3.2: (A) Survey scan confirming the presence of Cu, Ni, Co, O, and (B--D) high-resolution fitted plots for Cu 2p, Ni 2p and Co 2p of biogenic Cu/Ni/Co oxide nanoparticles synthesized using *M. oleifera* leaves extract……..65

Figure 3.3: TEM image along with SAED pattern of biogenic Cu/Ni/Co oxide nanoparticles synthesized using *M. oleifera* leaves extract……66

Figure 3.4: Comparative analysis of nitrogen (N), phosphorus (P), and potassium (K) content (%) in raw materials and vermicompost-treated samples (T0--T3). Data shows enhanced nutrient levels in vermicompost treatments, with significant differences ($P < 0.05$) indicated by different letters. Bars represent the mean values ± standard error (SE)……68

Figure 3.5: Cumulative mortality (%) of *E. fetida* over a 21-day exposure period to different concentrations (50--500 ppm) of biogenic *TmONs* compared to the control. Bars represent Mean ± SE (n = 3)……70

Figure 3.6: Germination performance across different treatments (T0, nT0, nT1, nT2, nT3). The figure presents (A) cumulative germination and (B) germination percentage. Bars with different letters (a, b, c, d) indicate statistically significant differences among treatments at $P < 0.05$. Error bars represent the mean values ± standard error (SE). T0 (without *TmONs*), positive control as nT0 (T0+*TmONs*), nT1 (T1+*TmONs*), nT2(T2+*TmONs*) and nT3 (T3+*TmONs*)……72

Figure 3.7: Plots showing (A) Seed Vigour Index (SVI); (B) Mean Germination Time (MGT) and Coefficient Velocity of Germination (CVG). Bars with different letters (a, b, c, d) indicate statistically significant differences among treatments at $P < 0.05$. Error bars represent the mean values ± standard error (SE)…….74

Figure 3.8: Chord diagram depicting the associations between different treatments and seed germination parameters. The diagram visualizes the interconnections between five treatment groups, T0 (control), nT0, nT1, nT2, and nT3, and key germination indices. The thickness and direction of the chords indicate the relative contribution of each treatment to the germination metrics. Notably, nT3 and nT2 treatments show stronger associations with higher germination percentage and CVG, suggesting enhanced germination performance compared to the control……..78

Figure 3.9: (A) Pictures showing root length in treatment groups. (B) Ionic pathway for the metal ions (Cu^{2+}, Ni^{2+} and Co^{2+}) moving from roots to leaves. IRT1, NRAMP, HMAS, FPN2, HMA1/6/3, and ABC are transporter proteins involved in translocation…….……84

Figure 4.1: (A) XRD patterns of NM1, N12, N22, N21, and NM2 (orange highlighted area shows peaks for oxide mixing) and (B) Simulated XRD patterns for N22 biogenic nanoparticles against standard references……...95

Figure 4.2: (A) XPS full scan spectra, (B) O 1s spectrum, (C) Cu 2p spectrum, and (D) Ni 2p spectrum of biogenic N22……..97

Figure 4.3: FTIR spectra before and after calcination for (A) N12, (B) N22, and (C) N21 biogenic nanoparticles……99

Figure 4.4: The N_2 adsorption-desorption isotherm (STP) for biogenic N22 nanoparticles…….....101

Figure 4.5: FE-SEM images of the biogenic NM1, N12, N22, N21, and NM2 nanoparticles……102

Figure 4.6: TEM images and SAED patterns of N12, N22, and N21 of biogenic nanoparticles……103

Figure 4.7: (A) UV-DRS spectra and (B)--(D) Tauc plots of the biogenic nanoparticles (N12, N22 and N21)……...105

Figure 4.8: Variation in magnetic properties for all ratios of biogenic nanoparticles (A) Room-temperature hysteresis loops (inset shows magnified view near zero field), (B) Coercivity values, and (C) Saturation magnetization (Ms) and remanent magnetization (Mr) variations among all ratios…….107

Figure 4.9: Temperature dependence of magnetization (M/H) for (A) N12 sample, showing the Curie temperature (Tc) near 250 K, (B) N22 sample, highlighting transition around 60 K, and (C) N21 displaying two distinct low-temperature transitions below 100 K, followed by a gradual increase in M/H at higher temperatures……108

Figure 4.10: Plots showing the effect of particle size on the coercivity (Hc) of NM1, N22, and NM2 nanoparticles, with corresponding particle size distributions displayed on the right…….....109

Figure 5.1: (A) FTIR spectra for B12, B21, and *Moringa* leaves extract and (B) Phenolic acids and polyphenols of *Moringa oleifera* indicating active sites for antimicrobial reactivity. Red circles indicate hydroxyl groups generating phenoxide radicals, and blue lines indicate chelating sites……121

Figure 5.2: UV-DRS patterns of B12 and B21. The dashed line shows absorption maxima for both the mixed oxides……122

Figure 5.3: Powder-XRD patterns of B12 and B21 along with matched references for NiO (Ref. ICSD-9866, red) and CuO (Ref. ICSD-69758, black) (dashed line and circle show mixing of peaks for both oxides)…….123

Figure 5.4: (A--B) SEM micrographs of B12 and B21 nanoparticles showing spherical morphology with slight agglomeration, (C--D) TEM images confirming nanoscale size and uniform distribution, (E--H) elemental mapping of B12 indicating the presence of Ni, O, and Cu, and (I--L) elemental mapping of B21 confirming homogeneous distribution of Ni, O, and Cu within the nanoparticles……..124

Figure 5.5: (A) Antibacterial activity of biogenic NiO/CuO nanoparticles synthesized in different ratios (B12 and B21) and concentrations (100 and 250 mg/mL) against four pathogenic bacterial strains. Inhibition zones (mm) were measured using the agar well diffusion method (mean ± SD, n = 3) and (B) Images showing the zones of inhibition on nutrient agar plates after treatment with the respective nanoparticle formulations against the tested bacterial strains……126

Figure 5.6: (A) Antifungal activity of biogenic NiO/CuO nanoparticles at different ratios (B12 and B21) and concentrations (100 and 250 mg/mL) against fungal strains. Inhibition zones (mm) were determined using the agar well diffusion method (mean ± SD, n = 3) and (B) Photographic representation of fungal inhibition zones on PDA plates for respective treatments……128

Figure 5.7: Growth inhibitory kinetics of microbial strains treated with biogenic NiO/CuO nanoparticles (B12-100, B12-250, B21-100, B21-250) at 2, 4, and 6 h, measured at 540 nm:(A) *E. coli*, (B) *S. flexneri*, (C) *S. enterica*, (D) *S. aureus*, (E) *F. oxysporum*, (F) *A. niger*, and (G) *A. flavus*. Data are mean ± SD (n = 3). Statistical significance: $*P < 0.01$; $**P < 0.001$. Different letters indicate significant differences at $P < 0.05$……..132

Figure 5.8: Molecular docking interactions of biogenic NiO and CuO nanoparticles with microbial enzymes: (A) FabH from *E. coli* and (B) chitin synthase from *F. oxysporum*. The left side depicts CuO docking, and the right side shows NiO interactions with their respective enzyme targets. NiO nanoparticles exhibit deeper binding within the active site pockets and form multiple interactions with catalytically essential residues, suggesting stronger and more stable inhibitory potential. In contrast, CuO nanoparticles demonstrate surface-level binding and reduced interaction density. The enzyme structures are rendered

in cartoon format (α-helices in red, β-sheets in cyan), with active site residues highlighted and nanoparticle interactions shown as stick and surface representations……135

Figure 5.9: Enzymatic mechanisms of beta-ketoacyl-acyl carrier protein synthase III (FabH) and Chitin Synthase highlighting substrate binding, product formation, and their roles in bacterial lipid and fungal cell wall biosynthesis…….137

Figure 6.1: Summary of key conclusions and future directions of the thesis……..144

List of Tables

Table 1.1: Comparison between traditional Bhasma preparation and modern green nanoparticle synthesis ……..…..…04

Table 1.2 Standard reduction potentials of selected metal ions and mechanistic roles of major phytochemical classes in plant-mediated nanoparticle synthesis ……..……..10

Table 1.3 Classification of nanomaterials based on dimensionality and representative examples ……...….19

Table 1.4 Classification of nanomaterials by origin …….……....19

Table 1.5 Classification of nanomaterials by composition ……...19

Table 1.6 Classification of nanomaterials by morphology…….....20

Table 1.7 Comparative summary of green-synthesized mixed metal oxide nanoparticles……..25

Table 2.1: Major Phytochemical Constituents Identified in *Moringa oleifera* Leaves Extract through GC-MS/MS Analysis……..36

Table 3.1 Physicochemical parameters of vermicompost derived from different feedstocks……..67

Table 3.2 Table showing LoD (limit of detection) values and coefficient of regression (r^2)…….71

Table 3.3 ICP-OES analysis of soil samples after growth of *A. esculentus*…….71

Table 3.4 Effects of nanoparticles on different plant growth parameters across different plant species and dosages……..77

Table 4.1 BET surface area, average pore diameter and pore volume of the biogenic NM1, N12, N22, N21, and NM2 nanoparticles……100

Table 4.2. Values of Hc, Ms, Mr, squareness, and magnetic anisotropy, K, for nanoparticles NM1, N12, N22, N21, and NM2…….110

Table 5.1 Drug-likeness predictions of *Moringa oleifera* leaves extract phytoconstituents computed by SwissADME……...118

Table 5.2 Results of molecular docking interaction of CuO and NiO with target proteins in *E. coli* and *F. oxysporum*…….133

List of Equations

Equation 2.1: Gibbs free energy equation……38

Equation 2.2: Vibrational frequency of harmonic oscillator (diatomic molecule)……43

Equation 2.3: Beer-Lambert law……...44

Equation 2.4: Tauc-Lorentz equation…….……...45

Equation 2.5: Absorption coefficient……45

Equation 2.6: Kubelka–Munk function……45

Equation 2.7: Modified Tauc equation……..45

Equation 2.8: Bragg's law……..46

Equation 2.9: Equation average crystallite sizes……..…….46

Equation 2.10: Einstein's photoelectric equation…….....47

Equation 2.11: de Broglie relationship……...47

Equation 2.12: Specific Surface Area…….51

Equation 2.13: Brunauer-Emmett-Teller equation…….51

Equation 2.14: Langmuir equation…….51

Equation 2.15: Faraday's law of electromagnetic induction……..52

Equation 2.16: Cumulative germination percentage (CGR)……...54

Equation 2.17: Coefficient of velocity of germination (CVG%)……54

Equation 2.18: Germination percentage (G%)……...54

Equation 2.19: Mean germination time (MGT%) …….54

Equation 2.20: Seedling Vigour Index(SVI)……..55

Equation 4.1: Debye-Scherrer equation …….……95

Equation 4.2: Tauc relation……..……..104

Preface

The conventional chemical way for fabricating nanomaterials is being paid ever-growing attention due to the environmental pollution, hazardous substances, and threats to human and ecological health. These traditional strategies frequently overlook the crucial demand of environmentally benign, scalable, and functionally versatile materials, particularly in the case of metal oxide nanostructures. The advancement of synthesis approaches combining both multifunctionality and environmental safety is still a major issue, especially in the case of mixed metal oxide nanoparticles (MMONs). Phytochemicals based synthesis has recently emerged as a revolutionary approach in the arena of nanomaterials science, since the bioactive agents (e.g., flavonoids, alkaloids, phenolic acids, and other plant secondary metabolites) are being exploited as natural reducing, capping, and stabilizing agents. This green approach of synthesis gives a two-fold benefit in terms of non-toxicity of the synthetic process, as well as the unique surface biochemistry of the resulting nanoparticles. These bioactive-functionalized surfaces with modulated phenolic compounds and their derivatives exhibit enhanced biological interactions, which are extremely difficult to achieve through traditional synthetic routes.

The present research systematically explores the green synthesis of multifunctional MMONs and their diverse applications in environmental remediation, sustainable agriculture, and antimicrobial defense. Importantly, the phytogenic MMONs developed in the present work demonstrate superior performance in terms of bioactivity, stability, and compositional complexity, which make them an eco-compatible alternative for the chemically synthesized analogues. In addition, this study highlights the need for extensive background impact assessments, particularly in the application of these materials in ecological and agricultural fields. This study develops an environmentally friendly synthesis strategy for ultra-high performance MMONs, which is promising in serving green and sustainable materials science

and better understanding the theoretical parameters, together with the potential global challenge in environment protection, energy harvesting, and renewable applications.

The thesis is structured as follows:

Chapter 1 offers an exhaustive review of the historical development and evolution of nanomaterial synthesis, starting from traditional *Bhasma* formulations to modern phytochemical-assisted techniques. Emphasis is placed on the comparative analysis of chemical and biological synthesis strategies, the role of phytoconstituents in nanoparticle formation. The literature survey along with research gaps and objectives is also presented.

Chapter 2 deals with the phytochemical characterization of medicinal plant utilized for MMONs synthesis. Comprehensive documentation of reagents, experimental methodologies, and instrumental techniques for nanoparticles synthesis and characterization, including advanced spectroscopic and microscopic approaches, is presented.

Chapter 3 investigates the synergistic effects of biogenic Cu/Ni/Co oxide nanoparticles on the agronomic performance of *Abelmoschus esculentus* (L.) in conjunction with organic compost amendments. This chapter also integrates ecotoxicological assessments, focusing on nanoparticles-soil-plant interactions during critical growth stages.

Chapter 4 examines the influence of compositional variation on the structural, morphological, optical, and magnetic properties of CuO/NiO MMONs synthesized using *Moringa oleifera* leaves extracts, employing comprehensive physicochemical characterization techniques.

Chapter 5 addresses the antimicrobial efficacy of biogenically synthesized NiO/CuO nanocomposites against a spectrum of pathogenic strains. The chapter also presents mechanistic insights derived from *in silico* molecular docking simulations, correlating phytochemical interactions with observed bioactivity. A manuscript on the results of this chapter has been submitted for publication.

Chapter 6 summarizes the core findings and discusses future prospects, advocating for the expanded utilization of green synthetic approaches in the development of functional nanomaterials for health, energy, and environmental applications.

***Note on Published Work**

Parts of this thesis are based on the author's published and accepted research papers.

- Chapter 3 is based on: "Optimizing growth performance of *Abelmoschus esculentus* (L.) via synergistic effects of biogenic Cu/Ni/Co oxide nanoparticles in conjunction with rice straw and pressmud-based vermicompost," accepted and in press in *Pedosphere*, available online on 26th August 2025, DOI: https://doi.org/10.1016/j.pedsph.2025.08.009.
- Chapter 4 is based on: "Composition dependent variation in structural, morphological, optical and magnetic properties of biogenic CuO/NiO mixed oxide nanoparticles," published in *Journal of Alloys and Compounds*, Vol. 979, 173422, 2024.
- Chapter 5 is based on: "Evaluation of broad-spectrum antimicrobial efficacy of biogenic NiO/CuO nanocomposite: In vitro, in silico, and molecular docking approach. *Biomass and Bioenergy*, 208, 108882. https://doi.org/10.1016/j.biombioe.2025.108882.

These papers were authored by Ms. Shalu Yadav (first author) under the supervision of Prof. Abhay Kumar Choubey. The results have been reproduced in this thesis with permission from the respective publishers, and all necessary acknowledgements have been provided.

***

CHAPTER 1

Introduction and Literature Survey

1.1 Background and Significance of Nanotechnology

1.1.1 Definition and Fundamental Concepts

Nanotechnology is a rapidly emerging and by nature, a multidisciplinary field involved with the manipulation and control of matter at dimensions typically between 1 and 100 nanometres[1]. At this nanoscale dimension, materials acquire some unique and augmented physical, chemical, and biological properties significantly different from their bulk counterparts. One of the most essential factors responsible for these novel properties is the dramatic increase in surface area relative to volume as particle sizes are reduced to the nanoscale[2]. This high surface-to-volume ratio enhances reactivity, surface energy, and interaction with surrounding environments, enabling nanomaterials to be highly efficient in catalysis, drug delivery, environmental remediation, and sensing.

1.1.2 Importance of Nanotechnology

The importance of nanotechnology lies in its broad applicability and its potential to solve longstanding challenges in healthcare, energy, agriculture, electronics, and environmental science[3]. In biomedical sciences, their nano sizes allow them to pass biological barriers and can be designed to perform at targeted drug delivery with minimal side effects, thus enhancing therapeutic outcomes[4]. In electronics, the use of smaller particles facilitate miniaturization and the development of faster and more efficient devices[5]. In materials science, nanomaterials enhance the mechanical strength, durability, and thermal stability of composites[6]. The revolutionary effect of this field

had a world market of $85 billion in 2021, which rose to $140 billion in 2024, and expected to rise further to $288 billion by 2030, at a compound annual growth rate of nearly 19.9% [7]. This rapid increase reveals regular investment and innovation across distinct domains. Global patents in the field of nanotechnology have increased by more than 150% from 2000 to 2024, with China grabbing around 40%. The United States is dedicating over $30 billion worldwide since 2001, highlighting its significance in research and development[8].

The rapid growth of the nanotechnology industry has simultaneously intensified the need for sustainable manufacturing strategies. Accordingly, plant-mediated green synthesis has emerged as a promising alternative to conventional chemical routes by reducing the use of hazardous reagents, minimizing environmental impacts, and supporting the principles of green chemistry and circular economy[9]

1.2 Historical Roots and Thermochemical Evolution of Green Nanotechnology

1.2.1 Traditional Metallurgy as a Precursor to Modern Nanoscience

The idea of manipulation of matter at the micro or nano level, though rooted ancient practices, was realized by scientists in the last few decades only. History indicates the accidental use of nanomaterials by ancient civilizations, and there is enough evidence that the art was particularly originated in India[10]. Ancient Indian medicine, particularly Ayurveda and Siddha systems, has the primary evidence of nanoscale manipulation in the use of finely powdered metals and minerals, known as *Bhasma*.

*Bhasma*s like *Swarna Bhasma* (gold ash), *Rajata Bhasma* (silver ash), and *Tamra Bhasma* (copper ash) were prepared by complicated incineration techniques and were presumed to improve bioavailability and therapeutic efficacy[11]. For instance, *Swarna Bhasma* works as a Rasayana and immune modulator with antioxidant and anti-inflammatory potential[12], while *Rajata Bhasma* exerts strong antimicrobial

activity[13]; *Tamra Bhasma* supports liver function and metabolic regulation[14], and *Yashada Bhasma* (zinc ash) assists in the management of diabetes and ocular disorders[15], [16], and *Abhraka Bhasma* (mica ash) prepares respiratory and reproductive health[17].

The preparation of these metallic and mineral-based medicines is described in ancient Indian texts like the *Charaka Samhita* and *Rasa Shastra*, which detail methods involving the purification, reduction in particle size, and bio-assimilation of these metals and minerals. Characterization using modern techniques has proved that most of the *Bhasma*s contain particles in the nanometre range[18]. These findings indicate that ancient metallurgists successfully produced nanocrystalline materials centuries before the development of modern nanoscience, relying solely on empirical observations and naturally occurring materials.

The preparation of Bhasma generally involves four sequential stages: *Shodhana* (purification), *Bhavana* (wet grinding with herbal extracts), *Marana* (controlled thermal calcination), and *Amritikarana* (post-treatment for stabilization and detoxification). Although these procedures were developed without modern theoretical knowledge, they closely resemble several stages involved in contemporary nanoparticle synthesis, as illustrated in Figure 1.1.

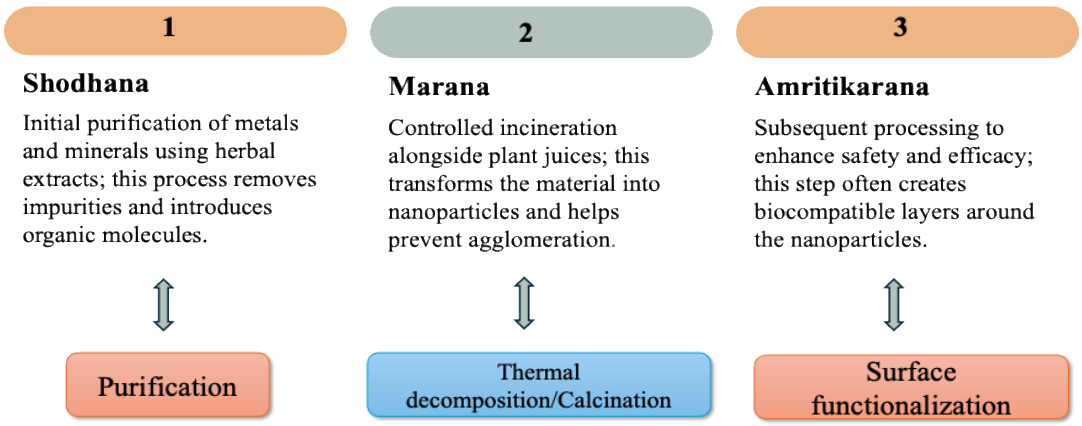

Figure 1.1: Comparative schematic of Bhasma preparation and nanomaterial synthesis.

Table 1.1 Comparison between traditional Bhasma preparation and modern green nanoparticle synthesis

Process Stage	**Traditional Bhasma (Ancient Metallurgy)**	**Modern Green Nanoscience Equivalent**	**Thermochemical Significance**
Purification / Activation	Shodhana: heating with herbal decoctions; removes impurities via reduction	Pre-treatment of metal salts; extract-mediated ligand exchange	$\Delta G° < 0$ for metal-ligand complexation; activation energy lowered by phytochelation
Particle formation / Nucleation	Marana: repeated incineration (600-900°C) in oxidative atmosphere	Solution combustion / calcination (300-600°C) with phytochemical fuel	Metal oxidation: $M^0 \rightarrow M^{n+} + ne^-$; exothermic ($\Delta H < 0$); drives phase formation
Redox cycling	Partial reduction by organic pyrolysis gases (CO, hydrocarbons); re-oxidation in air	Phytochemical electron donation (flavonoids, phenols) reduces $M^{n+} \rightarrow M^0$; oxide capping follows	Cyclic $Cu^{2+}/Cu^{+}/Cu^0$ and Ni^{2+}/Ni^0 redox enables controlled nucleation kinetics
Stabilization / Capping	Organic residues from Bhavana coat particles; prevent sintering	Polyphenols and proteins adsorb on NP surface; zeta potential $\geq \lvert\pm 25$ mV$\rvert$	Surface free energy minimized; thermodynamic driving force for capping: $\Delta G_surf < 0$
Particle size control	Iterative grinding (Bhavana) reduces size to nano-range	Phytochemical concentration governs nucleation rate	Scherrer equation: $D = k\lambda/(\beta\cos\theta)$; particle size is governed by nucleation kinetics and crystallite evolution

From a thermochemical viewpoint, the *Marana* stage closely resembles the calcination processes employed in modern nanoparticle synthesis. During controlled heating, metals undergo oxidation reactions that produce thermodynamically stable oxide phases. These reactions are characterized by negative Gibbs free energy changes ($\Delta G° < 0$), indicating spontaneous oxide formation under elevated temperatures according to Ellingham-type thermodynamic principles[19]. Such transformations are directly analogous to modern thermal decomposition of metal precursors, where nitrates, acetates, or

hydroxides convert into stable oxide phases such as CuO, NiO, and Co_3O_4 under controlled heating regimes.

A distinctive feature of ancient metallurgical systems is the incorporation of organic materials derived from plant extracts during intermediate processing stages. Upon heating, these biomolecules undergo pyrolytic decomposition, generating reducing species (e.g., CO, hydrocarbons) and transient carbonaceous environments. Consequently, repeated oxidation and reduction cycles occur during heating, closely resembling the redox environments observed in modern solution combustion synthesis (SCS) and other fuel-assisted thermochemical methods [20].

Repeated heating and cooling cycles characteristic of traditional *puta* systems also generate thermal gradients that promote lattice fragmentation, defect generation, recrystallization, and crystallite refinement. These processes closely parallel contemporary concepts of non-equilibrium thermodynamics, where repeated thermal cycling stabilizes energetically favourable phases while simultaneously controlling crystallite size and microstructure. Collectively, these observations suggest that ancient metallurgical practices can be interpreted as early thermochemical reactors in which thermal energy governed phase transformations, organic constituents regulated redox chemistry, and cyclic thermal processing controlled particle growth and crystallinity. Although these techniques were developed empirically, they embody several of the same physicochemical principles that underpin contemporary green nanotechnology.

1.2.2 Mechanistic Bridging from Ancient Processing to Modern Green Nanoscience

While the preparation of traditional *Bhasma* was based primarily on empirical knowledge, it followed the basic principles of plant based nanomaterials synthesis: reduction, oxidation, nucleation, and stabilization [21]. The herbal decoctions used in *Shodhana* and *Marana* contained phytochemicals such as polyphenols, alkaloids, and

terpenoids, which act today as reducing and capping agents in plant-mediated green synthesis.

Green nanotechnology has scientifically refined these age-old principles into a mechanistic understanding with controlled reaction parameters and advanced characterization techniques. Contemporary synthesis protocols precisely regulate precursor concentration, reaction temperature, pH, extract composition, and reaction kinetics, enabling reproducible control over nanoparticle size, crystallinity, morphology, and surface chemistry[21]. Several stages of traditional Bhasma preparation exhibit direct mechanistic parallels with modern nanomaterial synthesis. For example, the *Marana* step, involving high-temperature incineration, finds its counterpart in modern calcination and thermal decomposition techniques for the preparation of metal oxide nanoparticles such as CuO, NiO, and Fe_2O_3 with controlled crystallinity and particle size. The cyclic heating in their traditional methods has its equivalent in microwave-assisted syntheses, which ensure rapid and uniform energy transfer to produce fine and homogeneous particles. Furthermore, extensive mechanical grinding of metals during *Marana* has its equivalent in high energy ball milling, a top-down nanofabrication approach[22].[23]. Incorporation of herbal media as natural templates reflects modern bio-templating strategies to guide particle shape and morphology, while the *Amritikarana* process is in alignment with surface functionalization approaches used today for improving nanoparticle dispersibility and biocompatibility. Collectively, these comparisons establish that ancient *Bhasma* practices represent an early integration of natural processes for material transformation, offering a historically rooted foundation for today's eco-inspired and green synthesis strategies.

1.3 Methods of Nanoparticles Synthesis

In general, the methods of nanoparticle synthesis are classified into top-down and bottom-up approaches. In the **Top-down approaches,** bulky materials are physically reduced to nanosized particles by mechanical milling, lithography, laser ablation, or sputtering[24], [25]. While these methods are effective in producing uniform nanoparticles, they suffer from various disadvantages such as being energy-intensive and often flawed by surface defects and contamination, with control over particle morphology not fully exercised. In contrast, in the **Bottom-up approaches**, nanoparticles are assembled atom-by-atom or molecule-by-molecule through chemical or biological routes, which include sol-gel synthesis[26], co-precipitation[27], hydrothermal processing[28], and biological synthesis. The bottom-up methodology allows for precise control over particle composition, crystallinity, and size distribution and thus is ideal for producing multifunctional nanomaterials.

However, most of the chemical and physical routes require toxic solvents, high temperatures, and reducing agents, which have a high cost in environmental and health risks. These disadvantages helped to develop green synthesis methods where nanoparticles are prepared using biological resources such as plants, microbes[29], or biomolecules[30], [31] that act like natural factories for nanoparticle formation.

1.4 The Need for Green Synthesis

Green synthesis processes demonstrate a strong adherence to the twelve principles of green chemistry, with environmental safety, sustainability, and waste stream reduction as critical design considerations[32], [33], [34]. Unlike conventional chemical synthesis, which depends on hazardous reducing agents such as hydrazine, sodium borohydride, or formaldehyde green synthesis utilizes naturally occurring plant biomolecules including flavonoids, terpenoids, alkaloids, phenolic acids, tannins, and reducing sugars[35], [36]

[37]. Each of them performs a dual function, reducing metal ions while also stabilizing new nanoparticles via surface capping mechanisms, eliminating the need for multiple processing steps or additional chemical reagents[38], [39]. This integrated mechanism makes plant-mediated synthesis an excellent choice for eco-friendly and cost-effective nanomaterial synthesis.

Another important advantage of plant-based pathways is its high energy efficiency. Most biogenic pathways function at ambient temperatures and pressures, avoiding energy-intensive thermal or hydrothermal conditions [33], [40], [41]. Compared with microbial or enzymatic synthesis, plant-based synthesis offers substantial advantages over microbial or enzymatic techniques in terms of scalability, ease of usage, and reproducibility, making it a viable option for synthesizing nanomaterials for large-scale and industrial applications [42].

The environmental and economic benefits of green synthesis have been demonstrated through several sustainability indicators. In comparison with traditional approaches, green synthesis has exhibited a reduction in energy consumption by around 30%, cost savings up to 40% and increase in industrial output up to 50% [43]. These enhancements translate into substantial savings in operating costs and environmental footprint for industrial-scale nanoparticle production. Particular green-metric evaluations of metal oxide nanoparticles offer tangible quantitative targets. For instance, the atom economy of TiO_2 nanoparticles prepared through green routes has been calculated as 19.37%, percentage yield 97%, stoichiometric factor 8.51 and Kernel reaction mass efficiency (RME) 18.79% [44]. Collectively, these metrics reflect the potential of plant material in waste reduction, improve resource utilization, and support large scale production of nanomaterials[34].

The growing adoption of plant-mediated synthesis therefore reflects a fundamental transition in nanotechnology from maximizing production efficiency alone toward balancing material performance with environmental stewardship and economic sustainability. As research continues to elucidate the molecular mechanisms governing biogenic nanoparticle formation, attention has increasingly focused on the phytochemicals responsible for metal-ion reduction, nucleation, particle growth, and stabilization.

1.5 Role of Phytochemicals in Plant Mediated Nanoparticle Synthesis

1.5.1 Major Phytochemical Classes

The success of plant-mediated nanoparticle synthesis largely depends on the diverse phytochemicals naturally present in plant extracts. These biomolecules serve as multifunctional reagents by simultaneously reducing metal ions, regulating nucleation and crystal growth, and stabilizing the resulting nanoparticles through surface adsorption. Unlike conventional chemical synthesis, where separate reducing and capping agents are generally required, plant extracts integrate these functions into a single reaction system, making nanoparticle synthesis both environmentally sustainable and economically attractive. Plant metabolites contain numerous electron-donating functional groups, including hydroxyl (–OH), carbonyl (C=O), carboxyl (–COOH), amino ($–NH_2$), and glycosidic moieties. These functional groups readily interact with dissolved metal ions through electron transfer and coordination bonding, initiating nanoparticle formation under mild reaction conditions. Besides reducing metal precursors, phytochemicals adsorb onto the nanoparticle surface, lowering surface free energy and preventing aggregation through steric and electrostatic stabilization. Consequently, they influence not only nanoparticle formation but also the final particle size, morphology, crystallinity, surface charge, and colloidal stability [45].

The efficiency of phytochemical-mediated reduction depends on the electrochemical characteristics of the metal precursor. Metal ions possessing relatively positive standard reduction potentials, such as Cu^{2+}, are reduced more readily than ions with lower reduction potentials, including Ni^{2+} and Co^{2+}. The overall reduction kinetics are therefore governed by the combined effects of metal-ion redox potential, phytochemical composition, reaction temperature, pH, and extract concentration. Understanding these interactions is essential for controlling nanoparticle nucleation and tailoring the physicochemical properties of green-synthesized nanomaterials. [46]

The principal phytochemical classes involved in plant-mediated nanoparticle synthesis include flavonoids, phenolic acids, tannins, alkaloids, terpenoids, proteins, polysaccharides, and saponins. Although each class exhibits distinct chemical structures, they collectively contribute to nanoparticle formation through complementary mechanisms involving electron transfer, metal-ion complexation, crystal growth regulation, and surface stabilization. Their respective electrochemical roles and mechanistic functions are summarized in Table 1.2.

Table 1.2 Standard reduction potentials of selected metal ions and mechanistic roles of major phytochemical classes in plant-mediated nanoparticle synthesis

Species / Phytochemical class	**Standard reduction potential, E° (V vs. SHE)***	**Major functional groups**	**Mechanistic role in nanoparticle synthesis**
$Cu^{2+} + 2e^- \rightarrow Cu$	+0.340	—	Easily reduced under mild phytochemical conditions; promotes rapid nucleation of Cu/CuO nanoparticles
$Ni^{2+} + 2e^- \rightarrow Ni$	−0.257	—	Requires stronger phytochemical concentration for reduction
$Co^{2+} + 2e^- \rightarrow Co$	−0.282	—	Similar reduction behaviour to Ni^{2+}; slower nucleation kinetics than Cu^{2+}
Flavonoids	—	Catechol, hydroxyl (–	Strong electron donors; reduce metal ions through oxidation of phenolic groups

		OH), carbonyl (=O)	to quinones and stabilize nanoparticles by surface capping
Phenolic acids	—	–OH, –COOH	Donate electrons and form coordination complexes with metal ions; contribute to reduction and stabilization
Tannins	—	Multiple phenolic –OH groups	Multiple electron transfer and strong chelation; provide steric stabilization and inhibit aggregation
Alkaloids	—	Amines, heterocyclic nitrogen	Coordinate with metal ions, influencing morphology and nanoparticle stabilization rather than acting as primary reducing agents
Terpenoids	—	Alcohol, aldehyde, ketone	Mild reducing agents; regulate crystal growth and surface stabilization
Saponins	—	Glycosidic hydroxyl groups	Surfactant-like molecules that improve dispersion and prevent nanoparticle aggregation

* Standard reduction potential (E°) are taken from the internationally accepted compilation of standard electrode potentials [46]. The mechanistic roles are summarized from recent reviews on plant mediated nanoparticle synthesis and therefore represent generalized mechanisms [39], [47], [48], [49].

The cooperative action of these phytochemicals determines the overall kinetics of nanoparticle synthesis. Strong electron donors initiate rapid reduction of metal ions and generate supersaturation, whereas larger biomolecules adsorb onto growing crystal surfaces to regulate particle growth and prevent uncontrolled aggregation. Consequently, variations in phytochemical composition among different plant species frequently produce nanoparticles with distinct sizes, morphologies, crystallinities, and functional properties despite identical reaction conditions.

Although the specific contribution of each phytochemical class is important, nanoparticle formation is fundamentally governed by classical nucleation and crystal growth

mechanisms. These theoretical models provide the mechanistic framework for understanding how metal ions are transformed into stable nanostructures during plant-mediated synthesis and are discussed in the following section.

1.5.2 Theoretical Background and Mechanistic Insights

The synthesis of nanoparticles, especially through plant-mediated green chemistry, can be theoretically explained by classical nucleation theory (CNT), LaMer's model of nucleation and growth, and Ostwald ripening mechanisms combined. These models explain collectively the transformation of ionic precursors into stable nanoscale materials, whereby phytochemicals act in each stage of nanoparticle formation- nucleation, growth, and stabilization[42].

1.5.2.1 Classical Nucleation Theory (CNT)

According to the principles of CNT, the formation of nanoparticles initiates the minute clusters or nuclei from a supersaturated solution of metal ions. In plant-mediated synthesis, this is initiated when phytochemicals interact with the metal ions, reducing them into their elemental or oxide forms. With an increase in the concentration of these reduced atoms, they start aggregating to form stable nuclei, which marks the onset of nanoparticle formation[50].

The hydroxyl (-OH), carboxyl (-COOH), and amine ($-NH_2$) groups in the phytochemicals participate in this process. They enable the reduction of metal ions by lowering the interfacial energy between the forming particles and the surrounding medium. This reduction in surface energy allows the nucleation to happen naturally, without any aggressive chemicals or high energy input, in mild conditions of temperature and pH[51]. After the nuclei were formed, they acted as seeds toward further particle growth, developing well-defined and stable nanoparticles[52].

1.5.2.2 LaMer Model: Burst Nucleation and Controlled Growth Mechanism

CNT was further refined by the model of LaMer and Dinegar (1950) into three distinct stages: pre-nucleation, nucleation burst, and growth phase. After the supersaturation threshold is achieved, as explained in CNT theory, a sudden formation of a lot of nuclei within a short duration reduces the metal ion concentration sharply. Extra ions and small clusters from this decompose and deposit onto existing nuclei, thus continuing particle growth. Phytochemicals will act not only as reducing agents but also as kinetic moderators. They will affect the rate of nucleation and growth, which governs nanoparticle size and morphology. High concentrations of reducing phytochemicals result in rapid nucleation and smaller particle sizes, while a low concentrations or stronger capping agents result in slower growth and larger, well-faceted nanoparticles. For instance, polyphenols like catechins and quercetin donate electrons rapidly, promoting burst nucleation while polysaccharides and proteins with bulky structures restrict diffusion, favoring gradual growth and shape control[53].

1.5.2.3 Oriented Attachment and Ostwald Ripening Mechanism

After the conclusion of nucleation and the initiation of the growth phase, further nanoparticles development run through two major pathways: Ostwald ripening and Oriented attachment. Both steps have critical roles in determining the final size, shape, and stability of nanoparticles synthesized via plant-mediated routes. In this green synthesis, Ostwald ripening (grow of larger nanoparticles at the expense of smaller ones due to differences in solubility and surface energy) is suppressed by phytochemical capping agents (such as polyphenols, proteins, and polysaccharides) through protective layers that slow down dissolution and prevent uncontrolled aggregation. The degree of ripening depends on factors such as extract composition and temperature[54]. On the other hand, the functional groups in plant metabolites selectively bind to particular crystal

facets to minimize the surface energy, directing Oriented attachment processes and leading to anisotropic structures such as rods, spheres, or plates[55], [56].

1.5.2.4 Role of Metal ion-Phytochemical Interaction

The coordination chemistry between metal ions and phytochemicals governs the initiation and evolution of nanoparticles. Hydroxyl and carboxyl groups in phenolic compounds form coordination complexes with metal ions such as Cu^{2+}, Ni^{2+}, and Zn^{2+}, which subsequently undergo reduction[57]. On the other hand, the electron-donating ability of phytochemicals is correlated with their redox potential; flavonoids and polyphenols can donate electrons through π–π conjugation systems, leading to metal ion reduction and oxide formation[58], [59]. Similarly, the binding of organic molecules to the nanoparticle surface stabilizes the colloidal system and modulates its zeta potential, preventing aggregation[60]. These interactions collectively explain the bio-directed assembly of nanoparticles, where plants act as natural nano-factories performing reduction, nucleation, growth, and stabilization in a single integrated process.

Overall, plant-mediated nanoparticle synthesis represents a highly coordinated process in which thermodynamics, reaction kinetics, nucleation theory, crystal growth mechanisms, and phytochemical coordination chemistry collectively determine the structural and functional characteristics of the final nanomaterial. While these theoretical models explain the mechanisms governing nanoparticle formation, the efficiency of each stage ultimately depends on the chemical nature of the phytochemicals present in the plant extract. Different classes of plant metabolites exhibit distinct reducing capacities, coordination behaviour, and surface-binding affinities, thereby influencing nanoparticle nucleation, growth, morphology, and stability. The following section therefore examines the major phytochemical classes individually and discusses their specific mechanistic roles in plant-mediated nanoparticle synthesis.

1.5.3 Major Phytochemical Classes Involved in Plant-Mediated Nanoparticle Synthesis

Although plant extracts contain hundreds of secondary metabolites, only a limited number of phytochemical classes actively participate in nanoparticle formation. Their contribution depends on molecular structure, redox potential, coordination chemistry, and affinity for nanoparticle surfaces. Collectively, these compounds regulate metal-ion reduction, nucleation kinetics, crystal growth, morphology, colloidal stability, and, ultimately, the physicochemical properties of the synthesized nanoparticles[45].

1.5.3.1 Flavonoids

Flavonoids constitute one of the most abundant classes of polyphenolic compounds found in higher plants and are regarded as the primary reducing agents during plant-mediated nanoparticle synthesis. Structurally, they possess a characteristic C6-C3-C6 carbon framework consisting of two aromatic rings connected by a three-carbon bridge [61]. The presence of multiple hydroxyl and carbonyl functional groups enables flavonoids to readily donate electrons through oxidation of phenolic hydroxyl groups to quinone structures. During nanoparticle synthesis, flavonoids reduce metal ions such as Cu^{2+}, Ag^{+}, Au^{3+}, and Fe^{3+} into their corresponding metallic or metal oxide forms while simultaneously coordinating with the nanoparticle surface through oxygen-containing functional groups[62]. This surface adsorption decreases interfacial free energy, suppresses particle aggregation, and improves colloidal stability through both steric and electrostatic stabilization.

In addition to initiating nucleation, flavonoids regulate crystal growth by selectively binding to energetically favourable crystal planes. Consequently, plant extracts rich in flavonoids frequently produce nanoparticles with smaller crystallite sizes, narrow particle-size distributions, and enhanced antioxidant activity. Because of their strong reducing ability and multifunctional surface interactions, flavonoids are generally

considered the dominant phytochemicals responsible for nanoparticle formation in most medicinal plants (Table 1.2).

1.5.3.2 Phenolic Acids

Phenolic acids represent another important group of electron-rich phytochemicals involved in nanoparticle synthesis. These compounds contain one or more hydroxyl groups attached to aromatic rings together with carboxylic acid functionalities that readily coordinate with metal ions [63].

The hydroxyl groups donate electrons during metal-ion reduction, whereas the carboxyl groups form stable coordination complexes that regulate nucleation and crystal growth. Following reduction, phenolic acids remain adsorbed on nanoparticle surfaces through hydrogen bonding and metal-oxygen coordination, improving colloidal stability and reducing particle aggregation [64].

Compared with flavonoids, phenolic acids generally exhibit moderate reducing power but stronger coordination behaviour, making them particularly effective in regulating crystal growth and improving nanoparticle dispersion. Their antioxidant properties also contribute to the long-term stability of colloidal suspensions [65].

1.5.3.3 Tannins

Tannins are high-molecular-weight polyphenolic compounds containing numerous hydroxyl groups capable of donating multiple electrons simultaneously. Their large molecular size and abundance of phenolic functionalities enable them to function as both powerful reducing agents and highly effective stabilizing molecules [66].

During nanoparticle synthesis, tannins rapidly chelate dissolved metal ions and promote reduction through multiple electron-transfer pathways. Owing to their polymeric structure, they form dense protective coatings around growing nanoparticles, producing strong steric stabilization that effectively suppresses agglomeration. Nanoparticles synthesized using tannin-rich extracts therefore frequently exhibit excellent colloidal

stability and improved resistance to oxidation. Moreover, the strong metal-chelating ability of tannins allows them to regulate crystal growth by selectively adsorbing onto specific crystallographic planes, thereby influencing particle morphology [67], [68].

1.5.3.4 Alkaloids

Unlike polyphenolic compounds, alkaloids contribute primarily through coordination chemistry rather than direct electron donation. Alkaloids are nitrogen-containing heterocyclic compounds possessing lone-pair electrons capable of coordinating strongly with transition-metal ions [69].

These coordination interactions influence the local chemical environment surrounding metal ions prior to reduction. Many alkaloids remain associated with nanoparticle surfaces after synthesis, contributing to enhanced biological activity, particularly antimicrobial and anticancer properties, by modifying surface chemistry and facilitating interactions with biological membranes[70].

1.5.3.5 Terpenoids

Terpenoids comprise a structurally diverse family of natural products derived from isoprene (C_5H_8) units. Their molecular structures commonly contain alcohol, aldehyde, ketone, and ester functional groups capable of participating in metal-ion reduction under mild conditions. Hydrophobic interactions between terpenoids and nanoparticle surfaces further contribute to colloidal stabilization by reducing particle aggregation and improving dispersion within the reaction medium [45], [71].

1.5.3.6 Saponins

Saponins are amphiphilic glycosides composed of a hydrophobic aglycone linked to one or more hydrophilic sugar chains. Owing to this unique molecular architecture, saponins behave similarly to natural surfactants during nanoparticle synthesis. Rather than acting as strong reducing agents, their principal function is to stabilize nanoparticles after nucleation has occurred[66], [72] .

1.5.3.7 Synergistic Role of Phytochemicals

In practice, nanoparticle synthesis is rarely governed by a single phytochemical. Instead, plant extracts contain complex mixtures of flavonoids, phenolic acids, tannins, alkaloids, terpenoids, proteins, polysaccharides, and other secondary metabolites that function cooperatively throughout nanoparticle formation. Strong reducing compounds such as flavonoids and tannins initiate rapid metal-ion reduction, whereas larger biomolecules-including proteins, polysaccharides, and saponins-predominantly regulate crystal growth and stabilize the resulting nanoparticles.

The relative abundance of these phytochemicals varies considerably among plant species, extraction solvents, geographical location, seasonal variation, and physiological age of the plant. Consequently, even under identical reaction conditions, different plant extracts frequently produce nanoparticles with distinct sizes, morphologies, crystallinities, and biological activities. Understanding these synergistic interactions is therefore essential for optimizing green synthesis protocols and tailoring nanoparticle properties for specific environmental, biomedical, catalytic, and agricultural applications.

The coordinated action of phytochemicals determines the structural characteristics of nanoparticles during synthesis. Depending on their composition, crystal structure, morphology, and dimensionality, the resulting nanomaterials exhibit distinct physicochemical properties that govern their performance in practical applications. These characteristics provide the basis for the classification of nanomaterials discussed in the following section.

1.6 Classification of Nanomaterials

1.6.1 Classification by Dimensionality

Nanomaterials are classified based on how many dimensions fall within the nanoscale (1--100 nm). The properties of nanomaterials significantly vary with their dimensional structure.

Table 1.3 Classification of nanomaterials based on dimensionality and representative examples

Type	Nanoscale Dimensions	Examples
0D	All three	Quantum dots, metal nanoparticles
1D	Two	Nanorods, nanowires, nanotubes
2D	One	Graphene, nanosheets
3D	All, or bulk with nano features	Nanoporous materials, nanocomposites

1.6.2 Classification by Origin

Nanomaterials can originate naturally, form as by-products of human activities, or be intentionally synthesized. This classification provides insight into their environmental presence and applications[73]:

Table 1.4 Classification of nanomaterials by origin

Type	Examples
Natural	Clays, volcanic ash, milk proteins
Incidental	Diesel exhaust, welding fumes
Engineered	Silver nanoparticles, CNTs, TiO_2 NPs

1.6.3 Classification by Composition

Nanomaterials can also be grouped by their chemical makeup. Each type has distinct physical and chemical properties[74] as shown.

Table 1.5 Classification of nanomaterials by composition

Type	Examples
Metallic	Ag, Au, Cu, Fe nanoparticles
Metal Oxide	ZnO, TiO_2, Fe_3O_4 nanoparticles
Carbon-Based	Fullerenes, carbon nanotubes, graphene
Polymeric	Dendrimers, PLA, chitosan NPs
Ceramic	Silicon carbide, alumina
Composite	Metal-polymer nanocomposites

1.6.4 Classification by Morphology

The shape and surface structure (morphology) of nanomaterials greatly influence their behavior and applications[75] as depicted below.

Table 1.6 Classification of nanomaterials by morphology

Morphology	Examples
Spherical	Gold nanoparticles, polymer spheres
Rod-shaped	ZnO nanorods, gold nanorods
Tubular	Carbon nanotubes (CNTs)
Sheet-like	Graphene, MoS_2 nanosheets
Porous	Mesoporous silica, zeolites
Core-shell	Fe_3O_4@SiO_2, Au@polymer nanoparticles

The classification of nanomaterials provides the structural framework necessary to understand their diverse physicochemical properties and technological applications. Among the various categories, plant-mediated metal oxide nanoparticles have attracted considerable attention because of their multifunctionality and sustainable production routes. The following section reviews recent advances in the green synthesis, characterization, and applications of metal oxide and mixed metal oxide nanoparticles, with particular emphasis on the current state of research and the knowledge gaps addressed in the present study.

1.7 Literature Review

Owing to their simplicity and environmentally friendly attributes, over the last decade, synthesis of metal oxide nanoparticles using plant extracts has received considerable research attention and hopefully brings in a host of multifunctional applications. This section will discuss the present status of the literature on green-synthesized metal oxide nanoparticles with respect to their synthesis methodologies, characterization, properties, and applications, especially with regard to mixed metal oxide nanoparticles and their potential advantages over single-component systems. The various steps pertaining to nanoparticle synthesis using plant extracts are depicted schematically below.

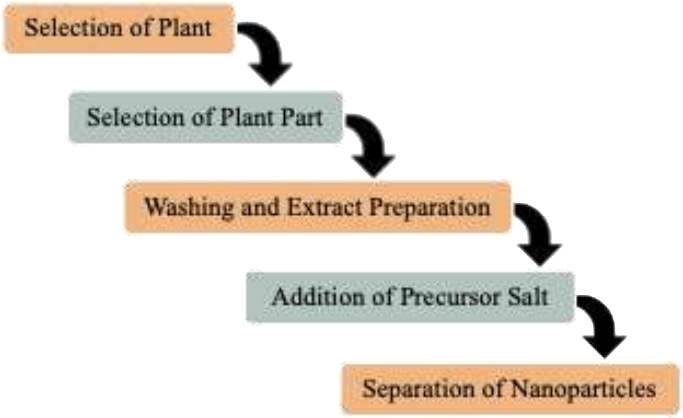

Figure 1.2: Flow chart illustrating the steps involved in plant mediated synthesis of nanoparticles.

1.7.1 Reported Synthesis and Applications of Mixed Metal Oxide Nanoparticles

Recent advances in green nanotechnology have demonstrated the successful synthesis of individual metal oxide nanoparticles such as CuO, NiO, ZnO, Fe_2O_3 and CoO using a variety of plant extracts rich in reducing and stabilizing phytochemicals. Copper oxide (CuO) nanoparticles synthesized using *Azadirachta indica* and *Aloe vera* extracts exhibit strong antimicrobial, antioxidant, and photocatalytic properties, attributed to efficient charge separation and high surface reactivity[76], [77]. Nickel oxide (NiO) nanoparticles produced from *Aloe vera*, *Azadirachta indica*, and *Camellia sinensis* extracts display outstanding electrocatalytic and energy storage behavior due to their p-type semiconducting nature and large surface area, making them suitable for supercapacitors, photocatalytic oxidation reactions, and gas sensing applications [78], [79], [80]. Similarly, cobalt oxide (Co_xO_y) nanoparticles synthesized using *Azadirachta indica*, *Calotropis*, and *Psidium guajava* extracts exhibit redox flexibility (Co^{2+}/Co^{3+}), magnetic functionality, and biological activity, supporting their use in battery/electrode, catalysis, and energy conversion systems[49], [81], [82], [83].

From success of single metal oxides, increasing research attention has been shifted to mixed metal oxide nanoparticles, showing a synergistic enhancements in structural, optical, and electronic behavior. The coupling of different metal oxides provides

heterojunction interfaces that help to enhance charge separation, redox potential, and surface reactivity. For instance, CuO-NiO (~30 nm) composites synthesized by the leaf extract of *Mimusops elengi* showed reasonable antibacterial activities against *E. coli* and *B. subtilis*[84]. Further, a CuO/NiO nanocomposite synthesized using *Saussurea costus* plant extract exhibited good performance as a supercapacitor electrode and further supported the pragmatic utility of such mixed oxides[85].

However, while literature on mixed oxides involving CoO or cobalt oxide phases via plant synthesis is at a low ebb, the opportunity is clear. Despite these promising findings, systematic studies focused on ternary mixed oxides, especially CuO/NiO/CoO prepared by plant-mediated routes, are also scarce. In addition, the phytochemical composition and process parameters-property correlations leading to such interesting multifunctional properties remain unclear yet, thus providing an opportunity for the development of sustainable, high-performance mixed metal oxide nanomaterials using green synthesis methodologies[39].

1.7.1.1 Nanoparticles for Environmental Applications

Several of these studies illustrated green synthesized nanoparticles showing potential for improving productivity and sustainability. Biosynthesized CuO-Fe_2O_3 and NiO-Fe_2O_3 systems synthesized from the leaves extracts of *Camellia sinensis* and *Ocimum sanctum* have yielded high photocatalytic degradation efficiencies (>90%) for organic dyes and pesticides under sunlight irradiation[59]. These composites also showed antimicrobial protection for crops and could improve nutrient uptake efficiency, thereby reducing the use of chemical fertilizers. Similarly, CuO-ZnO nanocomposites prepared with *Citrus sinensis* and *Azadirachta indica* extracts were found to show broad-spectrum antibacterial and antifungal properties, which could be useful in the priming of seeds and controlling pathogens in crops[86]. The synergy between CuO and ZnO enhances the

formation of ROS and surface adsorption, accounting for improved disinfection efficiency and photocatalytic soil pollutant degradation. On the other hand, some of the recent studies warned that excess nanoparticle concentration might disturb the soil microbial balance, indicating ecological trade-offs[87].

Despite such promising results, these agricultural studies still suffer from a lack of standardized synthesis methods and optimized dosage; thus, inconsistent results are obtained among different plant species and under variable soil conditions. Besides, the long-term effects of nanoparticles on soil microbes, nutrient balance, and toxicity require more detailed studies[88]. Moreover, environmental advantages of green synthesis are better confirmed by studies on life cycle assessment, however research on this topic is limited. The comparative LCA of green and chemical synthesis of TiO_2 nanoparticles indicates that chemically manufactured TiO_2 contributes significantly to greenhouse gas emissions and respiratory impacts. In contrast, the green method considerably reduces both toxicity and greenhouse gas emissions [89], [90]. Another framework for assessing sustainability is the waste to product mass ratio (i.e. E-factor). A green one-pot synthetic approach minimizes the E-factor by removing multi-step additions of reagents and the total amount of raw materials required per unit of product [34], [90]. The quantitative indicators such as- energy reduction, cost savings, increased output, atom economy, yield, stoichiometric efficiency, and LCA confirmed reductions in greenhouse gas emissions and toxicity, establishing green synthesis as a more sustainable approach to nanoparticle production.

1.7.1.2 Magnetic and Structural Properties

Mixed oxides may show tunable magnetic coupling (ferromagnetic, antiferromagnetic, exchange bias) due to interactions between cation sublattices. Al-Yunus and co-workers produced saponin-assisted CuO-NiO composites showing both ferromagnetic and

superparamagnetic phases, controlled by the Cu:Ni ratio[91]. Magnetic characteristics in biogenic MMOs originate from exchange interactions between mixed-valence ions and oxygen vacancies. NiO-CoO composites synthesized via *Tridax procumbens* and *Aloe vera* extracts showed soft magnetic behavior, improved coercivity, and enhanced electrochemical stability suitable for supercapacitor and magnetic sensing applications[92], [93].

However, most studies lack direct correlation between the phase composition and magnetic response with their focus remained largely on pH and oxidation state effects rather than compositional optimization. Some studies also lacked quantitative coercivity or magnetization data, limiting its magnetic depth.

1.7.1.3 Pharmaceutical and Biomedical Applications

Nanoparticles synthesized via plant extracts exhibit significant antimicrobial and biomedical potential due to their redox-active surfaces and nanoscale interactions. *Aegle marmelos*-derived CuO-NiO nanocomposites with strong antibacterial effects against *E. coli* and *B. subtilis*[94], while Cu doping in NiO showed efficient antibacterial and antifungal properties through oxygen vacancy generation[95]. In addition, during a plant-mediated synthesis study, the CuO-ZnO-MnO mixed oxide NPs were more antimicrobial compared to their individual oxides[96]. From these studies, it is concluded that green-synthesized nanoparticles can be used as multifunctional antimicrobial agents, which might provide safer alternatives to conventional antibiotics and catalysts.

Despite promising results, there is still a lack of phytochemical evaluation, biodistribution, and biocompatibility data under physiological conditions. Thus the linkage between nanoparticle surface chemistry and biological response is not well investigated, hindering the mechanistic understanding of the biological responses. Future work should be directed at systematic nanotoxicology, dose-response analysis, and

clinical validation, and mechanistic understanding by models to enable safe biomedical application.

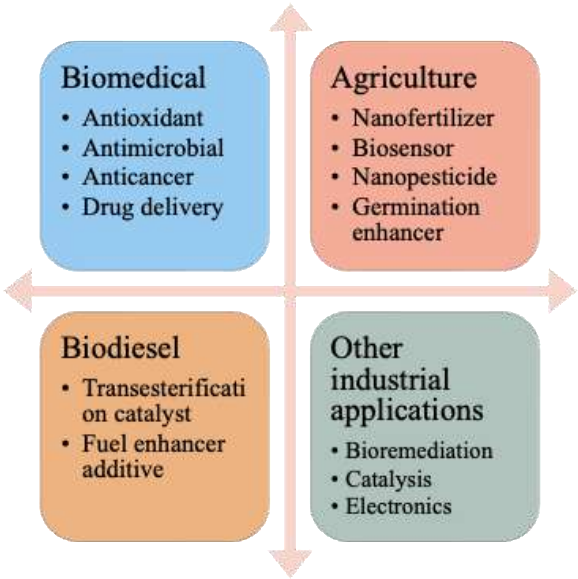

Figure 1.3: Major applications of nanomaterials in biomedical, agricultural, energy, and industrial sectors.

Table 1.7 Comparative summary of green-synthesized mixed metal oxide nanoparticles

Nanoparticle System	**Plant Extract**	**Particle Size (nm)**	**Efficacy**	**References**
CuO	*Azadirachta indica*	68.72	Antibacterial activity and dye degradation	[76]
CuO	*Azadirachta indica, Simmondsia chinensis*	30.90-10.70	Antibacterial and antifungal activity	[77]
NiO	*Aloe vera*	40.07	Energy storage	[78]
ZnO-CuO-NiO	*Azadirachta indica*	25.26, 18.42, 10.50	Photocatalytic activity	[79]
NiO	*Camellia sinensis*	26, 35	Gas sensor applications	[80]
CoO	*Psidium guajava*	30.90	Photocatalytic and antibacterial activity	[81]
CuO-NiO	*Mimusops elengi*	30	Antibacterial activity	[84]
CuO/NiO	*Saussurea costus*	18-30	Supercapacitor	[85]
$NiCO_2O_4$	*Hyphaene thebaica*	20-30	Photocatalytic and electrochemical activity	[92]

TiO_2	*Cymbopogon citratus*	-	Life cycle assessment	[89]
$Ni_xCo_{1-x}Fe_2O_4$	*Aloe vera*	28	Magnetic study and antimicrobial activity	[93]
NiCuO	*Cullon tomentosum*	31	Antibacterial and anticancer activity	[95]

From Table 1.7 it can be observed that smaller crystallite sizes (18-35 nm) generally correspond to enhanced antibacterial activity due to increased surface reactivity, whereas larger particles are often reported for photocatalytic applications where crystallinity becomes more influential than particle size. Surface characterization was inconsistently reported across studies, hence direct quantitative comparison was not possible. These shortcomings provide a strong rationale for the present work, which aims to establish comprehensive structure-property relationships in green synthesis.

1.8 Motivation and Research Gaps

The rapid development of nanotechnology has opened new horizons in materials science, while conventional chemical synthesis routes are particularly problematic due to their dependence upon toxic reagents and high energy inputs, together with hazardous by-products. Keeping in view the discussed limitations, plant-mediated synthesis is being modernly considered a sustainable and eco-friendly alternative. However, there is still a number of critical research gaps derived from existing literature which encourage a systematic investigation.

1.8.1 Research Gaps

1) Most of the work on green synthesis are restricted to single oxides, while binary and especially ternary composites such as CuO/NiO/CoO have been rarely reported, though they might combine synergistic performance improvements, which restricts our understanding of multicomponent systems.

2) The discrete role of each phytochemical in the processes of nucleation, growth, and stabilization of mixed oxides remains very poorly described. Previous studies usually regarded plant extracts as homogenous reducing agents without deep characterization of their phytochemical composition and explanation regarding how different metabolite classes contribute to different synthesis stages. This mechanistic gap hinders rational optimization of green synthesis processes and reproducible production of nanoparticles with tailored properties.

3) Previous reports typically highlight one property, for instance, photocatalytic or antimicrobial activity, without probing multifunctional behavior in the same system. Few reports relate morphological, compositional, and surface chemistry changes to several functional properties; hence, a general understanding of the influence of nanoparticle design on diverse applications remains incomplete.

4) While biocompatibility studies exist for some green synthesized nanoparticles, comprehensive ecotoxicological evaluations examining soil-nanoparticle-plant interactions, environmental persistence, and long-term ecological impacts remain limited, particularly for agricultural applications of metal oxide nanoparticles.

5) Few studies combine green nanoparticle synthesis with the principles of a circular economy by applying agricultural or industrial waste streams for nanoparticle synthesis and related processes in general.

1.8.2 Thesis Objectives

The present research effort has systematically pursued the green synthesis of multifunctional mixed metal oxide nanoparticles (MMONs), with emphasis on binary and ternary systems, in order to address these identified gaps. The overriding motivation is to find environmentally benign, sustainable synthesis methodologies that concurrently

pursue high performance while addressing global priorities in waste reduction, resource efficiency, and ecological protection.

Primary Goals:

1. Elaboration and optimization of green synthesis methodology of binary CuO/NiO and ternary CuO/NiO/CoO mixed metal oxide nanoparticles using *Moringa oleifera* leaves extracts as natural reducing and stabilizing agent.

2. Characterization and explanation of compositional dependence of structural, morphological, optical, and magnetic properties of biogenic mixed metal oxide nanoparticles.

3. To analyze multifunctional properties, such as soil reclamation and antimicrobial properties, including bactericidal and fungicidal activities.

4. To establish structure-property relationships that relate the nanoparticle characteristics with observed functional properties.

5. To assess the agronomic efficacy of biogenic CuO/NiO/CoO nanoparticles in enhancing crop productivity, coupled with proper ecotoxicological assessments.

6. To illustrate the integrated approach of green synthesis with waste valorization by using agricultural residues for vermicompost preparation and nanoparticle synthesis.

7. To underpin the mechanistic basis of antimicrobial efficacy by molecular docking and in-silico simulations correlating phytochemical-pathogen interactions with observed bioactivity.

1.9 Conclusions

Chapter 1 highlighted the development and importance of green nanotechnology, underlining plant-mediated synthesis as a sustainable route for synthesizing multifunctional mixed metal oxide nanoparticles (MMONs). It provides the scientific link between ancient metallurgical practices and modern eco-friendly nanoscience, yet it

identified key research gaps, mainly in unexplored binary and ternary systems, unidentified phytochemicals, and poor structure-property relationships. Filling these gaps has high relevance for developing high-performance, biocompatible nanomaterials applicable to environmental, agricultural, and biomedical fields. These are essential research areas, where biogenic metal oxide nanoparticles promise to play an important role in the near future. With ongoing research, they are expected to bring breakthroughs in tackling global challenges in healthcare, environmental remediation, and sustainable energy solutions.

"Building on this foundation, ***Chapter 2*** *focuses on the experimental design for the synthesis and characterization of biogenic CuO/NiO and CuO/NiO/CoO nanoparticles using Moringa oleifera extract. It elaborates on the materials, green synthesis methodology, analytical techniques, biological assays, and agricultural performance evaluations. This chapter bridges theoretical understanding with practical implementation, contributing to the development of sustainable, application-driven nanomaterial."*

CHAPTER 2

Materials and Methods

2.1 Materials

The chemicals cupric acetate [$Cu(CH_3COO)_2.H_2O$, 98%], copper nitrate [$Cu(NO_3)_2 \cdot 3H_2O$, 97%], nickel acetate [$Ni(CH_3COO)_2.4H_2O$, 98%], nickel nitrate [$Ni(NO_3)_2 \cdot 6H_2O$, 97%], cobalt nitrate [$Co(NO_3)_2.6H_2O$, 97%], methanol [CH_3OH], and ethanol [C_2H_5OH, 99.9%] were procured from Molychem, India. Leaves of *Moringa oleifera* were obtained from the premises of Rajiv Gandhi Institute of Petroleum Technology, Jais, India. Okra seeds were purchased from a local seed vendor in Jais, India. The earthworm species *E. fetida* was used to bio-transform agricultural wastes into vermicompost at the Bioconversion and Engineering Laboratory, Rajiv Gandhi Institute of Petroleum Technology, Jais, India. A multi-elemental standard stock of 100 μg/mL, FINAR-92, provided by Inorganic ventures, was used for the preparation of standards of 1 ppm, 5 ppm, 50 ppm, and 100 ppm. Ultrapure (Milli-Q®, Millipore, USA) water was used for preparing solutions and for dilutions during ICP-OES analysis. Glassware was soaked in a 10% (v/v) nitric acid solution for 6 hours and rinsed with deionized water before use.

The bacterial strains *Staphylococcus aureus* (Microbial Type Culture Collection, MTCC-96), *Escherichia coli* (MTCC-40), *Shigella flexneri* (MTCC-1457), and *Salmonella enterica* (MTCC-3858) and fungal test pathogens *Fusarium oxysporum* (MTCC-1755), *Aspergillus niger* (MTCC-252), and *Aspergillus flavus* (MTCC-798) were obtained from MTCC, IMTECH Chandigarh, and preserved at 4°C on nutrient agar slants.

2.2 Selection of plant (*Moringa oleifera*) for biosynthesis

The selection of an appropriate plant is a critical determinant in the success of biogenic synthesis. Plants exhibiting year-round availability and rich phytochemical diversity are particularly advantageous, ensuring both practicality and reproducibility of the synthesis process. Considering the criteria, *Moringa oleifera*, commonly known as the "drumstick tree" or "miracle tree," is an ideal raw material for nanoparticle synthesis. It is a highly valued plant which has gained significant scientific interest due to its rich nutritional profile and diverse pharmacological properties, including antioxidant, anti-inflammatory, antimicrobial, and anticancer activities. Almost every part of the plant viz. leaves, pods, bark, and seeds, contains a wide array of bioactive compounds such as flavonoids, alkaloids, phenolics, terpenoids, tannins, and saponins, which collectively contribute to its strong reducing, capping, and stabilizing capabilities[97].

The concentration and composition of reducing phytochemicals directly influence nanoparticle nucleation, crystal growth, and surface stabilization. Recent studies have reported that *Moringa* contains exceptionally high total phenolic content (TPC) (around 49.02 mg gallic acid equivalents/g extract) and total flavonoid contents (TFC) (near 52.96 mg quercetin equivalents/g) [98] relative to other plant sources commonly used in biogenic synthesis. The contents depend on extraction solvent and geographical origin and hence are variable. Plants possessing high TPC, TFC, and abundant antioxidant metabolites generally exhibit greater reducing power and produce more stable nanoparticles, hence *Moringa oleifera* was utilized for the synthesis[99], [100]. This study experimentally validates this selection through GC-MS and UPLC analyses in further sections confirming the presence of key phytoconstituents directly involved in the nanoparticle reduction and stabilization.

Despite the extensive use of *Moringa oleifera* in biogenic nanoparticle synthesis, critical research gaps remain that justify its continued investigation as discussed in Chapter 1. Along with lack of mechanistic clarity most studies rely on qualitative rather than quantitative analyses[101]. Many plant-based nanoparticle synthesis assume broad classes of molecules (phenolics, flavonoids, proteins) action, but rarely quantify their individual roles as pointed in a review by Coelho and co-workers[102] . Moreover, integrated use of chromatography (GC-MS or UPLC) along with spectroscopic techniques to track the fate and interplay of lipophilic and hydrophilic constituents is rarely done in MO-based nanoparticle work[103]. Although some recent studies have started exploring the intermediate mechanism, but not to the level of full quantitative kinetics or molecular-level dissection. Therefore, this thesis aims to address these limitations by employing an integrated analytical approach to achieve a more detailed understanding of the underlying biochemical mechanisms and reaction dynamics involved in the biogenic synthesis process.

2.3 Preparation of *Moringa oleifera* Leaves Extract

Freshly collected leaves of *Moringa oleifera* were first washed with tap water to remove dust and then by distilled water to remove further impurities. The leaves extract was prepared in a fixed ratio of dried leaves to solvent i.e., 1:10. For instance, 10 grams of *M. oleifera* powder were soaked in 100 mL solvent (water-methanol or ethanol) mixture for 1 hour. Thereafter, the mixture was given ample time to stir well at 60±5 °C for 2 hours. It was then filtered using Whatman filter paper (pore size 125 mm) to obtain the leaves extract (1:10 ratio). The *M. oleifera* leaves extract was kept under refrigeration until further use.

2.4 Phytochemical Profiling of *Moringa oleifera* Extract

2.4.1 Qualitative screening of *Moringa oleifera* Leaves Extract

Initial biochemical screening confirmed the presence of various categories of organic compounds within the *M. oleifera* leaves extract through standard qualitative assays (Figure 2.1).

The identification included:

- Flavonoids: verified through lead acetate precipitation assay
- Alkaloid molecules: detected using Wagner's precipitation method
- Saponin glycosides: confirmed via foam formation examination
- Tannin polyphenols: identified through lead acetate precipitation assay
- Terpenoid structures: established using Salkowski's color development test

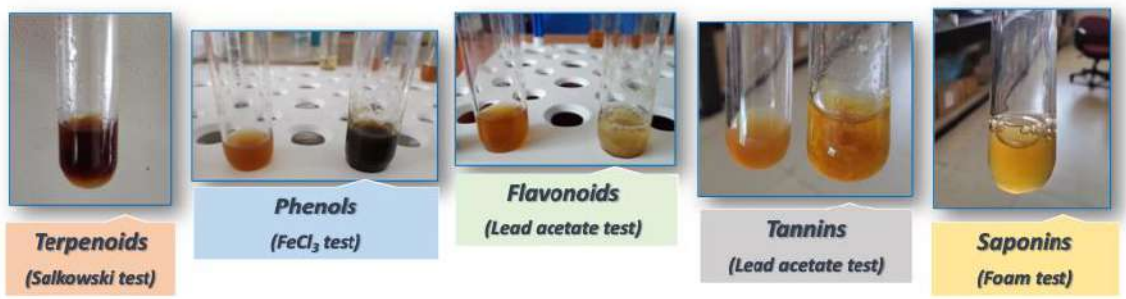

Figure 2.1: Qualitative assays for phytoconstituent screening of *Moringa oleifera* extract

2.4.2 Gas Chromatography-Mass Spectrometry (GC–MS/MS) Analysis

2.4.2.1 Instrumentation and Sample Preparation

The phytochemical constituents of Moringa oleifera leaf extract were analyzed using a GC-MS/MS system (Shimadzu GCMS-TQ8040) equipped with an AOC-20i auto-injector. Separation was achieved on a SH-Rxi-5Sil MS column (30 m × 0.25 mm ID × 0.25 µm film thickness; 5% biphenyl, 95% dimethylpolysiloxane), providing high thermal stability and low bleed. The injector, ion source, and interface temperatures were maintained at 250 °C, 230 °C, and 250 °C, respectively, with injections performed in

splitless mode. The oven temperature was programmed from 50 °C (2 min hold) to 310 °C at 10 °C/min, with a 25 min final hold and a total run time of 53 minutes. The system operated in Q3 scanning mode under electron impact ionization (70 eV), recording spectra across m/z 50–600. Compounds were identified by comparing their mass spectra with the NIST 20 and Wiley 11 libraries and accepted only for spectral similarity scores ≥90%, enabling detection of both volatile and semi-volatile phytochemicals in the extract with high accuracy.

Approximately 100-200 mg of dried extract was dissolved in methanol, ethyl acetate, or hexane, depending on solubility. The solution was further diluted (1 mL to 10 mL) using the same solvent prior to injection. A 1 µL aliquot of each prepared sample was introduced into the GC-MS/MS system using the auto-injector to ensure precision and reproducibility.

2.4.2.2 Analysis of GC-MS Profile

The GC-MS separation technique identified a diverse array of bioactive phytochemicals, including fatty acids, sterols, tocopherols, terpenoids, and long-chain hydrocarbons as listed in Table 2.1 (Chromatogram A12). The fatty acids identified in the extract, particularly n-hexadecanoic acid and α-linolenic acid, serve as natural reducing agents that initiate the nucleation stage by coordinating with metal centres and donating electrons or H-atoms by their -COOH and -OH groups during nanoparticle synthesis[104]. In parallel, phytol, a diterpenoid alcohol, supports this redox process through its unsaturated and -OH rich chain structure, facilitating rapid electron transfer and enhancing the stability of nascent nanoclusters[102].

Compounds belonging to the tocopherol family (β- and γ-forms) function dually as antioxidants and capping agents. Their phenolic moieties neutralize reactive oxygen species produced during synthesis, preserving nanoparticle integrity and preventing

oxidation of the metallic surface. These molecules also form a protective organic layer around the nanoparticles, introducing steric stabilization that maintains uniform dispersion and colloidal stability[105].

In addition, sterols and triterpenoids such as γ-sitosterol, fucosterol, and β-amyrin modulate morphology. Their large hydrophobic frameworks create van der Waals interactions that influence particle uniformity and shape control[106], while squalene, a triterpene hydrocarbon, acts as a hydrophobic spacer, enhancing dispersion and biocompatibility by forming an amphiphilic interface around the core[102].

Together, these biomolecules reflect the cooperative interaction between hydrophilic (carboxylic, phenolic) and lipophilic (sterol, terpenoid) phytochemicals, which together ensure controlled growth and surface passivation of nanoparticles.

Table 2.1: Major Phytochemical Constituents Identified in *Moringa oleifera* Leaves Extract through GC-MS/MS Analysis

Retention Time (min)	Compound Name	Molecular Formula	Base m/z	Area %	Probable Role in Nanoparticle Synthesis
18.55	n-Hexadecanoic acid (Palmitic acid)	$C_{16}H_{32}O_2$	73.10	15.85	Acts as a reducing and capping agent; stabilizes nanoparticle surfaces.
20.19	9,12,15-Octadecatrienoic acid (α-Linolenic acid)	$C_{18}H_{30}O_2$	79.10	8.84	Polyunsaturated fatty acid contributing to reduction and surface modification.
27.62	β-Tocopherol, O-methyl-	$C_{29}H_{50}O_2$	165.15	22.35	Potent antioxidant aiding in stabilization and preventing agglomeration.
28.96	γ-Sitosterol	$C_{29}H_{50}O$	43.10	8.54	Sterol molecule contributing to nanoparticle morphology regulation.
29.07	Fucosterol	$C_{29}H_{48}O$	314.30	5.88	Enhances surface activity and biocompatibility of nanoparticles.

Retention Time (min)	Compound Name	Molecular Formula	Base m/z	Area %	Probable Role in Nanoparticle Synthesis
19.87	Phytol	$C_{20}H_{40}O$	71.10	5.90	Alcohol derivative acting as a strong reducing agent.
29.33	β-Amyrin	$C_{30}H_{50}O$	218.20	3.22	Triterpenoid compound aiding in nanoparticle nucleation and stability.
19.77	9,12,15-Octadecatrienoic acid, methyl ester (Methyl linolenate)	$C_{19}H_{32}O_2$	79.10	2.00	Functions as a mild reducing agent and capping molecule.
25.47	Squalene	$C_{30}H_{50}$	69.10	0.75	Lipid precursor facilitating organic shell formation around nanoparticles.
27.10	γ-Tocopherol (Vitamin E)	$C_{28}H_{48}O_2$	151.15	1.18	Provides antioxidant stabilization to prevent oxidation of metal cores.

2.4.3 Ultra-Performance Liquid Chromatography (UPLC) Analysis

2.4.3.1 Instrumentation and Sample Preparation

The quantitative analysis of extract was performed by Waters Acquity UPLC, H-class system. Mobile phase: A = 0.1 % formic acid in water, B= 0.1 % formic acid in CAN; Column – ACE Super C18, 2.1 × 100 mm, 2.5 µm; Flow rate **–** 0.30 mL/min.; Detection wavelength – 270 nm; Temperature **-** Sample manager – 10^{o}C.

2.4.3.2 Analysis of chromatographic Profile

The technique exploits differences in chemical properties such as polarity, hydrogen bonding capacity, and molecular size to achieve separation, while PDA detection provides electronic absorption spectra for molecular identification. It uses the UV-Vis spectrum for the separation of organic components and is considered faster and more efficient than high-performance liquid chromatography. The chemical basis of UPLC separation lies in the differential interactions between analyte molecules and both the

stationary and mobile phases. The partition coefficient K, which governs retention, is determined by thermodynamic factors (Equation 2.1):

$$K = exp\left(\frac{-\Delta G^{\circ}}{RT}\right) = exp\left(\frac{-\Delta H^{\circ}}{RT} + \frac{\Delta S^{\circ}}{R}\right) \qquad \text{Equation 2.1}$$

where ΔG°, ΔH°, and ΔS° are the standard free energy, enthalpy, and entropy changes for the process.

A total of ten bioactive compounds, comprising four phenolic acid derivatives and six flavonoid molecules: Vanillic acid (4-hydroxy-3-methoxybenzoic acid), Protocatechuic acid (3,4-dihydroxybenzoic acid), *p*-Coumaric acid (4-hydroxycinnamic acid), Ferulic acid (4-hydroxy-3-methoxycinnamic acid), Luteolin (3',4',5,7-tetrahydroxyflavone), Caffeic acid (3,4-dihydroxycinnamic acid), Kaempferol (3,4',5,7-tetrahydroxyflavone), Epigallocatechin (flavanol catechin derivative), Quercetin (3,3',4',5,7-pentahydroxyflavone), and Rutin (quercetin-3-O-rutinoside)[107](Figure 2.2).

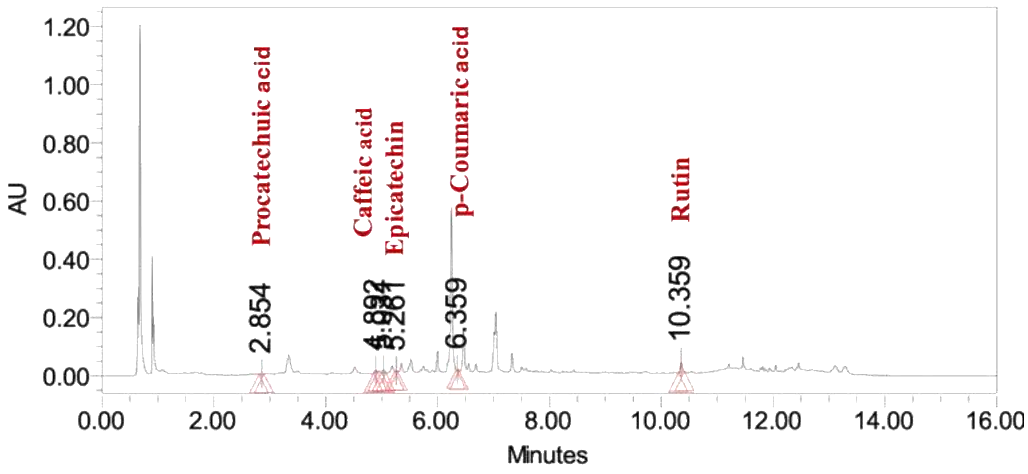

Figure 2.2: UPLC-PDA spectrogram of bioactive molecules of *Moringa oleifera* leaves extract.

Phenolic acids such as vanillic, protocatechuic, p-coumaric, ferulic, and caffeic acids act as primary reducing agents, owing to their -OH and -OCH_3 groups that readily donate electrons to metal ions. Their carboxyl and aromatic ring structures also chelate metal surfaces, facilitating nucleation and preventing uncontrolled particle growth. In

particular, ferulic and p-coumaric acids possess conjugated cinnamic frameworks that promote π–electron transfer, accelerating reduction kinetics and leading to uniform nanoparticle formation. Caffeic acid, with its ortho-dihydroxyl configuration, shows strong redox potential, forming intermediate quinonoid species that contribute to nanoparticle surface capping and stabilization[108].

Luteolin, kaempferol, quercetin, epigallocatechin, and rutin compounds serve primarily as capping and stabilizing agents, ensuring the colloidal integrity of nanoparticles. Their multiple -OH groups and conjugated aromatic rings enable metal chelation, hydrogen bonding, and π–π stacking, forming a protective organic layer around the nanoparticle core. Quercetin and epigallocatechin, in particular, provide rapid electron transfer and strong binding interactions, resulting in smaller, monodisperse particles with enhanced antioxidant stability. Rutin, a glycosylated form of quercetin, further improves solubility and dispersion in aqueous media, while luteolin and kaempferol contribute to structural stabilization through planar ring-metal coordination. Together, these bioactives establish a synergistic mechanism in which phenolic acids initiate metal-ion reduction and flavonoids maintain nanoparticle stability and morphology[109], [110].

2.5 Synthesis Methodologies

All metal-oxide and mixed metal oxide nanoparticles were fabricated using the green solution combustion method, using the extract as fuel and salt precursors as oxidants. Several modifications to the conventional solution combustion method have been reported for instance, solid state decomposition method, in which a homogenous paste of precursor salts and fuel (citric acid/aminophenol etc.) is used [111]. In our modification we have used *Moringa oleifera* plant leaves extract as fuel instead of harmful chemicals like urea which is a green and eco-friendly method. Since *M. oleifera* extract is a multi-

component fuel system without a single defined molecular formula, a classical stoichiometric fuel-to-oxidizer ratio could not be computed; instead, an operational extract-to-precursor ratio of 12 mL extract per gram of combined precursor salt was maintained across all batches to ensure reproducible combustion behaviour. The whole process can be understood in three thermal phases: (1) room-temperature bio reduction, (2) solution combustion (~350 °C), and (3) high-temperature calcination (~600 °C). In the first phase, phytochemical polyphenols, flavonoids, fatty acids serve as reductants and stabilizers, donating electrons to metal ions and forming metal-phyto complexes. Because the reaction is gentle, thermolabile antioxidants retain functional groups (hydroxyls, carbonyls) that support controlled nucleation and limit agglomeration, producing relatively uniform nanoparticles[47]. All combustion and calcination steps were carried out in a muffle furnace under static ambient air atmosphere. The pH of each precursor-extract mixture was recorded prior to combustion and was consistently in mild acidic range(pH≈ 5-6).

During the combustion stage (~350 °C), the organic-metal complexes break down through oxidation, generating heat that promotes in situ crystallization and densification of the material. As the temperature rises, volatile organic components are released, while a temporary carbon-rich matrix forms and briefly acts as a self-fueling medium for particle consolidation. This process ultimately results in the formation of phase-pure metal oxides with enhanced crystallinity[112]. In the final calcination stage near 600 °C, residual carbon and organic moieties are eliminated, hydroxyl groups are removed, and further grain growth and lattice ordering occur. This step enhances structural integrity, stability, and functional performance, though excessive temperature may induce sintering or loss of surface defects critical for activity as mentioned by some studies[113]. Discussed below are some of the biogenic nanoparticles that were synthesised.

2.5.1 Biosynthesis of Cu/Ni/Co Oxide Nanoparticles

Cu/Ni/Co oxide nanoparticles (*TmONs*) were fabricated using the green solution combustion method, using the extract as fuel and salt precursors as oxidants. 3 g, 2 g, and 1 g of Cu, Ni, and Co precursor salts were mixed with 60 mL of extract, respectively(0.25 M, 0.13 M, 0.06 M respectively). The ratios of precursor were selected considering the Irving-William series (Co^{2+}<Ni^{2+}<Cu^{2+}), as these metals mimic the naturally occurring metalloenzymes and bind in order of affinity according to the series.

The solution was stirred at room temperature for 4 hours. Afterwards, the solution was transferred to a 100 mL silica crucible and kept in a muffle furnace for combustion at 350 °C. After combustion, black pellet was obtained, which was powdered and washed with a 1:1 ratio of acetone and ethanol. The powder was further calcined at 600 °C for 1 h. The scheme is shown in Figure 2.3 below.

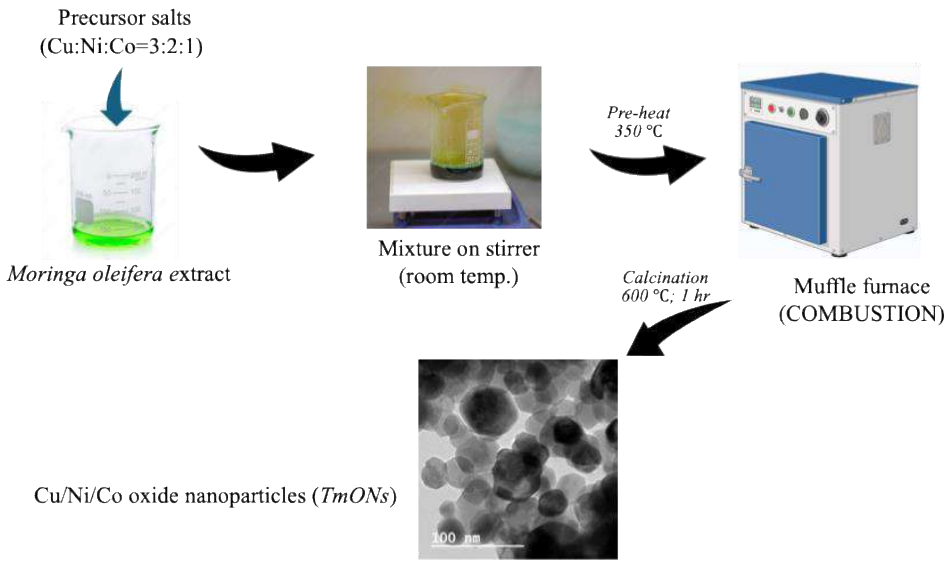

Figure 2.3: Schematic representation of *Moringa oleifera* assisted synthesis of Cu/Ni/Co oxide nanoparticles using green solution combustion method.

2.5.2 Biosynthesis of CuO/NiO Nanoparticles

The CuO/NiO nanoparticles were synthesized in three different ratio (1:2, 1:1, and 2:1) by a modified solution combustion method. The sample with 1:2 ratio was named as N12,

1:1 was named N22, and 2:1was named N21. Firstly, appropriate amounts of precursor salts (e.g., 0.6g each for 1:1 ratio) were taken and mixed with 50 mL *Moringa* extract, to obtain 0.06M of Cu mixture and 0.05 M for Ni mixture. The solution was kept under moderate stirring on a hot plate for 1 hr at room temperature until the solution became homogenous. Afterwards it was kept in a muffle furnace that had been preheated to 350°C. The combustion reaction happened within 30 min. The sample was crushed using mortar and pestle, centrifuged and washed to remove any impurity. The powder was calcined at 600°C for an hour. A fine greyish-black powder was obtained. The abovementioned process was repeated with varying concentrations of precursor salt solutions for the synthesis of other ratio of mixed oxides nanoparticles as shown in the Figure 2.4. For comparison, single metal oxides (CuO, NiO) nanoparticles were also prepared by adding 1 g of precursor salt (copper/nickel) in 12 mL extract (0.42 M and 0.34 M respectively) and repeating the process as discussed above.

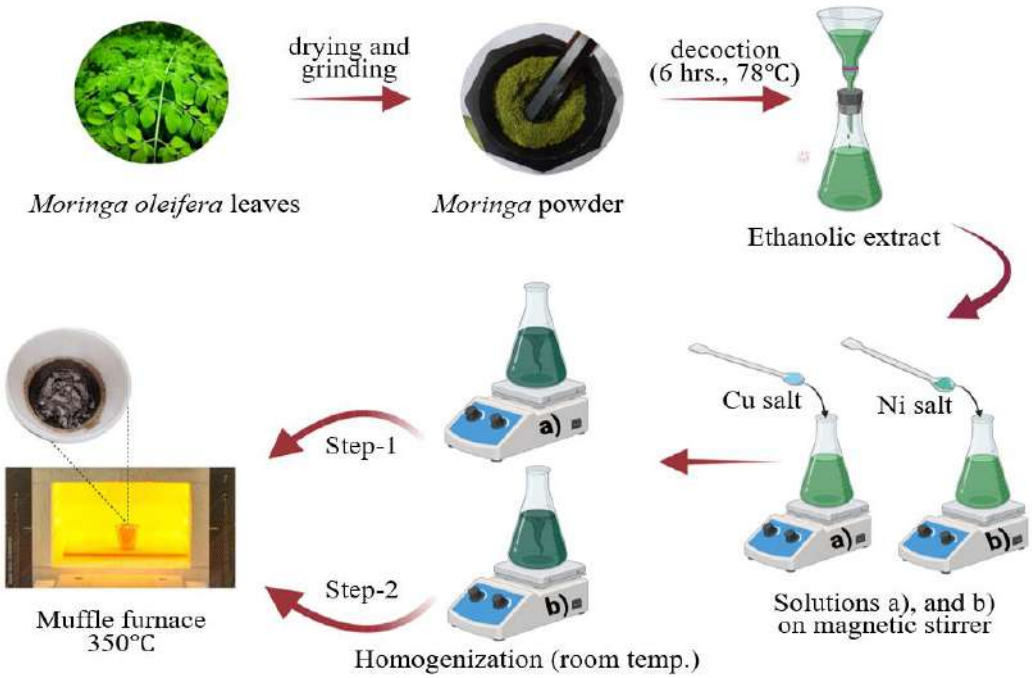

Figure 2.4: Schematic representation of *Moringa oleifera* assisted synthesis of CuO/NiO nanoparticles using green solution combustion method.

2.6 Experimental Techniques for Nanoparticle Characterization

The characterization of materials relies on a diverse set of analytical methods that provide complementary information about structural, morphological, chemical, and electronic properties. In this work, Fourier Transform Infrared Spectroscopy (FTIR), Ultraviolet–Visible Spectroscopy (UV-Vis), Diffuse Reflectance Spectroscopy (DRS), X-ray Diffraction (XRD), X-ray Photoelectron Spectroscopy (XPS), Transmission Electron Microscopy (TEM), Field Emission Scanning Electron Microscopy (FESEM), Energy-Dispersive X-ray Analysis (EDAX), Inductively Coupled Plasma Optical Emission Spectroscopy (ICP-OES), Brunauer-Emmett-Teller Surface Area Analysis (BET), and Vibrating Sample Magnetometer (VSM) were employed. Each technique is discussed in detail below:

2.6.1 Fourier Transform Infrared Spectroscopy (FTIR)

Fourier Transform Infrared Spectroscopy represents a powerful analytical technique for identifying functional groups and chemical bonding within materials through the measurement of molecular vibrations. The fundamental principle of FTIR is: when infrared light reaches a molecule, certain frequencies of this light are absorbed owing to the vibrational modes of chemical bonds in that molecule. This theoretical basis of FTIR is originally based on quantum mechanical treatment of molecular motions. For a diatomic molecule, the frequency of vibration can be approximated by the harmonic oscillator model:

$$\nu = \frac{1}{2\pi}\left(\frac{k}{\mu}\right) \qquad \text{Equation 2.2}$$

where ν is the vibrational frequency, k is the force constant of the bond, and μ is the reduced mass given by $\mu = m_1m_2/(m_1 + m_2)$, where m_1 and m_2 are the masses of the two atoms. The selection rule for infrared absorption implies that the vibration must cause a

change in the dipole moment of the molecule. In FTIR, an interferogram generated by a Michelson interferometer is subsequently converted to a conventional frequency spectrum through Fourier transformation.

FTIR spectroscopy was used to obtain valuable information about molecular structure, hydrogen bonding, crystallinity, and phase identification. The technique is particularly sensitive to changes in the local environment of functional groups, making it an excellent tool for studying surface modifications, adsorption phenomena, and chemical reactions. The Thermoscientific, NICOLET Is20 FT-IR spectrometer was used to record the FT-IR spectra of all samples. The spectral range from 4000 to 400 cm^{-1} was used, which corresponds to the fundamental vibrational modes of most organic and inorganic compounds. Plant extract data was recorded using attenuated total reflectance (ATR) mode.

2.6.2 Ultraviolet–Visible Spectroscopy (UV-Vis)

Ultraviolet-Visible spectroscopy is a widely used tool for exploring electronic transitions in materials and molecules. It is best suited for determining optical properties such as absorption behaviour and band gap energy. The technique operates on the principal that electrons in atoms or molecules absorb ultraviolet or visible radiation, leading to transitions from their ground states to higher excited states. Quantitative analysis of absorption follows the Beer-Lambert law, expressed as:

$$A = \varepsilon \times c \times l = log_{10}\left(\frac{I_0}{I}\right) \qquad \text{Equation 2.3}$$

where A represents the absorbance, ε is the molar absorptivity coefficient, *l* is the path length (1 cm), c is the concentration, I_0 is the intensity of incident light, and I is the transmitted light intensity.

For materials, the optical absorption edge provide a means to estimate the band gap energy (*Eg*). This relationship between the absorption coefficient (α) and the photon energy (*hν*) is described by the Tauc relation:

$$(\alpha h\nu)^n = A(h\nu - Eg) \qquad \text{Equation 2.4}$$

where n depicts the type of the electronic transition (n = 2 for indirect and n = 1/2 for direct band gap transitions). The absorption coefficient α can be derived from *A* through:

$$\alpha = \frac{2.303\ A}{t} \qquad \text{Equation 2.5}$$

where t is the thickness of the sample. By plotting $(\alpha h\nu)^{1/n}$ versus hν and extrapolating the linear portion to the energy-axis, the optical band gap was calculated. The measurement in thus study were performed using a Perkin Elmer spectrophotometer.

2.6.3 Diffuse Reflectance Spectroscopy (DRS)

For powdered and opaque materials, where direct light transmission is not feasible, DRS is employed in place of conventional transmission UV-Vis. The Kubelka-Munk function is used to transform the measured reflectance (R_∞) into quantity proportional to absorption coefficient, expressed as:

$$F(R\infty) = \frac{(1-R\infty)^2}{2R\infty} = \left(\frac{\mathrm{K}}{S}\right) \qquad \text{Equation 2.6}$$

Here, R_∞ represents diffuse reflectance of the powdered sample, K is absorption coefficient, and S denotes scattering coefficient. Further, the Tauc relation is applied to Kubelka-Munk data to find band gap by linking light absorption behaviour with its electronic energy structure as:

$$[F(R\infty) \times h\nu]^{\mathrm{n}} = A(h\nu - Eg) \qquad \text{Equation 2.7}$$

Here, hν is photon energy, *A* is constant, *Eg* is band gap energy, and n corresponds to transition type. Band gap values help in tailoring materials for specific applications. The

initial optical characterization of all the powdered samples was performed using Perkin Elmer spectrophotometer equipped for diffuse reflectance measurements.

2.6.4 X-Ray Diffraction (XRD)

X-ray Diffraction is a non-destructive analytical technique used to obtain detailed information about a material's crystalline structure, phase composition, crystallite size, and lattice parameters. The technique is based on the constructive interference of X-rays that are scattered by the array of atoms within a crystal. When X-rays interact with crystalline nanoparticles, diffraction occurs according to Bragg's law,

$$n\lambda = 2d\ sin\theta \qquad \text{Equation 2.8}$$

where n is the diffraction order, λ is the X-rays wavelength, d is the interplanar spacing between crystal planes, and θ is the Bragg angle. Each diffraction peak appears at a specific angle corresponding to a unique d-spacing, which serves as characteristic fingerprint for identifying metal oxide phases. For nanoparticles, the small size of crystallites leads to peak broadening, which can be analyzed to estimate the average crystallite size (D) using the Scherrer equation:

$$D = \frac{K\lambda}{\beta cos\theta} \qquad \text{Equation 2.9}$$

Where K is shape factor (typically 0.89 for spherical particles), λ is X-ray wavelength, β is the full width at half maximum (FWHM) of the diffraction peak (in radians), and θ is the Bragg angle. The positions of peaks reveal lattice parameters and can indicate structural variations due to doping, defects, or phase transformations, while peak intensities provide information about crystalline orientation and quality. All measurements were performed using a Panalytical diffractometer equipped with Cu Kα radiation (λ=1.5406 Å). XRD patterns of nanoparticles were observed over a 2θ range of 20°--90° with a scan rate of 0.0038 °/sec.

2.6.5 X-Ray Photoelectron Spectroscopy (XPS)

XPS is a surface-sensitive analytical technique that provide chemical information by measuring the kinetic energy of photoemitted electrons by using Einstein's photoelectric equation:

$$E_k = h\nu - E_b - \varphi \qquad \text{Equation 2.10}$$

where E_b is binding energy, $h\nu$ is photon energy, E_k is kinetic energy, and φ is the work function. Shifts in binding energy values indicate differences in oxidation states and bonding environments. Generally, higher oxidation states correspond to higher binding energies because of reduced electron shielding. XPS provides quantitative elemental analysis with detection limits typically between 0.1--1 atomic percent, making it a powerful tool for surface study. Due to the limited escape depth of photoelectrons, it is surface-sensitive (~1--10 nm depth), making it suitable for analyzing surface chemistry and oxidation states of metal oxide nanoparticles. In this study, Thermoscientific, K-ALPHA$^+$ Surface Analysis system with an x-ray source Al Kα (Monochromatic) with a 6 mA beam current at 12 kV was used.

2.6.6 Transmission Electron Microscopy (TEM)

Transmission Electron Microscopy is one of the most advance techniques for high-resolution structural analysis of materials at the atomic scale. It operates by transmitting a focused beam of electrons through an ultra-thin specimen to produce highly magnified images, achieving resolutions that can extend to sub-angstrom levels. The theoretical foundation of TEM is based on the wave nature of electrons, described by the de Broglie relationship:

$$\lambda = \frac{h}{p} = \frac{h}{\sqrt{2m_0\, eV}} \qquad \text{Equation 2.11}$$

where λ is the electron wavelength, h is Planck's constant, p is the electron momentum, m_0 is the electron rest mass, e is the electron charge, and V is the accelerating voltage applied to the electron beam.

High-resolution TEM (HRTEM) enables direct visualization of atomic level arrangements, crystal lattices and defects. Selected Area Electron Diffraction (SAED) complements HRTEM gives local crystallographic information at the nanoscale. It uses a selected area aperture to isolate electrons from a specific region (typically 0.1--5 μm) of nanoparticles, which are then focused by TEM lenses to generate a diffraction pattern on the detector. For metal oxide nanoparticles, the resulting patterns generally appears as concentric rings, characterising their polycrystalline nature. Each ring corresponds to distinct crystallographic planes, allowing determination of crystal structure, lattice spacing, and phase purity. Analysis of ring spacing and intensity helps identify specific oxide phases (such as anatase vs. rutile TiO_2), estimate crystallite sizes from ring broadening, and assess structural defects or amorphous content within the nanoparticles. For HR-TEM analysis, the samples were drop-casted on C-grid and dried. The TEM images were collected using JOEL JEM 2100 HR-TEM operating at a voltage of 200 kV.

2.6.7 Field Emission Scanning Electron Microscopy (FESEM) and Energy-Dispersive X-ray Analysis (EDAX)

FESEM operates based on the interaction between a focused electron beam and the specimen surface. It employs a field emission electron gun, which produces a highly focused, high-energy beam by emitting electrons from a sharp tungsten or cold cathode tip. When this primary beam strikes the surface of the sample, it generates various signals due to secondary electrons (SE), backscattered electrons (BSE), and characteristic X-rays through elastic and inelastic scattering processes. The secondary electrons, which possess relatively low energy (typically <50 eV), originate from the top few nanometres of the

sample surface. These are collected by detectors, converted into electrical signals, and subsequently amplified to produce grayscale images on a monitor.

FESEM is particularly advantageous for analyzing metal oxide nanoparticles because of its exceptional spatial resolution (1--3 nm) and magnification capabilities reaching up to 1,000,000×. It allows precise characterization of particle morphology, including size distribution, shape (spherical, rod-like, cubic, or irregular), surface texture and porosity, and agglomeration. When coupled with energy-dispersive X-ray spectroscopy (EDAX), FESEM further enables elemental composition and distribution mapping of the nanoparticles. It works by detecting characteristic X-rays emitted from atoms that have been excited by the incident beam. Each element gives unique X-ray peaks that allow identification and elemental mapping, making it an essential tool nanomaterials. For FE-SEM analysis, dried powder samples were mounted on carbon tape and the images were recorded using JEOL, JSM-7900F FE-SEM at an accelerating voltage of 5--10 kV. For EDAX spectra and elemental mappings were acquired and analyzed using SMILE VIEW™ Lab software.

2.6.8 Inductively Coupled Plasma Optical Emission Spectroscopy (ICP-OES)

ICP-OES technique is based on the principle of atomic emission spectroscopy. In this method, the sample is introduced into an inductively coupled plasma ionized gas (6000--10000K), where its constituent elements are atomized, ionized, and excited. When these excited atoms and ions return to their ground states, they emit characteristic radiation at specific wavelengths unique to each element. The emitted light is dispersed by a spectrometer and detected using photomultiplier tubes or charge-coupled devices allowing elemental analysis. ICP-OES provides highly precise and accurate measurements of elemental composition for determining metal contents, stoichiometric

ratios in complex oxides nanoparticles, and detecting impurities or dopants at trace levels, typically parts per million to parts per billion.

The technique was used in this study to determine the element concentrations in soil and plant leaves, which requires complete digestion of samples using acids. Calibration curves were prepared using standards of known concentrations to establish the value of calibration constant k, which allows determination of unknown sample concentrations based on their measured emission intensities. Deviations from linearity may occur at higher concentrations due to instrumental limitations and mostly chemical interferences. ICP-OES is known for its excellent precision, broad elemental coverage, and multiple element detection capability, making it an essential tool for comprehensive characterization of materials. Thermo Fisher Scientific, iCAP pro X Duo ICP-OES system at plasma flow of 15 $Lmin^{-1}$, a pump rate of 15 rpm, and a rinse time of 30 s was used for analysis. Data acquisition and processing were performed using QTEGRA software. The wavelengths for Cu, Ni, and Co were chosen as 324.754, 231.604, and 238.892 nm, respectively for quantitative analysis.

2.6.9 BET (Brunauer-Emmett-Teller) Surface Area Analysis

BET analysis is based on the principle of multilayer gas adsorption, most commonly performed using nitrogen gas at 77K (liquid nitrogen). As the relative pressure increases, gas molecules successively adsorb onto the material surface, forming multiple layers. The BET theory extends the Langmuir monolayer adsorption model by assuming that the first adsorbed layer follows Langmuir kinetics, while subsequent layers behaving similar to bulk liquid adsorption.

For metal oxide nanoparticles, BET analysis provides key surface characteristics such as specific surface area (m^2/g), pore size distribution, pore volume, and surface morphology. The specific surface area can be calculated as:

$$S_{BET} = \frac{V_m \times N_A \times \sigma}{V_m}$$ Equation 2.12

where N_A is Avogadro's number, σ is the cross-sectional area of the adsorbate molecule (for instance, 16.2 Ų for N_2), and Vm is the molar volume of gas at STP. BET Equation and Langmuir equations are given as:

$$\frac{1}{V\left(\frac{P^\circ}{P} - 1\right)} = \frac{1}{V_m \times C} + \frac{C-1}{V_m \times C} \times \frac{P}{P^\circ}$$ Equation 2.13

where V is the volume of gas adsorbed at pressure P, P_0 is the saturation pressure, V_m is the monolayer capacity, and C is the BET constant.

$$V = \frac{V_m b P}{1 + bP}$$ Equation 2.14

where b is the Langmuir constant related to adsorption energy.

The technique generates nitrogen adsorption-desorption isotherms that are classified into six IUPAC types: Type I isotherms indicate microporous materials (pore width <2 nm), Type II represents non-porous or macroporous materials with unrestricted multilayer adsorption, Type III shows weak adsorbent-adsorbate interactions, Type IV exhibits mesoporous materials (2--50 nm pores) with hysteresis loops due to capillary condensation, Type V indicates weak interactions in mesoporous materials, and Type VI represents stepwise multilayer adsorption on uniform surfaces. Metal oxide nanoparticles commonly exhibit Type II or Type IV isotherms, where the hysteresis loop provides valuable information about pore shape and connectivity, making BET analysis essential for optimizing catalytic, adsorption, and photocatalytic applications of metal oxide nanomaterials. N_2 adsorption–desorption isotherm data was measured employing BELSORP MAX sorption analyser at LN_2 temperature (77 K). Prior to measurements, the samples were degassed under reduced pressure at 150°C for 12 hours. Thereafter, the samples were examined using the single/multipoint adsorption method for surface area

assessment. The specific surface area and pore volume were calculated by BET method and adsorption amount of N_2 gas at a relative pressure of 0.99 bar.

2.6.10 Vibrating Sample Magnetometer (VSM)

VSM operates based on the principle of electromagnetic induction, where a sample is mechanically vibrated at a constant frequency (mostly 50--100 Hz) within a uniform magnetic field. The vibration causes periodic changes in the magnetic flux Φ through nearby detection coils according to Faraday's law of electromagnetic induction. The induced voltage is directly proportional to the magnetic moment of the sample and the amplitude of vibration, as expressed by following relationship:

$$V = \frac{-d\Phi}{dt} \qquad \text{Equation 2.15}$$

where V is the induced voltage, Φ is the magnetic flux, and t is time.

The setup comprises a vibrating sample holder attached to a transducer (a loudspeaker coil) that provide controlled mechanical oscillation. The system includes an electromagnet or superconducting magnet to generate the applied magnetic field (ranging from a few gauss to several Tesla), sensitive pickup coils symmetrically placed around the sample to detect flux variations, and a lock-in amplifier for processing signal to noise ratio. Advance temperature control units for measurements at various temperatures (typically 2K to 1000K) is also included in some.

For metal oxide nanoparticles, VSM enables detailed magnetic characterization, including determination of saturation magnetization (Ms), coercivity (Hc), remanent magnetization (Mr), magnetic susceptibility (χ), and hysteresis loop behaviour. These measurements help differentiate between various magnetic behaviours such as ferromagnetism, antiferromagnetism, paramagnetism, and superparamagnetism. VSM measurements provides valuable insights into particle size effects on magnetic performance, magnetic anisotropy, and blocking temperatures in superparamagnetic

nanoparticles, making it indispensable for tailoring magnetic nanoparticles for various applications. In this study, the measurements were conducted using a Quantum Design Inc. Model: 3 Tesla Cryogen free vibrating sample magnetometer. The M-H hysteresis data were recorded at room temperature (300 K) under an applied field upto 10 kOe (DC). Zero-field cooling (ZFC) and Field cooling (FC) measurements were performed over a temperature range of 5K to 375K.

2.7 Statistical Analysis

Data were expressed as mean ± standard deviation (SD) and analyzed using one-way analysis of variance (ANOVA), followed by Duncan's multiple range test for post-hoc comparison. Statistical analysis was performed using IBM SPSS Statistics version 26, with significance levels set at $P < 0.05$, $P < 0.01$, *and* $P < 0.001$. Apart from this, we calculated effect sizes (η^2) for ANOVA to quantify the magnitude of treatment effects and included 95% confidence intervals for key findings to enhance interpretability. All related experiments were done in triplicate. Data visualization plotting was performed using OriginLab 2024b and Microsoft® Excel version 16.89.1 (24091630).

2.8 Experimental Design and Methodology

2.8.1 Production of Nano-Organic Vermicompost

2.8.1.1 Feedstock Formulation and Composting Setup

The development of blended vermicompost formulations utilizing rice straw and pressmud (RS+PM) as growth treatments for plant cultivation was accomplished through the preparation of mature vermicompost products following modified protocols based on established methodologies referenced in Text A1[114]. Four distinct experimental treatments were mixed and prepared according to specific mixing proportions incorporating cow dung as the base material, finely chopped rice straw residues, and pressmud waste:

Feedstock (T0) – CD (dry weight)

Feedstock (T1) – CD + RS in 1:1

Feedstock (T2) – CD + PM in 1:1

Feedstock (T3) – CD + RS + PM in 1:1:1

1 kg of derived vermicompost was mixed with 100 ppm of biogenic Cu/Ni/Co oxide nanoparticles. Furthermore, it was used with soil (1:4) to evaluate the growth parameters of plants. These mixtures were: negative control as T0 (without NPs), positive control as nT0 (T0 + NPs), nT1 (T1 + NPs), nT2 (T2 + NPs), and nT3 (T3 + NPs).

2.8.2 Evaluation of Plant Growth Parameters in *Abelmoschus esculentus*

2.8.2.1 Seed Germination Assay

The germination study was performed on 30 seeds sown in above-prepared soil mixes. They were allowed to germinate in open sunlight at ambient temperatures. The seedlings were monitored at 10 a.m. for 21 days in continuation. The completion of germination was indicated by radicle elongation to a minimum length of 2 mm.

2.8.2.2 Growth Indices and Calculations

The data of shoot length, root length, and number of seed germinated were also collected to calculate cumulative germination percentage (CGR), co-efficient velocity of germination (CVG), germination percentage (G%), mean germination time (MGT), and seedling vigour index (SVI) using the formulae given [115], [116]:

$$\text{CGR}\ (\%) = \sum_{i=1}^{n} \left(\frac{Ni}{Ts}\right) X\ 100 \qquad \text{Equation 2.16}$$

$$\text{CVG}\ (\%) = \frac{\text{G1+G2+G3+}\cdots\text{Gn}}{(1\ \text{x}\ \text{G1})+(2\ \text{x}\ \text{G2})+\cdots n\ \text{x}\ Gn)} \times 100 \qquad \text{Equation 2.17}$$

$$\text{G}\ (\%) = \frac{\text{Total seed germinated at end of test}}{\text{Total number of initial seed}} \times 100 \qquad \text{Equation 2.18}$$

$$\text{MGT}\ (\%) = \frac{\sum(\text{n} \times \text{d})}{\text{N}} \times 100 \qquad \text{Equation 2.19}$$

$$\text{SVI} = \text{Average of seedling length (cm)} \times \text{G}(\%) \qquad \text{Equation 2.20}$$

where *Ni* denotes the number of seeds germinated on day *i*; *Ts*, total number of seeds in each treatment; *i*, alternate day after start; G, germination on each day after start; *n*, number of seeds germinated on each day; *d*, number of days from the start of the test; *N*, total number of seeds germinated at the experiment's completion.

2.8.3 Earthworm (*Eisenia fetida*) Survival Assay for Toxicity Assessment

Prior to the application of synthesized nanoparticles, the toxicity assessment was also conducted to ascertain the survival of earthworms. A concentration of 50, 100, 200, 300, and 500 ppm of derived Cu/Ni/Co oxide nanoparticles was used with 1 kg of cow dung to perform the toxicity assay. A three-week study was performed on earthworms (10 earthworms in each treatment) to assess the impacts of nanoparticles on *E. fetida* by monitoring survival to visually evaluate the toxicity and risk. Data was collected every third day for calculation and the experiment was performed in triplicate.

2.8.4 Sample Digestion and Preparation for ICP-OES analysis (metal toxicity)

Acid digestion, also known as wet digestion, reduces interference by breaking down the sample matrix, making it efficient for organic compounds[117]. For soil samples, a triple acid digestion process was performed in which 0.1 g of sample was mixed with a reagent HF: HNO_3:HCl:H_2O (3:3:1:3), and the solution was heated till dryness. Using HF removes reactive silicon, which tends to precipitate into undissolved acids, and hence makes the solution stable. Moreover, using HNO_3 with HF removes insoluble fluorides[118]. Thereafter, 3 mL of aqua-regia was further added until a clear solution was obtained. The remains were made up to 25 mL using Milli-Q water with 1% HNO_3.

For okra leaves, the open vessel hot method was used, in which 0.5 g of leaves powder was added to 10 mL of HNO_3, and the mixture was heated for 3 h, then cooled, and further

H_2O_2 was added till a clear solution was obtained. After digestion, the samples were filtered and made up to 30 mL for the leaves sample. Pre-cleaned PTFE tubes were used to put the digested samples in until the quantification was done using ICP-OES. No internal standard was used for analysis, and each sample was read in triplicate. A blank solution containing 2% HNO_3 was also run before the standard solution. A calibration test was also performed by taking 1, 5, 50, and 100 ppm standards as quality control.

2.8.5 Computational Screening for Drug-Likeness

The drug-likeness of the identified phytoconstituents was evaluated using Lipinski's rule of five [119]. The molecular structures of phenolic acids and flavonoids were first converted into canonical SMILES (Simplified Molecular Input Line Entry System) format. These SMILES codes were then submitted to the SwissADME online tool to predict pharmacokinetic properties, including hydrogen bond donors and acceptors, total polar surface area (TPSA), and the number of rotatable bonds.

2.8.6 Antimicrobial Assay

To evaluate the broad-spectrum antibacterial and antifungal properties of *M. oleifera*-based NPs, a range of gram-positive and gram-negative bacterial strains, along with common fungal pathogens, were selected. The bacterial strains included *Staphylococcus aureus* (Microbial Type Culture Collection, MTCC-96), a gram-positive organism, and gram-negative bacteria such as *Escherichia coli* (MTCC-40), *Shigella flexneri* (MTCC-1457), and *Salmonella enterica* (MTCC-3858). Fungal test pathogens included *Fusarium oxysporum* (MTCC-1755), *Aspergillus niger* (MTCC-252), and *Aspergillus flavus* (MTCC-798). The antimicrobial efficacy of ethanolic leaf extract of *M. oleifera* and green synthesized NiO/CuO nanoparticles (1:2 and 2:1) was assessed using the agar well diffusion method. Mueller Hinton Agar (MHA) plates were prepared and seeded with

100 µl of bacterial broth culture. For fungal pathogens, inoculum were adjusted to match the turbidity of a 0.5 McFarland standard. Wells were punched into the agar using a sterile cork borer and filled with 100 µl of the test extract. DMSO served as a negative control. Plates were pre-incubated at room temperature for 30 minutes to allow diffusion and then incubated at 35±1°C for 48 hours. Zones of inhibition were measured in millimeters to evaluate antimicrobial activity [120], [121].

2.8.7 Molecular Docking Analysis of NPs Against *E. coli* and *F. oxysporum*

Molecular docking analysis of the biogenic NiO and CuO nanoparticles was conducted against *Escherichia coli* and *Fusarium oxysporum* to investigate their binding interactions with key microbial target proteins. A molecular docking study against *E. coli* and *F. oxysporum* was conducted using the PyRx software[122] because both the nanoparticles at all the concentrations demonstrated maximum inhibitions against both the organisms as discussed in Chapter 5. The structure for CuO was retrieved from the Material Project database (https://next-gen.materialsproject.org/) and converted to PDB format using Avogadro software, whereas the NiO structure was constructed again using Avogadro software. The interaction was visualized by BIOVIA Discovery Studio software[123].

2.8.8 Spectrophotometric Quantification of Antimicrobial Activity

The antimicrobial potential of the plant extract and the synthesized nanoparticles (NPs) was evaluated by monitoring the reduction in optical density using a spectrophotometer. Prior to testing, all microbial strains were activated by culturing them overnight in Luria Broth nutrient medium at 37 °C. The antimicrobial activity was assessed at two nanoparticle concentrations: 100 mg/ml and 250 mg/ml. For the assay, 5 ml of nutrient broth was inoculated with 100 µl of the respective microbial suspension and treated with the test formulations. A control group without any treatment was maintained under the

same conditions. Changes in turbidity, indicative of microbial growth inhibition, were recorded at two-hour intervals using a spectrophotometer set at 540 nm. A comparison between treated samples and the untreated control allowed the determination of antimicrobial efficacy based on differences in optical density [124].

2.9 Concluding Remarks

This chapter established an integrated methodological framework combining biogenic synthesis, phytochemical profiling, physicochemical characterization, and biological evaluation to develop sustainable metal oxide nanoparticles. The use of *Moringa oleifera* leaves extract as a green reducing and stabilizing agent proved efficient and eco-friendly, with GC-MS and UPLC analyses confirming the role of its phytoconstituents. The inclusion of toxicological, in silico, and antimicrobial studies confirmed the biosafety and multifunctional potential of the synthesized materials, demonstrating a strong foundation for their practical and agricultural applications.

"The nanoparticles synthesized in this chapter form the basis for the experimental investigations presented in the following sections. Building on this foundation, the next chapter examines the agricultural potential of biogenically synthesized trimetallic nanoparticles (Cu/Ni/Co oxide NPs) when integrated with agro-waste derived organic compost amendments, with a focus on soil health and crop performance."

CHAPTER 3

Synergistic effects of biogenic Cu/Ni/Co oxide nanoparticles on the agronomic performance of *Abelmoschus esculentus* (L.) in conjunction with organic compost amendments[1]

3.1. Introduction

The field of nanotechnology has captured significant research interest across multiple disciplines, particularly in agricultural applications. Metal oxide nanoparticles represent a promising frontier in promoting environmentally sustainable farming practices [125], [126]. Research efforts are increasingly focused on developing soil enhancement materials using metallic oxide nanoparticles to modify soil characteristics and boost agricultural productivity. The primary goals of soil modification materials encompass three critical areas: (1) to provide nutrients; (2) to prevent insect- and microbe-induced disease; and (3) to increase nutrient availability in the soil[127]. The unique characteristics of nanoparticles including their nano dimensions, high surface-to-volume ratios, regulated release properties, and adsorption capabilities make them as ideal candidates for next-generation fertilizer development[128]. Traditional chemical synthesis methods for producing mixed metal oxide nanoparticles often involve hazardous chemicals, creating limitations for biological compatibility and commercial-scale production. Therefore, developing cost-effective, environmentally friendly, and

[1] A manuscript based on this chapter has been published in *Pedosphere.*

scalable synthesis approaches has become essential. Plant-based biosynthesis offers an appealing alternative, with *Moringa oleifera* being particularly valuable due to its rich phytochemical composition that facilitates nanoparticle formation[129], [130].

Simultaneously, the rapidly expanding global population has necessitated increased agricultural production, resulting in heavy reliance on synthetic chemicals and inorganic fertilizers. Unfortunately, a significant portion of these inputs is lost through soil leaching, contributing to environmental contamination of water sources [131]. Furthermore, farming methods adopted during the green revolution have generated substantial agricultural waste that is often improperly disposed of through burning or dumping, creating air and soil pollution [132]. Two particularly problematic agricultural byproducts viz. rice straw and pressmud (sugar industry waste) cannot be directly used as fertilizers and contribute to environmental degradation. Pressmud's waxy composition and high sulfur levels can compromise soil structure, aeration, and permeability over time. Meanwhile, incomplete combustion of rice straw releases toxic gases including carbon monoxide and carcinogenic compounds, while also depleting soil NPK content [133].

Converting these agricultural wastes into valuable organic fertilizer through vermicomposting represents a sustainable solution. This process offers economic benefits while improving organic matter decomposition and producing beneficial bioconversion products [134]. Incorporating nanotechnology into vermicomposting can significantly enhance the resulting fertilizer's quality, pest control capabilities, and disease resistance properties. Nanoparticles can increase vermicompost's nutrient retention capacity while providing antimicrobial benefits that help control plant diseases and reduce dependence on chemical pesticides [135], [136]. Essential micronutrients such as copper, cobalt, and nickel are crucial for plant health, and their deficiency can cause structural abnormalities,

reduced photosynthetic efficiency, increased susceptibility to fungal diseases, and diminished crop yields [137], [138]. Individual copper, nickel, and cobalt oxide nanoparticles have demonstrated promising applications in environmental cleanup, energy systems, and medical applications [139], [140]. However, their collective potential in agricultural applications, particularly for soil improvement, remains largely unexplored. Research has shown that copper nanoparticles can influence grain development, carbohydrate content, and mineral accumulation in crops [141]. CuO nanoparticles have been found to enhance iron uptake in rice plants, suggesting their potential as nano-fertilizers. NiO-NPs significantly boost antioxidant enzyme activity in *Nigella arvensis* [142]. Co_3O_4-NPs positively affect photosynthetic parameters of the *Arabidopsis* plant [143]. Apart from that, the antibacterial effect of bivalent metal chelates containing cobalt and nickel against harmful soil bacteria such as *Staphylococcus aureus* and *S. faecalis* have been described, suggesting potential for developing novel antibacterial treatments for vermicompost applications [144]. Copper serves as a vital micronutrient in photosynthetic processes, cell wall formation, and cellular respiration, supporting key enzymes including cytochrome c oxidase and superoxide dismutase. Nickel is essential for urease enzyme function, while cobalt acts as a crucial trace element in enzyme systems, particularly as a component of vitamin B12. It also works synergistically with manganese in soil to promote plant development [145]. Thus, combining these three metals as trimetallic oxide nanoparticles could create new opportunities for sustainable crop management by simultaneously providing plant nutrition and protection.

This chapter emphasizes improving nutrient recovery, soil rehabilitation, and plant growth performance analysis. While copper and nickel benefits are well-documented, cobalt research remains limited, and this metal is frequently overlooked by agricultural

practitioners due to insufficient information availability [146]. Despite being considered a non-essential trace element, recent studies highlight cobalt's important role in various plant physiological processes[147]. Even its specific accumulation and transport mechanisms within plant systems remain poorly understood[148]. The economic viability of these metals, being more affordable than precious metal nanoparticle precursors like gold or silver, makes them practical choices for large-scale green nanomaterial production and commercialization.

Hence, the objective was to shed light on the importance of these metal ions as Cu/Ni/Co oxide nanoparticles (*TmONs*) in soil reclamation, plant micronutrients, and their effects on plant growth. Okra represents an economically significant vegetable crop, with India leading global production. This crop provides numerous health-beneficial nutrients including iron, amino acids, essential fatty acids, vitamins, and minerals [149]. Previous research has explored various nanoparticles including SiO_2, Al_2O_3, TiO_2, and Se nanoparticles for enhancing okra's nutritional compounds and stress tolerance [150]. These studies have demonstrated that okra readily responds to nano-enabled fertilizers through changes in germination, chlorophyll synthesis, micronutrient accumulation, antioxidant metabolism, and biomass production, making it an excellent model for investigating nanoparticle–plant–soil interactions. *Abelmoschus esculentus* was selected as the experimental crop because of its rapid germination, fast growth rate, well developed root system, and high responsiveness to nutrient amendments. Furthermore, its relatively short growth cycle facilitates the early assessment of both beneficial and potential phytotoxic effects of nanoparticles, enabling rapid evaluation of our hypothesis[151], [152].

To the best of the authors' knowledge, no research has examined the impact of trimetallic oxide nanoparticles combined with agricultural waste-based biofertilizer on

soil restoration and plant growth of okra (*A. esculentus*). This research employs a variety of sophisticated analytical techniques, including field emission scanning electron microscopy with energy dispersive X-ray (FESEM-EDX), powder X-ray diffraction (XRD), ultra-performance liquid chromatography (UPLC-PDA), high-resolution transmission electron microscopy (HR-TEM), fourier-transform infrared spectroscopy (FTIR), X-ray photoelectron spectroscopy (XPS), and inductively coupled plasma optical emission spectroscopy (ICP-OES) to characterize trimetallic nanoparticles and evaluate vermicompost and nano-enhanced vermicompost quality and maturity.

3.2 Results

3.2.1 FTIR Analysis

FTIR spectroscopy provides information on chemical structure by detecting the type of infrared vibrations present in the sample. The FTIR spectra of *TmONs* are shown in Figure 3.1A, representing various stretching and bending vibrations (Table A1) that occurred due to different types of functional groups in bioactives of *M. oleifera* extract.

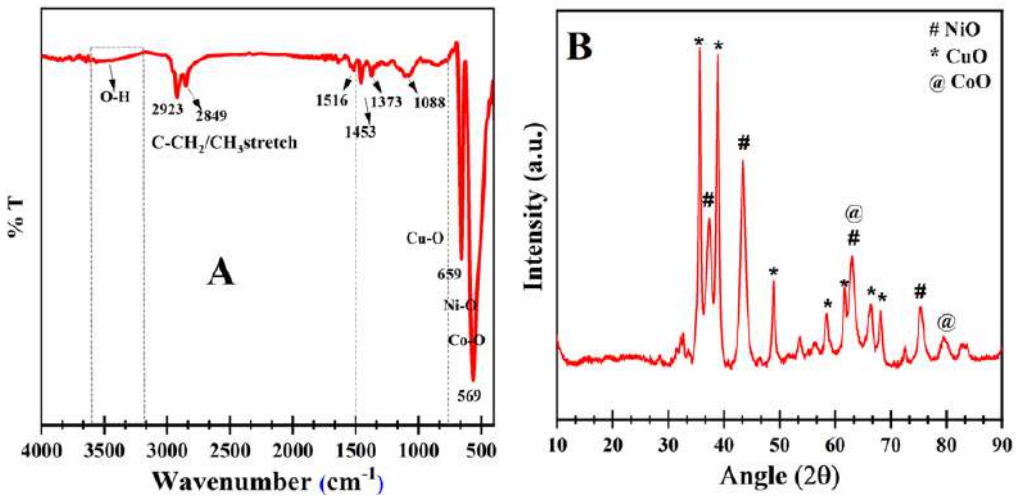

Figure 3.1: (A) FTIR spectrum and (B) XRD patterns of biogenic Cu/Ni/Co oxide nanoparticles synthesized using *M. oleifera* leaves extract.

3.2.2 XRD Analysis

Particle size and defects are revealed by XRD patterns, while the atomic distribution within the unit cell is shown by relative peak intensities. Figure 3.1B (Table A1) depicts

the XRD patterns of the synthesized *TmONs*. The diffraction peaks are indexed to (110), (002), (111), (-020), (020), (202), (113), (022), and (311) planes of the monoclinic phase of CuO (Ref. 00-041-0254), respectively, moving from lower to higher angles [153]. Moreover, the well-defined diffraction peaks are ascribed to (111), (200), (220), (311), and (222) planes of rhombohedral NiO (Ref. 00-044-1159). Similar XRD patterns for the planes of cubic CoO (Ref. 00-002-1217) can be assumed as the mixing of both oxides. The peak density and intensity for the corresponding metal oxide further validate the ratio of precursors taken ($3Cu^{2+}$:$2Ni^{2+}$:$1Co^{2+}$), where major peaks corresponding to CuO are present.

The average crystallite size was estimated using the Debye-Scherrer equation (details covered in Chapter 2) and found to be 35 nm. Peak fitting and background correction were performed prior to crystallite size estimation.

3.2.3 XPS Analysis

The chemical states of *TmONs* and their specific orbitals were also confirmed by XPS measurements. Figure 3.2A shows the survey scan, which clearly indicates the existence of Cu, Ni, Co, C, N, and O, with some auger peaks corresponding to metal oxides. The core-level spectra were fitted with a Gaussian function to separate the overlapping contribution that may appear due to the presence of the element in different environments. The background that results from inelastic scattering of electrons was subtracted by employing a Shirley background correction. The characteristic peaks for binding energies of N 1s, O 1s, and C 1s are present at 399, 531.9, and 284 eV, respectively. Four peaks in the Cu 2p region were seen in the high-resolution XPS spectra of *TmONs* shown in Figure 3.2B [154]. Cu^{2+} ion satellite peaks are located at 942.1 and 962.0 eV, which is a feature of partially filled d-block ($3d^9$) Cu^{2+}. It ruled out the occurrence of Cu^{+} (Cu_2O) and proved the presence of Cu^{2+} ions (CuO) [155]. In the Ni 2p spectra (Figure 3.2C), the

major peaks located at 861.26 eV, 855.9 eV, and 854.36 eV are distinctive NiO peaks [156]. Similarly, the high-resolution XPS spectra of Co 2p may also be fitted into four Gaussian peaks as shown in Figure 3.2D [157]. Based on the area under the peaks, the atomic percents of the elements in nanoparticles are 2.83%, 2.17%, and 1% for Cu, Ni, and Co, respectively, which is nearly consistent with the ratio initially taken for synthesis.

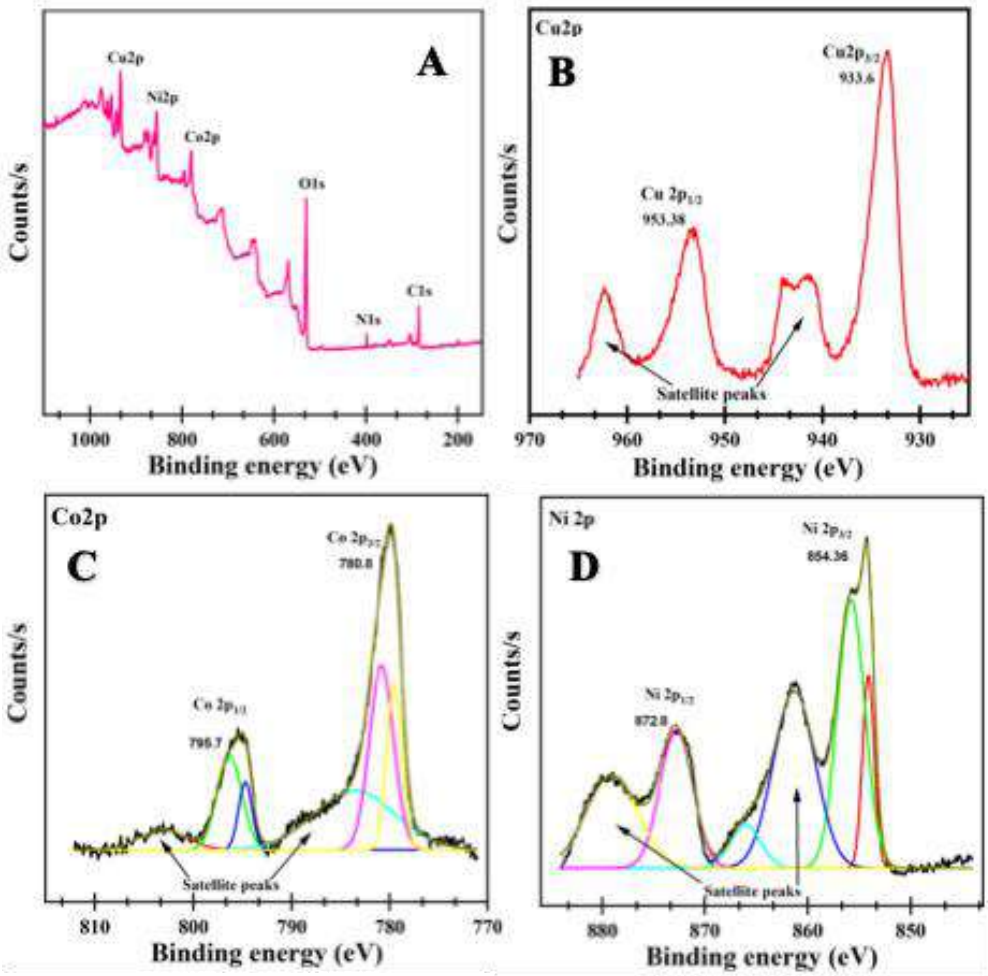

Figure 3.2: (A) survey scan confirming the presence of Cu, Ni, Co, O, and (B--D) high-resolution fitted plots for Cu 2p, Ni 2p and Co 2p of biogenic Cu/Ni/Co oxide nanoparticles synthesized using *M. oleifera* leaves extract.

3.2.4 EDAX and TEM Analysis

The EDAX analysis is a quantitative element detection technique, which confirmed the *TmONs* contain Cu, Ni, Co, C, N, and O elements, as shown in Figure A1. Moreover, the

morphology, shape, size, and crystalline phase of the nanoparticles were analyzed by TEM at an acceleration voltage of 200 kV. The nanoparticles were submerged in ethanol at room temperature for 10 minutes before being ultrasonically dispersed. Further, the samples were placed on copper grids coated with amorphous carbon sheets. Figure 3.3 depicts the various morphologies of each metal oxide, such as hexagonal, spherical, and nearly spherical. The substance was found to include nanoparticles ranging in size from 14 to 54 nm, with a mean size of 29 nm. Furthermore, the d-spacing, which denotes the minimum distance between two successive planes in a lattice, was found to be 0.266 nm corresponds to CuO(111) plane and 0.206 nm matches NiO (200) plane, which is quite consistent with the d-spacing obtained through XRD, calculated using the FFT (Fast Fourier Transformation) and inverse FFT image filtering processes. This process resulted in lattice fringes, and the distance between two parallel lines was calculated manually as d spacing. Furthermore, the SAED pattern shows diffraction rings with particle spots, indicating the polycrystalline nature of the *TmONs*.

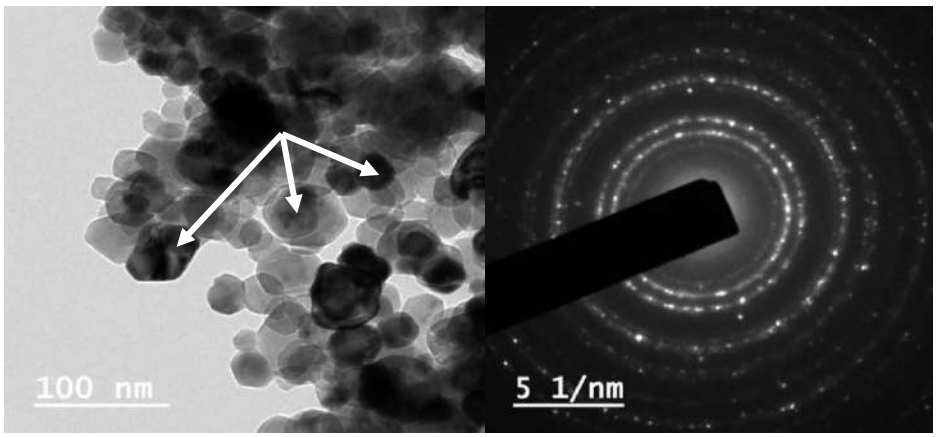

Figure 3.3: TEM image along with SAED pattern of biogenic Cu/Ni/Co oxide nanoparticles synthesized using *M. oleifera* leaves extract.

3.2.5 Physicochemical Properties, Nutrient Composition, And Surface Analysis of Vermicompost

Table 3.1 represents a typical nutritional status in terms of C/N, % total organic carbon (TOC), electrical conductivity (EC), and pH, whereas Table A2 illustrates the nutritional status of raw materials used as feedstock. C/N is a measure of decomposition and microbial activity during vermicomposting. The higher C content denote better decomposition during vermicomposting. On the other hand, EC is widely used to measure manure salinity, which arises due to the presence of dissolved salts. TOC is another important indicator of soil health to measure the long-term impact of fertilizers. All treatments maintained EC levels below 8 dS m^{-1}, a threshold considered safe for plant growth, with a slightly higher value in the case of the T2 feedstock group (9.83± 0.3 dS m^{-1}) in comparison to others. The pH of the developed vermicompost was observed to be within an optimum range of 7.1--8.1. The pH in the treated groups varied between 7.1 and 7.6 and stabilized at a value close to neutral on day 90.

Table 3.1 Physicochemical parameters of vermicompost derived from different feedstocks

Parameters		pH	EC (dsm^{-1})	TOC (%)	C/N
Vermicompost used for plant culture*	T0	8.10 ± 0.0	6.66 ± 0.5	34.35 ± 0.2	22 ± 0.1
	T1	7.36 ± 0.3	6.81 ± 0.3	24.80 ± 0.2	14 ± 0.9
	T2	7.65 ± 0.1	9.83± 0.3	27.85 ± 1.4	18 ± 0.8
	T3	7.11 ± 0.2	7.55 ± 0.1	24.10 ± 1.4	11 ± 2.0

* T0 (Control), T1 (CD + RS), T2, (CD + PM), T3 (CD + RS + PM).

NPK are three primary essential macronutrients essential for plant growth. The percentages of NPK for vermicompost treatments, in comparison to raw materials is shown in Figure 3.4. There was a statistically significant ($P < 0.05$) rise in the percentage of NPK macronutrients in the treatments. The N% of the vermicompost from the T3 fed group (1.82 ± 0.1) was higher compared to the T2 (1.50 ± 0.1), T1 (1.67 ± 0.1), and T0

(1.39 ± 0.1) fed feedstock groups, respectively, by 21%, 16%, and 31%. Moreover, an overall increase of 62% was observed as compared to the raw materials. Similarly, all treated groups had a higher P% than the control (T0) feedstock group that changed significantly ($P < 0.05$) after the complete process of vermicomposting. Among all, the P% of the T3 group was comparatively higher by 14%, 41%, and 60% than that of the T2, T1, and T0 groups, respectively. Furthermore, the K% in the blended (RS+PM) feedstock groups was discovered to be higher than the control feedstock group and the original raw materials used for vermicomposting. The mature vermicompost feedstock T2 had the highest K%, followed by treatments T3 and T0. Quantitatively, it was 35%, 20%, and 4% higher than T0, T1, and T3 fed feedstock groups, respectively. This ambiguity could be due to the variation in the cation exchange capacity and relatively higher pressmud content.

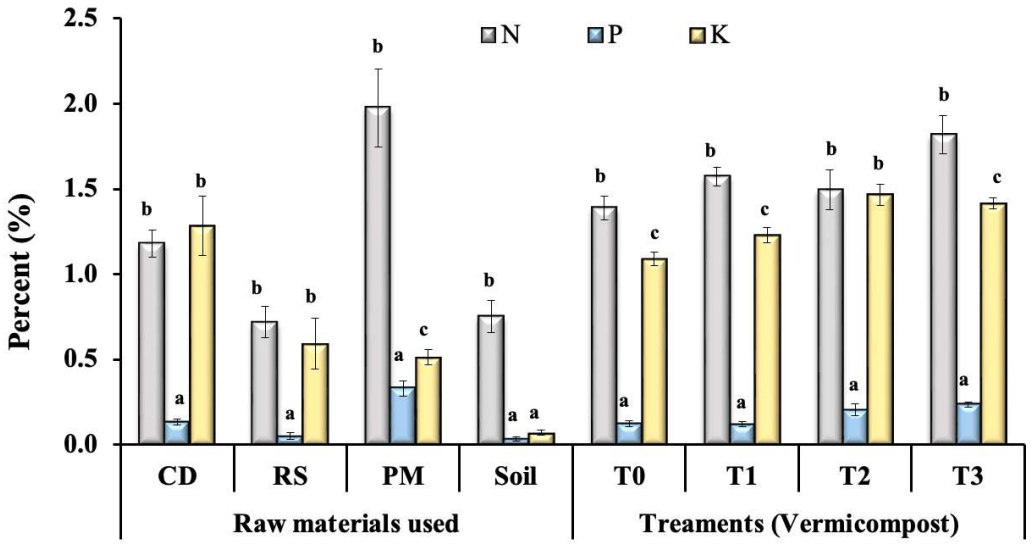

Figure 3.4: Comparative analysis of nitrogen (N), phosphorus (P), and potassium (K) content (%) in raw materials and vermicompost-treated samples (T0--T3). Data shows enhanced nutrient levels in vermicompost treatments, with significant differences ($P < 0.05$) indicated by different letters. Bars represent the mean values ± standard error (SE).

The surface structure and elemental makeup of all produced vermicompost from various feedstock combinations were determined using the FESEM-EDX technology.

Vermicompost was found to be more disaggregated than controls, but no significant changes were seen after *TmONs* treatment (Figures A2 and A3). Furthermore, when vermicompost samples from different feedstocks were compared, (T3) had the highest proportion of rough matrix surface, followed by (T2), (T1), and (T0).

3.2.6 Toxicological Evaluation of Biogenic CuO/NiO/CoO Nanoparticles on Earthworms

Earthworms are always employed as model organisms for toxicological risk assessments since they are also considered to be monitors and natural indicators of soil health[158]. Figure 3.5 presents both cumulative mortality over time and final percentage mortality of earthworm exposed to different concentrations (50--500 ppm) of biogenic CuO/NiO/CoO NPs, alongside a control group. The maximum concentration (500 ppm) treated group showed significantly higher ($P < 0.005$) and early mortality as compared to other treated groups and reaching 100% by day 15. Similarly, 300 and 200 ppm concentration also exhibited progressive mortality, attaining 80% and 60% respectively by day 21. On the other hand, lower concentrations (100 and 50 ppm) and control result in minimal mortality (~10--35%), showing reduced or negligible toxic effects throughout the experimental period.

Similarly, Figure A4 supports these findings with statistically analyzed final mortality data. Treatments with 500 and 300 ppm also had the highest mortality rate and were not significantly ($P < 0.05$) different from each other. 200 ppm treatment showed intermediate mortality, significantly lower than above two but still indicative of sublethal effects. Lower doses (100 and 50 ppm) and control show low or baseline mortality, indistinguishable statistically. Therefore, these results affirm that mortality in earthworm increases significantly with rising concentrations of CuO/NiO/CoO NPs and indicates a potential threshold effect, where toxicity escalates sharply beyond a concentration of 100

ppm. Therefore, in our study, 100 ppm NPs concentration was used with soil (vermi + soil) for the evaluation of plant growth performance to avoid maximum toxicity. The observed toxicological effects at higher doses may be attributed to enhanced ROS (reactive oxygen species) generation, cellular membrane disruption, and NPs accumulation in tissues. Moreover, minimal effects at lower concentrations suggest a threshold below which these nanoparticles may be environmentally safe.

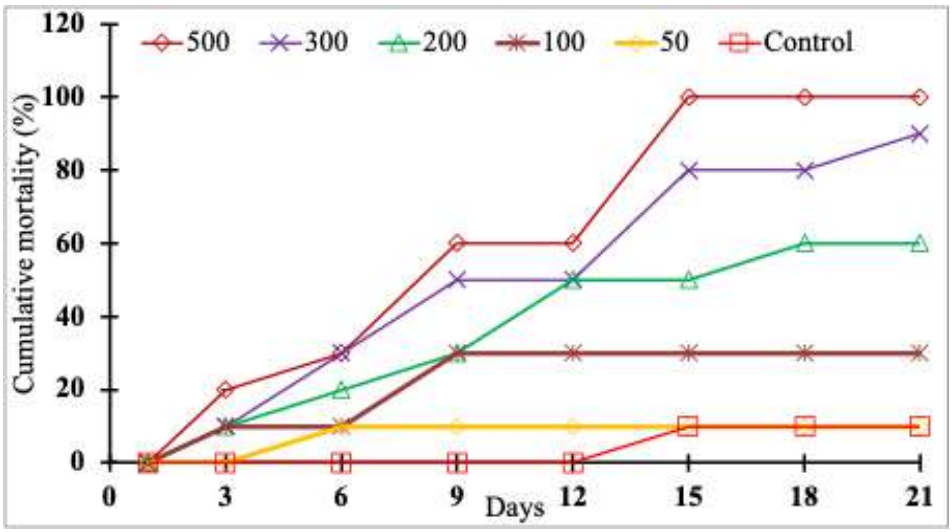

Figure 3.5: Cumulative mortality (%) of *E. fetida* over a 21 day exposure period to different concentrations (50-500 ppm) of biogenic *TmONs* compared to the control. Bars represent Mean ± SE (n = 3).

3.2.7 Toxicological Evaluation of Heavy Metals (Cu/Ni/Co) in Soil and Leaves of Okra Plant

ICP-OES is a sensitive technique to measure trace metal concentrations by ionizing them in plasma and detecting their emitted light at specific wavelengths. The calibration test performed to validate the obtained values gave good coefficient of determination values near 0.99 (Table 3.2). According to ICP-OES results, all acid-digested samples of soil and plant leaves contained metals (Cu, Ni, and Co) within permissible limits set by WHO (1996) (Table 3.3).

Table 3.2 Table showing LoD (limit of detection) values and coefficient of regression (r^2)

Sample	Elements	LoD (ppm)	r^2
Plant	Cu	0.030	0.994
	Ni	0.050	0.990
	Co	0.020	0.997
Soil	Cu	0.002	0.991
	Ni	0.005	0.996
	Co	0.002	0.985

Table 3.3 ICP-OES analysis of soil samples after growth of *A. esculentus*

Treatments*	Sample	Cu (ppm)	Ni (ppm)	Co (ppm)
T0	Soil	0.028	0.008	-0.166
	Plant	1.488	0.460	-0.097
nT0	Soil	0.162	0.066	-0.150
	Plant	0.070	0.328	-0.348
nT1	Soil	0.019	0.077	-0.089
	Plant	0.078	0.188	0.891
nT2	Soil	0.060	0.162	-0.430
	Plant	0.991	0.953	-1.254
nT3	Soil	0.089	0.115	-0.229
	Plant	1.408	1.203	-2.223
Permissible limits (soil) WHO (1996)		30	80	50[$]
Permissible limits (plant) WHO (1996)		10	10	0.2-0.5[#]

*T0 (without *TmONs*), positive control as nT0 (T0+*TmONs*), nT1 (T1+*TmONs*), nT2(T2+*TmONs*) and nT3 (T3+*TmONs*). [#]maximum tolerable limit [159]; [$] [160].

3.2.8 Evaluation of Growth Performance of *A. esculentus*

The initiation of seed germination commenced on the fourth day after sowing the seeds in soil amended with vermicompost and *TmONs*. The recorded germination events for seeds in the T0 group were documented on the seventh day. In contrast, in groups treated with *TmONs* (nT0--nT3), the first germination instances were observed on the fourth day post-sowing, as illustrated in Figure 3.6A. The T0 group exhibited a modest germination rate, with only 7 to 12% of plants germinating within the 10- to 15 day timeframe. In contrast, the groups treated with *TmONs* (nT0--nT3) displayed enhanced germination

rates, ranging from 18 to 25% (nT0), 25 to 35% (nT1), and 25 to 40% (nT3). As the observation period extended to 21 days post-sowing, the germination percentages increased to 32%, 47%, 52%, 63%, and 80%, as depicted in Figure 3.6B. These findings unequivocally demonstrate that the incorporation of *TmONs* into the vermicompost significantly augmented both the germination rates and seedling growth. Hence, the improved performance observed across the nanoparticle-treated groups highlights the positive impact of *TmONs* on seed germination and early seedling development.

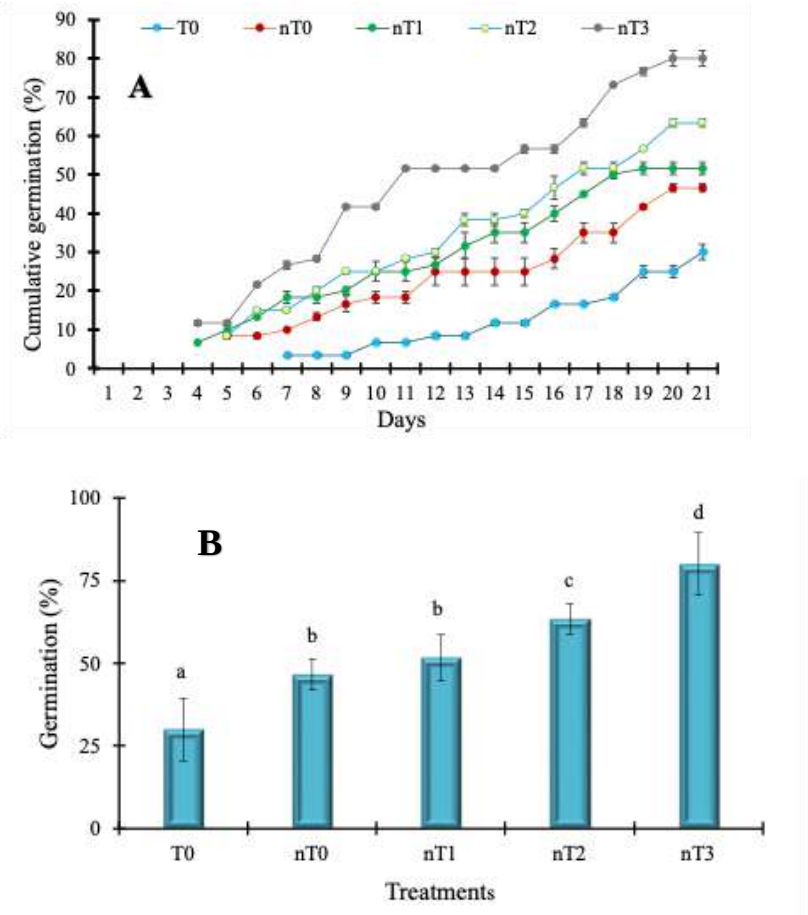

Figure 3.6: Germination performance across different treatments (T0, nT0, nT1, nT2, nT3). The figure presents (A) cumulative germination and (B) germination percentage. Bars with different letters (a, b, c, d) indicate statistically significant differences among treatments at $P < 0.05$. Error bars represent the mean values ± standard error (SE). T0 (without NPs), positive control as nT0 (T0+ NPs), nT1 (T1+ NPs), nT2(T2+ NPs) and nT3 (T3+ NPs).

3.2.8.1 The Seed Vigour Index (SVI)

SVI, a crucial indicator of seed quality with a direct impact on the potential for plant emergence, is assessed through the SVI [161]. The SVI is calculated by multiplying the germination percentage and seedling length (mm) [162]. Across all nT0--nT3 groups, the SVI values were consistently higher than the T0 control group (Figure 3.7A). Furthermore, the highest SVI in the nT3 treatment (1640 ± 40) was notably 29%, 47%, and 21% higher than the nT0 (840 ± 0.3), nT1 (1118 ± 0.8), and nT2 (1355 ± 1.0) groups, respectively. Furthermore, these results collectively emphasize the positive influence of trimetallic oxide nanoparticles on both the speed and vigour of seed germination, highlighting the potential for improved plant emergence and growth in nanoparticle-treated groups.

3.2.8.2 The Mean Germination Time (MGT)

MGT serves as a crucial parameter, representing the average duration required for the maximum germination of seedlings. In comparison to the negative control group, a significant ($P < 0.05$) reduction in MGT was observed across all groups treated with *TmONs* blended with vermicompost, as depicted in Figure 3.7B. Remarkably, the lowest MGT value was recorded for the nT3 group (10.1± 0.9), signifying a rapid and efficient germination process. Quantitatively, the MGT values were 28%, 51%, 41%, and 63% lower for nT0, nT1, nT2, and nT3 groups, respectively, when compared to the control (T0) group. Hence, the substantial reduction in MGT across the treated groups underscores the positive impact of *TmONs* on accelerating and optimizing the germination process, thereby promoting robust seedling emergence.

3.2.8.3 The Coefficient Velocity of Germination (CVG)

The CVG serves as an important metric for assessing the speed and uniformity of seed germination. In our study, the highest and lowest CVG values were observed for the nT3

group (10 ± 1.0) and the T0 control group (6 ± 0.5), respectively, as illustrated in Figure 3.7B. Additionally, the CVG for the nT3 group exhibited an approximate increase of 67%, 25%, 5%, and 18% over the T0, nT0, nT1, and nT2 groups, respectively. However, the CVG values increases for vermicompost mixed with *TmONs* relative to control group (T0).

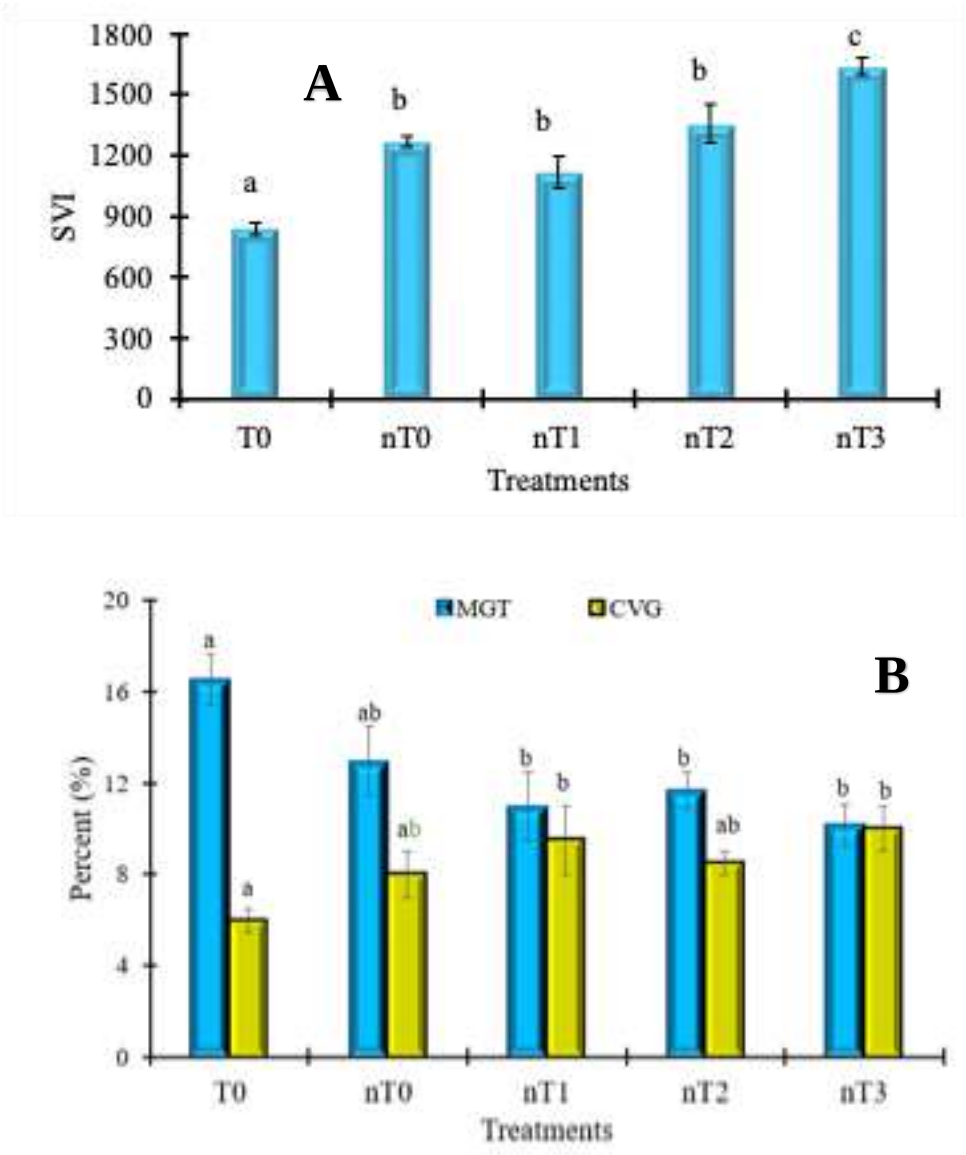

Figure 3.7: Plots showing (A) Seed Vigour Index (SVI); (B) Mean Germination Time (MGT) and Coefficient Velocity of Germination (CVG). Bars with different letters (a, b, c, d) indicate statistically significant differences among treatments at $P < 0.05$. Error bars represent the mean values ± standard error (SE).

3.3 Discussion

3.3.1 Evaluation of Agro-Waste Derived Vermicompost Maturity

EC, pH, and C/N ratio are considered maturity parameters of vermicompost as mentioned in Table 3.1. EC arises as a result of the breakdown of organic matter in soil and freely available salts/ions created during earthworm metabolism. Therefore, the higher EC in all blended feedstock groups (except T0) was due to a higher concentration of salts/ions[163]. A lower C/N ratio may suggest an excess of nitrogen, while a higher ratio may indicate an excess of carbon. It's important to note that the C/N ratio of vermicompost may vary based on the initial mix of materials used in the composting process. As a result, the C/N ratio of the T3 (CD+RS+PM) fed group was shown to be lower ($P < 0.05$) than the other feedstock groups, indicating faster decomposition of organic matter and release of nutrients for long term soil fertility. Moreover, a vermicompost with a C/N between 12 and 25, and preferably less than 15, is considered a good indication of mature vermicompost[164]. The pH variation in the range 7.1--8.1 was ascribed to a surge in nitrogenous waste excretion during vermicomposting, which had the ability to bring the pH level back to neutral[165].

Earthworm castings contain more NPK than substrate materials, which in turn increases the soil's NPK content and lowers the C/N ratio[166]. Our study showed increased NPK after vermicomposting. Moreover, one major factor contributing to this increase in P is the activity of earthworm gut enzymes. In plants, phosphorus plays a crucial role in the photosynthetic process and is essential for efficient nutrient uptake from the soil. Similarly, nitrogen influences chlorophyll synthesis, directly affecting photosynthetic efficiency and overall biomass production[167]. These factors likely improved okra physiological outcomes.

3.3.2 Influence of *TmONs*-Enriched Vermicompost on Okra Growth Performance

The synergistic effect of *TmONs*, PM, and RS may explain the increased germination, CVG, SVI, and lower MGT. Bhaskar and co-workers compared the effects of NiO, CuO, and ZnO NPs individually on *A. esculentus* at concentrations varying from 100 to 1000 mg/L and found repression of shoot and root length and germination[168]. However, *TmONs*, where CuO, NiO, and CoO are present together, showed enhanced growth parameters at 100 ppm concentration. The synergy optimized the concentration of individual components, which served as an effective way to tolerate Cu, Ni, and Co stress and toxicity. Hence, the fastest growth of the population of okra seed for nT3 is attributed to the lowest MGT value. The ability of *TmONs* to penetrate the seed coat and speed up embryogenesis through enzyme activity may have led to seed dormancy breaking down and accelerated the germination process[169]. However, the CVG values increases for vermicompost mixed with *TmONs* relative to control group (T0). These coefficient values vary from 0 to 100, with high values towards 100 suggesting rapid germination and low values near 0 indicating very sluggish or even blocked germination. Overall, this coefficient is used to calculate the rate and spread of germination, i.e., it is a pure rate measurement devoid of germinability interference[170]. An elevated SVI indicates that the soil provides a conducive environment for early plant development characterized by adequate nutrient availability, active microbial communities, and minimal phytotoxic stress. The high seed vigour obtained in our study could be attributed to the potency of *TmONs* based soil amendment in enhancing growth[171]. In addition, numerous studies have reported the effects of various metal oxide nanoparticles on plant growth, as summarized in Table 3.4.

Table 3.4 Effects of nanoparticles on different plant growth parameters across different plant species and dosages

Nanoparticles/Dosage	Plant	Parameters				Ref.
		MGT	CVG	%G	SVI	
ZnO(10--200 mgL^{-1})	*Zea mays*	-	2932.9	-	-	[172]
$nSiO_2$(2--14 gL^{-1})	Tomato	3.98%	507.82%	22.16 %	22.15%	[173]
CuO(0.1--10 mgL^{-1})	Wheat	1.92±0.054	50.6±1.46	100%	-	[174]
Fe(25--250 mgL^{-1})	Soyabean	-	-	99.34 %	-	[175]
ZnO(25--500 mgL^{-1})				94.74 %		
Cu(5--50 mgL^{-1})				96.71 %		
Co(0.05--2.5 mgL^{-1})				95.36 %		
MgO(10--100 mgL^{-1})	*Vigna radiata*	-	-	100%	1340 ± 10	[176]
ZnO(5--20 mgL^{-1})	Wheat	-	-	100%	94%	[177]
ZnO(750--1250 $mgkg^{-1}$)	*Capsicum annum*			73%	1177	
TiO_2(750--1250$mgkg^{-1}$)		-	-	67%	993	[178]
Ag(750--1250 mg kg^{-1})				69%	1075	
CuO/NiO/CoO(100 ppm)	*A. esculentus*	10.10 ± 0.9	10 ± 1.0	80%	1640 ± 40	This work

MGT: Mean germination time, CVG: Coefficient velocity of germination, %G: Percent germination, and SVI: Seed vigour index.

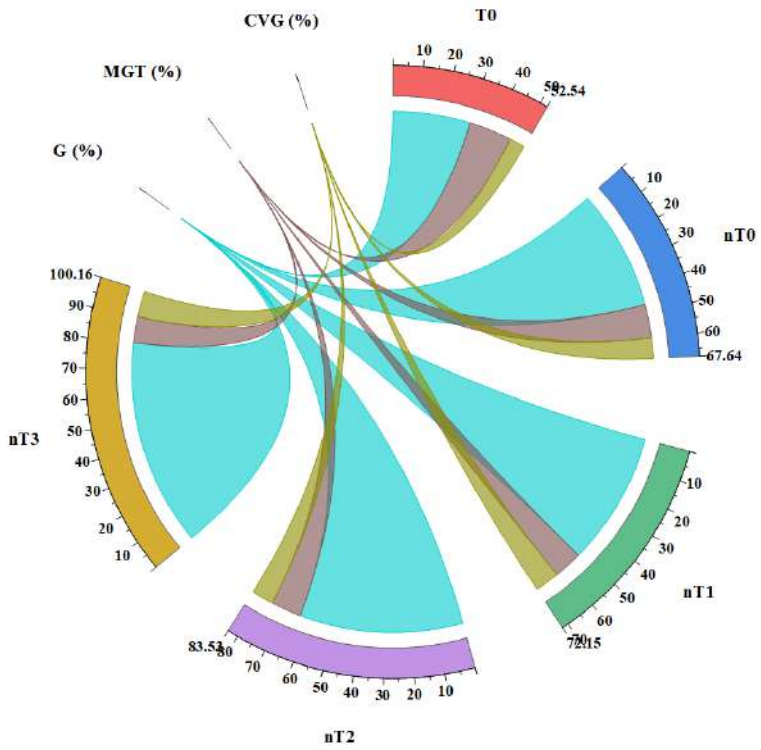

Figure 3.8: Chord diagram depicting the associations between different treatments and seed germination parameters. The diagram visualizes the interconnections between five treatment groups T0 (control), nT0, nT1, nT2, and nT3 and key germination indices. The thickness and direction of the chords indicate the relative contribution of each treatment to the germination metrics. Notably, nT3 and nT2 treatments show stronger associations with higher germination percentage and CVG, suggesting enhanced germination performance compared to the control.

The chord diagram in Figure 3.8 visually represents the strength and direction of associations between various treatments (T0, nT0, nT1, nT2, nT3) and germination-related biological parameters G%, MGT, and CVG. Each segment corresponds to a treatment or parameter, with connecting ribbons indicating the magnitude of their relationships. Notably, the nT3 treatment exhibits the most substantial association with G%, suggesting a significant enhancement in seed germination under this condition. Similarly, treatments nT2 and nT1 show notable connections to both G% and CVG, implying improved seed performance. In contrast, MGT, which inversely relates to germination efficiency, is more strongly associated with the untreated or less optimized treatments (T0, nT0), indicating slower germination rates. These observations align with

previous studies demonstrating that nanoparticles can enhance seed germination and growth by improving nutrient availability and microbial activity[179]. Moreover, the correlation matrix and heatmap (Figure A5 and A6) were also used to investigate the interaction of *TmONs* with the physicochemical and biological parameters of vermicompost.

3.3.3 Impact and Interaction of Biogenic Cu/Ni/Co Oxide Nanoparticles with Soil Health, Biodiversity, and Soil Biota

Literature reveals copper, nickel, and cobalt oxide nanoparticles have demonstrated both beneficial and potentially adverse effects on soil health and biodiversity, with their impact largely dependent on concentration and interaction with soil constituents. Elevated concentrations of Cu^{2+}, Ni^{2+}, and Co^{2+} metal ions can interfere with ion channel functioning, impairing key physiological processes such as osmoregulation, digestion, and nutrient uptake in soil organisms. While concentrations ranging from 50 to 100 ppm are commonly encountered in agricultural soils, levels exceeding this range are typically considered contaminative. Nevertheless, studies have shown that at concentrations below 100 ppm, these nanoparticles do not induce significant long-term toxicity in earthworms, particularly in terms of survival, growth, or bioaccumulation[180]. Biogenic nanoparticles also interact dynamically with soil organic matter and microbial communities. These interactions are particularly relevant during early plant developmental stages, such as germination, which involves complex metabolic events including lipid mobilization, hormonal regulation, and nucleic acid biosynthesis[181]. The surface of phytosynthesized nanoparticles often contains functional moieties such as hydroxyl (-OH) and carboxyl (-COOH) groups, which facilitate bonding with humic and fulvic acids, leading to the formation of stable, nutrient-enriched complexes. These interactions contribute to the mitigation of metal toxicity while enhancing nutrient

bioavailability [182]. In addition, the gradual release of Cu^{2+}, Ni^{2+}, and Co^{2+} ions from nano-oxides can influence soil microbial dynamics. These ions exhibit a strong binding affinity toward thiol (-SH) groups in microbial enzymes and membrane proteins, imparting mild antimicrobial properties that may contribute to the suppression of pathogenic soil microbes without severely impacting beneficial populations[183].

Furthermore, these nanoparticles are known to catalyze the oxidative degradation of recalcitrant organic materials such as lignin and cellulose, derived from agricultural residues like rice straw and pressmud, by promoting reactive oxygen species (ROS) generation during microbial respiration. The uptake and biological activity of these nanoparticles in plants have also been supported by recent studies. For instance, increased lipid accumulation in the plumule and cotyledon of mung bean seeds has been observed in response to nanoparticle exposure during germination, indicating a stimulatory effect on early development[184]. The presence of organic acids and proteins from *Moringa*-based phytoconstituents may enhance nanoparticle entry into plant tissues by forming chelated complexes that facilitate membrane transport[185]. The small size (<50 nm) nanoparticles can absorb onto seed surfaces and release metal ions in a controlled manner over time. Collectively, these findings suggest that biogenic Cu/Ni/Co oxide nanoparticles, when applied within environmentally acceptable limits, can improve soil fertility, enhance organic matter composition, and promote microbial equilibrium, thereby supporting soil health and ecological biodiversity.

3.3.4 Physiochemical and Biochemical Roles of Cu, Ni, And Co in Plant Growth and Stress Tolerance

These elements (Cu, Ni, and Co) have been discovered to be components of several enzymes involved in photosynthesis, nitrogen metabolism, electron transport, plant defense mechanisms, secondary metabolites, stress tolerance, antibacterial and antifungal

capabilities [186], [187], [188]. Some researchers mentioned the concept of the oxidative window for germination, which is a critical range of the ROS at which the occurrence of the cellular events associated with germination is optimal [189]. The ICP-OES results support oxidative window hypothesis, as all the concentrations within leaves and soil are under optimum ppm levels. The earthworm tolerance study was useful in deciding the concentration of the *TmONs*. At higher concentrations of 200--500 ppm, the earthworms were not able to survive, while at lower concentrations of 50 and 100 ppm, the survival rate was high (Figure 3.6). Furthermore, the point is again justified in the studies, where higher concentrations of NiO (250 and 500 mg L^{-1}) caused toxicity in Chinese cabbage seedlings, while lower concentrations of 50 mg/L had positive effects [185], [190].

3.3.4.1 Role of Cu in Germination and Antifungal Activity

Researchers have studied the production of copper oxide nanoparticles (CuO NPs) using *Eudrilus eugeniae* vermi wash, identifying its practicality in the germination mechanism of *Vigna radiata* seeds [191]. Their results show that CuO NPs have a favourable effect on seed germination, and their lower concentrations can be used as fungicides, while high doses can alter the levels of acidic, basic amino acids, and total protein [192], [193]. In our study, *TmONs* showed visual antifungal effects for the treated plants with respect to the control. They might have been coated by root exudates or other organic moieties present in the soil, which lead to surface modifications and hence reduce the toxicity of metals. A similar observation is reported, where a coating of citric acid reduced the toxicity of CuO NPs in soyabean [141].

3.3.4.2 Role of Ni in Nitrogen Metabolism and ROS Signalling

Nickel is also an essential micronutrient for seed germination and senescence. It is a major component of the urease enzyme, which hydrolyzes urea into ammonia and carbamic acid, a source of nitrogen for plants. It increases the solubility of nitrogen and

phosphorus in the soil, making these nutrients more available to plants. Germination parameters were considerably enhanced in okra seedlings by using an optimized concentration of NiO in *TmONs*, which helped in regulating the plant's stress response through the generation of ROS and thereby triggering several signalling pathways and stress-responsive gene expression. A similar effect was seen in *Vigna mungo* plants when NiO-NPs were supplemented in a dose-dependent manner [194]. Further, it was proved that nano NiO at environmentally relevant concentrations does not produce significant phytotoxicity [190]. Along with this, nickel serves in nitrogen fixation, along with cobalt and vitamin B12. Furthermore, an enhancement in shoot and root lengths was also observed by using *TmONs*, which led to an increase in overall biomass and justified the concentration of *TmONs* used [142].

3.3.4.3 Role of Co in Chlorophyll Synthesis, Metal Transport and Root Development

Cobalt in lower concentration may have aided in better nodulation and, as a result, improved growth and yield in our study. In fact, the specific mechanisms of accumulation, translocation, and specific transporter are still unknown to a great extent for cobalt. It is considered a non-essential element in plants, but recent studies have marked the vital role of Co in a number of physiological processes involving the synthesis of photosynthetic pigments which result in increased biomass [146]. Instilling drought and stress resistance within the wheat plant is another essential function of Co, since it plays a regulatory role in reducing transpirational rate through water use regulation [195]. A study provides valuable insight about the role of Co in redox homeostasis over melatonin in improving yield under salt stress conditions in cucumber [196]. In continuation, our study also gave positive results in terms of increased seedling height and growth index, which indicate the synergy between Cu and Co, as reported by Talankova and co-workers, where adding colloidal solutions of Co and Cu to Murashige

and Skoog nutrient medium led to increased microplant height and growth index [197]. Moreover, the increased root hair formation in all the treated plants (Figure 3.9A) could be due to the effect of Co, which led to increased absorption of water and nutrients, further boosting growth. CoO in *TmONs* improved plant nutrient uptake by chelating with other metal ions (like Fe) and making them more available to plants. Further, due to similar chemical properties, the synergy between Co and Ni played an important role in plant metabolism. A supporting work also mentioned an ATP-binding cassette (ABC) transporter that aids in the transportation of Co and Ni into and out of the chloroplast [198] (Figure 3.9B). Moreover, in our study the chlorophyll content was also found to be highest for nT3 group, as shown in Table A3.

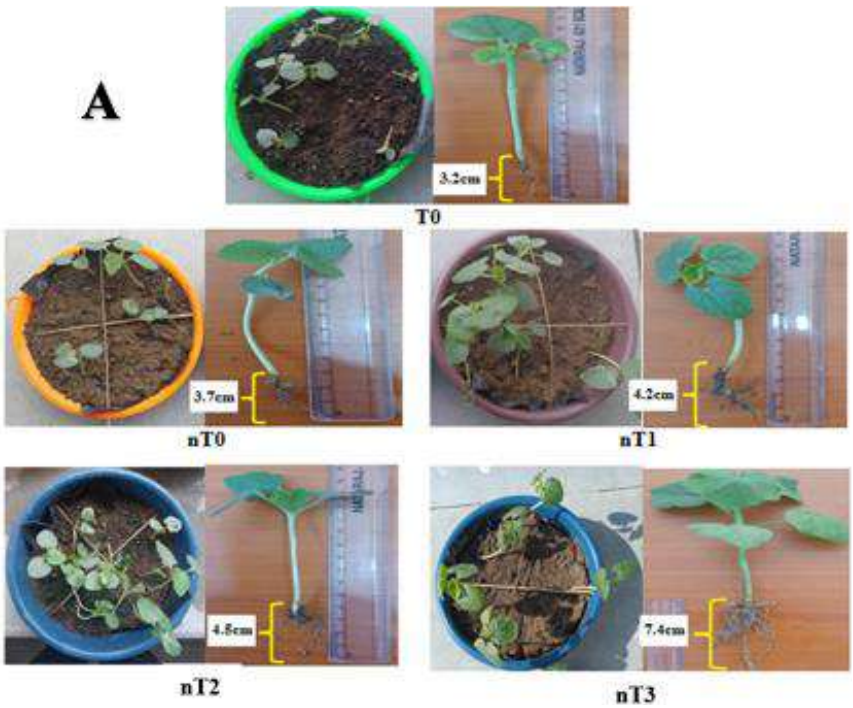

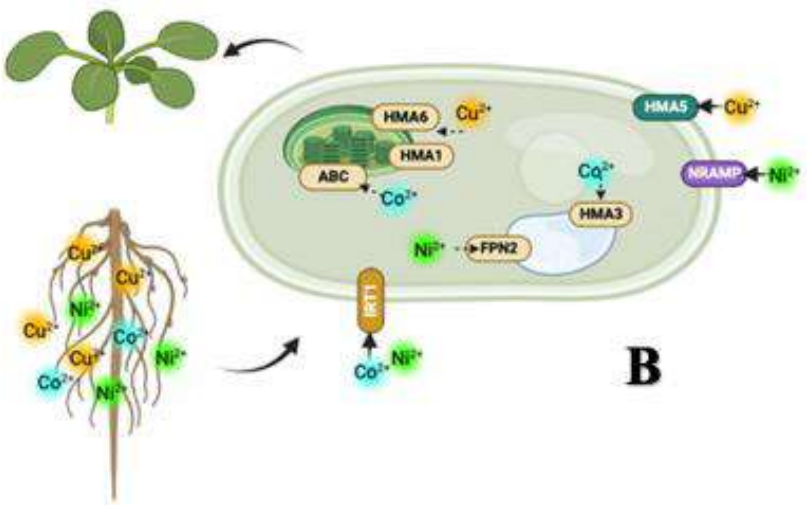

Figure 3.9: (A) Pictures showing root length in treatment groups. (B) Ionic pathway for the metal ions (Cu^{2+}, Ni^{2+} and Co^{2+}) moving from roots to leaves. IRT1, NRAMP, HMAS, FPN2, HMA1/6/3, and ABC are transporter proteins involved in translocation.

3.3.5 Mechanism of *TmONs* Uptake and Metal Ion Transport in Plants

Based on literature, the *TmONs* may have entered root cells via the apoplastic/symplastic process, the ABC (ATP-Binding Cassette) transporter, endocytosis, ion carriers like IRT1 (Iron-Regulated Transporter 1), etc., where they get involved in various metabolic processes upon interaction with different organelles [199]. The apoplastic pathway allows passive movement through the extracellular space, while the symplastic pathway involves transport through the cytoplasm via plasmodesmata. Furthermore, various transporter proteins are present in plants for the selective translocation of respective metal ions. The cations are taken up by the plant cells as they form complexes with organic compounds in the soil. These noncovalent interactions could be coordinate bonds or electrostatic bonds. The soil is slightly acidic due to the presence of acids like tartaric acid and malic acid etc. The polyvalent cations bind with the O and N groups by the unshared electrons present on them as a result the positive charge neutralizes. On the other hand, these ions can also attract negatively charged groups (-COOH) to form electrostatic bonds where the positive charge retains [200]. For instance, Co^{2+} is transported from soil to the

epidermis along with iron with the help of iron-regulated transportin proteins, IRT1, Cu^{2+} by HMA5 (Heavy Metal ATPase 5), and Ni^{2+} by NRAMP (Natural Resistance-Associated Macrophage Protein) including NRAMP1 and NRAMP6 (Figure 3.9B) facilitates the uptake and intracellular remobilization of divalent metal ions such as Fe^{2+}, Mn^{2+}, and Co^{2+}, particularly under deficiency conditions[201]. Similarly, IRT1, although primarily responsive to iron deficiency, exhibits promiscuity in substrate selectivity and enables Co^{2+} uptake across the root epidermis [202]. Once inside, Ferroportins like FPN1 and FPN2 mediate the efflux of Co^{2+} from root cortical cells into the xylem, ensuring its delivery to aerial tissues while preventing local ion toxicity [203]. ABC transporters such as AtABCC1 and AtABCC2 are involved in the vacuolar sequestration and detoxification of excess Co^{2+}, thus maintaining cytosolic homeostasis and minimizing oxidative damage [204], [205].

Before being transported to shoots, these ions form complexes with citrate, histidine, methionine, or nicotinamide in the xylem, preventing precipitation. In leaves, these ions are released and take part in metabolisms involving ABC transporters. For example, Cu^{2+} ions are involved in the function of enzymes like plastocyanin, which is essential for the electron transport chain in photosynthesis. Additionally, Ni^{2+} is required for the activation of urease, an enzyme critical for nitrogen metabolism, while Co^{2+} is necessary for the synthesis of certain cofactors like vitamin B12 in specific plants.

Cobalt ions (Co^{2+}) reduce leaf abscission in *A. esculentus* by specifically inhibiting 1-aminocyclopropane-1-carboxylic acid (ACC) oxidase, the key enzyme catalyzing the conversion of ACC to ethylene. This inhibition lowers ethylene levels in plant tissues, which in turn delays the activation of abscission-related processes in the leaf abscission zone. In the presence of Co^{2+}, auxin transport from the leaf blade to the abscission zone remains uninterrupted, preventing the hormonal imbalance that typically initiates cell

separation. Similar results were seen in a study on *Rosa hybrida*[206]. Additionally, Co^{2+} suppresses the expression of hydrolytic enzymes like cellulases and polygalacturonases, which are responsible for degrading the middle lamella. It also enhances the activity of antioxidant enzymes such as superoxide dismutase and catalase, reducing ROS accumulation that would otherwise promote abscission . These combined effects preserve the structural integrity of the abscission zone and delay leaf detachment in treated okra plants[200].

As a consequence, deficiency of any of these metals can lead to stunted growth, reduced root development, reduced seed production, changes in leaf shape, and decreased chlorophyll content. On the other hand, an excessive amount can have similar negative effects. Therefore, a balanced and controlled application of these nanoparticles is crucial for maximizing their benefits and minimizing potential adverse effects. It is worth mentioning that no such adverse effects were seen in the treated vermicompost plants during the whole study period, which may be related to the optimal *TmONs* concentration.

3.3.6 Comparison of Agro-Waste Derived Vermicompost with Chemical Fertilizers

Compared to chemical fertilizer, vermicompost contains less NPK and more organic compounds like polysaccharides, proteins, and lipids, which boost the microbial colony[207]. Due to its eco-friendly nature, vermicompost feeding could greatly influence crop quality management by addressing the problems associated with chemical fertilizers [136]. Furthermore, the more disaggregated vermicompost as compared to controls could be due to the action of bacteria and enzymes produced by *E. fetida*, which was enhanced by adding nanoparticles in nT3. High surface area, tunable porosity, and strong cation exchange interactions could have resulted in massive holes, fragmentation, and porosity allowing good absorption, aeration, and drainage [114]. Moreover, during toxicological risk assessment on earthworms, it was found that at concentrations higher

than 100 ppm the mortality was high, which was primarily due to desiccation, likely due to disruption of water regulation mechanisms.

3.3.7 Potential Regulatory Challenges Associated with the Use of Nanoparticles

In India, various agencies, like the Indian Council of Agricultural Research (ICAR), Department of Biotechnology (DBT), the Food Safety and Standards Authority of India (FSSAI), and the Ministry of Environment, Forest and Climate Change (MoEFCC), have framed some laws and safety regulations, but they are still evolving and subject to change with time [208].

3.3.8 Leaching and Bioaccumulation of Cu, Ni, And Co Metals

Nanoparticles influence at the cell level, thus increasing the pace of physiological processes in plants. Plant based materials seem to be the best candidates for synthesizing biocompatible NPs due to the biochemical diversity of plant extracts, non-toxic phytochemical constituents, non-pathogenicity, low cost, and flexibility in reaction parameters as compared to chemical synthesis methods. It is well established that nano-fertilizers follow slow-release and minimum leaching properties as compared to bulk counterparts when used in low concentrations (<100 ppm)[209]. The controlled release of nutrients from these nanoparticles reduces leaching into groundwater, thereby minimizing nutrient runoff and environmental pollution. Moreover, conventional fertilizers such as urea, PK, ammonium phosphate, etc., pose serious issues like loss in soil fertility and runoff. Nitrogen fertilizers in general have an efficiency of only 30--50%, hence biogenic nanofertilizers can be a better substitute to improve soil quality and boost yield . Copper oxide (CuO), nickel oxide (NiO), and cobalt oxide (CoO) nanoparticles, when used in soil as fertilizers in a given ratio of precursors, can positively impact plant growth and soil health through controlled bioaccumulation and leaching

processes. Moreover, our study is also supported by previous studies that mention concentrations below 100 ppm cause no substantial long-term harmful effect on earthworm survival and combinations/mixtures of nanoparticles to be considered [210].

3.4 Conclusions

Novel biogenic trimetallic (Cu/Ni/Co) oxide nanoparticles derived from *Moringa oleifera* leaves extract significantly enhanced vermicompost quality and okra seedling performance. When combined with industrial wastes (RS and PM), these *TmONs* work as an efficient nano-organic fertilizer. The electrical conductivity, total organic carbon, and NPK content of the produced vermicompost were significantly increased ($P < 0.05$) due to the effect of PM and RS, while the C/N ratio was dropped. The efficiency of the nano-organic amendment was evident in the growth parameters of okra plants, as a significant increase in cumulative germination, CVG, and SVI by 167%, 67%, and 95%, respectively, was achieved with respect to control. Among all treatments, the best growth parameters were observed for nT3. Moreover, ecological risk assessment of *TmONs* concentration has also been evaluated and found to be under the maximum permissible limits of WHO (1996), establishing a foundation for environmental safety. This synergetic approach for nano-organic amendment continues to serve a dual purpose: recycling agro-waste and, at the same time, impacting the agricultural transformation by using eco-friendly fertilizer. Therefore, these findings support the use of biogenic *TmONs* in conjunction with RS and PM as a nano-organic amendment for soil reclamation. To ensure biocompatibility, future nano formulations should prioritize metal oxides that naturally occur in plant metalloenzymes, applied at concentrations <100 ppm. For policymakers, it is suggested to develop strict guidelines that monitor and regulate the use of biogenic nanoparticles.

3.5 Limitations and Future Research Directions

While this study establishes the immediate benefits of *TmONs*-enriched vermicompost, several critical areas require investigation before widespread agricultural implementation. To evaluate nanoparticles agglomeration in soil and their effect on important microbial communities (particularly nitrogen-fixing bacteria) and soil properties, further research is required. Evaluation of cumulative effects on soil fertility and microbial diversity across different crops as well as under varying soil pH and climatic conditions should be done through multi-season field trials employing techniques like 16S rRNA sequencing and soil enzyme profiling. Although our current research work confirmed metal concentrations within WHO limits, long-term leaching studies are required to monitor metal accumulation and groundwater contamination to assess environmental safety. Moreover, stress-related gene expression and metabolic shifts induced by metal oxide nanoparticles' exposure must be explained by molecular-level research employing proteomics, transcriptomics, and enzyme activity assays, providing fundamental insights for optimized nanoparticles synthesis. Knowledge of nanomaterial-based products, availability of trustworthy information, and confidence in new technologies are required by the farmers. Such efforts may include building confidence by field demonstrations. Additionally, regulatory frameworks controlling the use of nanoparticles in agriculture are still evolving, therefore, influencing the path of commercialization of the formulation. Hence, the establishment of standardized international guidelines for the agricultural application of biogenic nanoparticles is strongly recommended, with particular emphasis on environmental monitoring frameworks and comprehensive safety evaluation protocols. Future efforts could include regulatory compliance, and cost-effective research to enable informed and responsible field-level adoption.

"While Chapter 3 explored the agricultural potential and eco-toxicity profile of the synthesized Cu/Ni/Co oxide nanoparticles, Chapter 4 advances the discussion toward a deeper material perspective elucidating structure-property relationship. Therefore, the next chapter shifts the focus toward the structural, morphological, optical, and magnetic properties of CuO/NiO mixed oxide nanoparticles."

CHAPTER 4

Influence of compositional variation on the structural, morphological, optical and magnetic properties of CuO/NiO NPs synthesized using *Moringa oleifera* leaves extract[2]

This chapter is adapted from: Composition dependent variation in structural, morphological, optical and magnetic properties of biogenic CuO/NiO mixed oxide nanoparticles. Journal of alloys and compounds, 979, (117):173422. https://doi.org/10.1016/j.jallcom.2024.173422.

4.1 Introduction

The engineering of nanoscale structures with meticulously regulated morphological characteristics, dimensional parameters, and compositional stoichiometry represents a cornerstone of contemporary materials science research. This precision in structural control stems from the exceptional physicochemical attributes exhibited by nanomaterials, which significantly differentiate them from their bulk counterparts and establish their superiority in diverse technological applications [211]. The enhanced surface-to-volume ratio, quantum confinement effects, and altered electronic properties inherent to nanoscale dimensions contribute to their unprecedented functionality across multiple domains [212].

Binary metal oxide nanomaterials comprising copper and nickel have garnered considerable scientific interest in recent decades due to their remarkable physicochemical characteristics and diverse technological applications. These nanostructures demonstrate exceptional features including ferromagnetic behavior[213], enhanced catalytic

[2] A manuscript based on this chapter has been published in *Journal of Alloys and Compounds.*

performance[214], [215], [216] and excellent biological compatibility,[217] making them valuable for numerous industrial processes. The integration of copper oxide with nickel oxide creates a unique hybrid system where each component contributes distinct advantages. Copper oxide nanomaterials are renowned for their antimicrobial efficacy, while nickel oxide exhibits pronounced magnetic characteristics. This complementary combination establishes novel research opportunities and technological possibilities. The optimization of these characteristics is directly influenced by the stoichiometric ratio of copper to nickel precursors. Moreover, the modifiable surface characteristics of CuO/NiO mixed oxides facilitate the incorporation of specific targeting molecules, enabling selective identification of biological markers and implementation in chemical sensor applications. These materials find extensive utilization in biomedical fields, serving as contrast enhancement agents for various imaging modalities, particularly magnetic resonance imaging (MRI)[218], [219]. Magnetic hyperthermia therapy exploits the ferromagnetic properties of nickel oxide components, wherein these nanostructures produce concentrated thermal energy to selectively eliminate malignant cells when exposed to alternating magnetic fields. Research indicates that the magnetic behavior of these composite materials correlates directly with nickel content concentration [220]. However, despite their promising applications, limited investigation has been conducted regarding the magnetic characteristics of CuO/NiO composite nanoparticles. Current literature reveals insufficient exploration of their magnetic properties and structure-property relationships.

Various synthetic approaches have been employed for fabricating mixed oxides CuO/NiO nanoparticles, including solvothermal process[221], sol-gel technique[222], hydrothermal methods[223], [224] and microemulsion approaches[225]. However, these conventional methodologies present several limitations including high energy

consumption, extended reaction durations, expensive instrumentation requirements, reduced product yields, and utilization of hazardous chemicals that raise environmental and safety concerns. This investigation employs an environmentally sustainable solution combustion methodology for synthesizing Cu-Ni mixed oxide nanoparticles as presented in Chapter 2. Recent research has demonstrated successful synthesis of various nano-oxides using solution combustion techniques with plant extracts, including ZnO spherical structures, Fe_2O_3 nanocubes, SnO_2 nanorods, and $ZnFe_2O_4$ nanoparticles[226], [227], [228], [229]. This methodology involves rapid combustion of a solution containing fuel and oxidizing agents. The combustion process generates substantial thermal energy, causing solution vaporization followed by condensation to form solid products. The resulting materials typically exhibit nanostructured morphology with superior purity and homogeneous composition [94]. This process enables early-stage formation with diverse morphological characteristics within minutes. A significant advantage of this methodology is the elimination of toxic reagents, instead utilizing plant extracts that are environmentally sustainable and incorporate functional groups onto nanoparticle surfaces, resulting in enhanced biocompatibility.

Therefore, this study represents the inaugural utilization of *Moringa oleifera* leaves extract for synthesizing CuO/NiO nanoparticles in three different ratios (N12=1:2, N21=2:1, N22=1:1) through green solution combustion methodology. Additionally, the investigation examines how varying salt precursor concentrations affect structural, morphological, optical, and magnetic properties comprehensively. The biologically synthesized nanoparticles underwent comprehensive analytical characterization using X-ray diffraction analysis (XRD), X-ray photoelectron spectroscopy (XPS), high-resolution transmission electron microscopy (HR-TEM), and vibrating sample magnetometry (VSM) techniques to evaluate their properties and suggest potential applications.

4.2 Results and Discussion

4.2.1 Characterization of Synthesized Nanoparticles

4.2.2.1 Structural and Functional Analysis

The crystallographic structures of mixed oxide nanomaterials featuring different Cu^{2+}:Ni^{2+} molar proportions (1:2, 1:1, and 2:1), designated as N12, N22, and N21 respectively, were examined alongside single-metal oxides NM1 and NM2 through powder X-ray diffraction analysis, as illustrated in Figure 4.1A. XRD characterization provides valuable information regarding crystallite dimensions and structural imperfections, while peak intensity ratios reveal the spatial arrangement of atoms within the crystal lattice. Figure. 4.1B displays the diffraction patterns for N22 nanomaterials compared with theoretical XRD profiles of standard references, where reflections attributed to CuO (depicted in red) corresponded to ICSD-69758 database entry, and those associated with NiO (shown in blue) matched ICSD-9866 reference data. The presence of a face-centered cubic crystal system for NiO (*Fm-3m* symmetry group) [214] monoclinic structure for CuO [230] were confirmed. Additionally, the absence of extraneous diffraction peaks demonstrated the synthesis of exceptionally pure CuO and NiO phases, suggesting that high-quality CuO/NiO nanomaterials can be successfully fabricated through environmentally friendly solution combustion methodology.

In the diffraction patterns of N12, N22, and N21 nanomaterials, reflections corresponding to both metallic oxides (marked in orange) were evident, confirming the development of composite oxide systems with optimal crystalline quality observed in N22 (Figure 4.1B). Peak intensities fluctuated according to compositional ratios; specifically, the N12 sample with enhanced nickel concentration exhibited prominent NiO reflections relative to CuO peaks. Conversely, N22 demonstrated well-resolved reflections throughout, indicating superior crystalline ordering compared to N12 and N21 compositions. Employing the Debye-Scherrer equation:

$$D = \frac{k\lambda}{\beta cos\theta}$$ Equation 4.1

where D represents the average crystallite dimension (nm); k denotes the shape factor constant with a value of 0.94; λ corresponds to the X-ray wavelength (0.15406 nm); β indicates the full-width at half-maximum (FWHM) expressed in radians for the diffraction peaks; and θ signifies the Bragg diffraction angle (in degrees), the average crystallite size of the composite oxide nanomaterials was determined to be 11, 34, and 22 nm for samples N12, N22, and N21, respectively [231].

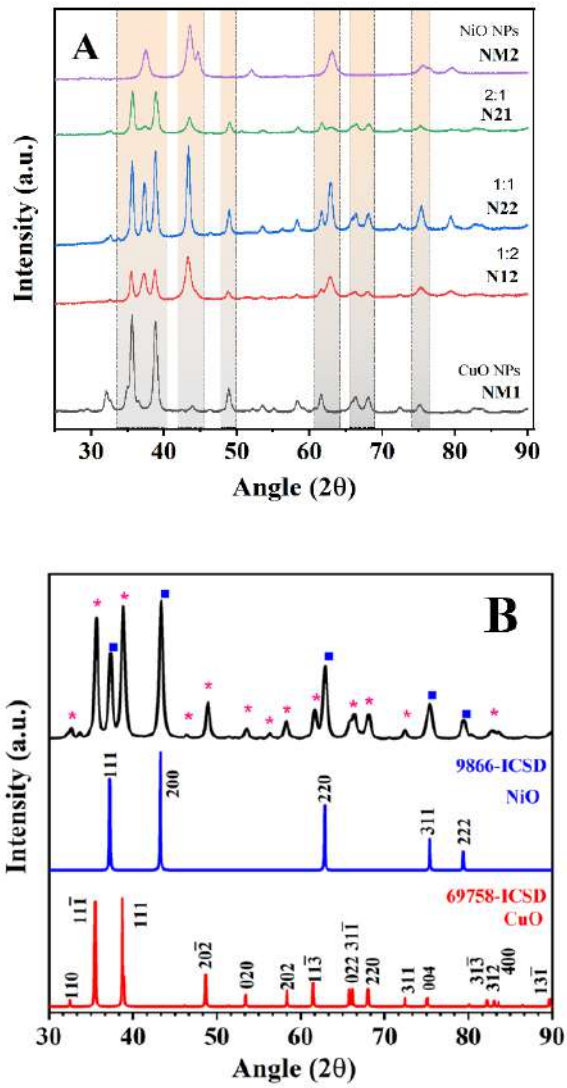

Figure 4.1: (A) XRD patterns of NM1, N12, N22, N21 and NM2 (orange highlighted area shows peaks for oxide mixing) and (B) simulated XRD patterns for N22 biogenic nanoparticles against standard references.

The surface composition of the biologically synthesized nanomaterials was analyzed through X-ray photoelectron spectroscopy (XPS) characterization. Both survey spectra and high-resolution core-level analyses are presented in Figure 4.2. Peak deconvolution was performed using a mixed Gaussian-Lorentzian line shape after Shirley background subtraction. The fitting was done till physically meaningful and supported by R^2 values near 0.99. The wide-scan spectrum revealed the presence of Cu, Ni, O, and C constituents alongside their corresponding Auger electron signals. The O 1s photoelectron spectrum was deconvoluted into four distinct peaks: lattice oxygen (O_L) positioned at 529.7 eV, oxygen defects (O_H) located at 531.8 eV, carbon-bonded oxygen species (C–O and O–C=O) (O_C) at 533.2 eV, and physisorbed oxygen (O_W) at 533.9 eV, which aligns with previously reported findings in the literature [232]. The presence of both C–O and O–C=O functional groups indicates that phytochemical molecules from the plant extract are not just physically adsorbed but are also chemically interacting with the surface Cu^{2+} and Ni^{2+} ions. This coordination plays a key role in stabilizing the nanoparticles and reducing their tendency to agglomerate. Such surface functionalization enhances the hydrophilic nature and colloidal stability of the particles, while also supporting favourable biological interactions. Moreover, the bio-derived organic layer improves overall biocompatibility and broadens the applicability of the nanoparticles in areas such as catalysis, antimicrobial activity, and drug delivery. The Cu 2p photoelectron spectrum exhibited two characteristic signals at binding energies of 933.2 eV and 953.2 eV, corresponding to Cu $2p_{3/2}$ and Cu $2p_{1/2}$ transitions, respectively. The observation of multiplet shake-up features for Cu $2p_{3/2}$ within the 940.8 to 942.3 eV energy range validated the existence of CuO (Cu^{2+}) oxidation state[215]. In the Ni 2p core-level analysis, the characteristic signatures of Ni $2p_{1/2}$ and Ni $2p_{3/2}$ were consistent with NiO spinel structure, with spectral deconvolution performed across the 853 to 870 eV binding energy window. The

confirmation of Ni^{2+} species in sample N22 was evidenced by principal photoelectron lines at 854.9 eV (Ni $2p_{3/2}$) and 872.8 eV (Ni $2p_{1/2}$), accompanied by their respective shake-up satellites at 861.2 eV and 879.6 eV[233]. The multiplet features observed between 854.14 to 855.8 eV provided additional confirmation of Ni^{2+} species within the N22 sample. The spin-orbit splitting characteristic of Ni^{2+} in its oxide environment was clearly evident from the 17.9 eV energy difference between the Ni $2p_{3/2}$ and Ni $2p_{1/2}$ peaks. The elemental composition from the XPS measurements, the Cu^{2+}:Ni^{2+} atomic ratio was determined to be 1.28 for sample N22. Similar spectral patterns and interpretations were found for both N12 and N21 samples.

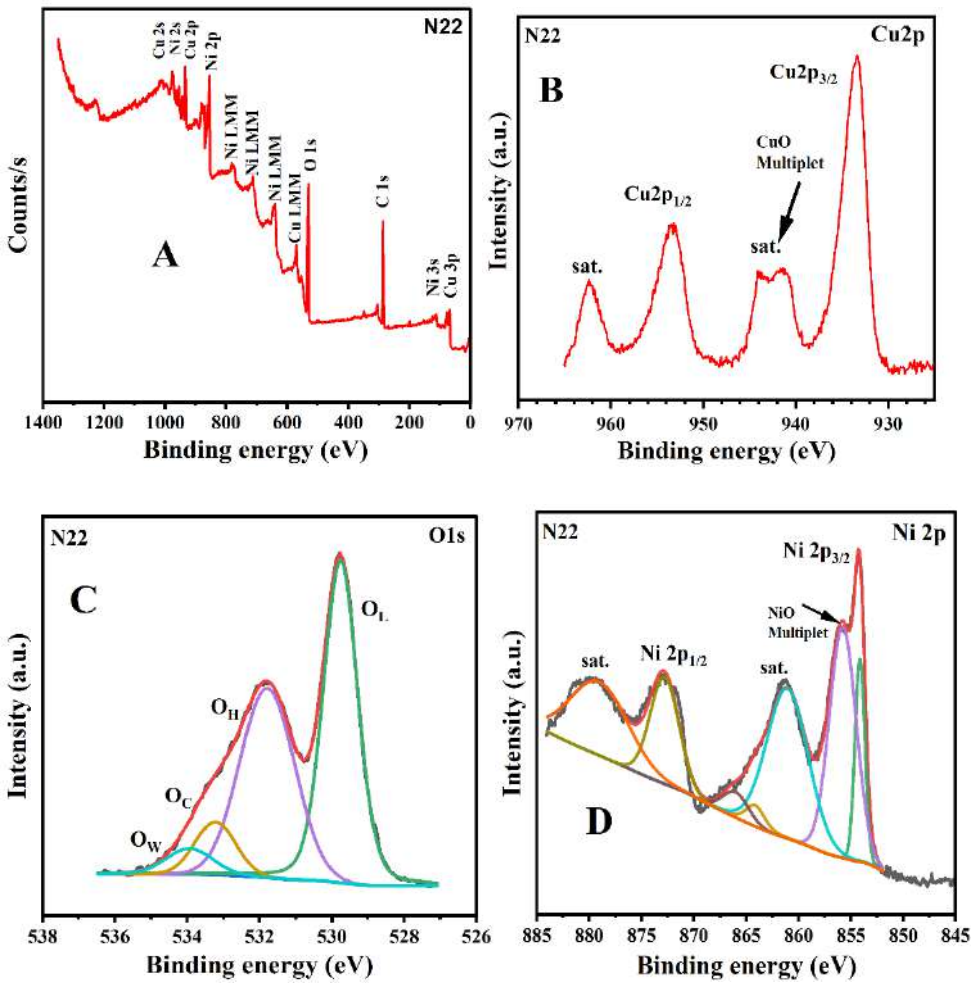

Figure 4.2: (A) XPS full scan spectra, (B) O 1s spectrum, (C) Cu 2p spectrum, and (D) Ni 2p spectrum of biogenic N22.

The vibrational spectroscopic characterization of the biologically synthesized nanomaterials before and after calcination is presented in the accompanying spectral data in Figure 4.3(A--C). The broad absorption bands spanning 3600 and 3300 cm^{-1} validate the existence of O-H groups associated with carboxylic acid functionalities. Additionally, the uncalcined samples exhibit distinct absorption features at 2923 and 2849 cm^{-1}, attributed to $C\text{-}CH_3$ and CH_2 stretching modes, respectively. The C=O stretching frequencies corresponding to amide I and II conformations are evidenced by absorption maxima at 1640 and 1516 cm^{-1}. The peaks at 1353 and 1373 cm^{-1} represent C-H bending. Dual absorption signals at 1108 and 1076 cm^{-1} substantiate the existence of C-O stretching in all uncalcined samples. Beyond these organic signatures, all mixed oxide nanomaterials demonstrate characteristic metal-oxygen vibrational modes within the 400-600 cm^{-1} spectral region. Following calcination, it is distinctly apparent that the predominant metal-oxygen absorption feature persists while organic-related peaks undergo significant attenuation, thereby confirming the successful formation of pure metal oxide nanostructures.

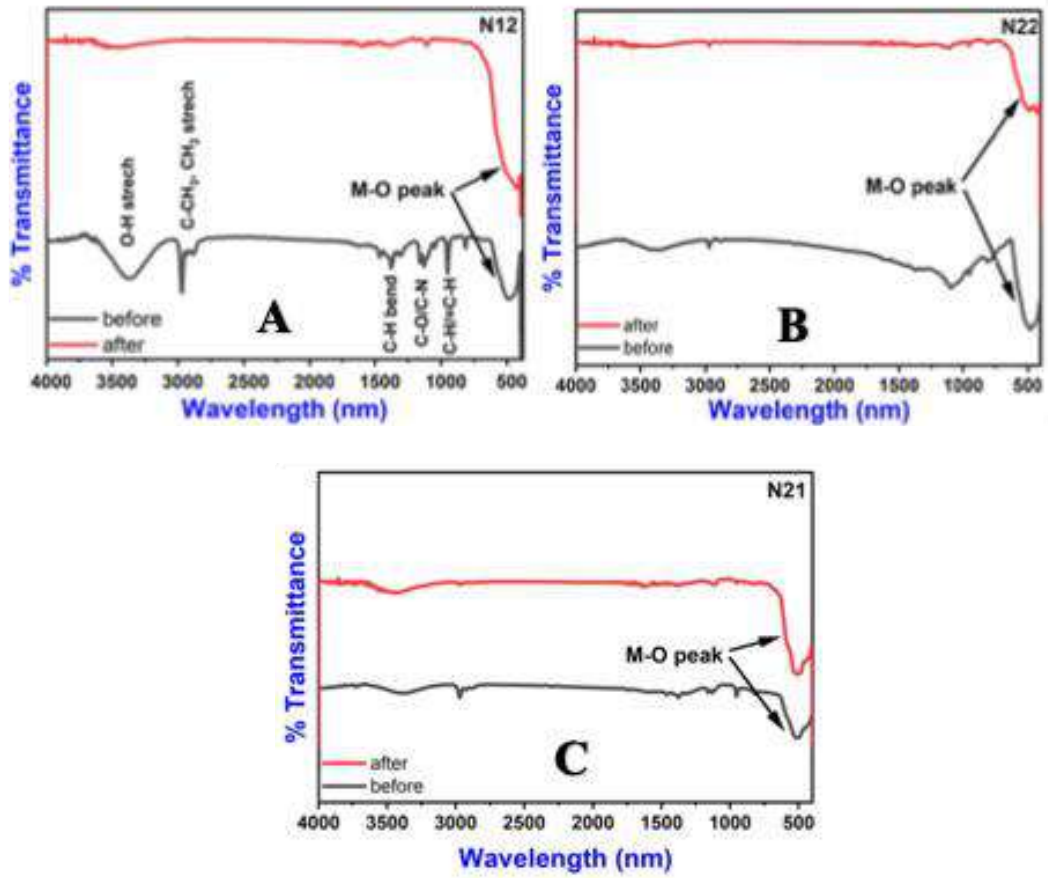

Figure 4.3: FTIR spectra before and after calcination for (A) N12, (B) N22 and (C) N21 biogenic nanoparticles.

4.2.2.2 Morphological and Surface Analysis

The N_2 adsorption-desorption isotherms (STP) of all five samples prepared by green solution combustion method using *Moringa oleifera* leaves extract are illustrated in Figure 4.4. Each oxide nanomaterial exhibits small hysteresis loops, with the isotherm shape corresponding to Type IV classification according to IUPAC standards. The BET specific surface area (SSA) calculations were performed across the relative pressure range of $0.1 < P/Po < 1.0$ for samples N12, N22, and N21, yielding values spanning 4.92--11.2 m^2/g, with the maximum surface area recorded for specimen N22. It is worth noticing that the SSA was increased for all mixed oxides (N12, N22 and N21) as compared to mono-oxides nanoparticles, which is similar to the results obtained by Zedan et al. 2022 [234]. The SSA, average pore diameter and pore volume are listed in the Table

4.1. The average pore diameter distribution of the materials also reflects the existence of partly mesoporous structure but an anomaly exists for N12 where the pore size is 55.4 nm, which is outside the mesoporous range as compared to other biogenic nanoparticles.

The higher specific surface area observed for sample N22 is consistent with its comparatively smaller crystallite size and more homogeneous particle distribution observed in the XRD and TEM analyses. A reduction in crystallite size generally increases the surface-to-volume ratio, thereby exposing a greater number of accessible adsorption sites. Conversely, particle agglomeration, as observed for sample N12, reduces the effective surface area by decreasing the accessible external surface despite a similar chemical composition. This inverse relationship between crystallite size and specific surface area has been widely reported for mixed metal oxide nanoparticles and plays an important role in determining their adsorption, catalytic, and electrochemical performance [92], [235], [236]. These low surface area biogenic nanoparticles are well suited for biomedical applications as they increase the biocompatibility and reduce the risk of toxicity [237].

Table 4.1 BET surface area, average pore diameter and pore volume of the biogenic NM1, N12, N22, N21 and NM2 nanoparticles

Biogenic NPs	**BET surface area (m^2/g)**	**Average pore diameter (nm)**	**Pore volume (cm^3/g)**
NM1	2.41	33.88	0.554
N12 (1:2)	4.92	55.7	0.069
N22 (1:1)	11.2	38.33	0.110
N21 (2:1)	5.07	40.56	0.05
NM2	10.2	39.37	0.081

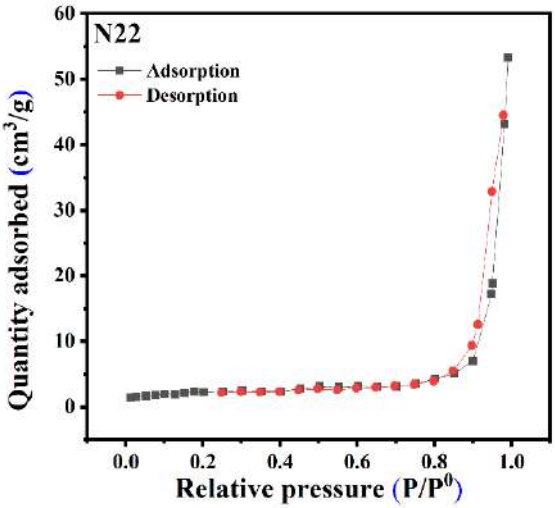

Figure 4.4: The N_2 adsorption-desorption isotherm (STP) for biogenic N22 nanoparticles.

Figure 4.5 shows FE-SEM images of as-synthesised NM1, N12, N22, N21, and NM2 biogenic nanoparticles. It is observed that NM2 (NiO) nanoparticles are much smaller and more spherical in nature while NM1 (CuO) nanoparticles are slightly bigger having irregular morphology. The surface energy of copper ions is large that leads to rapid nucleation and growth even in the presence of nickel ions. This could be the reason for comparatively bigger particles of CuO than NiO even at equal ratios of the precursors. For N21, where the concentration of copper is high, we can see larger particles while for N12 the number of larger particles is significantly reduced. Hence, when both precursors are added in a certain ratio, the nanoparticle size changes and the agglomeration becomes homogeneous. It should be highlighted that employing synthetic chemicals as a reducing agent makes it exceedingly challenging to create required size nanoparticles with variable shape and monodispersity [238]. However, using *Moringa oleifera* extract, we were able to achieve definite shaped nanoparticles by simple variation of concentration of metal ion and calcination temperature indicating its significant role in making such shape. The average particle sizes for N12, N22 and NM2 nanoparticles are found in the range of 29--56 nm. The presence of Cu, Ni, C, N and O in NM1, N12, N22, N21 and NM2

nanoparticles have been evidenced through energy dispersive spectrometry analysis (Figure A7--A9).

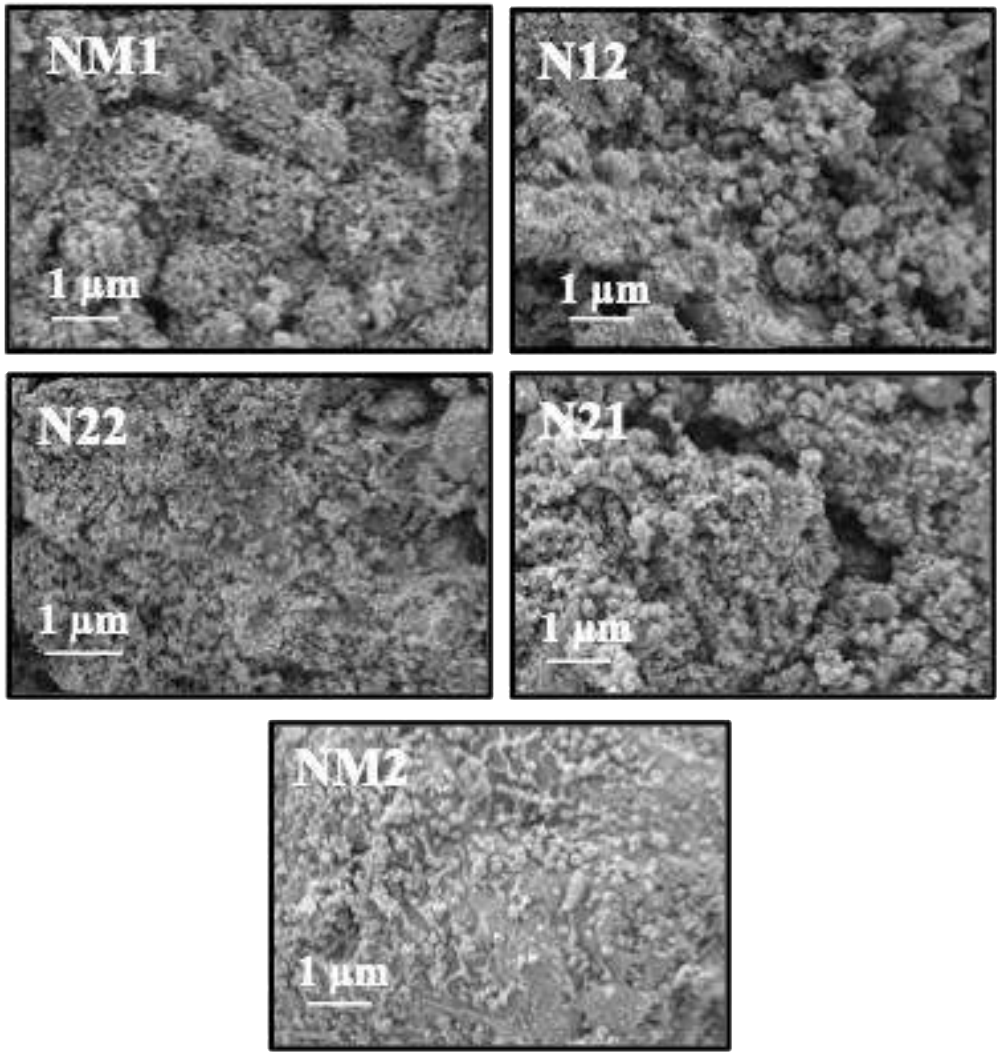

Figure 4.5: FE-SEM images of the biogenic NM1, N12, N22, N21, and NM2 nanoparticles.

The morphology of the nanoparticles was further studied using transmission electron microscopy (TEM). From the images in Figure 4.6, nearly spherical shape particles as well as hexagonal particles with round corners can be seen for N12, N22 and N21 nanoparticles, which is in line with the SEM discussion. The persistent parallel lattice fringes and cross fringes visible on individual particles in the high-resolution TEM (HR-TEM) images are indicative of the existence of mixed oxides. The lattice spacing was

determined to be 0.23 nm for the CuO (111) plane and 0.20 nm for the NiO (200) interplanar spacing [239].

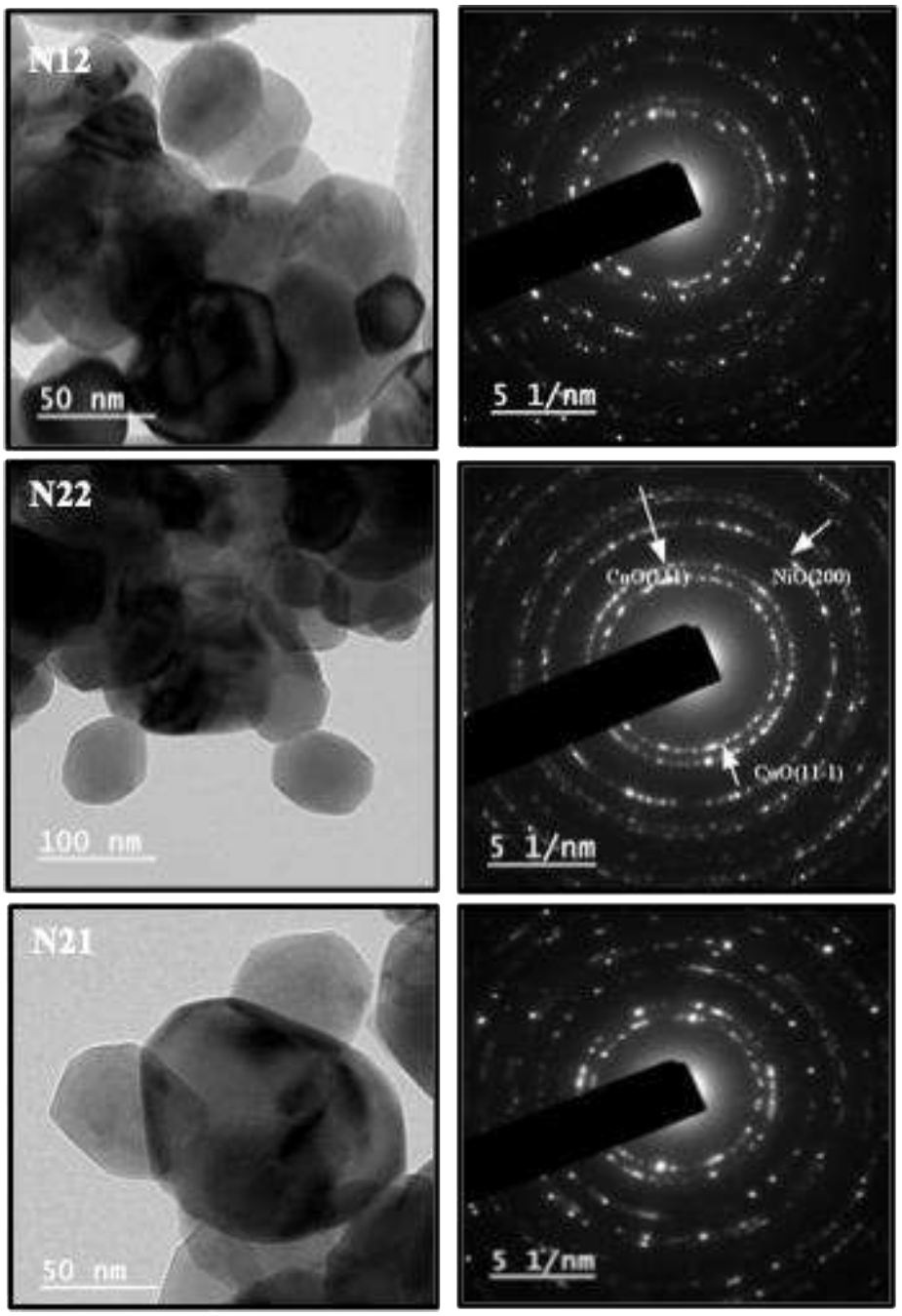

Figure 4.6: TEM images and SAED patterns of N12, N22, and N21 of biogenic nanoparticles.

The selected area electron diffraction (SAED) patterns for all mixed oxides revealed spots on concentric rings, indicating that the synthesized nanoparticles are polycrystalline in nature. It can be seen that the rings in N22 are more prominent as compared to N12

and N21 that could be attributed to the fact that N22 has more homogenous arrangement of particles, which are majorly spherical. Spherical particles have a more uniform scattering cross-section, while the irregular shaped nanoparticles have a more variable scattering cross-section. In other words, N22 is having more regular lattice structure, so they scatter the electrons efficiently. Each ring represents a distinct interplanar spacing of the Bragg reflection planes, which further demonstrated the presence of both types of NiO and CuO particles.

4.2.2.3 Optical Properties

Figure 4.7A shows the DRS spectra of the as-formed NM1, NM2 along with mixed oxides N12, N21 and N22 NPs exhibiting the absorption maxima at 284 nm for all followed by one major shoulder peak at 440 nm for mixed oxides. The absorption range has been found to be increased and covers visible region too for mixed oxides indicating their photo-activity in UV as well as visible region. A similar pattern has been observed by Bakre and co-workers [240]. The peaks appear as a result of surface plasmon resonance phenomenon of the nano-metal oxides. It is caused when the incident electromagnetic radiation-induce collective oscillation of free conduction band electrons. When the wavelength of the incoming light is significantly larger than the particle diameter, this form of resonance occurs [241].

The lowest wavelength needed to excite an electron is determined by the material's band-gap energy (Eg). The optical band gap was determined using the Tauc relation,

$$(\alpha h\nu)^n = A\left(h\nu - E_g\right) \qquad \text{Equation 4.2}$$

where α is the absorption coefficient, hν is the incident photon energy, A is a proportionality constant, and Eg is the optical band gap. Since CuO and NiO are generally reported to exhibit direct allowed electronic transitions, the exponent n = 2 was employed for constructing the Tauc plots. The band-gap values were therefore obtained by

extrapolating the linear region of the $(\alpha h\nu)^2$ versus $h\nu$ plots to $(\alpha h\nu)^2 = 0$, following the widely accepted procedure for direct band-gap semiconductors. The band-gap values for mixed oxides were found in the range of 2.19--2.46 eV (Figure 4.8 B--D) [242].

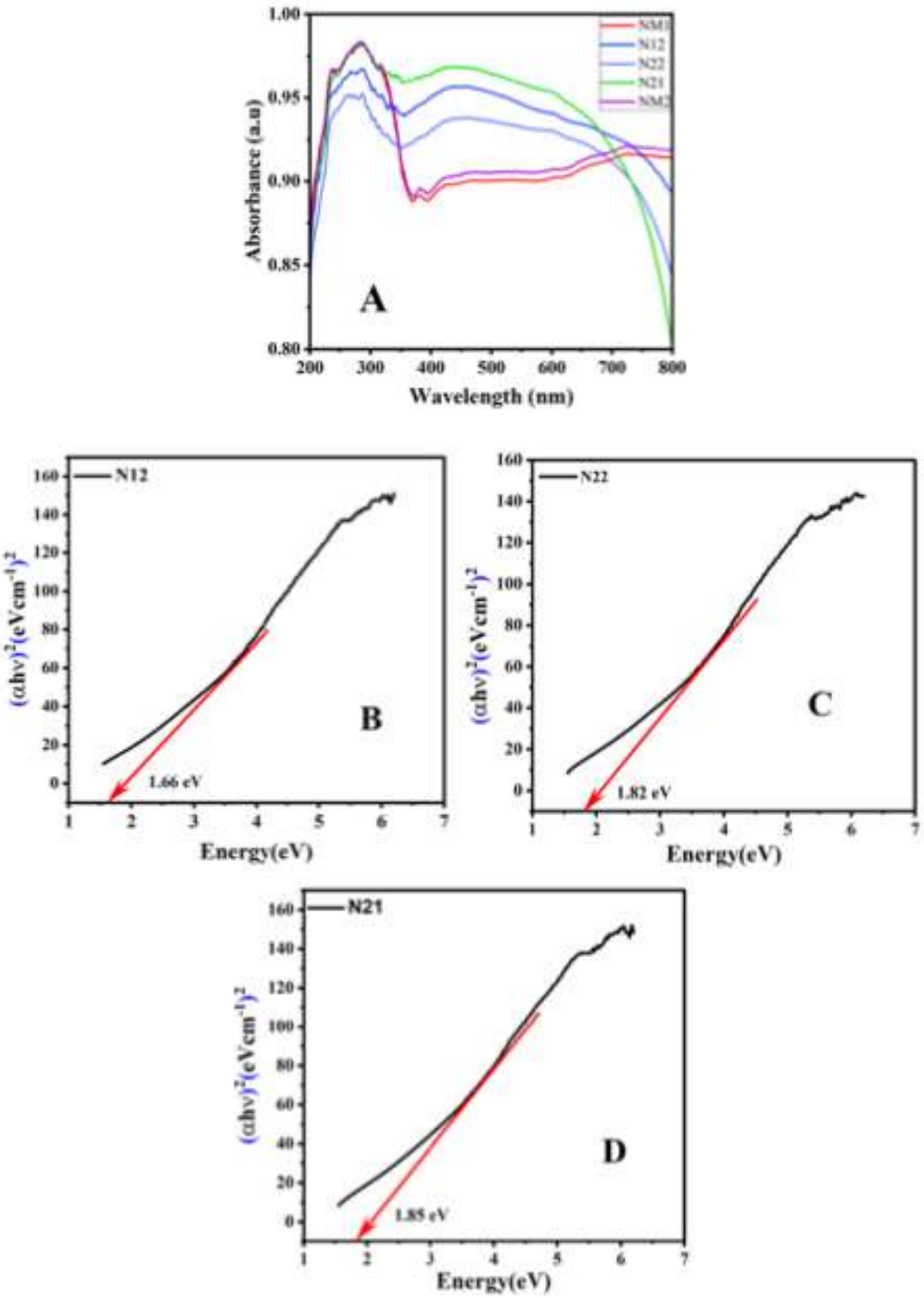

Figure 4.7: (A) UV-DRS spectra and (B)--(D)Tauc plots of the biogenic nanoparticles (N12, N22 and N21).

4.2.2.4 Magnetic Properties and Size-Dependent Behaviour of CuO/NiO Biogenic Nanoparticles

Magnetic field vs magnetization behaviour of the synthesized samples was analysed using Vibrating sample magnetometer (VSM) at 300K. Figure 4.8A depicts the cumulative M-H hysteresis loops of NM1, N12, N22, N21 and NM2 biogenic nanoparticles. The observation of negligible magnetic hysteresis loops for all the calcined samples illustrates the soft magnetic behaviour [243]. The values for coercivity (Hc), saturation magnetisation (Ms) and remanence (Mr) were determined and it was found that the Ms values of the nanoparticles increases with nickel content with Mr following the same trend (N22>N12>N21). However, the Hc follows opposite trend as: N22>N21>N12 (Table 4.2). The variation in Hc, Ms and Mr with different ratio of nanoparticles is shown in Figure 4.8B and 4.8C.

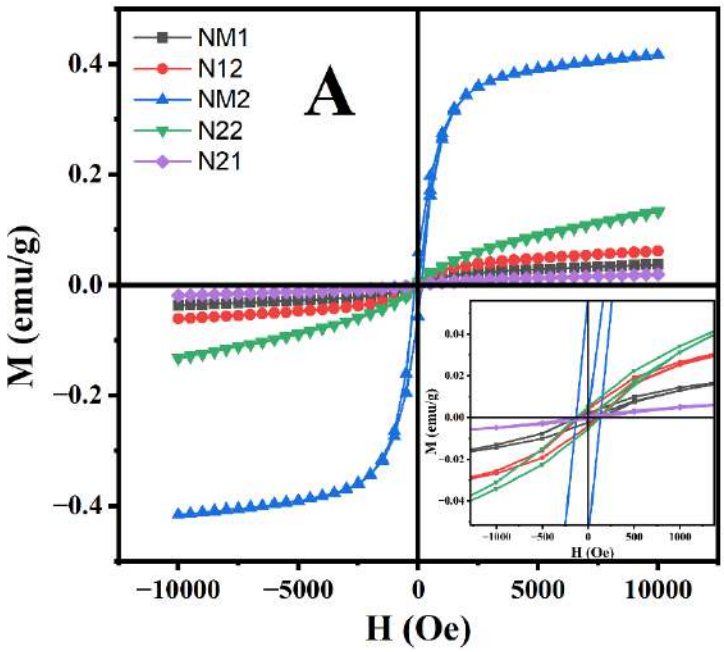

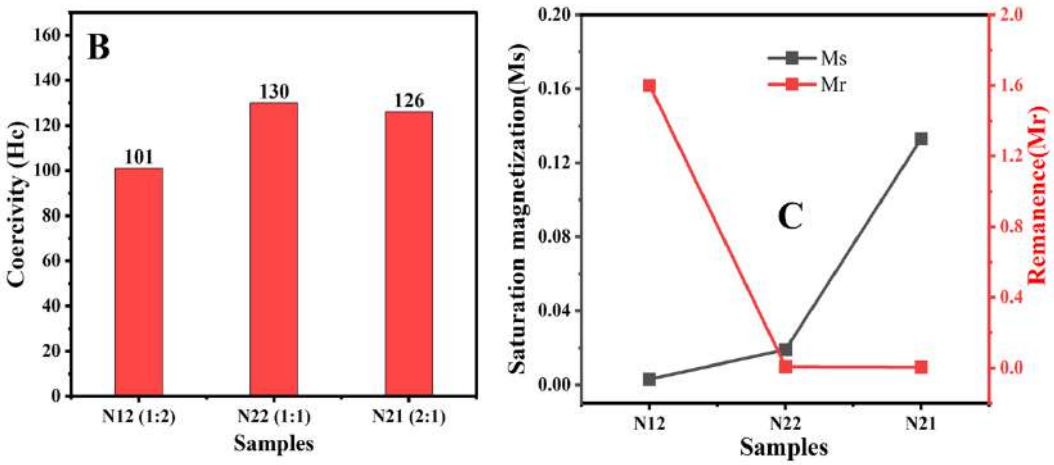

Figure 4.8: Variation in magnetic properties for all ratios of biogenic nanoparticles (A) Room-temperature hysteresis loops (inset shows magnified view near zero field), (B) Coercivity values, and (C) Saturation magnetization (Ms) and remanent magnetization (Mr) variations among all ratios.

Further observing the hysteresis reveals NM1 and NM2 show superparamagnetic characteristics with NM1 exhibiting very feeble superparamagnetism as evident from Langevin fit (Figure A10) to the hysteresis loop. It was fascinating to note that different ratio of the nanoparticles exhibited different magnetic behaviours. To further delve deep into their magnetic behaviours, ZFC and FC measurements were performed at two different fields i.e., 1000 Oe and 3000 Oe. It was investigated that there was no major difference in the shape of the curves at these two fields so susceptibility was plotted against temperature regime (5K to 378 K) to further confirm the nature of the particles (Figure 4.9). N12 follows typical curve for ferromagnetic particles wherein after curie temperature (Tc) the particles start to behave like paramagnetic. It was also confirmed from the overlapping curve obtained for M_{ZFC}-M_{FC} which is the indication of presence of single phase[244]. For N22, the curve follows the behaviour of paramagnetic materials and when observed closely there was a small cusp like peak in the susceptibility plot which could have raised due to transition towards ferromagnetic behaviour. A different type of transition from para to superconducting material was observed for N21. It should be noted that the reported transition temperatures were estimated qualitatively from the

inflection observed in the ZFC-FC susceptibility curves rather than from direct measurements. A more rigorous determination would require complementary analyses such as Arrott plots.

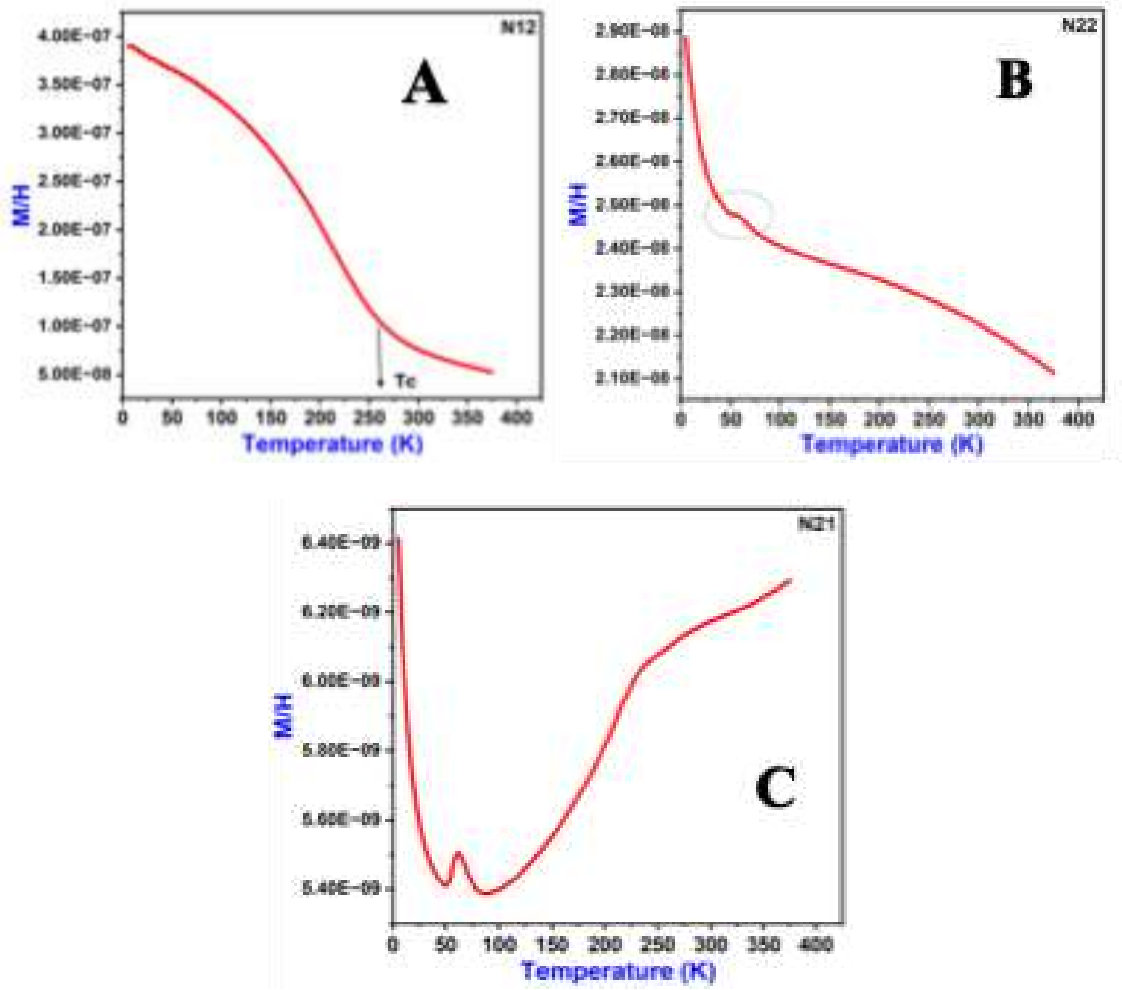

Figure 4.9: Temperature dependence of magnetization (M/H) for (A) N12 sample, showing the Curie temperature (Tc) near 250 K, (B) N22 sample, highlighting transition around 60 K, and (C) N21 displaying two distinct low-temperature transitions below 100 K, followed by a gradual increase in M/H at higher temperatures.

Nanoparticles NM1, N22 and NM2 were resynthesized to get smaller particles and study the effect of size on coercivity. Figure 4.10 suggests that decreasing the size decreases the H_C values[245], [246]. Moreover, there is an increase in M_S values. On the basis of this impact, it could be presented that smaller particles have high thermal energy, which can possibly overcome the magnetic interaction among the particles.

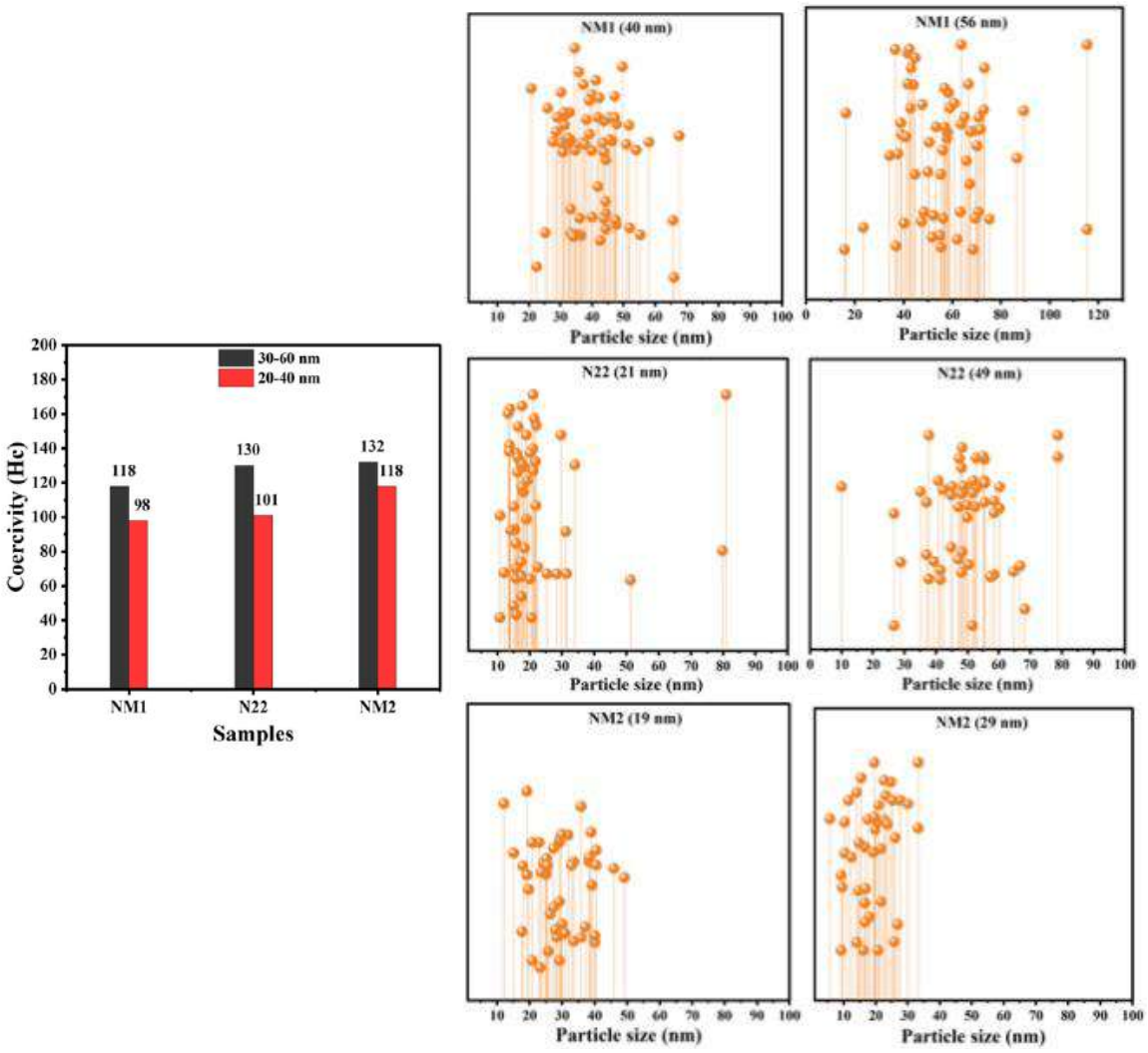

Figure 4.10: Plots showing the effect of particle size on the coercivity (Hc) of NM1, N22, and NM2 nanoparticles, with corresponding particle size distributions displayed on the right.

The magnetocrystalline anisotropy (K) is determined by the super-exchange interaction between the octahedral and tetrahedral sites of Cu^{2+} and Ni^{2+}. Low K value represents soft materials with high symmetry lattice and poor spin-orbit interaction causing orbital magnetic moments to be quenched [247], [248](Table 4.2). Also, it is envisaged that dipolar interaction between single domain particles would lead to the presence of magnetic anisotropy although they are polycrystalline this could be due to the shape and sufficiently small size which lead to the moments to behave as a whole [249]. Finally, VSM results concludes that CuO/NiO mixed oxides nanoparticles are

more suited for biomedical and device applications where a variable magnetism is required as these biogenic nanoparticles have M_R values close to zero so they tend to lose their magnetic property when the applied field is removed.

Table 4.2. Values of Hc, Ms, Mr, squareness and magnetic anisotropy, K for nanoparticles NM1, N12, N22, N21 and NM2

Sl. No.	Biogenic NPs	Hc (Oe)	Ms (emu/g)	Mr (emu/g)	Mr/Ms	$K\times10^3$ (emu/g^{-1})
1	NM1	118	0.037	0.002	0.054	0.005
2	N12 (1:2)	101	0.061	0.004	0.066	0.007
3	N22 (1:1)	129	0.133	0.005	0.038	0.018
4	N21 (2:1)	126	0.019	0.0009	0.047	0.003
5	NM2	132	0.416	0.059	0.142	0.059

4.3 Conclusions

In summary, a productive synthesis of biogenic CuO/NiO (Cu^{+2}:Ni^{+2}; 1:2, 1:1 and 2:1) nanoparticles through green solution combustion route has been done. XRD analysis confirms that the crystal structure of the synthesized nanoparticles consists of monoclinic CuO along with cubic NiO lattice. UV-Vis study confirms that the band gap of mixed nano-oxides vary from 2.19 to 2.49 eV for N12, N22 and N21 nanoparticles. SEM images reveal that the particle size of N22 is 35 nm that is supported by XRD crystallite sizes. EDS spectra confirmed the presence of only Cu, Ni, C, N and O and there are no other detectable impurities. XPS spectra majorly confirms the presence of +2 oxidation state for Cu and +2 oxidation states for Ni. VSM result concludes that the Ms and Hc values increase with nickel ratio while Mr value decrease. Overall, among all the mixed oxides nanoparticles, N22 nanoparticles show more homogenous lattice arrangement leading to high surface area (11.2 m^2/g). N12, N22 and N21 show interesting magnetic behaviour as ferro, para to ferro and para to superconductive transitions respectively. The

information presented at this point leads to the conclusion that these green nanoparticles have remarkable magnetic and structural characteristics, which can be exploited in a variety of applications, particularly in the healthcare sector.

"By establishing how compositional variations alter physicochemical and functional properties, Chapter 4 provides critical insights into the material behavior of biogenic nanoparticles with their exceptional biological applicability owing to their soft magnetic behaviour. To translate these findings into practical biological outcomes, the next chapter evaluates their antimicrobial efficacy against pathogenic microorganisms and provides mechanistic insights through molecular docking studies."

CHAPTER 5

Evaluation of broad-spectrum antimicrobial efficacy of biogenic NiO/CuO nanocomposite: In vitro, in silico, and molecular docking approach[3]

Building upon the structural and surface-chemistry findings discussed in Chapter 4, this chapter examines the antimicrobial potential of biogenic NiO/CuO nanocomposites. The objective is to correlate physicochemical characteristics with biological performance through experimental assays and molecular-docking analyses.
This chapter is adapted from: Evaluation of broad-spectrum antimicrobial efficacy of biogenic NiO/CuO nanocomposite: In vitro, in silico, and molecular docking approach. Biomass and Bioenergy, 208, 108882. https://doi.org/10.1016/j.biombioe.2025.108882.

5.1 Introduction

Antimicrobial resistance (AMR) has emerged as one of the most formidable challenges confronting global public health in the 21st century, fundamentally compromising the therapeutic efficacy of conventional antibiotics and antifungals that have historically served as cornerstones in combating infectious diseases. The WHO has categorically identified AMR among the top ten critical global public health threats, with resistant microbial infections directly contributing to prolonged morbidity, increased mortality rates, and substantially elevated healthcare expenditures worldwide[250], [251]. The phenomenon of antimicrobial resistance encompasses the inherent or acquired capability of diverse microorganisms, including bacteria, fungi, viruses, and parasites, to survive and proliferate despite exposure to antimicrobial agents that previously demonstrated effective neutralization capabilities[252], [253], [254]. The escalating prevalence of drug-resistant pathogens can be attributed to multifactorial determinants, predominantly

[3] A manuscript based on this chapter has been published in Journal of *Biomass and Bioenergy*.

including the widespread misuse and overuse of antibiotics in clinical healthcare settings, excessive deployment in livestock production and agricultural practices, indiscriminate environmental exposure to antimicrobial compounds, and inadequate infection prevention and control measures[255].

Among the critical bacterial pathogens of clinical significance, *Staphylococcus aureus*, particularly methicillin-resistant strains (MRSA), continues to be responsible for severe life-threatening infections including sepsis, endocarditis, skin and soft tissue infections, and hospital-acquired pneumonia[256]. Gram-negative enteric pathogens such as *Escherichia coli*, *Salmonella enterica*, and *Shigella flexneri* represent major causative agents of foodborne illnesses and gastrointestinal infections, with increasing documentation of multidrug-resistant (MDR) strains exhibiting resistance to multiple antibiotic classes[257], [258]. Fungal infections, despite being frequently underreported and underdiagnosed in clinical practice, constitute a substantial threat to global health security, with epidemiological data indicating that over 1.5 million individuals succumb annually to fungal diseases from approximately 300 million documented infections worldwide[259]. Agriculturally significant pathogenic fungi including *Fusarium oxysporum*, *Aspergillus flavus*, and *Aspergillus niger* pose dual threats to human health through opportunistic infections and global food security through devastating crop losses and mycotoxin contamination[260], [261]. *F. oxysporum*, recognized among the top three economically important plant pathogens worldwide, causes substantial agricultural losses while infecting immunocompromised patients[262], [263]. *A. flavus* and *A. niger* produce carcinogenic aflatoxins contaminating crops and stored commodities, causing billions in economic losses annually and serious public health concerns[264], [265].

In response to these mounting concerns, there exists an urgent and critical need to explore innovative, sustainable, and environmentally benign antimicrobial agents that

demonstrate broad-spectrum efficacy against resistant microbial strains while maintaining biocompatibility and ecological safety profiles. Nanotechnology has emerged as a revolutionary and promising frontier in antimicrobial development, offering unprecedented opportunities for combating resistant pathogens through novel mechanisms of action. Among various nanomaterials investigated, metal oxide nanoparticles have demonstrated exceptional potential attributed to their high surface area-to-volume ratios, unique physiochemical properties, and distinctive ability to interact with microbial cellular membranes, intracellular components, and essential enzymatic systems [187], [266], [267], [268], [269], [270], [271], [272]. However, conventional chemical synthesis methodologies for nanoparticle production typically involve toxic reducing agents, expensive chemical precursors, harsh reaction conditions, and environmentally hazardous procedures, significantly limiting their practical large-scale applications, particularly in medical, agricultural, and environmental domains [273], [274], [275].

Therefore, to address these significant limitations and promote sustainable nanotechnology development, green synthesis approaches utilizing natural plant extracts have gained substantial momentum and scientific interest as discussed in Chapter 2. *Moringa* possesses an extraordinarily rich profile of bioactive compounds including moringin, glucomoringin, glucotropaeolin, palmitic acid, quercetin, kaempferol, isorhamnetin, antimicrobial peptides and numerous other pharmaceutically significant molecules[276]. These naturally occurring compounds contribute additional antimicrobial, antioxidant, and anti-inflammatory properties to the synthesized nanomaterials.

This study utilizes the green synthesis of NiO/CuO mixed metal oxide nanoparticles synthesized using *Moringa oleifera* leaves extract. The enhanced antimicrobial

performance of CuO/NiO nanocomposites can be attributed to the synergistic interaction between the two semiconducting metal oxides. The heterojunction interface facilitates interfacial electron transfer while suppressing electron-hole recombination, thereby promoting enhanced generation of reactive oxygen species (ROS). Simultaneously, the controlled release of Cu^{2+} and Ni^{2+} ions contributes to oxidative damage of microbial cell membranes, proteins, nucleic acids, and essential intracellular enzymes. The complementary redox characteristics of CuO and NiO therefore provide multiple antimicrobial mechanisms, including membrane disruption, oxidative stress induction, and enzyme inactivation, resulting in broader-spectrum antibacterial and antifungal activity than that achieved by the individual metal oxides. Consequently, biogenic CuO/NiO nanocomposites represent promising multifunctional antimicrobial materials that combine enhanced biological efficacy with the environmental advantages of green synthesis [85], [91], [92]. The NPs were prepared in two CuO:NiO ratios (1:2 and 2:1), named as B12 and B21, respectively. CuO exhibits strong bactericidal activity via Cu^{2+} ion release, oxidative stress, and membrane disruption[277], while NiO demonstrates broad-spectrum antibacterial and antifungal potential[278], [279]. However, their strategic combination is expected to produce synergistic antimicrobial effects through multi-target mechanisms and enhanced bioavailability, offering a sustainable and potent alternative to conventional antimicrobials.

To the best of our knowledge, this is the first study to comprehensively evaluate the antimicrobial efficacy of biogenically synthesized NiO/CuO nanoparticles using *M. oleifera* leaves extract, supported by advanced physicochemical characterization and molecular docking analysis. Although CuO and NiO nanoparticles have individually demonstrated antimicrobial potential, their synergistic interaction in a mixed-metal oxide system remains underexplored. However, this research aims to synthesize and

characterize stable CuO/NiO nanocomposites and investigate their broad-spectrum antimicrobial activity against bacterial and fungal pathogens. The nanoparticles were synthesized through a green, sustainable combustion method and characterized using advanced techniques such as Fourier-Transform Infrared Spectroscopy (FTIR), UV-Visible Diffuse Reflectance Spectroscopy (UV-DRS), powder X-ray diffraction (PXRD) for phase and crystallinity analysis, and Field Emission Scanning Electron Microscopy (FE-SEM) and High-Resolution Transmission Electron Microscopy (HR-TEM) for morphological and elemental evaluation. Furthermore, molecular docking simulations were employed to elucidate the underlying antimicrobial mechanisms of the synthesized nanoparticles by targeting essential microbial enzymes, providing mechanistic insights into their mode of action and addressing the escalating challenge of antimicrobial resistance through innovative, non-antibiotic strategies. The outcomes not only highlight the potent and broad-spectrum antimicrobial behavior of CuO/NiO nanocomposites but also underscore their promise as eco-friendly alternatives for biomedical and agricultural applications.

5.2 Results and Discussion

5.2.1 *In Silico* Drug-Likeness study of *M. oleifera*

M. oleifera is a multipurpose medicinal plant known for its diverse pharmacological properties. Historically, *M. oleifera* has been employed in the treatment of infections, bronchitis, and fever, owing to its antimicrobial, immunomodulatory, and anti-pyretic effects [280]. To evaluate their oral bioavailability and therapeutic potential, the identified phytochemicals were converted into SMILES (Simplified Molecular Input Line Entry System) format and assessed using the SwissADME tool. This platform enables in silico screening of key ADME (absorption, distribution, metabolism, and excretion) parameters and evaluates compliance with Lipinski's Rule of Five, a well-

established framework for predicting drug-likeness. According to Lipinski, drug candidates are more likely to be orally active if they possess a molecular weight under 500 Daltons, have no more than 5 hydrogen bond donors and 10 hydrogen bond acceptors, and a log P (octanol–water partition coefficient) value not exceeding 5. Additionally, a total polar surface area (TPSA) under 140 Å^2 is preferred for optimal membrane permeability.

In silico screening revealed that most of the phytochemicals complied with Lipinski's parameters, indicating favourable oral bioavailability. Notably, all compounds except epigallocatechin and rutin passed all five criteria, while ferulic acid and p-coumaric acid showed potential to cross the blood-brain barrier, as reflected in Table 5.1. (Figure A11). These findings suggest the phytocompounds' potential for systemic delivery without central nervous system (CNS) effects, which can be advantageous or limiting depending on the intended therapeutic target.

Table 5.1 Drug-likeness predictions of leaves extract phytoconstituents computed by SwissADME

Component	**Mol. Wt.**	**Rotatable bonds**	**H-bond acceptors**	**H-bond donors**	**TPSA**	**i log P**	**Lipinski violations**	**BBB permeant**
Vanillic acid	168.15	2	4	2	66.76	1.4	0	No
Protocatechuic acid	154.12	1	4	3	77.76	0.66	0	No
p-Coumaric acid	164.16	2	3	2	57.53	0.95	0	Yes
Ferulic acid	194.18	3	4	2	66.76	1.62	0	Yes
Luteolin	286.24	1	6	4	111.13	1.86	0	No
Caffeic acid	180.16	2	4	3	77.76	0.97	0	No
Kaempferol	286.24	1	6	4	111.13	1.7	0	No
Epigallocatechin	306.27	1	7	6	130.61	0.98	1	No

Quercetin	302.24	1	7	5	131.36	1.63	0	No
Rutin	610.52	6	16	10	269.43	1.58	3	No

The antimicrobial activity of these phytochemicals is further enhanced when utilized in nanoparticle formulations. The conjugation of these plant-based compounds with metal oxide nanoparticles not only improves their stability and bioavailability but also increases their ability to disrupt microbial membranes, inhibit enzyme functions, and generate reactive oxygen species (ROS). The biosynthesized nanoparticles thus act synergistically with the plant-derived compounds, providing a multifaceted mechanism of action against a broad spectrum of pathogens.

Therefore, *M. oleifera* holds immense potential as a sustainable source of bioactive compounds for the synthesis of effective antimicrobial nanomaterials. Its phytochemical richness, coupled with favourable pharmacokinetic profiles and synergistic activity with nanoparticles, positions it as a promising candidate for advanced antimicrobial therapeutics.

5.2.2 Characterizations of Biogenic NiO/CuO NPs

5.2.2.1 FTIR Analysis

Functional group analysis of ethanolic extract and NiO/CuO nanoparticles synthesized as described in chapter 2 is plotted in Figure 5.1A. The broad absorptions in region I, from 3500-3200 cm^{-1} for extract, confirm the existence of H-bonded O-H groups, whereas a higher shift in broadness for B12 and B21 is observed due to the presence of free O-H groups. The antimicrobial activity is highly influenced by the position of hydroxyl groups. The receptor proteins of cells strongly bind with the mildly acidic functional groups like -COOH. Twin peaks in region II confirm the presence of $-CH_2$ and $-CH_3$ stretching vibrations in alkanes, where a shift is again observed for metal oxide nanoparticles. A cluster of peaks in region III for extract denotes the presence of C=O

linkage in ester or aldehyde, -CH_2/-CH_3 bending, C-O of ester/alcohol/acid/ether, and C-H bending of benzene derivatives, respectively. Additionally, peaks in region III for B12 and B21 denote the existence of C-O stretch, C=C stretch, and C-H bending vibrations (active sites, Figure 5.1B). Noticeably, strong metal-O peaks are present for B12 and B21, while they are absent in the extract. Alkyl substitution in aromatic rings enhances the activity by the formation of radicals. Moreover, conjugated unsaturated bonds interact with ion channel proteins of microbes via electron transfer interactions and play a vital role in antimicrobial activity[281].

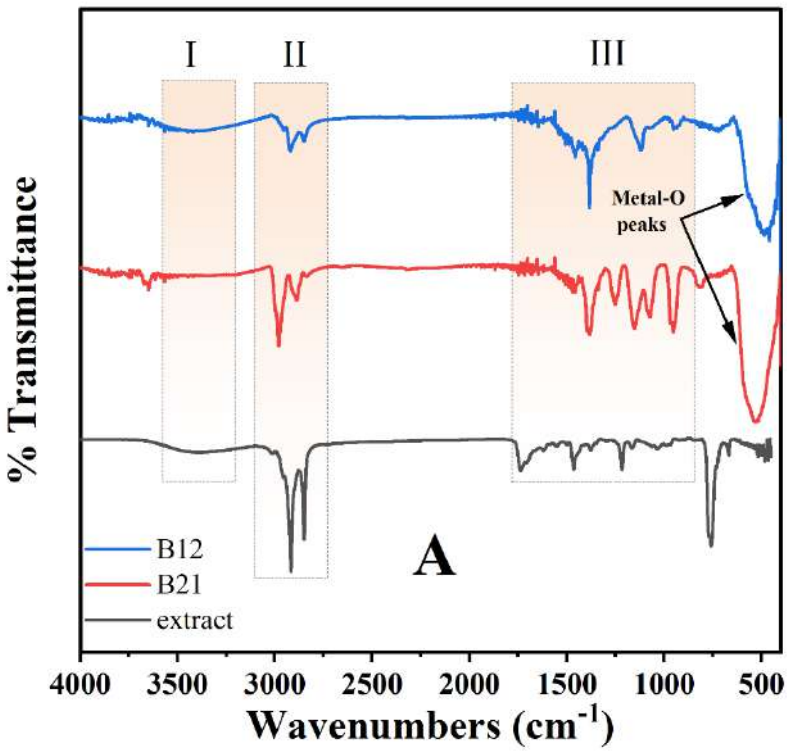

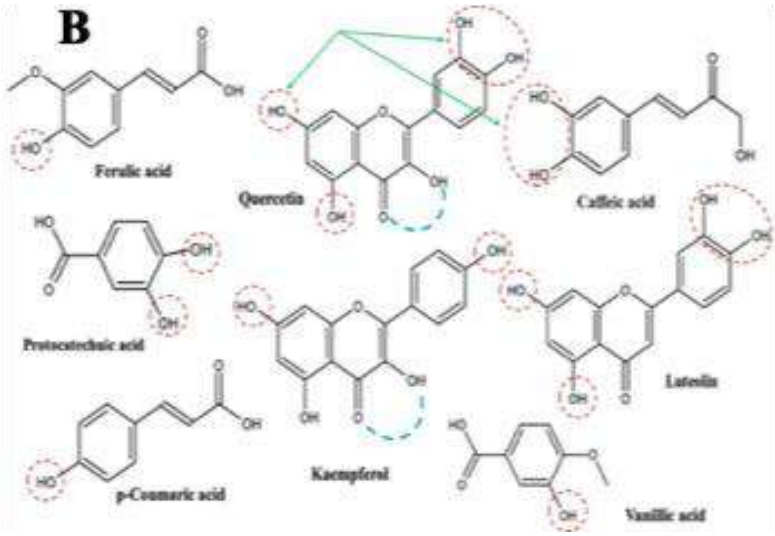

Figure 5.1: (A) FTIR spectra for B12, B21, and *Moringa* leaves extract and (B) Phenolic acids and polyphenols of *Moringa oleifera* indicating active sites for antimicrobial reactivity. Red circles indicate hydroxyl groups generating phenoxide radicals, and blue lines indicate chelating sites.

5.2.2.2 UV-DRS Analysis

Figure 5.2 depicts the DRS spectra of B12 and B21 nanoparticles, both displaying the absorption maxima at 284 nm, along with a hump at 440 nm. The phenomenon of surface plasmon resonance exhibited by nanometal oxides triggers a synchronized oscillation of delocalized electrons of the conduction band when hit by the electromagnetic radiation, resulting in the metal-specific absorption peaks. The broadening of peaks after 400 nm is indicative of agglomeration, with B12 showing higher agglomeration. This is due to the higher copper content in B12; the high surface energy of copper has led to the formation of larger particles as compared to nickel. Bakre and co-workers have recorded a similar pattern for CuO-NiO-TiO_2 nanocomposites[240].

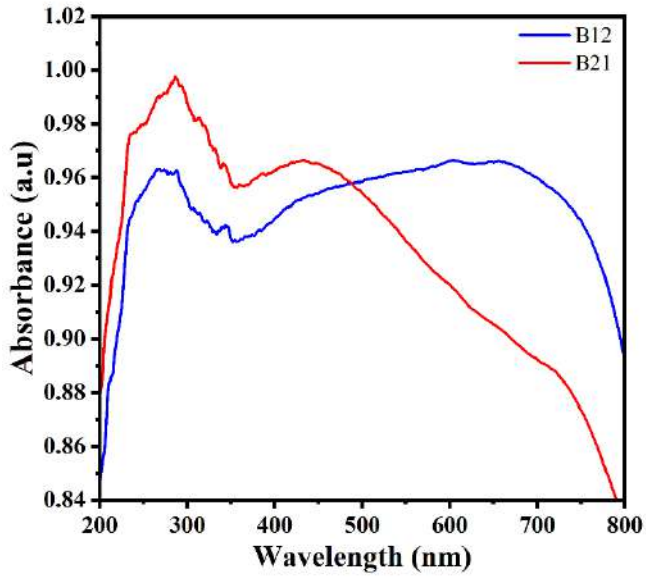

Figure 5.2: UV-DRS patterns of B12, and B21. Dashed line shows absorption maxima for both the mixed oxides.

5.2.2.3 PXRD Analysis

The crystallinity and phase purity of both the mixed oxide nanoparticles, B12 and B21, were investigated using powder XRD in Figure 5.3. Both the ratio contain a face-centered cubic unit cell corresponding to NiO with an *Fm-3m* space group and a monoclinic lattice structure for CuO, as confirmed by Xpert highscore software. For B12 and B21 nanoparticles, a comparison of peaks for CuO and NiO nanoparticles can be observed as dotted lines. The variation in intensities of the peaks can be seen for B12 and B21 as the ratio of CuO and NiO varies. In the pattern for B12, the hkl planes ($11\bar{1}$ and 111) corresponding to CuO are predominant due to the presence of more copper content. On the contrary, the hkl plane (200), corresponding to NiO, is predominant in B21. Also, the planes (220) and ($11\bar{3}$) for NiO and CuO, respectively, merged in the form of twin peaks in both the mixed oxides as highlighted by dashed circles. Additionally, the formation of pure phases can be inferred due to the absence of any extra peaks.

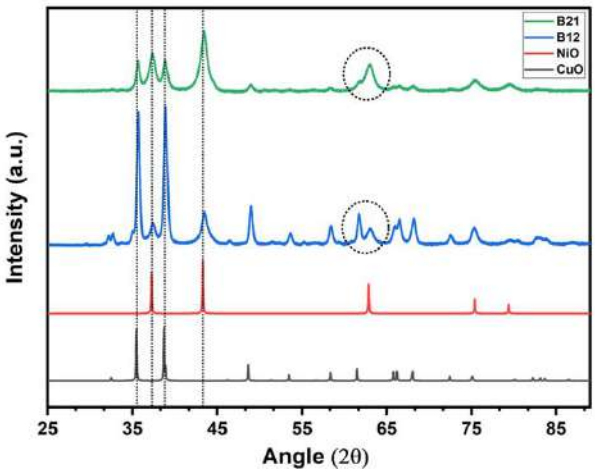

Figure 5.3: Powder-XRD patterns of B12 and B21 along with matched references for NiO (Ref. ICSD-9866, red), CuO (Ref. ICSD-69758, black) (dashed line and circle show mixing of peaks for both oxides)

5.2.2.4 FE-SEM and TEM Analysis

The morphological and elemental characterization of the green-synthesized B12 and B21 nanoparticles was carried out using FE-SEM, TEM, and elemental mapping techniques. The SEM electron micrographs (Figure 5.4A-B) show well dispersed spherical and quasi-spherical nanoparticles with slight agglomeration, revealing the size, morphology, and distribution of the B12 and B21 nanoparticles. The TEM images (Figure 5.4C&D) show a narrow size and uniform distribution for both the oxide nanoparticles with nearly spherical and hexagonal shapes. It should be noted that spherical nanoparticles provide the largest cellular uptake in terms of weight rather than quantity [282], which is helpful in controlling dose. The corresponding EDS elemental mapping in Figure 5.4(E-L) further verified the homogeneity and stability of particles with some bigger aggregates of CuO in both B12 and B21 nanoparticles. This can be attributed to either the higher surface energy of Cu and/or the magnetic nature of NiO. The mean particle sizes of 50 nm and 37 nm for B12 and B21 nanoparticles were calculated using ImageJ software. The lattice spacings were also calculated as 0.20 nm and 0.23 nm for NiO (200) and CuO (111), respectively.

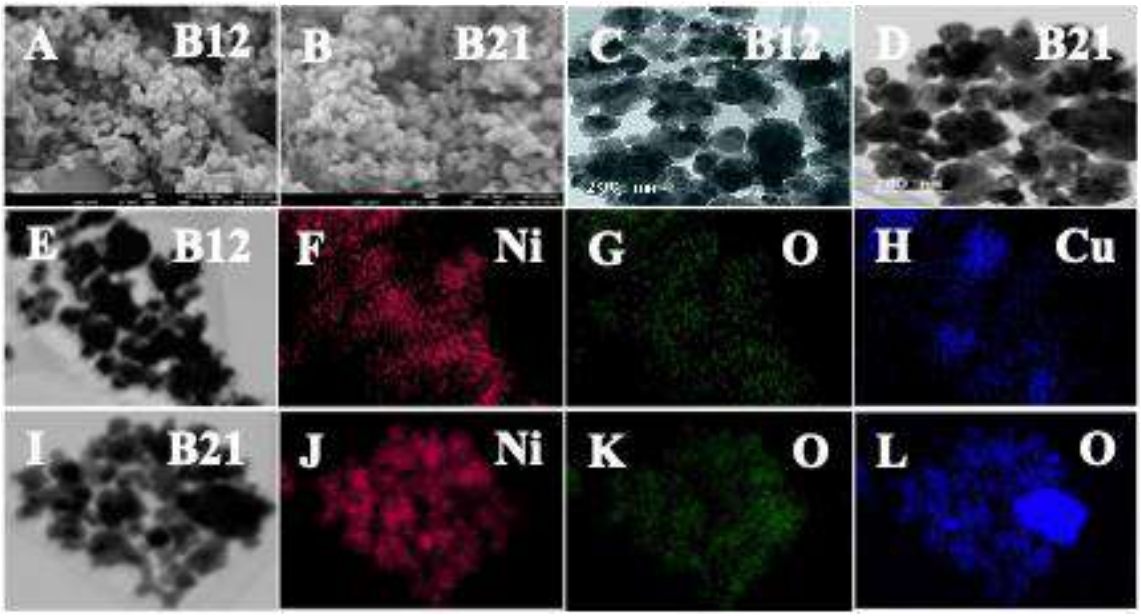

Figure 5.4: (A--B) SEM micrographs of B12 and B21 nanoparticles showing spherical morphology with slight agglomeration, (C--D) TEM images confirming nanoscale size and uniform distribution, (E--H) elemental mapping of B12 indicating the presence of Ni, O, and Cu, and (I--L) elemental mapping of B21 confirming homogeneous distribution of Ni, O, and Cu within the nanoparticles.

5.2.3 Antimicrobial Efficacy of Biogenic NiO/CuO Nanoparticles

5.2.3.1 Antibacterial Activity

The antibacterial efficacy of biogenic NiO/CuO NPs has been shown in Figure 5.5A and 5.5B. Among the treated groups, B12-250 (NiO/CuO in 1:2 ratio at 250 mg/mL) and B21-250 (NiO/CuO in 2:1 ratio at 250 mg/mL) exhibited the highest zones (27 mm) of inhibition against *E. coli*, representing an 8% increase compared to B12-100. This significantly increase ($P < 0.05$) suggests enhanced antimicrobial potency with increased CuO content and concentration, as CuO is known for potent ROS generation and membrane penetration [240], [282]. Against *S. flexneri*, B12-250 showed a 20% increase in inhibition zone compared to B12-100 (24 mm vs 20 mm), while B21 treatments showed comparable or slightly reduced activity, implying the role of CuO dominance in enhancing bactericidal effects. In the case of *S. enterica*, inhibition zones ranged narrowly (13--15 mm), with B12-250 again showing the highest (15 mm), a 7.1% improvement

over B12-100. Moreover, all treatments had moderate effects on *S. aureus*, with inhibition zones between 12--14 mm. B12-250 showed a 16.7% increase over the baseline, suggesting that Gram-positive strains may require higher or modified nanomaterial exposure for optimal effect. The observed significant differences ($P < 0.05$, $P < 0.01$, *and* $P < 0.001$) confirm the concentration and ratio dependent antimicrobial efficiency of NiO/CuO NPs, corroborating earlier findings that nanoparticle formulation strongly influences antibacterial outcomes [281], [283]. Furthermore, the agar plates (Figure 5. 5B) visibly support quantitative data, as larger clear zones were observed for higher concentration treatments. The superior efficacy of CuO-rich treatments could be attributed to its higher oxidative potential, cell wall destabilization, and interaction with DNA and proteins [284]. NiO, on the other hand, is known to disrupt enzymatic activities and induce cellular stress responses. The combination of both in optimal ratios appears to offer a synergistic advantage, leveraging the redox activity of CuO and the protein-binding affinity of NiO. This biogenic synthesis from *M. oleifera* extracts enhances nanoparticle stability and bioactivity due to the presence of flavonoids and polyphenols, which act as reducing and capping agents. Collectively, these results highlight the promising potential of biogenic NiO/CuO nanoparticles as broad-spectrum antimicrobial agents and justify further in vivo and mechanistic studies for clinical and agricultural applications.

In continuation of previous findings, several recent studies have highlighted the potent antimicrobial properties of metal-based nanoparticles synthesized through green methods. A group of researchers developed lectin-functionalized cationic copper sulfide nanoparticles with dual targeting capabilities and demonstrated their efficacy against carbapenem-resistant *Acinetobacter baumannii*, underscoring the potential of Cu-based nanomaterials in combating multidrug-resistant pathogens [285]. The effectiveness of

citrus pectin-capped CuS nanoparticles in disrupting *Candida* biofilms was further confirmed validating the broad-spectrum activity of copper-based nanoparticles [286]. These nanoparticles are known to induce oxidative stress by releasing metal ions inside microbial cells, which impairs cellular processes and inhibits growth [287]. Similarly, cerium oxide nanoparticles synthesized using *M. oleifera* leaf extract and demonstrated strong antibacterial activity against *E. coli*, *S. aureus*, and *P. aeruginosa* [288]. Also, the bactericidal activity of ZnO nanoparticles against multidrug-resistant strains reinforce the significance of metal oxide nanoparticles as effective antimicrobial agents [289].

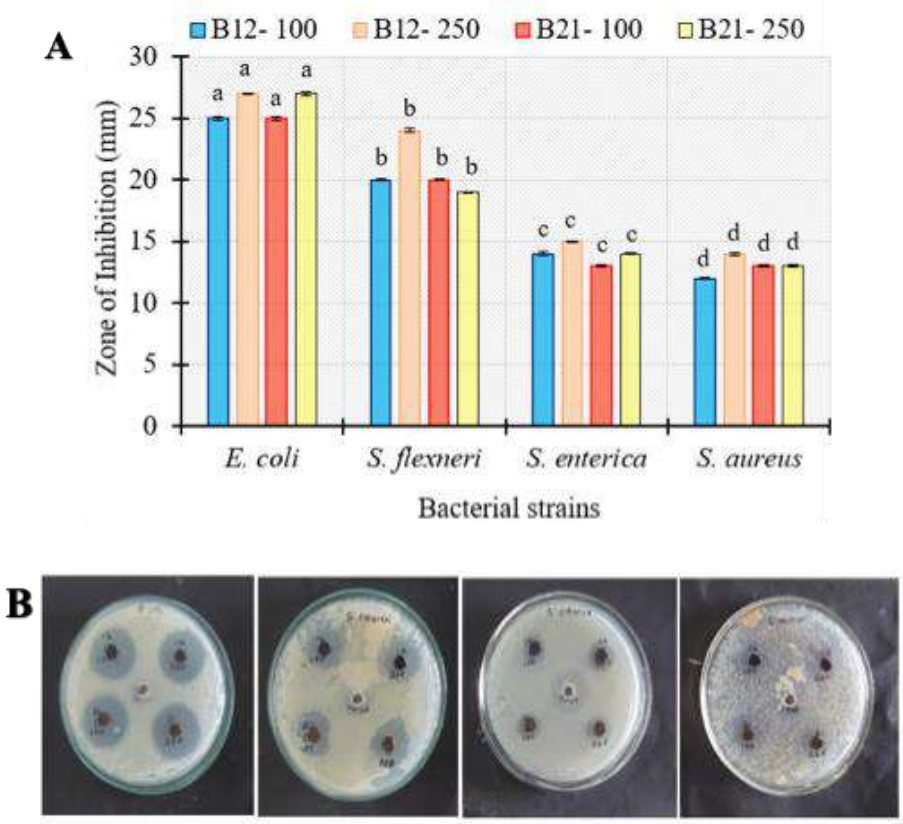

Figure 5.5: (A) Antibacterial activity of biogenic NiO/CuO nanoparticles synthesized in different ratios (B12 and B21) and concentrations (100 and 250 mg/mL) against four pathogenic bacterial strains. Inhibition zones (mm) were measured using the agar well diffusion method (mean ± SD, n = 3) and (B) Images showing the zones of inhibition on nutrient agar plates after treatment with the respective nanoparticle formulations against the tested bacterial strains.

5.2.3.2 Antifungal Activity

The antifungal efficacy of biogenically synthesized NiO/CuO NPs against different fungal strains like *F. oxysporum*, *A. flavus*, and *A. niger* is illustrated in Figure 5.6A and 5.6B. The findings demonstrated a dose-dependent and treatment-specific antifungal activity. Among the fungal strains, *F. oxysporum* exhibited the highest susceptibility, with inhibition zones ranging from 20 mm (B12-100) to 25 mm (B21-250), followed by *A. niger* (18-22 mm) and *A. flavus* (13-17 mm). The increase in inhibition zone from B12-100 to B21-250 was statistically significant ($P < 0.001$), suggesting potent antifungal effects due to higher nanoparticle concentration and altered metal ratios. Notably, B21-250 exhibited the highest antifungal activity across all strains, showing a 25%, 30.7%, and 22.2% increase in inhibition against *F. oxysporum*, *A. flavus*, and *A. niger*, respectively, compared to B12-100.

This enhanced antifungal activity of B21-250 could be attributed to the synergistic interplay between Ni and Cu ions in a 2:1 ratio, resulting in higher reactive oxygen species (ROS) generation, improved metal ion release, and effective disruption of fungal membranes [290]. Moreover, biogenic synthesis using *Moringa oleifera* extracts enriched the nanoparticles with phytochemicals such as flavonoids, terpenoids, and phenolic acids, which may have enhanced the interaction with fungal cells and increased their oxidative stress [291]. The visible zone formation in Figure 5.6B validates the quantitative results, where B21-250 showed more distinct and wider inhibition halos.

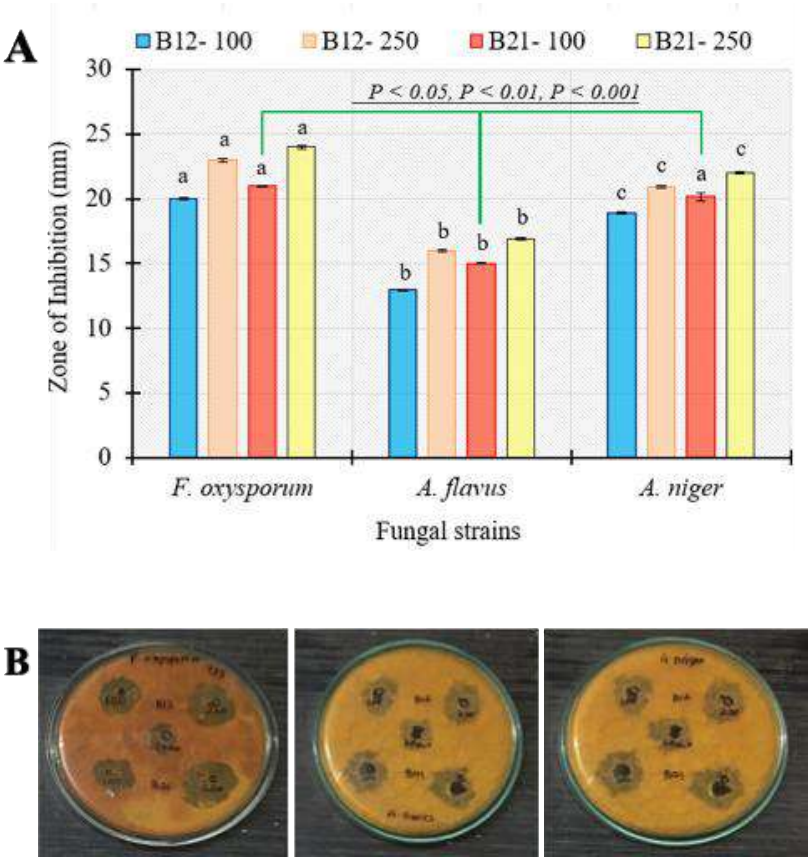

Figure 5.6: (A) Antifungal activity of biogenic NiO/CuO nanoparticles at different ratios (B12 and B21) and concentrations (100 and 250 mg/mL) against fungal strains. Inhibition zones (mm) were determined using the agar well diffusion method (mean ± SD, n = 3) and (B) Photographic representation of fungal inhibition zones on PDA plates for respective treatments.

Statistical significance was confirmed using Duncan's multiple range test, showing distinct letters (a, b, c) indicating $P < 0.05$, $P < 0.01$, *and* $P < 0.001$ levels. The results align with prior reports where metal oxide nanoparticles showed excellent antifungal properties due to their nanoscale penetration ability, generation of intracellular ROS, and inhibition of spore germination [292]. The superior efficacy of Cu-rich (B12) formulations, particularly at 250 mg/mL, against *A. flavus* suggests specific susceptibility of this strain to Cu-based oxidative and membrane-disruptive mechanisms [293].

These findings support the application of green-synthesized bimetallic nanoparticles as sustainable antifungal agents in agricultural and biomedical sectors, with metal ratio

and dosage playing critical roles in determining efficacy. The enhanced activity of nanoparticles is because of their high surface-to-volume ratio [294]. Cu NPs are known for antifungal activity by inhibiting ergosterol production. In research, Cu NPs confirmed inhibitory effects against *A. niger*, *A. flavus*, *C. albicans*, and *C. glabrata*. *M. oleifera* leaves were also utilized for the synthesis of nanoparticles using cerium oxide, exhibiting antifungal activity against *C. albicans* and *A. fumigatus* [295]. The exact mechanism underlying the antifungal activity is still unclear; however, it is largely attributed to electromagnetic interactions and ROS generation, and these in turn lead to oxidative damage to lipids [296], causing denaturation of cell permeability leading to cell death[297].

5.2.3.3 Evaluation of Time-Dependent and Species-Specific Microbial Inhibition

The antimicrobial efficacy of biogenic NiO/CuO nanoparticles demonstrated distinctive time-dependent and species-specific inhibitory characteristics across bacterial and fungal strains throughout the 6-hour experimental duration, revealing significant variations in microbial susceptibility patterns (Figure 5.7). Among the bacterial strains examined, *E. coli* (Figure 5.7A) exhibited progressive growth inhibition reaching 16-18% reduction at 6 hours with statistical significance *($P < 0.05$)*, attributed to enhanced reactive oxygen species generation facilitated by elevated nanoparticle concentrations and their bioactive potential [293]. *S. flexneri* (Figure 5.7B) demonstrated comparable inhibitory responses initiating at 4 hours ($P < 0.01$) and achieving approximately 20-25% growth suppression by 6 hours, while the moderate resistance observed in these gram-negative bacteria can be attributed to lipopolysaccharide-mediated cellular protection mechanisms that partially shield against nanoparticle penetration [286], [298]. *S. enterica* (Figure 5.7C) presented the most pronounced bacterial susceptibility with substantial growth inhibition of 26-32% at 6 hours *($P < 0.001$)*, reflecting the heightened sensitivity of *Salmonella*

species to nanoparticle-induced oxidative stress and their enhanced vulnerability to copper-mediated cellular damage through cavity formation in cell walls and disruption of bacterial protein mechanisms [299], [300], [301]. *S. aureus* (Figure 5.7D), representing gram-positive bacteria, displayed moderate growth inhibition of 15-25% at 6 hours *($P < 0.001$)*, potentially due to robust antioxidant defense mechanisms that effectively mitigate nanoparticle-mediated damage through cellular protective pathways [302].

Fungal strains exhibited markedly enhanced sensitivity to nanoparticle treatments compared to bacterial counterparts, with *F. oxysporum* (Figure 5.7E) demonstrating remarkable growth inhibition of 35-40% at 6 hours with high statistical significance *($P<0.001$)*, attributed to increased permeability of fungal hyphae facilitating nanoparticle penetration and subsequent disruption of essential metabolic pathways and cell wall integrity [303]. Similarly, *A. niger* (Figure 5.7F) and *A. flavus* (Figure 5.7G) exhibited dramatic inhibitory responses reaching 38-40% inhibition at 6 hours *($P<0.001$)*, with their heightened susceptibility resulting from nanoparticle-induced structural disruptions in fungal cell walls through mechanisms involving chitin and β-glucan breakdown processes [304], [305]. The superior antimicrobial performance of copper-rich formulations suggests crucial roles for copper ions in enhancing antimicrobial activity through increased surface contact with bacterial lipid membranes promoting copper ion dissolution and subsequent toxicity enhancement [306], [307]. The *Moringa oleifera*-mediated synthesis produced smaller NiO nanoparticles (<50 nm), with particle size playing crucial roles in antibacterial activity enhancement, as Ni^{2+} ions released from NiO nanoparticles infiltrate cell walls causing DNA, protein, and mitochondrial damage while interrupting electron transport and inducing apoptosis through membrane permeability variations and protein leakage [308], [309], [310]. These progressive, cumulative nanoparticle-cell interactions ultimately resulted in membrane damage, oxidative stress,

and microbial cell death through well-documented mechanisms involving reactive oxygen species generation, protein denaturation, and enzymatic dysfunction, establishing biogenic NiO/CuO nanoparticles as potent antimicrobial agents suitable for biomedical and agricultural applications [311].

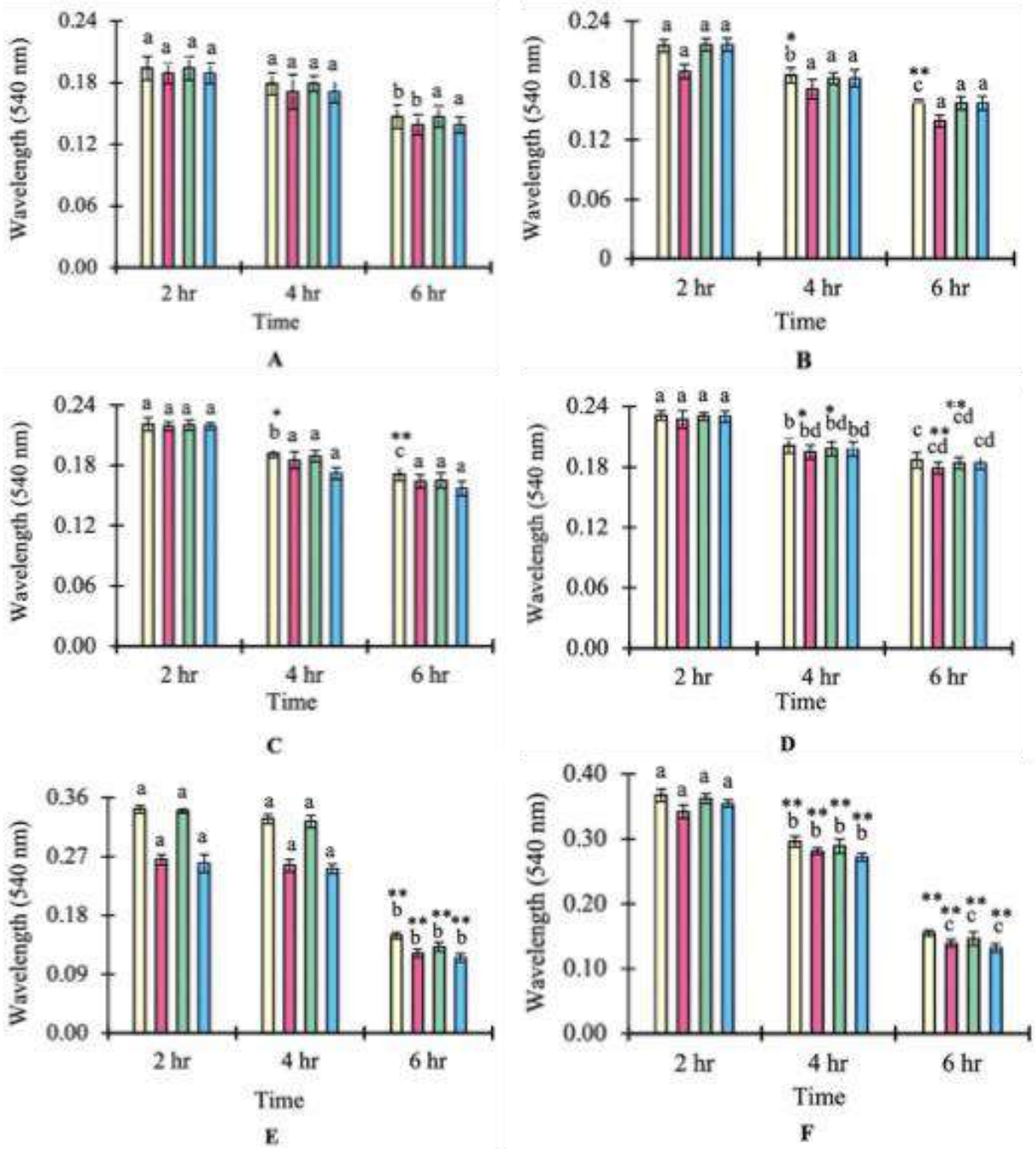

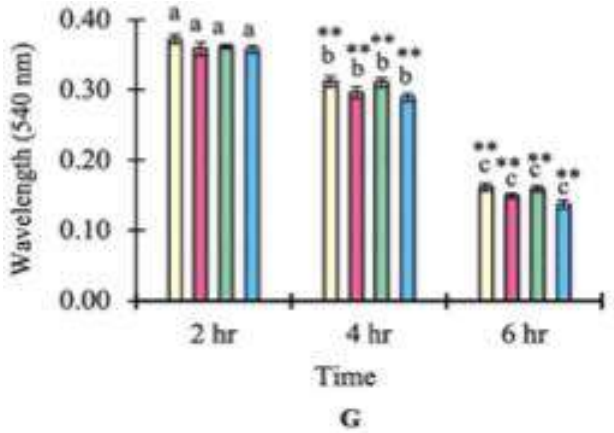

Figure 5.7: Growth inhibitory kinetics of microbial strains treated with biogenic NiO/CuO nanoparticles (B12-100, B12-250, B21-100, B21-250) at 2, 4, and 6 h, measured at 540 nm: (A) *E. coli*, (B) *S. flexneri*, (C) *S. enterica*, (D) *S. aureus*, (E) *F. oxysporum*, (F) *A. niger*, and (G) *A. flavus*. Data are mean ± SD (n = 3). Statistical significance: *$P < 0.01$; **$P < 0.001$. Different letters indicate significant differences at $P < 0.05$.

5.2.4 Molecular Docking and Interaction Analysis

Molecular docking simulations were employed to investigate the antimicrobial mechanisms of biogenically synthesized nickel oxide (NiO) and copper oxide (CuO) nanoparticles against essential microbial enzymes, addressing the escalating threat of antimicrobial resistance through innovative therapeutic approaches beyond conventional antibiotics[312]. Two strategically important enzymes were selected as molecular targets: β-ketoacyl-acyl carrier protein synthase III (FabH) from *Escherichia coli*, which catalyzes the initial condensation reaction in bacterial fatty acid biosynthesis and serves as a critical determinant of membrane integrity and cellular viability, and chitin synthase from *Fusarium oxysporum*, a key enzyme in fungal cell wall biosynthesis that catalyze the polymerization of N-acetylglucosamine into chitin[313], [314]. The conservation of FabH across bacterial species and its essential role in membrane lipid homeostasis position it as an attractive target for broad-spectrum antibacterial development, while chitin synthase represents a validated antifungal target due to its role in maintaining fungal structural integrity[315], [316]. Hence, binding mode estimation between CuO and

NiO NPs and β-ketoacyl-acyl carrier protein synthase III (FabH) plays a significant role in bacterial to fatty acid bioavailability in *Escherichia coli*[317], and chitin synthase is responsible for fungal cell wall synthesis[318]. Molecular docking simulations revealed significant differences in binding affinities between the tested nanoparticles (Table 5.2), with NiO demonstrating superior binding interactions exhibiting binding energies of -5.5 kcal/mol with FabH and -4.6 kcal/mol with chitin synthase, compared to CuO's weaker binding affinities of -3.4 kcal/mol and -3.1 kcal/mol for FabH and chitin synthase, respectively [277], [319]. The superior performance of NiO can be attributed to the distinctive properties of nickel ions, particularly the smaller ionic radius of Ni^{2+} which facilitates deeper penetration into enzyme active sites, and enhanced metal-ligand coordination capabilities that enable formation of more stable protein-nanoparticle complexes compared to copper-based systems [320].

Table 5.2 Results of molecular docking interaction of CuO and NiO with target proteins in *E. coli* and *F. oxysporum*

Nanoparticles	Test organisms	Targets	Binding energy (kcal/mol)
CuO	*E. coli*	β-ketoacyl-acyl carrier protein synthase III (FabH)	-3.4
	F. oxysporum	Chitin synthase	-3.1
NiO	*E. coli*	β-ketoacyl-acyl carrier protein synthase III (FabH)	-5.5
	F. oxysporum	Chitin synthase	-4.6

Three-dimensional visualization analysis revealed that NiO nanoparticles adopt compact conformational arrangements allowing deeper insertion into enzyme binding pockets with extensive interaction with catalytically critical amino acid residues, while CuO nanoparticles exhibited more superficial binding patterns with limited active site penetration (Figure 5.8A and 5.8B). The molecular docking results provide mechanistic

explanations for observed antimicrobial activities, where NiO nanoparticles' strong binding affinity to FabH suggests effective disruption of fatty acid biosynthesis, compromising bacterial membrane synthesis and leading to growth arrest or cell death, while binding to chitin synthase interferes with chitin polymerization, compromising fungal cell wall integrity and promoting cellular lysis[321]. The dual mechanism of action combining physical membrane damage with specific enzymatic inhibition explains the enhanced antimicrobial efficacy observed in biological assays, offering a multi-target approach that reduces the likelihood of resistance development compared to single-target conventional antibiotics [322]. The correlation between computational predictions and experimental antimicrobial results validates the utility of integrated research approaches in nanoparticle development, providing molecular-level insights that support mechanism-based antimicrobial strategies and cost-effective preliminary screening for nanoparticle optimization. This molecular docking investigation demonstrates the superior antimicrobial potential of biogenically synthesized NiO nanoparticles compared to CuO variants, where stronger binding affinities and deeper active site penetration correlate with enhanced biological activity against both bacterial and fungal pathogens, offering promising broad-spectrum antimicrobial activity through targeting conserved essential enzymes involved in fatty acid biosynthesis and cell wall formation, ultimately providing valuable mechanistic insights for rational nanoparticle design and optimization in combating antimicrobial resistance [323].

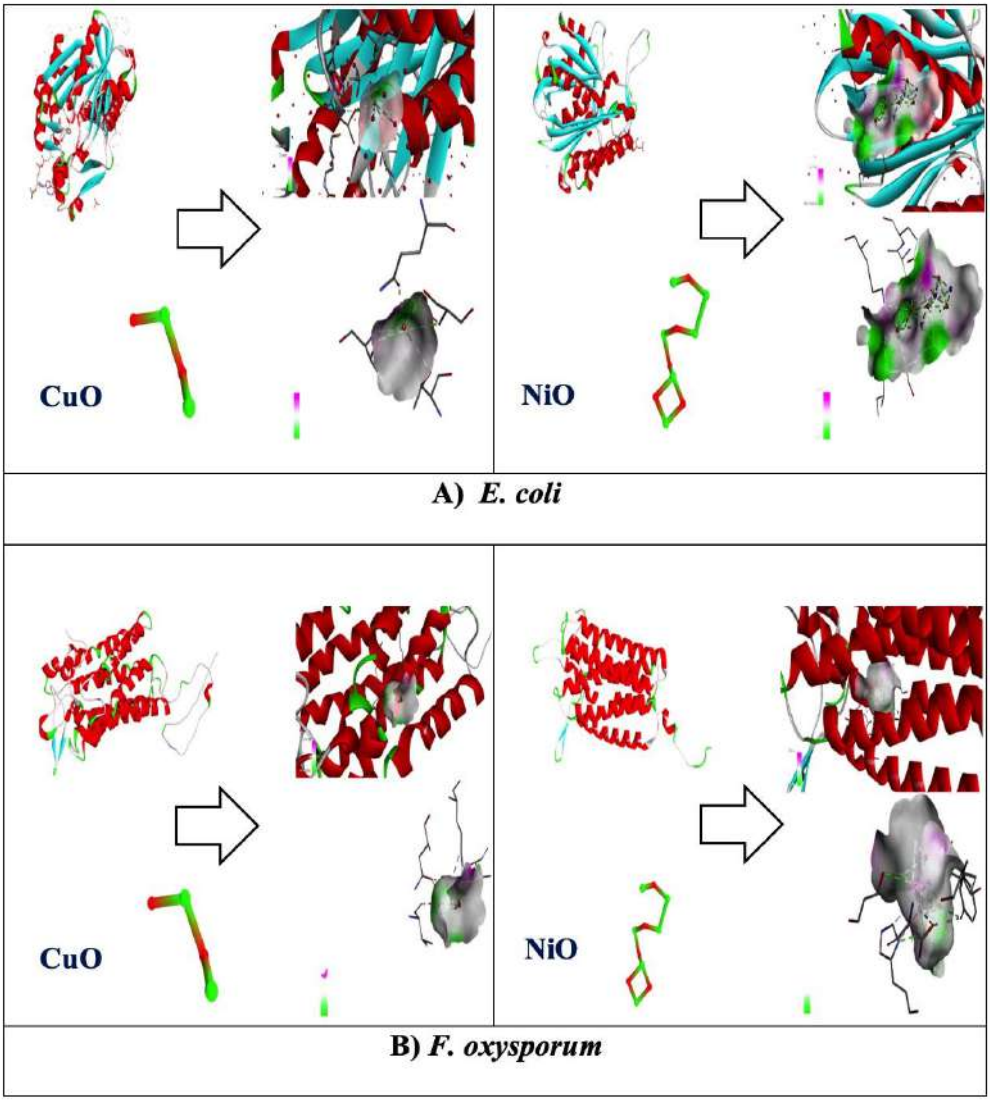

Figure 5.8: Molecular docking interactions of biogenic NiO and CuO nanoparticles with microbial enzymes: (A) FabH from *E. coli* and (B) chitin synthase from *F. oxysporum*. The left side depict CuO docking and the right-side show NiO interactions with their respective enzyme targets. NiO nanoparticles exhibit deeper binding within the active site pockets and form multiple interactions with catalytically essential residues, suggesting stronger and more stable inhibitory potential. In contrast, CuO nanoparticles demonstrate surface-level binding and reduced interaction density. The enzyme structures are rendered in cartoon format (α-helices in red, β-sheets in cyan), with active site residues highlighted and nanoparticle interactions shown as stick and surface representations.

5.2.4.1 Enzymatic Mechanisms of Action: FabH & Chitin Synthase

The enzymatic mechanisms (Figure 5.9) of action for FabH (β-ketoacyl-ACP synthase III) and chitin synthase represent critical pathways in microbial metabolism that serve as potential targets for antimicrobial intervention. FabH catalyze the initiation of fatty acid

biosynthesis through a three-step mechanism beginning with substrate binding, where acetyl-CoA ($C_{23}H_{38}N_7O_{17}P_3S$) and malonyl-ACP bind to the enzyme active site, followed by a condensation reaction in which FabH catalyze the Claisen condensation of acetyl-CoA with malonyl-ACP, ultimately producing acetoacetyl-ACP (C_4-ACP) as the first committed intermediate in bacterial fatty acid synthesis [324], [325]. This enzyme serves as the primary determinant of fatty acid composition and is essential for bacterial membrane formation, controlling cell envelope integrity and being critical for bacterial survival and growth across both Gram-positive and Gram-negative species [326].

Similarly, chitin synthase operates through a three-step mechanism involving UDP-GlcNAc ($C_{17}H_{27}N_3O_{17}P_2$) binding to the enzyme active site, followed by sequential polymerization where GlcNAc units are added forming β-1,4 glycosidic bonds, and culminating in chitin chain formation that produces linear chitin polymer chains [$(C_8H_{13}NO_5)_n$] essential for fungal cell wall structure [315], [327]. The biological significance of chitin synthase extends to synthesizing chitin for fungal cell walls, maintaining structural integrity, controlling cell shape and morphology, and being essential for fungal growth and reproduction, as these integral plasma membrane proteins translocate the polymeric chitin product through the membrane during biosynthesis [328], [329].

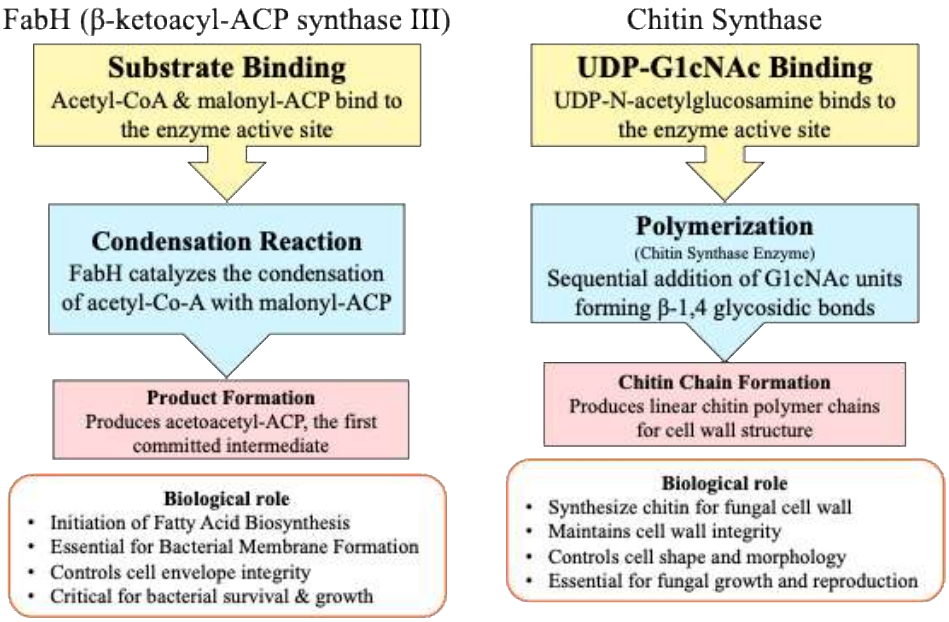

Figure 5.9: Enzymatic mechanisms of beta-ketoacyl-acyl carrier protein synthase III (FabH) and Chitin Synthase highlighting substrate binding, product formation, and their roles in bacterial lipid and fungal cell wall biosynthesis.

The antimicrobial mechanism of NiO/CuO nanoparticles involves disrupting these enzyme functions by binding to active sites and preventing substrate access and catalytic activity, with molecular docking studies revealing that NiO nanoparticles demonstrate superior binding affinity and deep active site penetration with binding energies of -5.5 kcal/mol for FabH and -4.6 kcal/mol for chitin synthase, compared to CuO nanoparticles which exhibit moderate binding affinity and surface-level interactions with weaker binding energies of -3.4 kcal/mol and -3.1 kcal/mol for FabH and chitin synthase, respectively, indicating that the smaller ionic radius and enhanced coordination capabilities of Ni^{2+} facilitate more effective enzymatic inhibition and broader antimicrobial efficacy against both bacterial and fungal pathogens.

5.3 Conclusion and Future Perspectives

This study successfully demonstrates the green synthesis of NiO/CuO bimetallic nanoparticles using *M. oleifera* leaf extract, offering an eco-friendly, cost-effective, and scalable approach for the development of broad-spectrum antimicrobial agents. The

synthesized nanoparticles (B12 and B21) exhibited well-defined structural and morphological features with particle sizes under 50 nm, confirmed by FTIR, UV-DRS, PXRD, FE-SEM, and HR-TEM analyses. Their significant ($P < 0.05$) antimicrobial efficacy was tested against multiple bacterial and fungal pathogens, revealing that CuO-rich nanocomposites were more effective against Gram-negative bacteria, while NiO-rich variants showed enhanced antifungal activity. The observed antimicrobial potential is attributed to a synergistic interplay of Cu^{2+} and Ni^{2+} ions, reactive oxygen species (ROS) generation, and structural disruption of microbial membranes. In addition to *in vitro* assays, molecular docking simulations against FabH (*E. coli*) and chitin synthase (*F. oxysporum*) provided mechanistic insights, indicating strong binding affinities of NiO over CuO nanoparticles, supporting enzyme-targeted inhibition and validating the dual antimicrobial mechanism.

Looking ahead, future research should aim to validate the antimicrobial potential of NiO/CuO nanocomposites for different ratio through in-vivo studies, focusing on their toxicity, biocompatibility, and pharmacokinetics. Developing encapsulation techniques and surface functionalization could further improve their stability and targeted delivery in biological systems. Beyond biomedical applications, incorporating these biogenic nanomaterials in agricultural formulations could provide a sustainable approach to controlling plant pathogens, offering an eco-friendly alternative for crop protection. Their potential integration into wound dressings, surface coatings, and disinfectants also presents exciting opportunities to broaden their clinical relevance. Overall, this study lays a strong foundation for the development of phytogenic metal oxide nanoparticles as effective, multi-target antimicrobial agents. It highlights the role of green nanobiotechnology in addressing global challenges such as antimicrobial resistance and promoting sustainable healthcare and agriculture.

“The antimicrobial assays and docking simulations carried out in this work demonstrate the dual functional potential of biogenic nanoparticles in both biomedical and agricultural contexts. Together with previous physicochemical and agronomic findings, these results form a comprehensive framework for understanding their multifunctionality. The final chapter consolidates the key outcomes of this thesis and discusses future research directions for advancing the application of green nanotechnology across diverse fields .”

CHAPTER 6

Conclusions and Future Horizons

6.1 Summary of Key Findings

The present thesis has moved in an orderly way from conceptual development of the synthesis of green nanomaterials, Chapter 1, through the design of experiments and characterization, Chapter 2, agronomic and structural, Chapters 3 and 4, respectively, to biological efficacy assessment, Chapter 5. These integrated studies collectively lead to a coherent framework for sustainable, multifunctional mixed metal oxide nanoparticles synthesized by plant-mediated green chemistry.

This chapter is aimed to conclude the findings of our research discussed in the thesis. We summarize the key points of the investigation and the contribution made to highlight the applicability and importance of multifunctional mixed metal oxide nanoparticles (MMONs). We further add the possible research scope that may be carried out to enhance this study.

6.1.1 Green Synthesis as a Sustainable Route

- The research successfully demonstrated the eco-friendly and phytogenic synthesis of mono-, bi-, and tri-metallic oxide nanoparticles (CuO, NiO, CoO, and their composites) using *Moringa oleifera* leaf extract.
- Biocompatible surface chemistry of nanoparticles from *Moringa oleifera* functionalization

- This approach avoided the use of hazardous chemicals, minimized environmental risks, and enhanced the value to phytoconstituents as natural reducing and stabilizing agents.

6.1.2 Comprehensive Physicochemical Characterization

- UPLC-PDA analysis identified ten major bioactive compounds in *Moringa* extract responsible for nanoparticle formation and stabilization
- A range of advanced tools such as XRD, FTIR, UV-Vis, HR-TEM, FESEM-EDX, XPS, VSM, etc. confirmed nanoparticle formation, morphology, and stability.

6.1.3 Agricultural Applications and Soil Reclamation

- **Enhanced germination performance**: Cu/Ni/Co oxide nanoparticle at 100 ppm significantly enhanced okra germination parameters, with nT3 treatment showing 80% germination compared to 32% in control
- **Sustainable waste utilization**: Successfully recycled agricultural wastes (rice straw and pressmud) into value-added vermicompost enhanced with nanoparticles
- **Soil fertility improvement**: Nano-based vermicompost increased NPK content by 21%, 60%, and 35% respectively compared to control treatments
- **Environmental safety**: Toxicological studies confirmed environmental safety at ≤100 ppm, highlighting concentration-dependent impacts on both earthworms and soil health

6.1.4 Structure-Property Relationships

- **Compositional effects:** CuO/NiO nanoparticles with 1:1 ratio (N22) exhibited optimal properties including highest surface area (11.2 m^2/g) and superior crystalline quality

- **Magnetic behavior:** Different Cu:Ni ratios resulted in distinct magnetic behaviours - ferromagnetic (N12), paramagnetic to ferromagnetic transition (N22), and paramagnetic to superconductive transition (N21)
- **Size-dependent properties**: Demonstrated inverse relationship between particle size and coercivity (Hc), with smaller particles showing enhanced magnetic saturation
- **Soft Magnetic Behaviour:** The negligible hysteresis loops in M-H plots for these CuO/NiO nanoparticles make them highly suitable for biomedical applications

6.1.5 Broad Spectrum Antimicrobial Efficacy

- **Multi-target antimicrobial action:** NiO/CuO nanocomposites (B12 & B21)showed significant antimicrobial activity against both Gram-positive and Gram-negative bacteria, as well as pathogenic fungi outperforming monometallic counterparts
- **Concentration-dependent activity**: Higher concentrations (250 mg/mL) showed superior antimicrobial performance, with B12-250 and B21-250 exhibiting up to 27 mm inhibition zones against *E. coli*
- **Inhibition kinetics assessment:** Progressive microbial growth inhibition observed over 6 hours, with fungal strains showing higher susceptibility (35-40% inhibition) compared to bacterial strains (15-32% inhibition)
- **Computational binding studies:** Mechanistic insights from molecular docking studies revealed strong binding of Ni^{2+} (NiO) ions with microbial enzymes (FabH in *E. coli*, chitin synthase in *Fusarium oxysporum*) compared to CuO, suggesting dual mechanism (ROS generation + enzyme disruption)

6.1.6 Eco-toxicological and Regulatory Awareness

- While acute toxicity was minimal at lower concentrations, higher nanoparticle concentrations revealed risks to soil biota.
- These findings emphasize the necessity of dose optimization, regulatory frameworks, and environmental monitoring before commercial application.

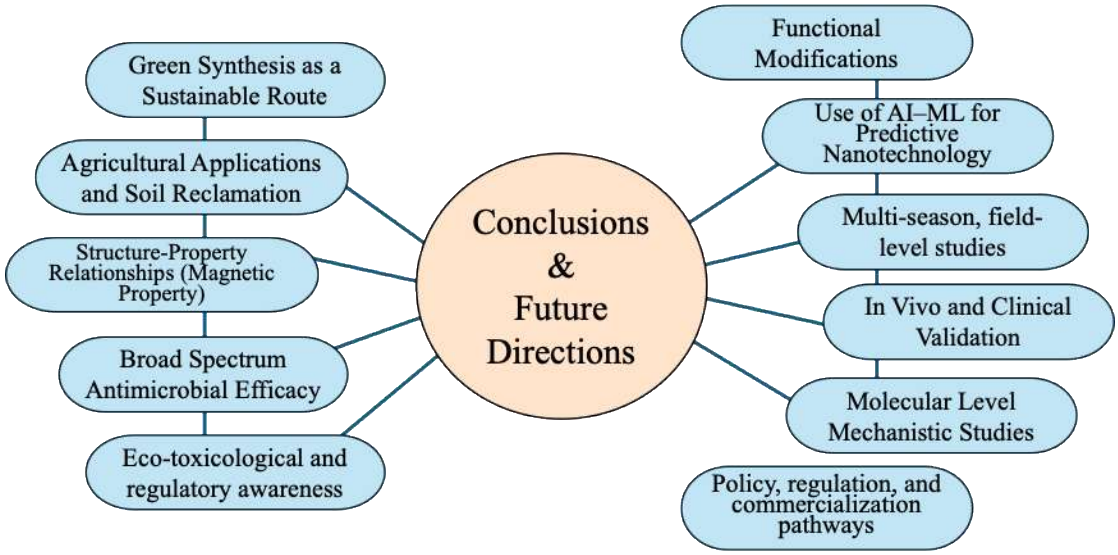

Figure 6.1: Summary of key conclusions and future directions of the thesis.

6.2 Future Horizons

6.2.1 Functional Modifications

- More control over particle size, surface area, and agglomeration using organic templates (like, waste derived cellulose)
- Surface functionalization of biogenic nanoparticles with specific plant phytoconstituents**,** peptides, or biopolymers could enhance their applicability

6.2.2 Use of AI–ML for Predictive Nanotechnology

- Optimize synthesis parameters (e.g. temperature and concentration) for desired nanoparticle properties using AI/ML algorithms

- Predict biological interactions (like, NPs–phytoconstituent; NPs–NPs; NPs–enzyme) by training data driven models to reduce trial-and-error studies
- Cut costs and time by minimizing experimental runs(for instance, using Response Surface Methodology)
- Align nanoparticle design with targeted applications (agriculture, medicine, energy, environment)

6.2.3 Advancement in Agriculture

- Multi-season, field-level studies across different agro-climatic zones are needed to validate the fertilizer efficiency for long term impact on soil microbial diversity.
- Standardized international protocols should be developed for nanoparticle application in agriculture, ensuring both responsible use and environmental safety

6.2.4 In Vivo and Clinical Validation

- Extend antimicrobial trials beyond in vitro studies to include animal models and clinical validation, assessing detailed pharmacokinetics, biodistribution, and long-term toxicity studies.
- Develop plant phytoconstituent based coatings or encapsulation systems for controlled release in therapeutic applications.

6.2.5 Molecular Level Mechanistic Studies

- Employ transcriptomics, proteomics, and metabolomics to unravel plant and microbial responses to nanoparticle exposure.
- These studies will help design nanoparticles that maximize benefits while minimizing unintended ecological consequences.

6.2.6 Policy, Regulation, and Commercialization Pathways

- Develop eco-regulatory guidelines for nanoparticle use in agriculture, healthcare, and consumer products.
- Promote cost-effective scale-up technologies to make phytogenic nanoparticles competitive with synthetic analogues.
- Encourage public engagement and farmer training to build trust in nanobiotechnology-driven solutions.

Appendix A

Text A1. Preparation of Vermicompost

Earthworms *Eisenia fetida* (procured from BNS Organics, Lucknow, India), cow dung (sourced from a nearby village), and pressmud (collected from Kisan Sahkari Sugar Mills LTD, Sultanpur, India) were pre-stabilized for 20 days prior to initiating pre-composting. Before the experiment, the earthworms were acclimatized to cow dung in a culture medium. The vermicomposting experiment was carried out in plastic containers with dimensions of 30 cm in diameter and 30 cm in depth. Four feedstock mixtures were prepared using cow dung as the control, along with rice straw (chopped into 4–6 mm pieces) and pressmud, in the following ratios: T0 (cow dung, CD, dry weight, control), T1 (CD + rice straw, RS, 1:1), T2 (CD + pressmud, PM, 1:1), and T3 (CD + RS + PM, 1:1:1). Each feedstock combination, weighing 2.0 kg (dry weight), was placed in a vermibin and stocked with 30 earthworms (E. fetida, 200 ± 2.7 mg). The feedstocks were maintained at an ambient room temperature of 26°C for 75 days, with moisture levels regulated between 65–70% through regular misting. No additional feed was provided during the experiment. The samples were collected from each feedstock at the end of the vermicomposting process (day 75). Mature vermicompost, free from earthworms and cocoons, was harvested after 75 days for subsequent application involving nanoparticles.

Table A1. List of FTIR vibration frequencies and XRD 2Theta values with planes for the biogenic *TmONs*

Wavenumber (cm^{-1})	**Vibrations**
3500	O-H bending
2923 and 2849	C-CH_3 and C-CH_2 stretching
1715	Aliphatic ketone
1516 and 1640	C=O stretching for amide I and amide II
1355 and 1373	C-CH_3 and C-CH_2 bending
1088	C-O linkage
Beyond 700	Metal-O bond

Degree (2theta)	**Planes**	**Degree (2theta)**	**Planes**
32.54°	(110)	66.29°	(022)
35.56°	(002)	68.17°	(311)
38.77°	(111)	37.18°	(111)
48.74°	(-020)	43.12°	(200)
53.53°	(020)	62.88°	(220)
58.37°	(202)	75.24°	(311)
61.56°	(113)	79.23°	(222)

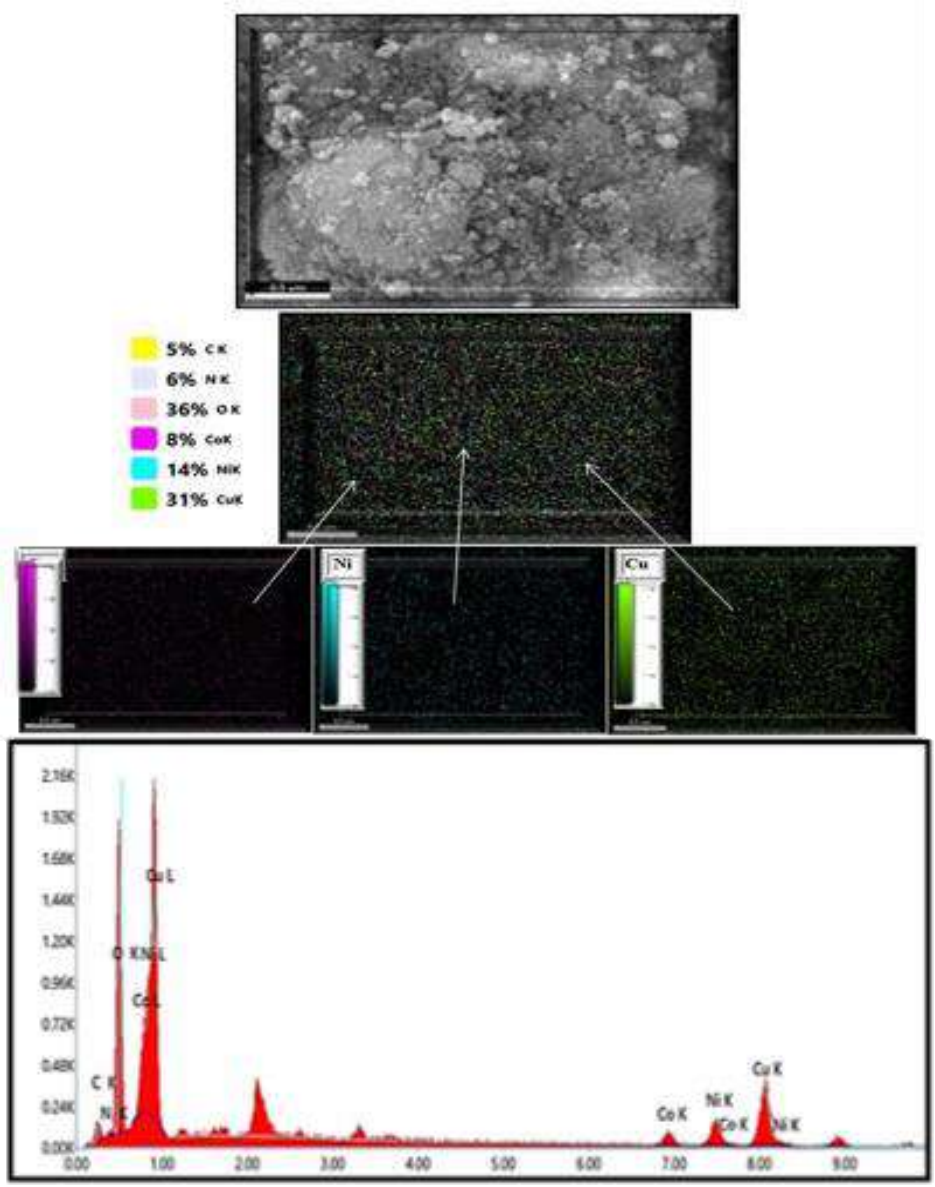

Figure A1: EDAX analysis for the confirmation of presence of Cu, Ni, Co, C, N, and O elements in *TmONs* and elemental mapping.

Table A2. Initial chemical characteristics of the cow dung (CD), rice straw (RS) press mud (PM)and Soil (Mean ± SE, n=3)[a].

Parameters	**Cow dung** [a]	**Rice straw** [a]	**Pressmud** [a]	**Soil**[a]
pH	8.34 ± 0.4[a]	8.5 ± 0.3[a]	7.03 ± 0.1[b]	9.03 ± 0.6[c]
EC (dSm^{-1})	9.89 ± 0.6[b]	3.78 ± 0.1[a]	4.77 ± 0.4[a]	4.77 ± 0.4[a]
TOC (%)	38.74 ± 2.4[c]	7.50 ± 0.8[a]	20.00 ± 1.2[b]	41.51 ±4.3[c]
N (%)	1.18 ± 0.1[b]	0.72 ± 0.1[a]	1.98 ± 0.2[c]	0.75 ± 0.1[a]
P (%)	0.13 ± 0.1[b]	0.05± 0.1[a]	0.33 ± 0.1[a]	0.03 ± 0.0[a]
K (%)	1.28 ± 0.2[c]	0.59 ± 0.2[b]	0.51 ± 0.1[b]	0.07 ± 0.0[a]
C/N	33 ± 1.2[b]	11 ± 2.4[a]	10 ± 1.7[a]	56 ± 5[c]

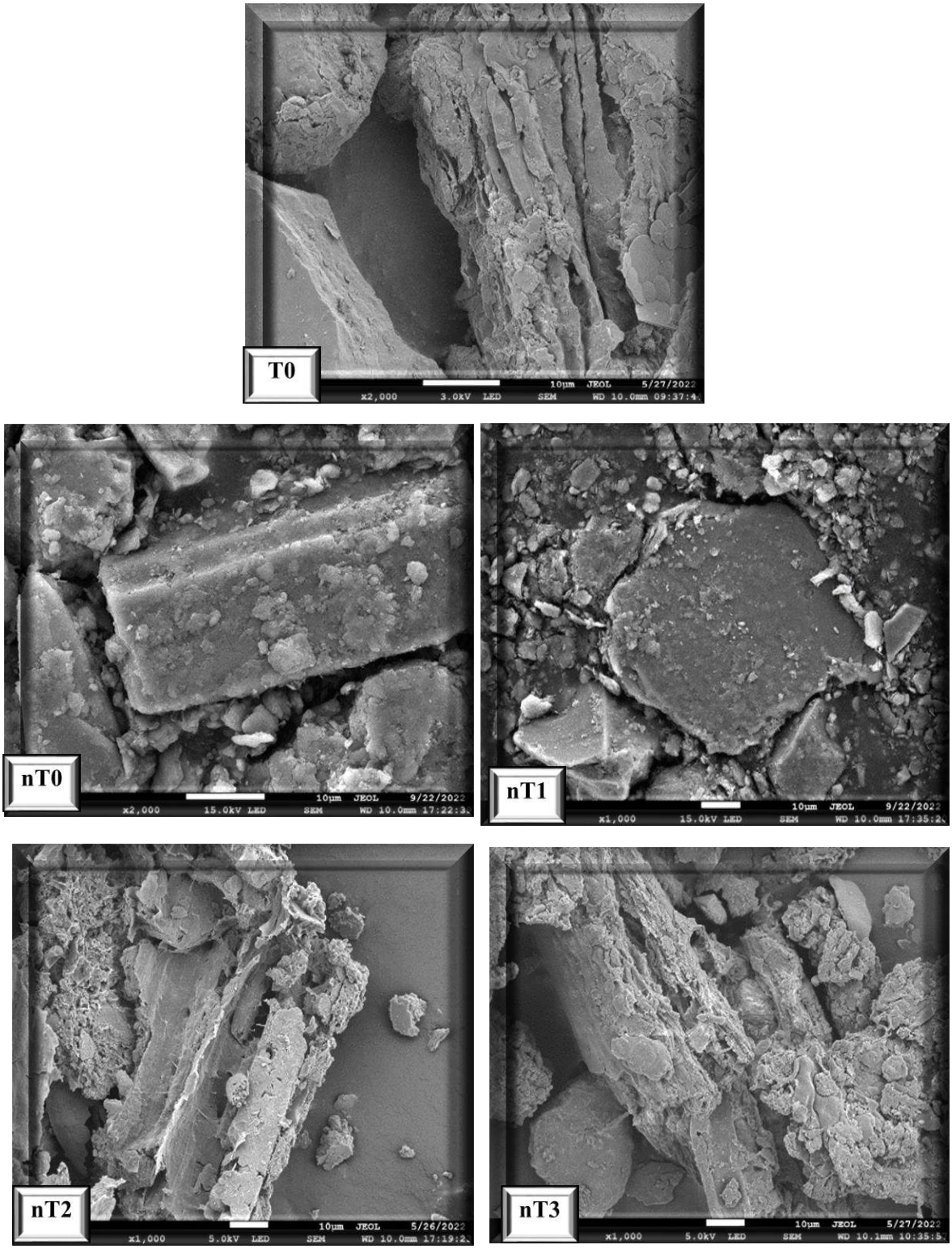

Figure A2: SEM analysis of produced vermimanure blended with *TmONs*.

T0, Vermimanure (cow dung) without *TmONs*; nT0; Vermimanure (cow dung) with *TmONs*; nT1; Vermimanure (CD + RS) with *TmONs*; nT2; Vermimanure (CD + PM) with *TmONs*; nT3, Vermimanure (CD + RS + PM) with *TmONs.*

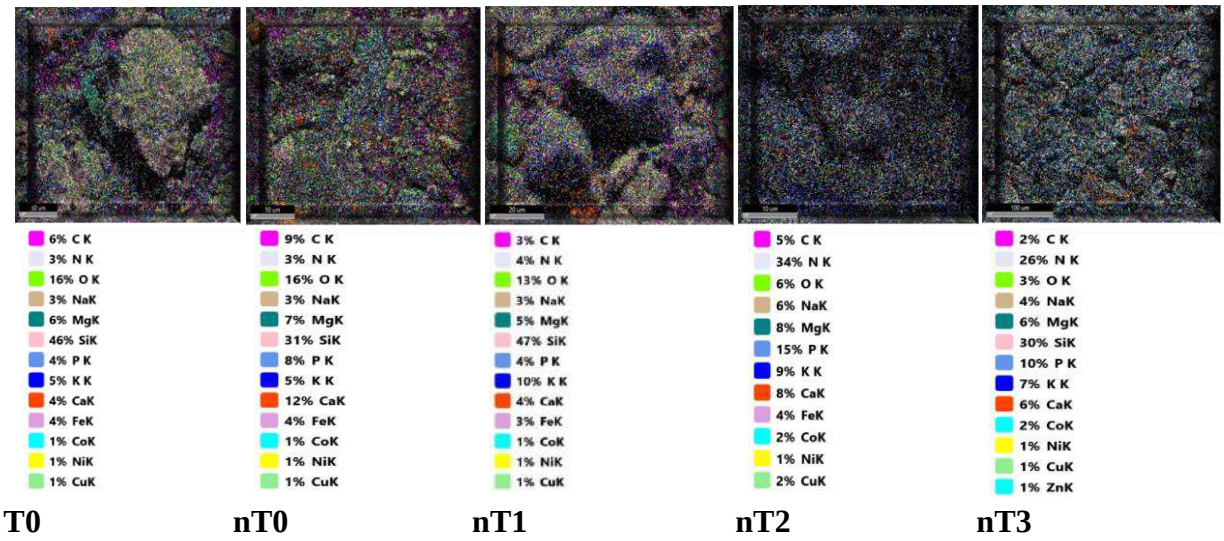

T0, Vermimanure (cow dung) without *TmONs*; nT0; Vermimanure (cow dung) with *TmONs*; nT1; Vermimanure (CD + RS) with *TmONs*; nT2; Vermimanure (CD + PM) with *TmONs*; nT3, Vermimanure (CD + RS + PM) with TmONs.

Figure A3: Mapping of produced vermimanure blended with *TmONs*.

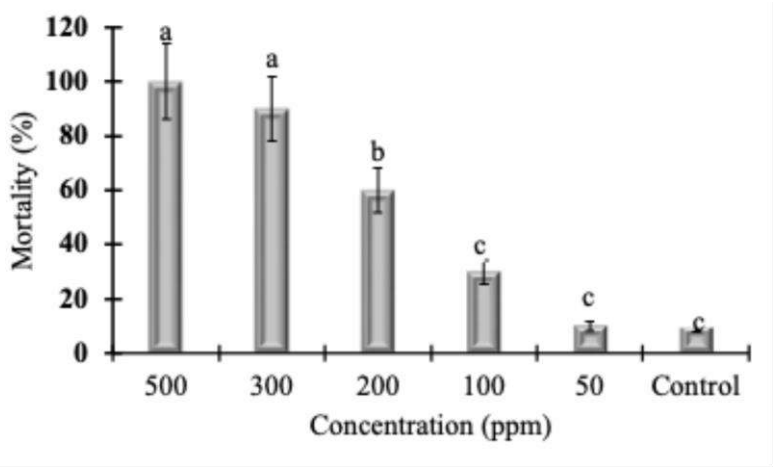

Figure A4: Final mortality (%) after 21 days across treatments. Bars represent Mean ± SE (n = 3). Different letters indicate statistically significant differences among treatments *($p < 0.05$)*

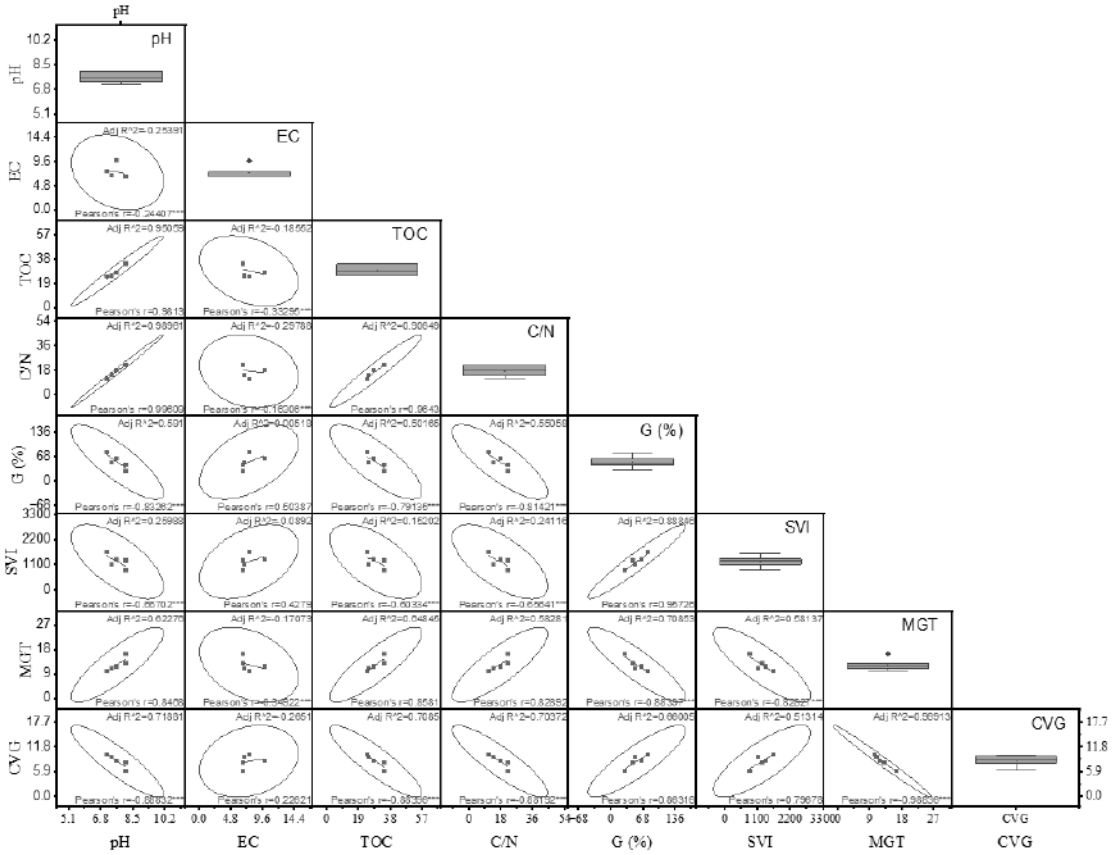

Figure A5. Correlation matrix of physicochemical and biological parameters of vermicompost treated with *TmONs*, showing Pearson coefficients, adjusted R^2, regression lines, and confidence ellipses.

The correlation matrix shown above were used to investigate the interaction of TmONs with the physicochemical and biological parameters of vermicompost. Figure displays a scatter matrix plot incorporating Pearson correlation coefficients, adjusted R^2 values, confidence ellipses, and regression lines for key parameters including pH, EC, TOC, C/N ratio, G%, SVI, MGT, and CVG. The analysis revealed a strong negative correlation between the C/N ratio and biological indices SVI ($r = –0.83$), G% ($r = –0.79$), and CVG ($r = –0.88$) suggesting that lower C/N values, indicative of more complete organic matter decomposition, significantly enhance germination and seed vigor, likely due to improved nutrient availability and microbial activity. EC exhibited a moderate positive correlation with germination parameters, implying that higher ionic strength may support early seedling development. Although pH showed only a weak correlation with biological traits, it remained within an optimal range (~7.3–8.5), contributing to stable microbial and enzymatic activity.

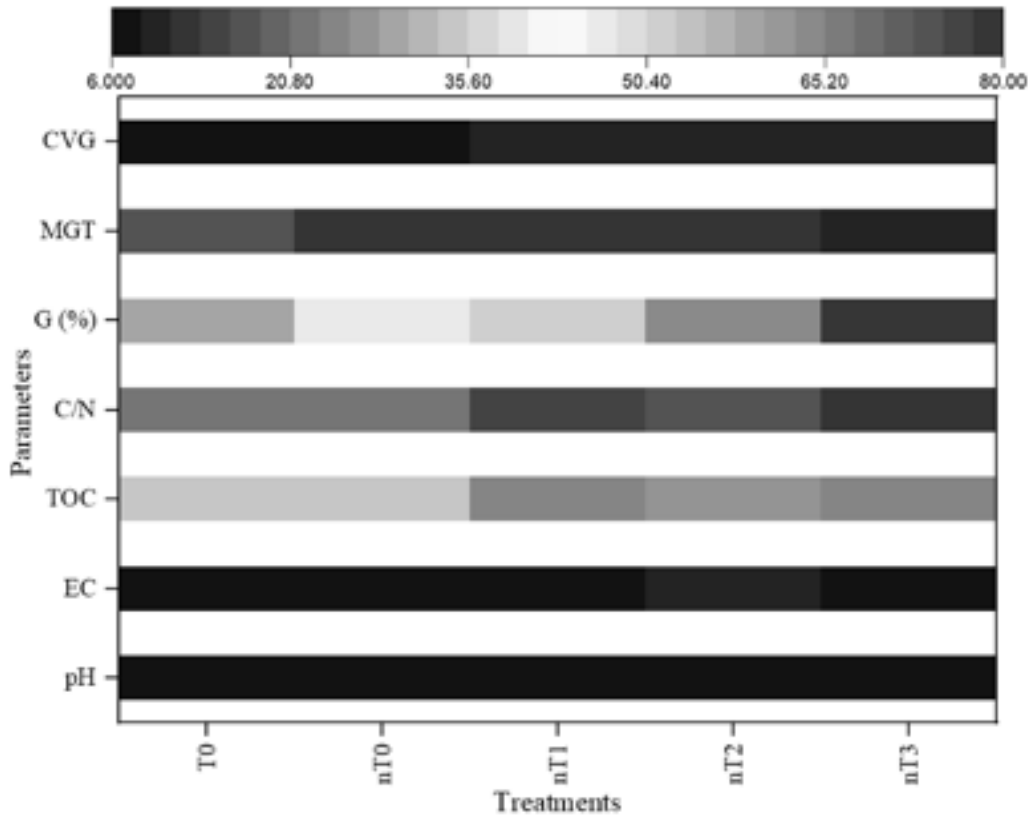

Figure A6. Heatmap showing the variation in these parameters across treatments (T0, nT0, nT1, nT2, nT3), where warmer colours represent higher intensities, highlighting the response of biological indices (G%, MGT, CVG) in relation to the underlying physicochemical characteristics.

The heatmap analysis provides valuable insight into the response of key vermicompost parameters to increasing concentrations of *TmONs*, where warmer tones denote higher parameter values. Notably, germination percentage (G%) exhibited a consistent and pronounced increase from the control (T0) through to the highest treatment (nT3), highlighting the positive influence of *TmONs* on seed germination. This enhancement may be attributed to improved nutrient bioavailability, stimulation of beneficial microbial activity, or the catalytic breakdown of organic matter, all of which are known to support early plant development. Interestingly, while germination rates improved, parameters such as MGT and CVG remained largely unchanged, suggesting that *TmONs* enhance germination efficiency without affecting its timing or uniformity. In terms of physicochemical properties, parameters including TOC, C/N ratio, EC, and pH showed minimal fluctuations across treatments. This indicates that the introduction of *TmONs* did not negatively impact the chemical balance of the vermicompost, maintaining a stable environment conducive to microbial activity and nutrient cycling. The stable C/N ratio also suggests sustained organic matter decomposition and compost maturity. These findings collectively support the hypothesis that biogenic *TmONs* can improve the biological quality of vermicompost without compromising its chemical integrity, making them promising agents for soil amendment in sustainable agriculture.

Table A3. Calculation of chlorophyll content in dried leaves of okra plant of all treatments

Treatments	Absorbance 663 nm	Absorbance 645 nm	Chl. a (mg/mL)	Chl. b (mg/mL)	Total Chl. (mg/mL)
T0	0.386	0.122	4.578	0.978	5.555
nT0	0.577	0.173	6.858	1.269	8.125
nT1	0.895	0.287	10.595	2.377	12.969
nT2	0.812	0.363	9.337	4.515	13.849
nT3	1.210	0.511	13.987	6.041	20.023

The preserved leaves were crushed in a mortar with 80% acetone to extract chlorophyll. The homogenate was filtered using a filter paper to remove debris, collecting the clear extract. The extract was diluted for UV-measurements in visible range. The absorbance values were recorded and the total chlorophyll content was calculated according to the given formulas in mg/mL:

$$Chl\ a = 12.7 \times A_{663} - 2.69 \times A_{645}$$
$$Chl\ b = 22.9 \times A_{645} - 4.68 \times A_{663}$$
$$Total\ (Chl\ a + Chl\ b) = 20.2 \times A_{645} + 8.02 \times A_{663}$$

The results show highest chlorophyll content in leaves in the treatment nT3 (CD+PM+RS) as compared to other treatments and control, indicating better photosynthesis which was evident by highest germination in nT3 treatment.

T0, Vermimanure (cow dung) without TmONs; nT0; Vermimanure (cow dung) with TmONs; nT1; Vermimanure (CD + RS) with TmONs; nT2; Vermimanure (CD + PM) with TmONs; nT3, Vermimanure (CD + RS + PM) with TmONs.

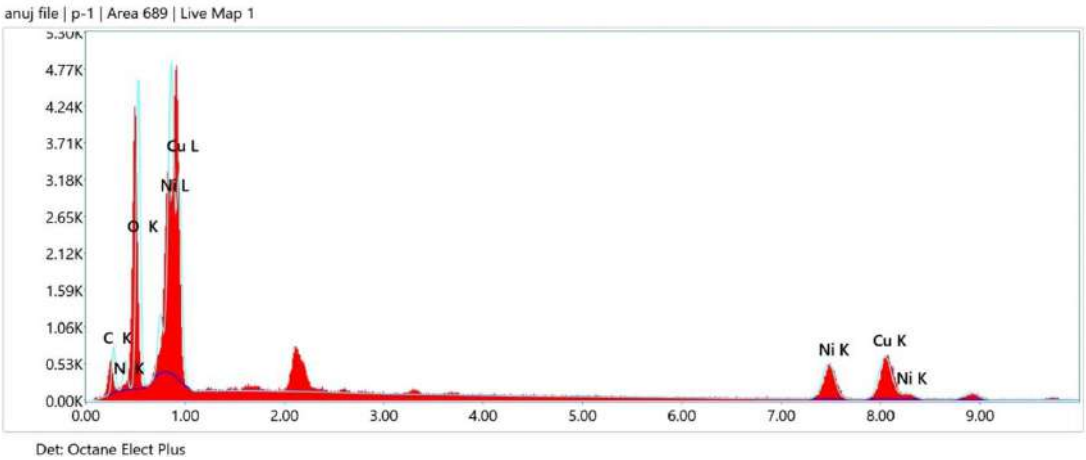

Element	Weight %	MDL	Atomic %	Net Int.	Error %	R	A	F
C K	8.9	0.41	21.5	37.4	13.0	0.8341	0.1025	1.0000
N K	3.9	0.34	8.1	25.5	13.5	0.8425	0.1594	1.0000

O K	22.0	0.19	39.9	294.0	9.5	0.8495	0.2623	1.0000
Ni K	23.4	0.69	11.5	94.9	4.9	0.9554	0.9901	1.0850
Cu K	41.7	0.96	19.0	119.7	4.7	0.9616	0.9910	1.0437

Figure A7: EDAX analysis of N22 nanoparticles.

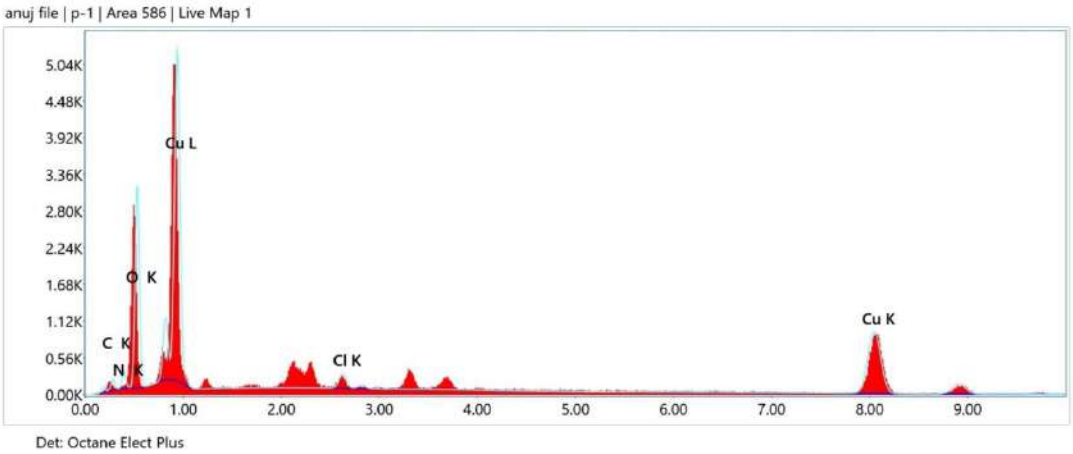

Element	Weight %	MDL	Atomic %	Net Int.	Error %	R	A	F
C K	3.3	0.45	9.8	9.8	17.9	0.8148	0.0870	1.0000
N K	2.7	0.29	7.0	15.9	15.3	0.8235	0.1667	1.0000
O K	17.4	0.17	39.1	203.3	9.5	0.8307	0.2723	1.0000
Cl K	1.7	0.20	1.7	26.4	10.2	0.8840	0.7713	1.0191
Cu K	74.9	1.12	42.4	182.0	4.3	0.9540	0.9905	1.0414

Figure A8: EDAX analysis of NM1nanoparticles.

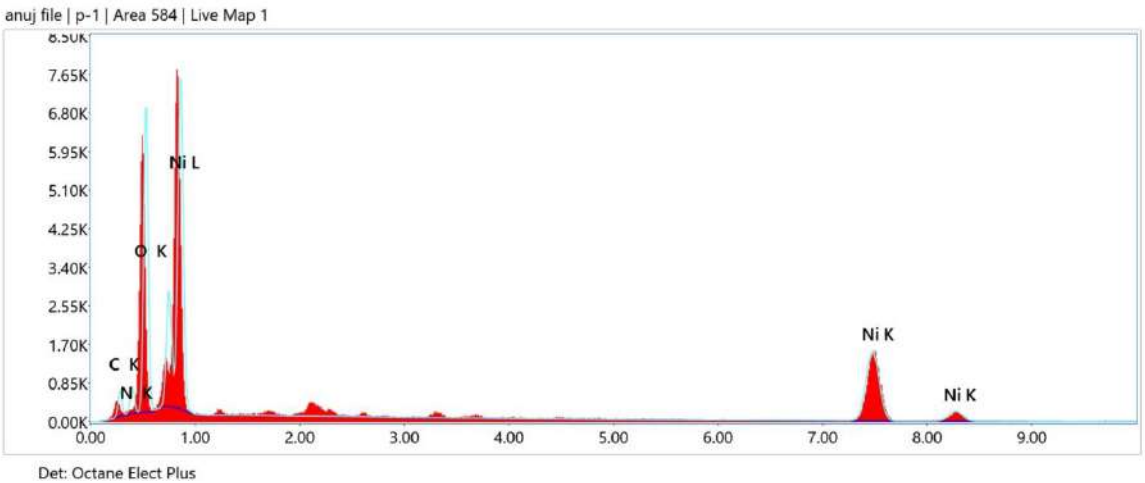

Element	Weight %	MDL	Atomic %	Net Int.	Error %	R	A	F
C K	6.5	0.37	15.2	32.3	13.1	0.8398	0.1036	1.0000
N K	4.3	0.28	8.5	35.5	12.7	0.8481	0.1745	1.0000

O K	26.6	0.17	46.5	443.7	9.0	0.8549	0.2813	1.0000
Ni K	62.6	0.78	29.8	282.2	3.7	0.9578	0.9909	1.0362

Figure A9: EDAX analysis of NM2 nanoparticles.

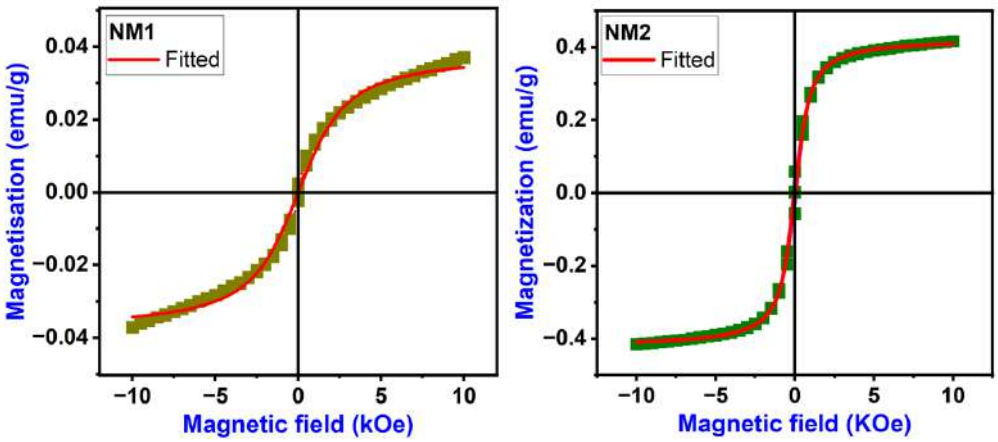

Figure A10: Langevin function fitting for NM1 and NM2.

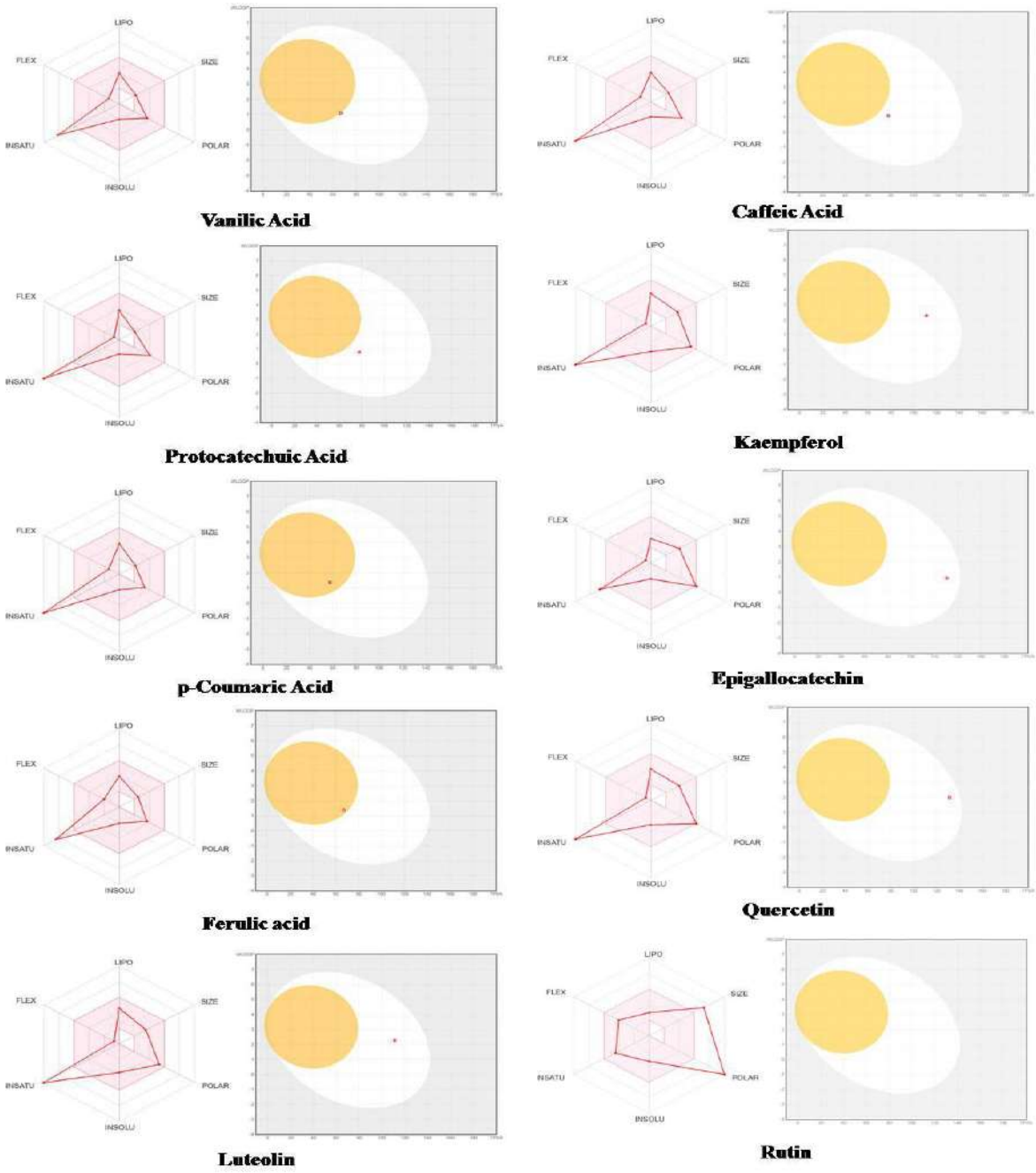

Figure A11: Radar and boiled egg images for certain phytoconstituents of *Moringa oleifera* leaves extract.

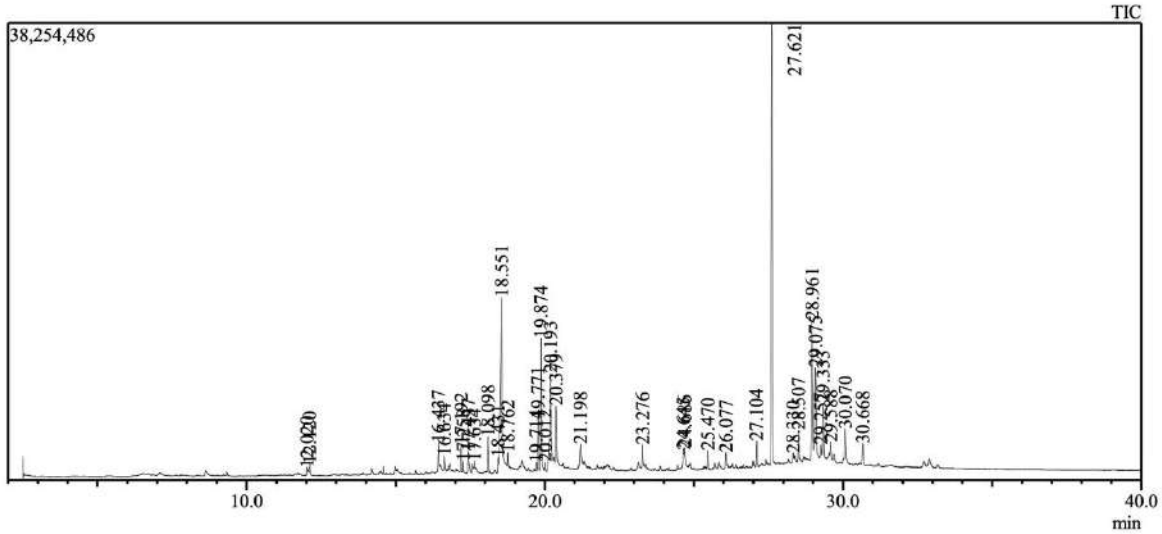

Figure A12: GC-MS Chromatogram of *Moringa oleifera* extract.

References:

[1] S. Hlali, A. Kalboussi, and A. Souifi, “Nanomaterials and Nanoelectronics: Synthesis, Properties, and Applications for Nanotechnology,” M. Amorim Fraga, Ed., Rijeka: IntechOpen, 2025. doi: 10.5772/intechopen.1007972.

[2] M. Pozzi *et al.*, “Visualization of the High Surface-to-Volume Ratio of Nanomaterials and Its Consequences,” *J. Chem. Educ.*, vol. 101, no. 8, pp. 3146–3155, Aug. 2024, doi: 10.1021/acs.jchemed.4c00089.

[3] I. Khan, K. Saeed, and I. Khan, “Nanoparticles: Properties, applications and toxicities,” *Arab. J. Chem.*, vol. 12, no. 7, pp. 908–931, 2019, doi: https://doi.org/10.1016/j.arabjc.2017.05.011.

[4] M. J. Mitchell, M. M. Billingsley, R. M. Haley, M. E. Wechsler, N. A. Peppas, and R. Langer, “Engineering precision nanoparticles for drug delivery,” *Nat. Rev. Drug Discov.*, vol. 20, no. 2, pp. 101–124, 2021, doi: 10.1038/s41573-020-0090-8.

[5] A. D. Franklin, “Nanomaterials in transistors: From high-performance to thin-film applications,” *Science*, vol. 349, no. 6249, p. aab2750, Aug. 2015, doi: 10.1126/science.aab2750.

[6] A. Ali and A. Andriyana, “Properties of multifunctional composite materials based on nanomaterials: a review,” *RSC Adv.*, vol. 10, no. 28, pp. 16390–16403, 2020, doi: 10.1039/C9RA10594H.

[7] G. E. Krichevsky and O. I. Odintsova, “Modification of fibre materials properties with the use of nanotechnologies,” *Chem. Technol. Step--Step*, vol. 4, no. 4, pp. 116–130, 2023.

[8] U. T. Khatoon and A. Velidandi, “An Overview on the Role of Government Initiatives in Nanotechnology Innovation for Sustainable Economic Development and Research Progress,” *Sustainability*, vol. 17, no. 3, p. 1250, 2025, doi: 10.3390/su17031250.

[9] A. Singh, A. Bardhan, S. Yadav, S. Sharma, and A. K. Choubey, “Application of Phyto-Mediated Microwave-Synthesized ZnO-SnO2 Nanocomposites in Water-Based Drilling Fluids,” *Ind. Eng. Chem. Res.*, vol. 64, no. 25, pp. 12463–12482, Jun. 2025, doi: 10.1021/acs.iecr.5c00790.

[10] R. D. Prasad *et al.*, “A Review on Nanotechnology from Prehistoric to Modern Age,” *ES General*, vol. 4. p. 1117, 2024. doi: 10.30919/esg1117.

[11] P. K. Sarkar and A. K. Chaudhary, “Ayurvedic Bhasma: the most ancient application of nanomedicine,” *J Sci Ind Res*, vol. 69, no. 12, pp. 901–905, 2010.

[12] S. Das, M. C. Das, and R. Paul, “Swarna Bhasma in cancer: A prospective clinical study.,” *Ayu*, vol. 33, no. 3, pp. 365–367, Jul. 2012, doi: 10.4103/0974-8520.108823.

[13] Kirtesh N Agey, Poorvi P. Mahabdi, and Dilip Prajapati, “Review of research works done on Rajata Bhasma [Incinerated Silver] at Institute of Teaching and Research in Ayurveda, Jamnagar,” *J. Ayurveda Integr. Med. Sci.*, vol. 9, no. 8, pp. 98–103, Nov. 2024, doi: 10.21760/jaims.9.8.14.

[14] Galib, M. Barve, M. Mashru, C. Jagtap, B. J. Patgiri, and P. K. Prajapati, “Therapeutic potentials of metals in ancient India: A review through Charaka Samhita.,” *J. Ayurveda Integr. Med.*, vol. 2, no. 2, pp. 55–63, Apr. 2011, doi: 10.4103/0975-9476.82523.

[15] A. Balkrishna, D. Sharma, R. K. Sharma, K. Bhattacharya, and A. Varshney, “Investigating the Role of Classical Ayurveda-Based Incineration Process on the Synthesis of Zinc Oxide Based Jasada Bhasma Nanoparticles and Zn2+ Bioavailability,” *ACS Omega*, vol. 8, no. 3, pp. 2942–2952, Jan. 2023, doi: 10.1021/acsomega.2c05391.

[16] S. Varma, S. Sultana, T. Sivaprakasam, V. Satyakumar, and P. Patki, “Yashada bhasma (Zinc calx) and Tankana (Borax) inhibit Propionibacterium acne and suppresses acne induced inflammation in vitro,” *Int. J. Cosmet. Sci.*, vol. 36, Apr. 2014, doi: 10.1111/ics.12134.

[17] Divya Yadav, Sanjay Kumar, Govind Sahay Shukla, Rajaram Agarwal, and Manisha Goyal, “Evidence Based Reality Checks on Safety & Efficacy of Herbo-Mineral/Metallic Formulations,” *AYUSHDHARA*, pp. 14–20, Jul. 2023, doi: 10.47070/ayushdhara.v10iSuppl3.1257.

[18] D. Pal, C. K. Sahu, and A. Haldar, “Bhasma : The ancient Indian nanomedicine.,” *J. Adv. Pharm. Technol. Res.*, vol. 5, no. 1, pp. 4–12, Jan. 2014, doi: 10.4103/2231-4040.126980.
[19] D. R. Gaskell and D. E. Laughlin, “Introduction to the Thermodynamics of Materials.” : CRC Press, Boca Raton, 2018. [Online]. Available: https://search.ebscohost.com/login.aspx?direct=true&db=nlebk&AN=1578912&site=ehost-live
[20] A. Varma, A. S. Mukasyan, A. S. Rogachev, and K. V. Manukyan, “Solution Combustion Synthesis of Nanoscale Materials,” *Chem. Rev.*, vol. 116, no. 23, pp. 14493–14586, 2016, doi: 10.1021/acs.chemrev.6b00279.
[21] A. Bhosale and S. H. PAWAR, “Bhasma as nanomedicines of Ayurveda,” *Nanotechnol. Appl. Med. Plants Their Bionanocomposites Ayurvedic Approach*, p. 146, 2024.
[22] R. K. Selvakesavan and G. Franklin, “Prospective application of nanoparticles green synthesized using medicinal plant extracts as novel nanomedicines,” *Nanotechnol. Sci. Appl.*, pp. 179–195, 2021.
[23] N. Abid *et al.*, “Synthesis of nanomaterials using various top-down and bottom-up approaches, influencing factors, advantages, and disadvantages: A review,” *Adv. Colloid Interface Sci.*, vol. 300, p. 102597, 2022, doi: https://doi.org/10.1016/j.cis.2021.102597.
[24] T. Cele, “Preparation of Nanoparticles,” S. M. Avramescu, I. Fierascu, K. Akhtar, S. B. Khan, F. Ali, and A. M. A. Asiri, Eds., Rijeka: IntechOpen, 2020. doi: 10.5772/intechopen.90771.
[25] S. Iravani, H. Korbekandi, S. V. Mirmohammadi, and B. Zolfaghari, “Synthesis of silver nanoparticles: chemical, physical and biological methods.,” *Res. Pharm. Sci.*, vol. 9, no. 6, pp. 385–406, 2014.
[26] S. Mahata, S. S. Mahato, D. Mahata, and S. Panda, “Perspective Chapter: Sol-Gel Science and Technology in Context of Nanomaterials – Recent Advances,” J. P. Singh, S. S. Acharya, S. Kumar, and S. K. Dixit, Eds., Rijeka: IntechOpen, 2023. doi: 10.5772/intechopen.111378.
[27] Z. Li *et al.*, “An Overview of Synthesis and Structural Regulation of Magnetic Nanomaterials Prepared by Chemical Coprecipitation,” *Metals*, vol. 13, no. 1, 2023, doi: 10.3390/met13010152.
[28] R. McGonigle *et al.*, “Autoclave reactor synthesis of upconversion nanoparticles, unreported variables, and safety considerations,” *Commun. Chem.*, vol. 8, no. 1, p. 36, 2025, doi: 10.1038/s42004-025-01415-3.
[29] S. Ahir, V. N. Mehta, J. B. Raval, J. H. Kagdi, S. K. Kailasa, and S. Jha, “Microbe-Assisted Synthesis of Nanomaterials: Insights and Applications,” *ChemistrySelect*, vol. 10, no. 30, p. e02966, Aug. 2025, doi: https://doi.org/10.1002/slct.202502966.
[30] S. Roy *et al.*, “Transforming Nanomaterial Synthesis through Advanced Microfluidic Approaches: A Review on Accessing Unrestricted Possibilities,” *J. Compos. Sci.*, vol. 8, no. 10, 2024, doi: 10.3390/jcs8100386.
[31] S. T. L., K. J. Rao, and T. Korumilli, “Natural Biogenic Templates for Nanomaterial Synthesis: Advances, Applications, and Environmental Perspectives,” *ACS Biomater. Sci. Eng.*, vol. 11, no. 3, pp. 1291–1316, Mar. 2025, doi: 10.1021/acsbiomaterials.4c02075.
[32] Z. Huma *et al.*, “Azadirachta indica-based Green Fabrication of Metal Oxide Nanoparticles: A State-of-the-Art Review,” *Nano Biomed. Eng.*, vol. 17, no. 3, pp. 373–385, 2025, doi: 10.26599/NBE.2024.9290070.
[33] P. Gupta, H. Ilyas, D. S. Raghav, and S. Tomar, “ECO-FRIENDLY SYNTHESIS OF SNO_2 NANOPARTICLES FROM Murraya koenigii: A COMPARATIVE STUDY OF LEAF, STEM, AND ROOT EXTRACTS,” *RASAYAN J. Chem.*, vol. 18, no. 04, pp. 2048–2054, 2025, doi: 10.31788/RJC.2025.1849407.
[34] F. Kurul, B. Doruk, and S. N. Topkaya, “Principles of green chemistry: building a sustainable future,” *Discov. Chem.*, vol. 2, no. 1, p. 68, Apr. 2025, doi: 10.1007/s44371-025-00152-9.

[35] Z. Ahmad *et al.*, “Green synthesis and multifaceted characterization of iron oxide nanoparticles derived from Senna bicapsularis for enhanced in vitro and in vivo biological investigation,” vol. 13, no. 1, 2024, doi: 10.1515/gps-2024-0001.
[36] V. Sakaray, Y. S. Rao, and N. V. Naidu, “Green Synthesis of Silver Nanoparticles by Acalypha indica Plant Extract and Their Approach towards Multifunctional Applications,” *Nano Biomed. Eng.*, vol. 16, no. 4, pp. 665–676, 2024, doi: 10.26599/NBE.2024.9290064.
[37] A. Jimtaisong, N. Saewan, and N. Panyachariwat, “Sustainable Fabrication of Zinc Oxide Nanoparticles Using Assam Green Tea Extract with Promising Oral Antimicrobial Potential,” *Appl. Biosci.*, vol. 4, no. 3, p. 44, 2025, doi: 10.3390/applbiosci4030044.
[38] A. Elbouzidi *et al.*, “Biochemical insights into specialized plant metabolites: Advancing cosmeceutical applications for skin benefits,” *J. Agric. Food Res.*, vol. 19, p. 101651, Mar. 2025, doi: 10.1016/j.jafr.2025.101651.
[39] I. J. Lithi, K. I. Ahmed Nakib, A. M. S. Chowdhury, and Md. Sahadat Hossain, “A review on the green synthesis of metal (Ag, Cu, and Au) and metal oxide (ZnO, MgO, Co3O4, and TiO2) nanoparticles using plant extracts for developing antimicrobial properties,” *Nanoscale Adv.*, vol. 7, no. 9, pp. 2446–2473, 2025, doi: 10.1039/D5NA00037H.
[40] “Recent Advances in Green Synthesis of TiO_2 Nanoparticles: Mechanisms, and Applications,” vol. 4, doi: https://doi.org/10.30595/rice.v4i2.316.
[41] G. da Silva Mota *et al.*, “Green synthesis of silver nanoparticles using Plathymenia reticulata bark extract and toxicological assessment in Allium cepa,” *J. Toxicol. Environ. Health A*, pp. 1–14, Jan. 2026, doi: 10.1080/15287394.2025.2611074.
[42] Nishant and S. Chandra, “Green Synthesis and Bioactivity Evaluation of Silver Nanoparticles from Stevia rebaudiana and the Endophyte Aspergillus versicolor,” *Curr. Microbiol.*, vol. 83, no. 2, p. 130, Jan. 2026, doi: 10.1007/s00284-025-04712-1.
[43] A. I. Osman *et al.*, “Synthesis of green nanoparticles for energy, biomedical, environmental, agricultural, and food applications: A review,” *Environ. Chem. Lett.*, vol. 22, no. 2, pp. 841–887, Apr. 2024, doi: 10.1007/s10311-023-01682-3.
[44] D. A. Gkika and G. Z. Kyzas, “Cost Evidence Yields the Viability of Metal Oxides Synthesis Routes,” *ACS Sustain. Chem. Eng.*, vol. 13, no. 41, pp. 17370–17379, Oct. 2025, doi: 10.1021/acssuschemeng.5c06752.
[45] F. Zanbili and A. Poursattar Marjani, “Innovative green and bio-based approaches for photosensitive nanoparticle synthesis: a review on methodologies, characterization, and applications,” *Micro Nano Syst. Lett.*, vol. 13, no. 1, p. 3, 2025, doi: 10.1186/s40486-025-00223-7.
[46] A. J. Bard, R. Parsons, and J. Jordan, *Standard potentials in aqueous solution*. United States: Marcel Dekker, Inc.,New York, NY, 1 AD. [Online]. Available: https://www.osti.gov/biblio/5826063
[47] H. Perumalsamy *et al.*, “A comprehensive review on Moringa oleifera nanoparticles: importance of polyphenols in nanoparticle synthesis, nanoparticle efficacy and their applications,” *J. Nanobiotechnology*, vol. 22, no. 1, p. 71, Feb. 2024, doi: 10.1186/s12951-024-02332-8.
[48] K. Jain, A. Takuli, T. K. Gupta, and D. Gupta, “Rethinking Nanoparticle Synthesis: A Sustainable Approach vs. Traditional Methods,” *Chem. – Asian J.*, vol. 19, no. 21, p. e202400701, Nov. 2024, doi: 10.1002/asia.202400701.
[49] Annu, M. Sahu, S. Singh, S. Prajapati, D. K. Verma, and D. K. Shin, “From green chemistry to biomedicine: the sustainable symphony of cobalt oxide nanoparticles,” *RSC Adv.*, vol. 14, no. 45, pp. 32733–32758, 2024, doi: 10.1039/D4RA05872K.
[50] H. Singh *et al.*, “Revisiting the Green Synthesis of Nanoparticles: Uncovering Influences of Plant Extracts as Reducing Agents for Enhanced Synthesis Efficiency and Its Biomedical Applications.,” *Int. J. Nanomedicine*, vol. 18, pp. 4727–4750, 2023, doi: 10.2147/IJN.S419369.

[51] K. Dhanuja, S. Manimegalai, A. Prithiba, G. Kanthimathi, and M. V. Ancy, “Telosma cordata and Zephyranthes candida mediated Green Synthesis of Zinc Oxide Nanoparticles using Plant Extract”, doi: https://doi.org/10.25303/2811rjce0990106.
[52] D. H. Hanna *et al.*, “Plant-derived nanoparticles: Green synthesis, factors, and bioactivities,” *Mater.*, vol. 9, p. 101275, Oct. 2025, doi: 10.1016/j.nxmate.2025.101275.
[53] N. Stozhko, A. Tarasov, V. Tamoshenko, M. Bukharinova, E. Khamzina, and V. Kolotygina, “Green Silver Nanoparticles: Plant-Extract-Mediated Synthesis, Optical and Electrochemical Properties,” *Physchem*, vol. 4, no. 4, pp. 402–419, 2024, doi: 10.3390/physchem4040028.
[54] A. Jain *et al.*, “Green Synthesis of Silver and Gold Nanoparticles: Plant-Mediated Approaches and Anticancer Potential,” *ChemistrySelect*, vol. 10, no. 33, p. e01849, Sep. 2025, doi: 10.1002/slct.202501849.
[55] B. B. V. Salzmann, M. M. van der Sluijs, G. Soligno, and D. Vanmaekelbergh, “Oriented Attachment: From Natural Crystal Growth to a Materials Engineering Tool,” *Acc. Chem. Res.*, vol. 54, no. 4, pp. 787–797, Feb. 2021, doi: 10.1021/acs.accounts.0c00739.
[56] Z. Shen, Z. Zhang, T. Li, Q. Yao, T. Zhang, and W. Chen, “Facet-Dependent Adsorption and Fractionation of Natural Organic Matter on Crystalline Metal Oxide Nanoparticles,” *Environ. Sci. Technol.*, vol. 54, no. 14, pp. 8622–8631, Jul. 2020, doi: 10.1021/acs.est.9b06111.
[57] “Therapeutic Plant Extract-Mediated Green Synthesis of Hydroxyapatite Nanoparticles for Biomedical Applications, Therapeutic Plants: Recent Advances in the Use of Herbs as Alternative Medications.” [Online]. Available: https://doi.org/10.2174/9789815322910125010019
[58] D.-M. Radulescu, V.-A. Surdu, A. Ficai, D. Ficai, A.-M. Grumezescu, and E. Andronescu, “Green Synthesis of Metal and Metal Oxide Nanoparticles: A Review of the Principles and Biomedical Applications,” *Int. J. Mol. Sci.*, vol. 24, no. 20, 2023, doi: 10.3390/ijms242015397.
[59] H. Khan, S. Piccolella, and S. Pacifico, “Harnessing plant extracts for green nanoparticle synthesis: Toward a sustainable future,” *Mater. Today Sustain.*, vol. 31, p. 101195, Sep. 2025, doi: 10.1016/j.mtsust.2025.101195.
[60] Z. Villagrán *et al.*, “Plant-Based Extracts as Reducing, Capping, and Stabilizing Agents for the Green Synthesis of Inorganic Nanoparticles,” *Resources*, vol. 13, no. 6, 2024, doi: 10.3390/resources13060070.
[61] H. Hasnat *et al.*, “Flavonoids: A treasure house of prospective pharmacological potentials,” *Heliyon*, vol. 10, no. 6, p. e27533, 2024, doi: https://doi.org/10.1016/j.heliyon.2024.e27533.
[62] P. K. Walencik, R. Choińska, E. Gołębiewska, and M. Kalinowska, “Metal-Flavonoid Interactions-From Simple Complexes to Advanced Systems.,” *Mol. Basel Switz.*, vol. 29, no. 11, May 2024, doi: 10.3390/molecules29112573.
[63] Y. Chen *et al.*, “A comprehensive review of stability enhancement strategies for metal nanoparticle additions to diesel/biodiesel and their methods of reducing pollutant,” *Process Saf. Environ. Prot.*, vol. 183, pp. 1258–1282, 2024, doi: https://doi.org/10.1016/j.psep.2024.01.052.
[64] N. P. S. Chauhan *et al.*, “Recent advances in the green synthesis of metal and metal oxide nanoparticles from plant extracts for biomedical and water remediation applications,” *Nanotechnol.*, vol. 9, p. 100451, Jun. 2026, doi: 10.1016/j.nxnano.2026.100451.
[65] I. A. Baba *et al.*, “Influence of plant-derived extracts on the synthesis, physicochemical properties, and applications of metal and metal oxide nanoparticles,” *Hybrid Adv.*, vol. 13, p. 100666, Jun. 2026, doi: 10.1016/j.hybadv.2026.100666.
[66] L. C. F. de Carvalho, Y. A. de Almeida, E. da Silva Machado, N. M. Rodrigues, and I. de Fátima Gimenez, “Polyphenol-mediated preparation of metal nanoparticles: experimental and theoretical study,” *Chem. Pap.*, vol. 78, no. 3, pp. 1625–1634, 2024, doi: 10.1007/s11696-023-03190-8.

[67] T. Ahmad, “Reviewing the Tannic Acid Mediated Synthesis of Metal Nanoparticles,” *J. Nanotechnol.*, vol. 2014, no. 1, p. 954206, Jan. 2014, doi: 10.1155/2014/954206.
[68] X. Huang, H. Wu, S. Pu, W. Zhang, X. Liao, and B. Shi, “One-step room-temperature synthesis of Au@Pd core–shell nanoparticles with tunable structure using plant tannin as reductant and stabilizer,” *Green Chem.*, vol. 13, no. 4, pp. 950–957, Apr. 2011, doi: 10.1039/c0gc00724b.
[69] M. Suthar, A. Malik, and A. Marwal, “Unveiling Phytochemical-Mediated Nanoparticle Synthesis in Euphorbiaceae: A Review of Current Trends and Future Prospects,” *Russ. J. Plant Physiol.*, vol. 72, no. 5, p. 149, 2025, doi: 10.1134/S1021443725601727.
[70] P. K. Sudhir, H. Venkatesan, and A. Vettrivel, “Green-Synthesized Nanoparticles of Catharanthus Roseus: A Review of Synthesis, Characterization and Biomedical Applications,” *Res. J. Biotechnol.*, vol. 10, no. 20, p. 345, Aug. 2025, doi: 10.25303/2010rjbt3450351.
[71] B. Raina, A. Sharma, P. S. Bajwa, K. Garg, and S. Bajaj, “Advancing Terpenes Through Nanotechnology:,” in *Analyzing Terpenes’ Role in Cancer Treatment*, B. Chopra, A. K. Dhingra, P. Kriplani, and R. Ojha, Eds., IGI Global, 2025, pp. 383–412. doi: 10.4018/979-8-3693-6972-2.ch015.
[72] P. Kumari, S. Kumari, M. Lal, and S. Sharma, “Biosurfactant Nanoparticles and Drug Delivery,” in *Microbial Surfactants in Pharmaceuticals and Cosmetics*, 1st ed., Boca Raton: CRC Press, 2024, pp. 206–229. doi: 10.1201/9781003424864-11.
[73] A. Barhoum *et al.*, “Review on Natural, Incidental, Bioinspired, and Engineered Nanomaterials: History, Definitions, Classifications, Synthesis, Properties, Market, Toxicities, Risks, and Regulations.,” *Nanomater. Basel Switz.*, vol. 12, no. 2, Jan. 2022, doi: 10.3390/nano12020177.
[74] S. Singh, N. K. Arkoti, V. Verma, and K. Pal, “Nanomaterials and Their Distinguishing Features BT - Nanomaterials for Advanced Technologies,” J. K. Katiyar, V. Panwar, and N. Ahlawat, Eds., Singapore: Springer Nature Singapore, 2022, pp. 1–18. doi: 10.1007/978-981-19-1384-6_1.
[75] N. Joudeh and D. Linke, “Nanoparticle classification, physicochemical properties, characterization, and applications: a comprehensive review for biologists,” *J. Nanobiotechnology*, vol. 20, no. 1, p. 262, 2022, doi: 10.1186/s12951-022-01477-8.
[76] S. Tabassum, Md. Sahadat Hossain, Md. Abu Saeed, Md. N. Uddin, and S. Ahmed, “Exploration of the antibacterial and photocatalytic properties of copper oxide (CuO) nanoparticles synthesized from Azadirachta indica leaf extract and electronic waste cable,” *Mater. Adv.*, vol. 6, no. 7, pp. 2338–2355, 2025, doi: 10.1039/D4MA01047G.
[77] T. Khairy *et al.*, “Antibacterial activity of green synthesized copper oxide nanoparticles against multidrug-resistant bacteria,” *Sci. Rep.*, vol. 14, no. 1, p. 25020, Oct. 2024, doi: 10.1038/s41598-024-75147-0.
[78] M. Bulla *et al.*, “Natural resource-derived NiO nanoparticles via aloe vera for high-performance symmetric supercapacitor,” *Sci. Rep.*, vol. 14, no. 1, p. 7389, 2024, doi: 10.1038/s41598-024-57606-w.
[79] L. Yadeta Gemachu and A. Lealem Birhanu, “Green synthesis of ZnO, CuO and NiO nanoparticles using Neem leaf extract and comparing their photocatalytic activity under solar irradiation,” *Green Chem. Lett. Rev.*, vol. 17, no. 1, p. 2293841, Dec. 2024, doi: 10.1080/17518253.2023.2293841.
[80] S. Ananthi *et al.*, “Synthesis, analysis and characterization of camellia sinensis mediated synthesis of NiO nanoparticles for ethanol gas sensor applications,” *Sens. Actuators B Chem.*, vol. 387, p. 133742, Jul. 2023, doi: 10.1016/j.snb.2023.133742.
[81] R. Govindasamy *et al.*, “Green Synthesis and Characterization of Cobalt Oxide Nanoparticles Using Psidium guajava Leaves Extracts and Their Photocatalytic and Biological Activities,” *Molecules*, vol. 27, no. 17, 2022, doi: 10.3390/molecules27175646.
[82] S. P. Patil, R. Y. Chaudhari, and M. S. Nemade, “Azadirachta indica leaves mediated green synthesis of metal oxide nanoparticles: A review,” *Talanta Open*, vol. 5, p. 100083, Aug. 2022, doi: 10.1016/j.talo.2022.100083.

[83] S. Dubey, J. Kumar, A. Kumar, and Y. C. Sharma, “Facile and green synthesis of highly dispersed cobalt oxide (Co3O4) nano powder: Characterization and screening of its eco-toxicity,” *Adv. Powder Technol.*, vol. 29, no. 11, pp. 2583–2590, Nov. 2018, doi: 10.1016/j.apt.2018.03.009.

[84] S. A. Prisrin, M. Priyanga, K. M. Ponvel, K. Kaviarasan, and S. Kalidass, “Plant Mediated Approach for the Fabrication of Nano CuO–NiO Mixed Oxides Using Aqueous Extract of Mimusops Elengi Leaf: Green Synthesis, Characterization and Antibacterial Activity Studies,” *J. Clust. Sci.*, vol. 33, no. 2, pp. 765–772, Mar. 2022, doi: 10.1007/s10876-021-02016-5.

[85] E. Da’na, N. Parveen, A. Taha, and M. R. El-Aassar, “CuO/NiO nanocomposite prepared with Saussurea costus extract for super-capacitor energy storage application,” *Nanocomposites*, vol. 10, no. 1, pp. 283–297, Nov. 2024, doi: 10.1080/20550324.2024.2363733.

[86] M. G. Gudisa, E. M. Deresa, G. Gebretsadik, G. Gonfa, and S. A. Kitte, “Green Synthesis of CuO-ZnO Nanocomposite using Citrus Sinensis Fruit Peel Extract for Electrochemical Detection of Hydrogen Peroxide,” *Anal. Bioanal. Electrochem.*, vol. 16, no. 5, pp. 389–404, 2024, doi: 10.22034/abec.2024.713500.

[87] H. K. S. Madusanka, A. G. B. Aruggoda, J. A. S. Chathurika, and S. Weerakoon, “Evaluating the Impact of Seed Nano-Priming with Green-Synthesized Copper Oxide Nanoparticles Using Mimosa pigra Leaf Extract on the Germination and Seedling Growth of Tomato (Solanum lycopersicum),” *Am. J. Biosci. Bioinforma.*, vol. 3, pp. 42–55, Dec. 2024, doi: 10.54536/ajbb.v3i1.3959.

[88] D. Maity, U. Gupta, and S. Saha, “Biosynthesized metal oxide nanoparticles for sustainable agriculture: next-generation nanotechnology for crop production, protection and management,” *Nanoscale*, vol. 14, no. 38, pp. 13950–13989, 2022, doi: 10.1039/D2NR03944C.

[89] M. D. Rodríguez-Rojas, V. Bustos-Terrones, M. Y. Díaz-Cárdenas, E. Vázquez-Vélez, and H. Martínez, “Life Cycle Assessment of Green Synthesis of TiO2 Nanoparticles vs. Chemical Synthesis,” *Sustainability*, vol. 16, no. 17, p. 7751, 2024, doi: 10.3390/su16177751.

[90] A. Khosravi, A. Zarepour, S. Iravani, R. S. Varma, and A. Zarrabi, “Sustainable synthesis: natural processes shaping the nanocircular economy,” *Environ. Sci. Nano*, vol. 11, no. 3, pp. 688–707, 2024, doi: 10.1039/D3EN00973D.

[91] A. Al-Yunus, W. Al-Arjan, H. Traboulsi, and M. Hessien, “The Effect of Composition on the Properties and Application of CuO-NiO Nanocomposites Synthesized Using a Saponin-Green/Microwave-Assisted Hydrothermal Method,” *Int. J. Mol. Sci.*, vol. 25, no. 7, 2024, doi: 10.3390/ijms25074119.

[92] A. Safdar, H. E. A. Mohamed, A. Muhaymin, K. Hkiri, N. Matinise, and M. Maaza, “Biogenic synthesis of nickel cobaltite nanoparticles via a green route for enhancing the photocatalytic and electrochemical performances,” *Sci. Rep.*, vol. 14, no. 1, p. 17620, 2024, doi: 10.1038/s41598-024-68574-6.

[93] N. Dhanda *et al.*, “Green-synthesis of Ni-Co nanoferrites using aloe vera extract: Structural, optical, magnetic, and antimicrobial studies,” *Appl. Organomet. Chem.*, vol. 37, no. 7, p. e7110, Jul. 2023, doi: 10.1002/aoc.7110.

[94] D. S. Kudlur *et al.*, “One pot synthesis of CuO-NiO nanoparticles using Aegle marmelos fruit extract and their antimicrobial activity,” *Int. Conf. Appl. Res. Eng. Sci.*, vol. 89, pp. 1–7, Jan. 2023, doi: 10.1016/j.matpr.2023.03.256.

[95] T. Indumathi, A. H. Hirad, A. A. Alarfaj, E. Ranjith Kumar, and K. Chandrasekaran, “Phytoextract-mediated synthesis of Cu doped NiO nanoparticle using cullon tomentosum plant extract with efficient antibacterial and anticancer property,” *Ceram. Int.*, vol. 49, no. 19, pp. 31829–31838, Oct. 2023, doi: 10.1016/j.ceramint.2023.07.142.

[96] S. Gillani, S. Khan, R. Nazir, and A. Qurashi (Ph.D), “Green Synthesis of Mixed Metal Oxide (MnO, CuO, ZnO) Nanoparticles (NPs) using Rose Petal Extract: An investigation of their Antimicrobial and Antifungal Activities,” *Sci. Inq. Rev.*, vol. 5, Dec. 2021, doi: 10.32350/sir/54.04.

[97] A. N. Jikah and G. I. Edo, “Moringa oleifera: a valuable insight into recent advances in medicinal uses and pharmacological activities,” *J. Sci. Food Agric.*, vol. 103, no. 15, pp. 7343–7361, Dec. 2023, doi: 10.1002/jsfa.12892.
[98] S. Perveen *et al.*, “Growth maturity stage defines nutritional, anti-nutrients and functional food aspects of Moringa oleifera Lam. leaves,” *Food Chem. Adv.*, vol. 7, p. 101010, Jun. 2025, doi: 10.1016/j.focha.2025.101010.
[99] N. Palani *et al.*, “Advancing one-pot green synthesis of plant-derived nanomaterials for extraction techniques, characterization, multifunctional biomedical applications, challenges and future perspectives,” *Mater. Today Commun.*, vol. 46, p. 112780, Jun. 2025, doi: 10.1016/j.mtcomm.2025.112780.
[100] K. G. G. Lakhani, R. Hamid, E. Motamedi, and G. V. Marviya, “A review on plant metabolite-mediated nanoparticle synthesis: sustainable applications in horticultural crops,” *Front. Nanotechnol.*, vol. Volume 7-2025, 2025, doi: 10.3389/fnano.2025.1545413.
[101] P. Perumal *et al.*, “Green synthesis of zinc oxide nanoparticles using aqueous extract of shilajit and their anticancer activity against HeLa cells,” *Sci. Rep.*, vol. 14, p. null, 2024, doi: 10.1038/s41598-024-52217-x.
[102] N. Coelho, A. S. Pereira, and P. Tavares, “Moringa oleifera Seed Cake: A Review on the Current Status of Green Nanoparticle Synthesis,” *Appl. Biosci.*, vol. 3, no. 2, pp. 197–212, 2024, doi: 10.3390/applbiosci3020013.
[103] G. Sharmila, M. Thirumarimurugan, and C. Muthukumaran, “Green synthesis of ZnO nanoparticles using Tecoma castanifolia leaf extract: Characterization and evaluation of its antioxidant, bactericidal and anticancer activities,” *Microchem. J.*, vol. 145, pp. 578–587, Mar. 2019, doi: 10.1016/j.microc.2018.11.022.
[104] G. Balasubramani *et al.*, “GC–MS analysis of bioactive components and synthesis of gold nanoparticle using Chloroxylon swietenia DC leaf extract and its larvicidal activity,” *J. Photochem. Photobiol. B*, vol. 148, pp. 1–8, Jul. 2015, doi: 10.1016/j.jphotobiol.2015.03.016.
[105] U. Kumar, “EXTRACTION, PURIFICATION, IDENTIFICATION AND THERAPEUTIC POTENTIAL OF TERPENES FROM PLANT SOURCES: A REVIEW,” in *Futuristic Trends in Chemical Material Sciences & Nano Technology Volume 3 Book 3*, First., Dr. (Mrs). Alagan Jeevika Ramesh, Dr. Partha Pratim Das, Dr. K. Chandra Mohan, and Mr. Ram Kumar P, Eds., Iterative International Publishers, Selfypage Developers Pvt Ltd, 2024, pp. 158–166. doi: 10.58532/V3BECM3CH10.
[106] E. Naji, H. F. Abdulfatah, and K. AlZawi, “Plant Secondary Metabolites, Their Classification and Biological Roles: A Review,” *J. Univ. Anbar Pure Sci.*, vol. 18, no. 1, pp. 106–115, Jun. 2024, doi: 10.37652/juaps.2023.144549.1164.
[107] S. Yadav, A. Singh, and A. K. Choubey, “Composition dependent variation in structural, morphological, optical and magnetic properties of biogenic CuO/NiO mixed oxides nanoparticles,” *J. Alloys Compd.*, vol. 979, p. 173422, Apr. 2024, doi: 10.1016/j.jallcom.2024.173422.
[108] N. Matinise, X. G. Fuku, K. Kaviyarasu, N. Mayedwa, and M. Maaza, “ZnO nanoparticles via Moringa oleifera green synthesis: Physical properties & mechanism of formation,” *Appl. Surf. Sci.*, vol. 406, pp. 339–347, Jun. 2017, doi: 10.1016/j.apsusc.2017.01.219.
[109] M. Isah, N. A. N. N. Malek, H. Susanto, M. H. Asraf, and J. Matmin, “Determination of Essential Factors Affecting Silver Nanoparticle Synthesis using *Moringa oleifera* Leaves,” *BIO Web Conf.*, vol. 117, p. 01005, 2024, doi: 10.1051/bioconf/202411701005.
[110] V. Jadhav *et al.*, “Role of Moringa oleifera on Green Synthesis of Metal/Metal Oxide Nanomaterials,” *J. Nanomater.*, vol. 2022, no. 1, p. 2147393, Jan. 2022, doi: 10.1155/2022/2147393.
[111] N. M. Hosny, I. Gomaa, M. G. Elmahgary, and M. A. Ibrahim, “ZnO doped C: Facile synthesis, characterization and photocatalytic degradation of dyes,” *Sci. Rep.*, vol. 13, no. 1, p. 14173, 2023, doi: 10.1038/s41598-023-41106-4.

[112] G. T. Tran, L. M. Nguyen, T. T. T. Nguyen, D. H. Nguyen, and T. V. Tran, “Recent developments in the bio-mediated synthesis of CoFe(2)O(4) nanoparticles using plant extracts for environmental and biomedical applications.,” *Nanoscale Adv.*, vol. 6, no. 21, pp. 5285–5300, Sep. 2024, doi: 10.1039/d4na00604f.
[113] N. Saikumari, S. M. Dev, and S. A. Dev, “Effect of calcination temperature on the properties and applications of bio extract mediated titania nano particles,” *Sci. Rep.*, vol. 11, no. 1, p. 1734, Jan. 2021, doi: 10.1038/s41598-021-80997-z.
[114] P. K. Srivastava, A. Singh, S. Kumari, S. Arora, A. K. Choubey, and A. S. K. Sinha, “Production and characterization of sustainable vermimanure derived from poultry litter and rice straw using tiger worm Eisenia fetida,” *Bioresour. Technol.*, vol. 369, p. 128377, Feb. 2023, doi: 10.1016/j.biortech.2022.128377.
[115] J. Xu and G. Du, “Seed germination response to diurnally alternating temperatures: Comparative studies on alpine and subalpine meadow populations,” *Glob. Ecol. Conserv.*, vol. 44, p. e02503, Aug. 2023, doi: 10.1016/j.gecco.2023.e02503.
[116] X. Zhao, J. C. Joo, and J. Y. Kim, “Evaluation of heavy metal phytotoxicity to Helianthus annuus L. using seedling vigor index-soil model,” *Chemosphere*, vol. 275, p. 130026, Jul. 2021, doi: 10.1016/j.chemosphere.2021.130026.
[117] A. B. M. H. Uddin, R. S. Khalid, M. Alaama, A. M. Abdualkader, A. Kasmuri, and S. A. Abbas, “Comparative study of three digestion methods for elemental analysis in traditional medicine products using atomic absorption spectrometry,” *J. Anal. Sci. Technol.*, vol. 7, no. 1, p. 6, 2016, doi: 10.1186/s40543-016-0085-6.
[118] Z. Hu and L. Qi, “15.5 - Sample Digestion Methods,” H. D. Holland and K. K. B. T.-T. on G. (Second E. Turekian, Eds., Oxford: Elsevier, 2014, pp. 87–109. doi: https://doi.org/10.1016/B978-0-08-095975-7.01406-6.
[119] C. A. Lipinski, F. Lombardo, B. W. Dominy, and P. J. Feeney, “Experimental and computational approaches to estimate solubility and permeability in drug discovery and development settings,” *Adv. Drug Deliv. Rev.*, vol. 23, no. 1, pp. 3–25, 1997, doi: https://doi.org/10.1016/S0169-409X(96)00423-1.
[120] K. K. Gupta and D. Rana, “Spectroscopic and chromatographic identification of bioprospecting bioactive compounds from cow feces: Antimicrobial and antioxidant activities evaluation of gut bacterium Pseudomonas aeruginosa KD155,” *Biotechnol. Rep.*, vol. 29, p. e00577, 2021, doi: https://doi.org/10.1016/j.btre.2020.e00577.
[121] J. R. Tagg and A. R. McGiven, “Assay System for Bacteriocins,” *Appl. Microbiol.*, vol. 21, no. 5, pp. 943–943, May 1971, doi: 10.1128/am.21.5.943-943.1971.
[122] S. Dallakyan and A. J. Olson, “Small-Molecule Library Screening by Docking with PyRx BT - Chemical Biology: Methods and Protocols,” J. E. Hempel, C. H. Williams, and C. C. Hong, Eds., New York, NY: Springer New York, 2015, pp. 243–250. doi: 10.1007/978-1-4939-2269-7_19.
[123] G. U. Sharma S, Sharma A, “Molecular Docking studies on the Anti-fungal activity of Allium sativum (Garlic) against Mucormycosis (black fungus) by BIOVIA discovery studio visualizer,” 2021, doi: 10.17352/aaa.000013.
[124] S. K. Sharma, D. V. N. Sudheer Pamidimarri, D. Y. Kim, and J.-G. Na, “Y-doped zinc oxide (YZO) nanoflowers, microstructural analysis and test their antibacterial activity,” *Mater. Sci. Eng. C*, vol. 53, pp. 104–110, Aug. 2015, doi: 10.1016/j.msec.2015.04.007.
[125] M. S. Bapat *et al.*, “Evaluating green silver nanoparticles as prospective biopesticides: An environmental standpoint,” *Chemosphere*, vol. 286, p. 131761, 2022, doi: https://doi.org/10.1016/j.chemosphere.2021.131761.
[126] N. T. T. Nguyen, L. M. Nguyen, T. T. T. Nguyen, D. H. Nguyen, D. T. C. Nguyen, and T. V. Tran, “Recent advances on biogenic nanoparticles for detection and control of plant pathogens in sustainable agriculture: A review,” *Ind. Crops Prod.*, vol. 198, p. 116700, Aug. 2023, doi: 10.1016/j.indcrop.2023.116700.
[127] B. Yan *et al.*, “Biochar amendments combined with organic fertilizer improve maize productivity and mitigate nutrient loss by regulating the C–N–P stoichiometry of soil, microbiome, and enzymes,” *Chemosphere*, vol. 324, p. 138293, May 2023, doi: 10.1016/j.chemosphere.2023.138293.

[128] N. T. T. Nguyen, L. M. Nguyen, T. T. T. Nguyen, U. P. N. Tran, D. T. C. Nguyen, and T. V. Tran, "A critical review on the bio-mediated green synthesis and multiple applications of magnesium oxide nanoparticles," *Chemosphere*, vol. 312, p. 137301, Jan. 2023, doi: 10.1016/j.chemosphere.2022.137301.
[129] T. M. Thakur, R. S. Lokhande, M. M. Thigle, and V. R. Patil, "Nanoparticles of chromium oxide by green synthesis using Eucalyptus globulous leaves extract; characterization and biological activity studies," *Innov. Adv. Eng. Technol. IAET-2022*, vol. 79, pp. 100–106, Jan. 2023, doi: 10.1016/j.matpr.2022.09.368.
[130] S. Tufail, Z. Ali, S. Hanif, A. Sajjad, and M. Zia, "Synthesis and morphological & biological characterization of Campsis radicans and Cascabela thevetia petals derived silver nanoparticles," *Biochem. Syst. Ecol.*, vol. 105, p. 104526, Dec. 2022, doi: 10.1016/j.bse.2022.104526.
[131] R. Aniza, W.-H. Chen, A. Pétrissans, A. T. Hoang, V. Ashokkumar, and M. Pétrissans, "A review of biowaste remediation and valorization for environmental sustainability: Artificial intelligence approach," *Environ. Pollut.*, vol. 324, p. 121363, May 2023, doi: 10.1016/j.envpol.2023.121363.
[132] J. Zhang, N. Hori, and A. Takemura, "Optimization of agricultural wastes liquefaction process and preparing bio-based polyurethane foams by the obtained polyols," *Ind. Crops Prod.*, vol. 138, p. 111455, Oct. 2019, doi: 10.1016/j.indcrop.2019.06.018.
[133] Y. Zong, H. Chen, Z. Malik, Q. Xiao, and S. Lu, "Comparative study on the potential risk of contaminated-rice straw, its derived biochar and phosphorus modified biochar as an amendment and their implication for environment," *Environ. Pollut.*, vol. 293, p. 118515, Jan. 2022, doi: 10.1016/j.envpol.2021.118515.
[134] Y. Wang *et al.*, "Potential of crop straw incorporation for replacing chemical fertilizer and reducing nutrient loss in Sichuan Province, China," *Environ. Pollut.*, vol. 320, p. 121034, Jan. 2023, doi: 10.1016/j.envpol.2023.121034.
[135] K. P., V. S., V. E., P. V.N, N. M., and P. PK, "Biogenesis of ZnO nanoparticles for revolutionizing agriculture: A step towards anti -infection and growth promotion in plants," *Ind. Crops Prod.*, vol. 170, p. 113762, Oct. 2021, doi: 10.1016/j.indcrop.2021.113762.
[136] S. Ruan, J. Qi, F. Wu, R. Lai, and X. Tang, "Response of yield, grain quality, and volatile organic compounds of aromatic rice to vermicompost application," *J. Cereal Sci.*, vol. 109, p. 103620, Jan. 2023, doi: 10.1016/j.jcs.2022.103620.
[137] A. Ahmad, S. S. Hashmi, J. M. Palma, and F. J. Corpas, "Influence of metallic, metallic oxide, and organic nanoparticles on plant physiology," *Chemosphere*, vol. 290, p. 133329, Mar. 2022, doi: 10.1016/j.chemosphere.2021.133329.
[138] M. S. A. Ahmad and M. Ashraf, "Essential Roles and Hazardous Effects of Nickel in Plants," in *Reviews of Environmental Contamination and Toxicology*, D. M. Whitacre, Ed., New York, NY: Springer New York, 2011, pp. 125–167. doi: 10.1007/978-1-4614-0668-6_6.
[139] A. Bardhan, A. Singh, H. Nishanta, S. Sharma, A. Choubey, and S. Kumar, "Biogenic Copper Oxide Nanoparticles for Improved Lubricity and Filtration Control in Water-Based Drilling Mud," *Energy Fuels*, vol. 38, Apr. 2024, doi: 10.1021/acs.energyfuels.4c00635.
[140] A. K. Prajapati and M. K. Mondal, "Novel green strategy for CuO–ZnO–C nanocomposites fabrication using marigold (Tagetes spp.) flower petals extract with and without CTAB treatment for adsorption of Cr(VI) and Congo red dye," *J. Environ. Manage.*, vol. 290, p. 112615, 2021, doi: https://doi.org/10.1016/j.jenvman.2021.112615.
[141] C. Deng *et al.*, "Soil and foliar exposure of soybean (Glycine max) to Cu: Nanoparticle coating-dependent plant responses," *NanoImpact*, vol. 26, Apr. 2022, doi: 10.1016/j.impact.2022.100406.
[142] A. Chahardoli, N. Karimi, X. Ma, and F. Qalekhani, "Effects of engineered aluminum and nickel oxide nanoparticles on the growth and antioxidant defense systems of Nigella

arvensis L.," *Sci. Rep.*, vol. 10, no. 1, p. 3847, Mar. 2020, doi: 10.1038/s41598-020-60841-6.
[143] S. O. Ogunyemi *et al.*, "Cobalt oxide nanoparticles: An effective growth promoter of Arabidopsis plants and nano-pesticide against bacterial leaf blight pathogen in rice," *Ecotoxicol. Environ. Saf.*, vol. 257, Jun. 2023, doi: 10.1016/j.ecoenv.2023.114935.
[144] S. Adewuyi, K. T. Kareem, A. O. Atayese, S. A. Amolegbe, and C. A. Akinremi, "Chitosan–cobalt(II) and nickel(II) chelates as antibacterial agents," *Int. J. Biol. Macromol.*, vol. 48, no. 2, pp. 301–303, Mar. 2011, doi: 10.1016/j.ijbiomac.2010.12.004.
[145] O. P. Missen *et al.*, "Natural cobalt–manganese oxide nanoparticles: speciation, detection and implications for cobalt cycling," *Environ. Chem.*, vol. 21, no. 2, 2024, [Online]. Available: https://doi.org/10.1071/EN23093
[146] P. Banerjee and P. Bhattacharya, "Investigating Cobalt in Soil-plant-animal-human system: Dynamics, Impact and Management," *J. Soil Sci. Plant Nutr.*, vol. 21, no. 3, pp. 2339–2354, Sep. 2021, doi: 10.1007/s42729-021-00525-w.
[147] Y. S. Perea-Vélez, R. Carrillo-González, Ma. del C. A. González-Chávez, J. Vangronsveld, D. Tapia Maruri, and J. López-Luna, "Nano-priming of Phaseolus vulgaris OTI cultivar with cobalt ferrite nanoparticles enhances the mineral composition of progeny seeds," *J. Nanoparticle Res.*, vol. 26, no. 9, p. 205, 2024, doi: 10.1007/s11051-024-06101-4.
[148] X. Hu, X. Wei, J. Ling, and J. Chen, "Cobalt: An Essential Micronutrient for Plant Growth?," *Front. Plant Sci.*, vol. Volume 12-2021, 2021, [Online]. Available: https://www.frontiersin.org/journals/plant-science/articles/10.3389/fpls.2021.768523
[149] R. Manimaran, M. Venkatesan, and K. Tharun Kumar, "Optimization of okra (Abelmoschus esculentus) biodiesel production using RSM technique coupled with GA: Addressing its performance and emission characteristics," *J. Clean. Prod.*, vol. 380, p. 134870, Dec. 2022, doi: 10.1016/j.jclepro.2022.134870.
[150] J. M. I. Sonali, K. V. Gayathri, G. Rangasamy, P. S. Kumar, and R. Rajagopal, "Efficacy of Biogenic Selenium Nanoparticles from Pseudomonas Libanesis Towards Growth Enhancement of Okra," *Waste Biomass Valorization*, vol. 15, no. 3, pp. 1793–1806, 2024, doi: 10.1007/s12649-023-02233-1.
[151] A. K. Goyal *et al.*, "Efficacy of Nano-fertilizers Applications on Growth Parameters and Flowering Dynamics in Okra (Abelmoschus esculentus)," *Int. J. Plant Soil Sci.*, vol. 36, no. 9, pp. 585–596, Sep. 2024, doi: 10.9734/ijpss/2024/v36i95008.
[152] N. C. Madlala, N. Khanyile, and A. Masenya, "Examining the Correlation between the Inorganic Nano-Fertilizer Physical Properties and Their Impact on Crop Performance and Nutrient Uptake Efficiency," *Nanomaterials*, vol. 14, no. 15, p. 1263, 2024, doi: 10.3390/nano14151263.
[153] J. Che, W. Zhang, B. Ma, and C. Wang, "An efficient process for recovering copper as CuO nanoparticles from acidic waste etchant via chemical precipitation and thermal decomposition: Turning waste into value-added product," *J. Clean. Prod.*, vol. 369, p. 133404, Oct. 2022, doi: 10.1016/j.jclepro.2022.133404.
[154] A. Mani, A. Ahamed, M. A. El-Sheikh, and I. Akbar, "Natural dried Vanilla Beans powder (VBP) mediated CuO nanoparticles catalysis: Aerobic oxidation of hydroxylamines from industrial waste water using ecofriendly method," *Ind. Crops Prod.*, vol. 191, p. 115915, Jan. 2023, doi: 10.1016/j.indcrop.2022.115915.
[155] K. Rajendran *et al.*, "CuO as a reactive and reusable reagent for the hydrogenation of nitroarenes," *Appl. Catal. B Environ.*, vol. 297, no. March, p. 120417, 2021, doi: 10.1016/j.apcatb.2021.120417.
[156] A. Singh *et al.*, "Structurally and morphologically engineered single-pot biogenic synthesis of NiO nanoparticles with enhanced photocatalytic and antimicrobial activities," *J. Clean. Prod.*, vol. 343, p. 131026, Apr. 2022, doi: 10.1016/j.jclepro.2022.131026.
[157] Rozina, M. Ahmad, M. Alruqi, and M. Zafar, "Cleaner production of biodiesel from novel and non-edible seed oil of Chamaerops humilis using recyclable cobalt oxide

nanoparticles: A contribution to resilient and sustainable world," *J. Clean. Prod.*, vol. 369, p. 133378, Oct. 2022, doi: 10.1016/j.jclepro.2022.133378.
[158] C. Huang *et al.*, "Impact of progressively cumulative exposure of AgNPs on earthworms (Eisenia fetida) and implication for eco-toxicological risk assessment," *Chemosphere*, vol. 322, p. 138163, May 2023, doi: 10.1016/j.chemosphere.2023.138163.
[159] S. Mahey, R. Kumar, M. Sharma, V. Kumar, and R. Bhardwaj, "A critical review on toxicity of cobalt and its bioremediation strategies," *SN Appl. Sci.*, vol. 2, no. 7, p. 1279, Jun. 2020, doi: 10.1007/s42452-020-3020-9.
[160] L. Aribal and J. Mercado, "Phytoremediation of Mangrove species exposed to effluents of mining ultramafic soils," Jan. 2020.
[161] D. Wen, H. Hou, A. Meng, J. Meng, L. Xie, and C. Zhang, "Rapid evaluation of seed vigor by the absolute content of protein in seed within the same crop," *Sci. Rep.*, vol. 8, no. 1, p. 5569, Apr. 2018, doi: 10.1038/s41598-018-23909-y.
[162] Q. Hu, C. Lin, Y. Guan, M. S. Sheteiwy, W. Hu, and J. Hu, "Inhibitory effect of eugenol on seed germination and pre-harvest sprouting of hybrid rice (Oryza sativa L.)," *Sci. Rep.*, vol. 7, no. 1, p. 5295, Jul. 2017, doi: 10.1038/s41598-017-04104-x.
[163] N. Alavi, M. Daneshpajou, M. Shirmardi, G. Goudarzi, A. Neisi, and A. A. Babaei, "Investigating the efficiency of co-composting and vermicomposting of vinasse with the mixture of cow manure wastes, bagasse, and natural zeolite," *Waste Manag.*, vol. 69, pp. 117–126, Nov. 2017, doi: 10.1016/j.wasman.2017.07.039.
[164] M. C. Enebe and M. Erasmus, "Vermicomposting technology - A perspective on vermicompost production technologies, limitations and prospects," *J. Environ. Manage.*, vol. 345, p. 118585, Nov. 2023, doi: 10.1016/j.jenvman.2023.118585.
[165] U. Hujuri, K. Sankar Paul, B. Kurmi, A. Borah, and F. A. Nongdhar, "Microbial composting and vermicomposting of temple waste using Eisenia fetida," *Adv. Chem. Eng. Sci. ACES 2022*, vol. 72, pp. 2780–2784, Jan. 2023, doi: 10.1016/j.matpr.2022.11.177.
[166] C. Devi and M. Khwairakpam, "Weed biomass: Bioconversion through composting followed by vermicomposting to optimize time required," *Bioresour. Technol. Rep.*, vol. 21, p. 101326, Feb. 2023, doi: 10.1016/j.biteb.2022.101326.
[167] J. C. García-López, G. L. López-Lizárraga, and J. C. García-Cañedo, "Nitrogen to biomass, chlorophyll and carotenoids transfer functions for microalgae Scenedesmus sp.," *Algal Res.*, vol. 90, p. 104257, Aug. 2025, doi: 10.1016/j.algal.2025.104257.
[168] V. Baskar, N. Safia, K. Sree Preethy, S. Dhivya, M. Thiruvengadam, and R. Sathishkumar, "A comparative study of phytotoxic effects of metal oxide (CuO, ZnO and NiO) nanoparticles on in-vitro grown Abelmoschus esculentus," *Plant Biosyst. - Int. J. Deal. Asp. Plant Biol.*, vol. 155, no. 2, pp. 374–383, Jan. 2021, doi: 10.1080/11263504.2020.1753843.
[169] N. A. Younes, H. S. Hassan, M. F. Elkady, A. M. Hamed, and M. F. A. Dawood, "Impact of synthesized metal oxide nanomaterials on seedlings production of three Solanaceae crops," *Heliyon*, vol. 6, no. 1, p. e03188, Jan. 2020, doi: 10.1016/j.heliyon.2020.e03188.
[170] R. Talská, J. Machalová, P. Smýkal, and K. Hron, "A comparison of seed germination coefficients using functional regression," *Appl. Plant Sci.*, vol. 8, no. 8, p. e11366, Aug. 2020, doi: 10.1002/aps3.11366.
[171] S. M. Seyyedi, M. Khajeh-Hosseini, P. R. Moghaddam, and H. Shahandeh, "Effects of phosphorus and seed priming on seed vigor, fatty acids composition and heterotrophic seedling growth of black seed (Nigella sativa L.) grown in a calcareous soil," *Ind. Crops Prod.*, vol. 74, pp. 939–949, Nov. 2015, doi: 10.1016/j.indcrop.2015.05.082.
[172] P. D. Itroutwar, G. Kasivelu, V. Raguraman, K. Malaichamy, and S. K. Sevathapandian, "Effects of biogenic zinc oxide nanoparticles on seed germination and seedling vigor of maize (Zea mays)," *Biocatal. Agric. Biotechnol.*, vol. 29, p. 101778, Oct. 2020, doi: 10.1016/j.bcab.2020.101778.

[173] M. H. Siddiqui and M. H. Al-Whaibi, “Role of nano-SiO2 in germination of tomato (Lycopersicum esculentum seeds Mill.),” *Saudi J. Biol. Sci.*, vol. 21, no. 1, pp. 13–17, Jan. 2014, doi: 10.1016/j.sjbs.2013.04.005.
[174] A. S. Ibrahim, G. A. M. Ali, A. Hassanein, A. M. Attia, and E. R. Marzouk, “Toxicity and Uptake of CuO Nanoparticles: Evaluation of an Emerging Nanofertilizer on Wheat (Triticum aestivum L.) Plant,” *Sustainability*, vol. 14, no. 9, 2022, doi: 10.3390/su14094914.
[175] P. T. Hoe *et al.*, “Germination responses of soybean seeds under Fe, ZnO, Cu and Co nanoparticle treatments,” *Int. J. Agric. Biol.*, vol. 20, pp. 1562–1568, Jan. 2018, doi: 10.17957/IJAB/15.0670.
[176] K. Vijai Anand, A. R. Anugraga, M. Kannan, G. Singaravelu, and K. Govindaraju, “Bio-engineered magnesium oxide nanoparticles as nano-priming agent for enhancing seed germination and seedling vigour of green gram (Vigna radiata L.),” *Mater. Lett.*, vol. 271, p. 127792, Jul. 2020, doi: 10.1016/j.matlet.2020.127792.
[177] P. Rai-Kalal and A. Jajoo, “Priming with zinc oxide nanoparticles improve germination and photosynthetic performance in wheat,” *Plant Physiol. Biochem.*, vol. 160, pp. 341–351, Mar. 2021, doi: 10.1016/j.plaphy.2021.01.032.
[178] D. kumar Gnanasekaran, K. Raja, N. Natarajan, K. Govindaraju, and K. Subramanian, “Invigouration treatment of metal and metal oxide nanoparticles for improving the seed quality of aged chilli seeds (Capsicum annum L.),” *Mater. Chem. Phys.*, vol. 242, p. 122492, Nov. 2019, doi: 10.1016/j.matchemphys.2019.122492.
[179] P. Visweswara Rao, T. N. V. K. V. Prasad, R. Balam, G. Thimmavajjula, and A. Shaik, “Size dependent effects of antimicrobial phytogenic silver nanoparticles on germination, growth and biochemical parameters of Rice (Oryza sativa L), Maize (Zea mays L) and Peanut (Arachis hypogaea L),” *IET Nanobiotechnol.*, vol. 11, Jul. 2016, doi: 10.1049/iet-nbt.2015.0122.
[180] S. Jain, A. Gupta, and N. Verma, *Industrial Applications of Soil Microbes: Volume 4*. in Industrial Applications of Soil Microbes Series. Bentham Science Publishers, 2024. [Online]. Available: https://books.google.co.in/books?id=YXk1EQAAQBAJ
[181] X. Wu, X. Wu, Y. Wang, and H. Tang, “Quantitative Metabonomic Analysis Reveals the Germination-Associated Dynamic and Systemic Biochemical Changes for Mung-Bean (Vigna radiata) Seeds,” *J. Proteome Res.*, vol. 19, no. 6, pp. 2457–2470, Jun. 2020, doi: 10.1021/acs.jproteome.0c00181.
[182] D. Madhupriyaa *et al.*, “Efficacy of Chelated Micronutrients in Plant Nutrition,” *Commun. Soil Sci. Plant Anal.*, vol. 55, no. 22, pp. 3609–3637, Dec. 2024, doi: 10.1080/00103624.2024.2397019.
[183] M. F. Salas-Orozco, A. C. Lorenzo-Leal, I. de Alba Montero, N. P. Marín, M. A. C. Santana, and H. Bach, “Mechanism of escape from the antibacterial activity of metal-based nanoparticles in clinically relevant bacteria: A systematic review,” *Nanomedicine Nanotechnol. Biol. Med.*, vol. 55, p. 102715, 2024, doi: https://doi.org/10.1016/j.nano.2023.102715.
[184] P. Xie, J. Chen, P. Wu, and Z. Cai, “Spatial Lipidomics Reveals Lipid Changes in the Cotyledon and Plumule of Mung Bean Seeds during Germination,” *J. Agric. Food Chem.*, vol. 71, no. 49, pp. 19879–19887, Dec. 2023, doi: 10.1021/acs.jafc.3c06029.
[185] I. M. Chung, B. Venkidasamy, and M. Thiruvengadam, “Nickel oxide nanoparticles cause substantial physiological, phytochemical, and molecular-level changes in Chinese cabbage seedlings,” *Plant Physiol. Biochem.*, vol. 139, pp. 92–101, Jun. 2019, doi: 10.1016/j.plaphy.2019.03.010.
[186] K. Azarin *et al.*, “Effects of ZnO nanoparticles and its bulk form on growth, antioxidant defense system and expression of oxidative stress related genes in Hordeum vulgare L,” *Chemosphere*, vol. 287, p. 132167, Jan. 2022, doi: 10.1016/j.chemosphere.2021.132167.
[187] S. Mariyam *et al.*, “Nanotechnology, a frontier in agricultural science, a novel approach in abiotic stress management and convergence with new age medicine-A review,” *Sci. Total Environ.*, vol. 912, p. 169097, Feb. 2024, doi: 10.1016/j.scitotenv.2023.169097.

[188] P. S. Vindhya and V. T. Kavitha, “Effect of cobalt doping on antimicrobial, antioxidant and photocatalytic activities of CuO nanoparticles,” *Mater. Sci. Eng. B*, vol. 289, p. 116258, Mar. 2023, doi: 10.1016/j.mseb.2022.116258.
[189] A. K. A. Ahmed *et al.*, “Influences of Air, Oxygen, Nitrogen, and Carbon Dioxide Nanobubbles on Seed Germination and Plant Growth,” *J. Agric. Food Chem.*, vol. 66, no. 20, pp. 5117–5124, May 2018, doi: 10.1021/acs.jafc.8b00333.
[190] P. Zhou *et al.*, “Nickel Oxide Nanoparticles Improve Soybean Yield and Enhance Nitrogen Assimilation,” *Environ. Sci. Technol.*, vol. 57, no. 19, pp. 7547–7558, May 2023, doi: 10.1021/acs.est.3c00959.
[191] S. Paulraj, K. Raman, C. R. Mohan, Ramachandiran Janarthanan, K. Ashokkumar, and M. Pambayan Ulagan, “Biosynthesis of Eudrilus eugeniae vermi wash based enzyme decorated copper oxide nanoparticles towards seed germination of green gram,” *J. Agric. Food Res.*, vol. 9, p. 100343, Sep. 2022, doi: 10.1016/j.jafr.2022.100343.
[192] H. Haider *et al.*, “Synthesis and characterization of copper oxide nanoparticles: its influence on Corn (Z. mays) and Wheat (Triticum) plants by inoculation of Bacillus subtilus,” *Environ. Sci. Pollut. Res.*, Dec. 2022, doi: 10.1007/s11356-022-24877-7.
[193] M. Hasanin, A. H. Hashem, I. Lashin, and S. A. M. Hassan, “In vitro improvement and rooting of banana plantlets using antifungal nanocomposite based on myco-synthesized copper oxide nanoparticles and starch,” *Biomass Convers. Biorefinery*, vol. 13, no. 10, pp. 8865–8875, Jul. 2023, doi: 10.1007/s13399-021-01784-4.
[194] Md. A. Rahman *et al.*, “Efficacy of the green synthesized nickel-oxide nanoparticles against pulse beetle, Callosobruchus maculatus (F.) in black gram (Vigna mungo L.),” *Int. J. Pest Manag.*, vol. 67, no. 4, pp. 306–314, Sep. 2021, doi: 10.1080/09670874.2020.1773572.
[195] F. Mahmood *et al.*, “Bioinspired Cobalt Oxide Nanoball Synthesis, Characterization, and Their Potential as Metal Stress Absorbants,” *ACS Omega*, vol. 8, no. 6, pp. 5836–5849, Feb. 2023, doi: 10.1021/acsomega.2c07545.
[196] S. H. Brengi, A. A. E. M. Khedr, and I. A. Abouelsaad, “Effect of melatonin or cobalt on growth, yield and physiological responses of cucumber (Cucumis sativus L.) plants under salt stress,” *J. Saudi Soc. Agric. Sci.*, vol. 21, no. 1, pp. 51–60, Jan. 2022, doi: 10.1016/j.jssas.2021.06.012.
[197] T. Talankova-Sereda *et al.*, “The Influence of Cu и Co Nanoparticles on Growth Characteristics and Biochemical Structure of Mentha Longifolia In Vitro,” vol. 183, 2016, pp. 427–436. doi: 10.1007/978-3-319-30737-4_36.
[198] H. Li *et al.*, “A rice chloroplast-localized ABC transporter ARG1 modulates cobalt and nickel homeostasis and contributes to photosynthetic capacity,” *New Phytol.*, vol. 228, no. 1, pp. 163–178, Oct. 2020, doi: 10.1111/nph.16708.
[199] M. Hatami, K. Kariman, and M. Ghorbanpour, “Engineered nanomaterial-mediated changes in the metabolism of terrestrial plants,” *Sci. Total Environ.*, vol. 571, pp. 275–291, Jul. 2016, doi: 10.1016/j.scitotenv.2016.07.184.
[200] L. Taiz, E. Zeiger, I. M. Møller, and A. Murphy, *Fisiologia e desenvolvimento vegetal*. Artmed Editora, 2017.
[201] A. Rasheed *et al.*, “Molecular characterization of genes involved in tolerance of cadmium in Triticum aestivum (L.) under Cd stress,” *J. Hazard. Mater.*, vol. 464, p. 132955, Feb. 2024, doi: 10.1016/j.jhazmat.2023.132955.
[202] D. R. J. Soviguidi, Z. Duan, B. Pan, R. Lei, and G. Liang, “Function, structure, and regulation of Iron Regulated Transporter 1,” *Plant Physiol. Biochem.*, vol. 219, p. 109457, Feb. 2025, doi: 10.1016/j.plaphy.2024.109457.
[203] J. Morrissey *et al.*, “The Ferroportin Metal Efflux Proteins Function in Iron and Cobalt Homeostasis in Arabidopsis,” *Plant Cell*, vol. 21, no. 10, pp. 3326–3338, Oct. 2009, doi: 10.1105/tpc.109.069401.
[204] J. Park *et al.*, “The phytochelatin transporters AtABCC1 and AtABCC2 mediate tolerance to cadmium and mercury,” *Plant J.*, vol. 69, no. 2, pp. 278–288, Jan. 2012, doi: 10.1111/j.1365-313X.2011.04789.x.

[205] K. Rekha, B. Usha, and N. S. Keeran, “3 - Role of ABC transporters and other vacuolar transporters during heavy metal stress in plants,” in *Metal and Nutrient Transporters in Abiotic Stress*, A. Roychoudhury, D. K. Tripathi, and R. Deshmukh, Eds., Academic Press, 2021, pp. 55–76. doi: 10.1016/B978-0-12-817955-0.00003-X.
[206] N. Ha, Đ. Cường, T. Hoang, N. Ngo, L. Bui, and N. Duong Tan, “The effect of cobalt and silver nanoparticles on overcoming leaf abscission and enhanced growth of rose (Rosa hybrida L. ‘Baby Love’) plantlets cultured in vitro,” *Plant Cell Tissue Organ Cult. PCTOC*, vol. 141, May 2020, doi: 10.1007/s11240-020-01796-4.
[207] S. Ali *et al.*, “Discovering Nature’s shield: Metabolomic insights into green zinc oxide nanoparticles Safeguarding Brassica parachinensis L. from cadmium stress,” *Plant Physiol. Biochem.*, vol. 206, p. 108126, Jan. 2024, doi: 10.1016/j.plaphy.2023.108126.
[208] R. Kumari *et al.*, “Regulation and safety measures for nanotechnology-based agri-products,” *Front. Genome Ed.*, vol. 5, 2023, [Online]. Available: https://www.frontiersin.org/journals/genome-editing/articles/10.3389/fgeed.2023.1200987
[209] U. Shahzad, M. Saqib, H. M. Jhanzab, S. Abou Fayssal, R. Ahmad, and A. Qayyum, “Different concentrations of silver nanoparticles trigger growth, yield, and quality of strawberry (Fragaria ananassa L.) fruits,” *J. Plant Nutr. Soil Sci.*, vol. 187, no. 5, pp. 668–677, Oct. 2024, doi: https://doi.org/10.1002/jpln.202300284.
[210] M. I. Cáceres-Wenzel, F. N. Bernassani, J. S. Fuchs, E. Cortón, and A. C. Cochón, “Mixture toxicity study of two metal oxide nanoparticles and chlorpyrifos on Eisenia andrei earthworms,” *Environ. Sci. Pollut. Res.*, vol. 31, no. 24, pp. 35470–35482, 2024, doi: 10.1007/s11356-024-33604-3.
[211] A. Nyabadza *et al.*, “A review of physical, chemical and biological synthesis methods of bimetallic nanoparticles and applications in sensing, water treatment, biomedicine, catalysis and hydrogen storage,” *Adv. Colloid Interface Sci.*, vol. 321, p. 103010, Nov. 2023, doi: 10.1016/j.cis.2023.103010.
[212] M. A. Darwish, W. Abd-Elaziem, A. Elsheikh, and A. A. Zayed, “Advancements in nanomaterials for nanosensors: a comprehensive review,” *Nanoscale Adv.*, vol. 6, no. 16, pp. 4015–4046, Aug. 2024, doi: 10.1039/d4na00214h.
[213] M. Hassanpour, H. Safardoust, D. Ghanbari, and M. Salavati-Niasari, “Microwave synthesis of CuO/NiO magnetic nanocomposites and its application in photo-degradation of methyl orange,” *J. Mater. Sci. Mater. Electron.*, vol. 27, no. 3, pp. 2718–2727, Mar. 2016, doi: 10.1007/s10854-015-4082-0.
[214] S. G. Hosseini and R. Abazari, “A facile one-step route for production of CuO, NiO, and CuO–NiO nanoparticles and comparison of their catalytic activity for ammonium perchlorate decomposition,” *RSC Adv.*, vol. 5, no. 117, pp. 96777–96784, 2015, doi: 10.1039/C5RA20155A.
[215] A. G. Ramu, M. L. A. Kumari, M. S. Elshikh, H. H. Alkhamis, A. F. Alrefaei, and D. Choi, “A facile and green synthesis of CuO/NiO nanoparticles and their removal activity of toxic nitro compounds in aqueous medium,” *Chemosphere*, vol. 271, p. 129475, May 2021, doi: 10.1016/j.chemosphere.2020.129475.
[216] S. Senobari and A. Nezamzadeh-Ejhieh, “A comprehensive study on the enhanced photocatalytic activity of CuO-NiO nanoparticles: Designing the experiments,” *J. Mol. Liq.*, vol. 261, pp. 208–217, Jul. 2018, doi: 10.1016/j.molliq.2018.04.028.
[217] S. Singh and K. Pal, “Exploration of polydopamine capped bimetallic oxide (CuO-NiO) nanoparticles inspired by mussels for enhanced and targeted paclitaxel delivery for synergistic breast cancer therapy,” *Appl. Surf. Sci.*, vol. 626, p. 157266, Jul. 2023, doi: 10.1016/j.apsusc.2023.157266.
[218] P. Anbu, S. C. B. Gopinath, K. Saravanakumar, S. Vijayakumar, S. Ramanathan, and M.-H. Wang, “Bimetallic mixed metal oxide (CuO/NiO) in fusion with nitrogen-doped graphene oxide: An alternate approach for developing potential biocarrier,” *J. Environ. Chem. Eng.*, vol. 9, no. 4, p. 105781, Aug. 2021, doi: 10.1016/j.jece.2021.105781.
[219] M. Li, K. Huan, D. Deng, X. Yan, Y. Li, and L. Luo, “Coaxial electrospinning synthesis of size-tunable CuO/NiO hollow heterostructured nanofibers: Towards detection of

glucose level in human serum," *Colloids Surf. B Biointerfaces*, vol. 222, p. 113047, Feb. 2023, doi: 10.1016/j.colsurfb.2022.113047.
[220] M. Srivastava, S. Chaubey, and A. K. Ojha, "Investigation on size dependent structural and magnetic behavior of nickel ferrite nanoparticles prepared by sol–gel and hydrothermal methods," *Mater. Chem. Phys.*, vol. 118, no. 1, pp. 174–180, Nov. 2009, doi: 10.1016/j.matchemphys.2009.07.023.
[221] F. Hazeghi, S. Mozaffari, and S. M. B. Ghorashi, "Metal organic framework–derived core-shell CuO@NiO nanospheres as hole transport material in perovskite solar cell," *J. Solid State Electrochem.*, vol. 24, no. 6, pp. 1427–1438, Jun. 2020, doi: 10.1007/s10008-020-04643-w.
[222] H.-K. Kim, W. Honda, B.-S. Kim, and I.-S. Kim, "Preparation and magnetic properties of electrospun CuO/NiO bimetallic nanofibers via sol–gel electrospinning," *J. Mater. Sci.*, vol. 48, no. 3, pp. 1111–1116, Feb. 2013, doi: 10.1007/s10853-012-6843-y.
[223] I. Chakraborty, N. Chakrabarty, A. Senapati, and A. K. Chakraborty, "CuO@NiO/Polyaniline/MWCNT Nanocomposite as High-Performance Electrode for Supercapacitor," *J. Phys. Chem. C*, vol. 122, no. 48, pp. 27180–27190, Dec. 2018, doi: 10.1021/acs.jpcc.8b08091.
[224] S. Veeman and S. Karuppuchamy, "H2O2 assisted hydrothermal and microwave synthesis of CuO–NiO hybrid MWCNT composite electrode materials for supercapacitor applications," *Ceram. Int.*, vol. 48, no. 18, pp. 26806–26817, Sep. 2022, doi: 10.1016/j.ceramint.2022.05.380.
[225] Y. Ge, T. Gao, C. Wang, Z. H. Shah, R. Lu, and S. Zhang, "Highly efficient silica coated CuNi bimetallic nanocatalyst from reverse microemulsion," *J. Colloid Interface Sci.*, vol. 491, pp. 123–132, Apr. 2017, doi: 10.1016/j.jcis.2016.12.043.
[226] M. S. AlSalhi, S. Devanesan, P. Shanmugam, Y. O. Kim, J.-T. Kwon, and H.-J. Kim, "Synthesis and biocompatible role of hierarchical structured carbon nanoplates incorporated α-Fe2O3 nanocomposites for biomedical applications with respect to cancer treatment," *Saudi J. Biol. Sci.*, vol. 27, no. 2, pp. 588–593, Feb. 2020, doi: 10.1016/j.sjbs.2019.11.028.
[227] K. Kombaiah, J. J. Vijaya, L. J. Kennedy, and M. Bououdina, "Studies on the microwave assisted and conventional combustion synthesis of Hibiscus rosa-sinensis plant extract based ZnFe2O4 nanoparticles and their optical and magnetic properties," *Ceram. Int.*, vol. 42, no. 2, Part A, pp. 2741–2749, Feb. 2016, doi: 10.1016/j.ceramint.2015.11.003.
[228] S. Matussin, M. H. Harunsani, A. L. Tan, and M. M. Khan, "Plant-Extract-Mediated SnO2 Nanoparticles: Synthesis and Applications," *ACS Sustain. Chem. Eng.*, vol. 8, no. 8, pp. 3040–3054, Mar. 2020, doi: 10.1021/acssuschemeng.9b06398.
[229] M. Swamy M, S. BS, M. C, P. S, and R. ND, "Bio-mediated synthesis of ZnO nanoparticles using Lantana Camara flower extract: Its characterizations, photocatalytic, electrochemical and anti-inflammatory applications," *Environ. Nanotechnol. Monit. Manag.*, vol. 15, p. 100442, May 2021, doi: 10.1016/j.enmm.2021.100442.
[230] A. O. Juma, E. A. A. Arbab, C. M. Muiva, L. M. Lepodise, and G. T. Mola, "Synthesis and characterization of CuO-NiO-ZnO mixed metal oxide nanocomposite," *J. Alloys Compd.*, vol. 723, pp. 866–872, Nov. 2017, doi: 10.1016/j.jallcom.2017.06.288.
[231] M. Kurian and C. Kunjachan, "Investigation of size dependency on lattice strain of nanoceria particles synthesised by wet chemical methods," *Int. Nano Lett.*, vol. 4, no. 4, pp. 73–80, Dec. 2014, doi: 10.1007/s40089-014-0122-7.
[232] D. Zeng, Y. Li, H. Ma, F. Cui, and J. Zhang, "CuO@NiO Nanoparticles Derived from Metal–Organic Framework Precursors for the Deoxygenation of Fatty Acids," *ACS Sustain. Chem. Eng.*, vol. 9, no. 46, pp. 15612–15622, Nov. 2021, doi: 10.1021/acssuschemeng.1c05773.
[233] N. Sandhiran *et al.*, "CuO–NiO binary transition metal oxide nanoparticle anchored on rGO nanosheets as high-performance electrocatalyst for the oxygen reduction reaction," *Environ. Res.*, vol. 211, p. 112992, Aug. 2022, doi: 10.1016/j.envres.2022.112992.
[234] A. F. Zedan, A. S. AlJaber, and M. S. El-Shall, "Facile Microwave Synthesis of Hierarchical Porous Copper Oxide and Its Catalytic Activity and Kinetics for Carbon

Monoxide Oxidation," *ACS Omega*, vol. 7, no. 48, pp. 44021–44032, Dec. 2022, doi: 10.1021/acsomega.2c05399.
[235] S. Sahoo, K. Y. Wickramathilaka, E. Njeri, D. Silva, and S. L. Suib, "A review on transition metal oxides in catalysis," *Front. Chem.*, vol. Volume 12-2024, 2024, doi: 10.3389/fchem.2024.1374878.
[236] A. Al Miad, S. P. Saikat, Md. K. Alam, Md. Sahadat Hossain, N. M. Bahadur, and S. Ahmed, "Metal oxide-based photocatalysts for the efficient degradation of organic pollutants for a sustainable environment: a review," *Nanoscale Adv.*, vol. 6, no. 19, pp. 4781–4803, Oct. 2024, doi: 10.1039/d4na00517a.
[237] Z. Gao, Y. Liu, Q. He, H. Ma, and Z. Li, "Preferential oxidation of CO and its subsequent methanation in H2-rich gas over CuO–NiO/CeO2 catalysts," *Int. J. Hydrog. Energy*, vol. 41, no. 8, pp. 4646–4659, Mar. 2016, doi: 10.1016/j.ijhydene.2016.01.054.
[238] H. Duan, D. Wang, and Y. Li, "Green chemistry for nanoparticle synthesis," *Chem. Soc. Rev.*, vol. 44, no. 16, pp. 5778–5792, 2015, doi: 10.1039/C4CS00363B.
[239] M. Chawla, J. K. Randhawa, and P. F. Siril, "Calcination temperature as a probe to tune the non-enzymatic glucose sensing activity of Cu–Ni bimetallic nanocomposites," *New J. Chem.*, vol. 41, no. 11, pp. 4582–4591, 2017, doi: 10.1039/C6NJ03920K.
[240] P. V. Bakre, D. P. Kamat, K. S. Mandrekar, S. G. Tilve, and N. N. Ghosh, "CuO-NiO-TiO2 bimetallic nanocomposites for catalytic applications," *Mol. Catal.*, vol. 496, p. 111193, 2020, doi: https://doi.org/10.1016/j.mcat.2020.111193.
[241] J. Li *et al.*, "Enhancing photodegradation of Methyl Orange by coupling piezo-phototronic effect and localized surface plasmon resonance," *Nano Energy*, vol. 108, p. 108234, Apr. 2023, doi: 10.1016/j.nanoen.2023.108234.
[242] S. Pooyandeh, S. Shahidi, A. Khajehnezhad, and R. Mongkholrattanasit, "In situ deposition of NiO nano particles on cotton fabric using sol–gel method- photocatalytic activation properties," *J. Mater. Res. Technol.*, vol. 12, pp. 1–14, May 2021, doi: 10.1016/j.jmrt.2021.02.056.
[243] K. Tamizh Selvi, K. Alamelu Mangai, M. Priya, and S. Sagadevan, "Enhanced electrical and magnetic properties of CuO/MgO nanocomposites," *Chem. Phys. Lett.*, vol. 765, p. 138320, Feb. 2021, doi: 10.1016/j.cplett.2021.138320.
[244] J. Datta *et al.*, "Application Possibility of Mn0.04Cu0.05Zn0.91O in Electronic and Magnetic Devices," *IEEE Trans. Electron Devices*, vol. 64, no. 11, pp. 4724–4730, Nov. 2017, doi: 10.1109/TED.2017.2754190.
[245] D. Gao, G. Yang, J. Li, J. Zhang, J. Zhang, and D. Xue, "Room-Temperature Ferromagnetism of Flowerlike CuO Nanostructures," *J. Phys. Chem. C*, vol. 114, no. 43, pp. 18347–18351, Nov. 2010, doi: 10.1021/jp106015t.
[246] K. Maaz, A. Mumtaz, S. K. Hasanain, and M. F. Bertino, "Temperature dependent coercivity and magnetization of nickel ferrite nanoparticles," *J. Magn. Magn. Mater.*, vol. 322, no. 15, pp. 2199–2202, Aug. 2010, doi: 10.1016/j.jmmm.2010.02.010.
[247] K. Nadeem, A. Ullah, M. Mushtaq, M. Kamran, S. S. Hussain, and M. Mumtaz, "Effect of air annealing on structural and magnetic properties of Ni/NiO nanoparticles," *J. Magn. Magn. Mater.*, vol. 417, pp. 6–10, Nov. 2016, doi: 10.1016/j.jmmm.2016.05.064.
[248] A. Rahdar, M. Aliahmad, Y. Azizi, N. Keikha, M. Moudi, and F. Keshavarzi, "CuO-NiO Nano composites: Synthesis, Characterization, and Cytotoxicity evaluation ," *Nanomedicine Res. J.*, vol. 2, no. 2, pp. 78–86, 2017, doi: 10.22034/nmrj.2017.56956.1057.
[249] V. Schaller, G. Wahnström, A. Sanz-Velasco, P. Enoksson, and C. Johansson, "Monte Carlo simulation of magnetic multi-core nanoparticles," *Proc. Seventh Int. Conf. Sci. Clin. Appl. Magn. Carr.*, vol. 321, no. 10, pp. 1400–1403, May 2009, doi: 10.1016/j.jmmm.2009.02.047.
[250] R. Kumar *et al.*, "Antimicrobial resistance in Salmonella: One Health perspective on global food safety challenges," *Sci. One Health*, vol. 4, p. 100117, Jan. 2025, doi: 10.1016/j.soh.2025.100117.
[251] C. Mu, S. Wang, A. Wang, and W. Li, "Genomic analysis elucidates characteristics and possible origins of high-risk antimicrobial resistance genes in Enterococcus faecium

from a global perspective," *One Health*, vol. 20, p. 101054, Jun. 2025, doi: 10.1016/j.onehlt.2025.101054.
[252] P. Prasad and S. Gupta, "Nanobioconjugates: Weapons against Antibacterial Resistance," *ACS Appl. Bio Mater.*, vol. 3, no. 12, pp. 8271–8285, Dec. 2020, doi: 10.1021/acsabm.0c01107.
[253] H. A. Sheerah *et al.*, "Strengthening global health security through antimicrobial resistance control: Insights from Saudi Arabia," *J. Infect. Public Health*, vol. 18, no. 7, p. 102788, Jul. 2025, doi: 10.1016/j.jiph.2025.102788.
[254] S. Sinha and L. S. B. Upadhyay, "Understanding antimicrobial resistance (AMR) mechanisms and advancements in AMR diagnostics," *Diagn. Microbiol. Infect. Dis.*, vol. 113, no. 2, p. 116949, Oct. 2025, doi: 10.1016/j.diagmicrobio.2025.116949.
[255] S. Bhattacharya *et al.*, "In silico exploration of 4(α-l-rhamnosyloxy)-benzyl isothiocyanate: A promising phytochemical-based drug discovery approach for combating multi-drug resistant Staphylococcus aureus," *Comput. Biol. Med.*, vol. 179, p. 108907, Sep. 2024, doi: 10.1016/j.compbiomed.2024.108907.
[256] M. F. Anjum, F. Marco-Jimenez, D. Duncan, C. Marín, R. P. Smith, and S. J. Evans, "Livestock-Associated Methicillin-Resistant Staphylococcus aureus From Animals and Animal Products in the UK," *Front. Microbiol.*, vol. 10, 2019, [Online]. Available: https://www.frontiersin.org/journals/microbiology/articles/10.3389/fmicb.2019.02136
[257] D. M. Alvarez, R. Barrón-Montenegro, J. Conejeros, D. Rivera, E. A. Undurraga, and A. I. Moreno-Switt, "A review of the global emergence of multidrug-resistant Salmonella enterica subsp. enterica Serovar Infantis," *Int. J. Food Microbiol.*, vol. 403, p. 110297, 2023, doi: https://doi.org/10.1016/j.ijfoodmicro.2023.110297.
[258] D. F. Hlashwayo *et al.*, "Susceptibility antibiotic screening reveals high rates of multidrug resistance of Salmonella, Shigella and Campylobacter in HIV infected and uninfected patients from Mozambique," *BMC Infect. Dis.*, vol. 23, no. 1, p. 255, 2023, doi: 10.1186/s12879-023-08219-7.
[259] E. Rayens and K. A. Norris, "Prevalence and Healthcare Burden of Fungal Infections in the United States, 2018," *Open Forum Infect. Dis.*, vol. 9, no. 1, p. ofab593, Jan. 2022, doi: 10.1093/ofid/ofab593.
[260] R. DEAN *et al.*, "The Top 10 fungal pathogens in molecular plant pathology," *Mol. Plant Pathol.*, vol. 13, no. 4, pp. 414–430, May 2012, doi: 10.1111/j.1364-3703.2011.00783.x.
[261] R. C. Ploetz, G. H. J. Kema, and L.-J. Ma, "Impact of Diseases on Export and Smallholder Production of Banana," *Annual Review of Phytopathology*, vol. 53, no. Volume 53, 2015. Annual Reviews, pp. 269–288, 2015. doi: https://doi.org/10.1146/annurev-phyto-080614-120305.
[262] A. Gutiérrez-Sánchez *et al.*, "Virulence factors of the genus Fusarium with targets in plants," *Microbiol. Res.*, vol. 277, p. 127506, Dec. 2023, doi: 10.1016/j.micres.2023.127506.
[263] C. Lecomte, C. Alabouvette, V. Edel-Hermann, F. Robert, and C. Steinberg, "Biological control of ornamental plant diseases caused by Fusarium oxysporum: A review," *Biol. Control*, vol. 101, pp. 17–30, Oct. 2016, doi: 10.1016/j.biocontrol.2016.06.004.
[264] N. J. Mitchell, E. Bowers, C. Hurburgh, and F. Wu, "Potential economic losses to the US corn industry from aflatoxin contamination," *Food Addit. Contam. Part A*, vol. 33, no. 3, pp. 540–550, Mar. 2016, doi: 10.1080/19440049.2016.1138545.
[265] B. R. Rushing and M. I. Selim, "Aflatoxin B1: A review on metabolism, toxicity, occurrence in food, occupational exposure, and detoxification methods," *Food Chem. Toxicol.*, vol. 124, pp. 81–100, Feb. 2019, doi: 10.1016/j.fct.2018.11.047.
[266] U. O. Aigbe and O. A. Osibote, "Green synthesis of metal oxide nanoparticles, and their various applications," *J. Hazard. Mater. Adv.*, vol. 13, p. 100401, 2024, doi: https://doi.org/10.1016/j.hazadv.2024.100401.
[267] R. Bhattacharjee *et al.*, "The emergence of metal oxide nanoparticles (NPs) as a phytomedicine: A two-facet role in plant growth, nano-toxicity and anti-phyto-microbial

activity," *Biomed. Pharmacother.*, vol. 155, p. 113658, Nov. 2022, doi: 10.1016/j.biopha.2022.113658.
[268] R. Kashyap, S. Tiwari, and S. Bhattacharya, "Innovative strategies in the fight against bacterial infections: Phage therapy, nanotechnology, and new antimicrobial agents for multidrug-resistant pathogens," *Results Chem.*, vol. 15, p. 102304, May 2025, doi: 10.1016/j.rechem.2025.102304.
[269] P. Kaushal, D. Maity, and R. Awasthi, "Nano-green: Harnessing the potential of plant extracts for sustainable antimicrobial metallic nanoparticles," *J. Drug Deliv. Sci. Technol.*, vol. 94, p. 105488, Apr. 2024, doi: 10.1016/j.jddst.2024.105488.
[270] B. S. Medic, N. Tomic, N. Lagopati, M. Gazouli, and L. Pojskic, "Advances in Metal and Metal Oxide Nanomaterials for Topical Antimicrobial Applications: Insights and Future Perspectives," *Molecules*, vol. 29, no. 23, 2024, doi: 10.3390/molecules29235551.
[271] S. K. Mondal, S. Chakraborty, S. Manna, and S. M. Mandal, "Antimicrobial nanoparticles: current landscape and future challenges," *RSC Pharm.*, vol. 1, no. 3, pp. 388–402, 2024, doi: 10.1039/D4PM00032C.
[272] D. Sharma, S. Gautam, S. Singh, N. Srivastava, A. M. Khan, and D. Bisht, "Unveiling the nanoworld of antimicrobial resistance: integrating nature and nanotechnology," *Front. Microbiol.*, vol. Volume 15-2024, 2025, [Online]. Available: https://www.frontiersin.org/journals/microbiology/articles/10.3389/fmicb.2024.1391345
[273] A. M. Ali *et al.*, "Green and chemical synthesis of iron oxide nanoparticles: Comparative study for antimicrobial activity and toxicity concerns," *J. Drug Deliv. Sci. Technol.*, vol. 103, p. 106434, Jan. 2025, doi: 10.1016/j.jddst.2024.106434.
[274] B. Cardoso, G. Nobrega, I. S. Afonso, J. E. Ribeiro, and R. A. Lima, "Sustainable green synthesis of metallic nanoparticle using plants and microorganisms: A review of biosynthesis methods, mechanisms, toxicity, and applications," *J. Environ. Chem. Eng.*, vol. 13, no. 3, p. 116921, Jun. 2025, doi: 10.1016/j.jece.2025.116921.
[275] R. A. H. Tabrani, G. Antarnusa, and F. Firdaus, "Facile synthesis of Fe3O4 via co-precipitation method: The role of Moringa oleifera in substituting chemical reducing agents," *Mater.*, vol. 8, p. 100927, Jul. 2025, doi: 10.1016/j.nxmate.2025.100927.
[276] S. Ghimire, L. Subedi, N. Acharya, and B. P. Gaire, "Moringa oleifera: A Tree of Life as a Promising Medicinal Plant for Neurodegenerative Diseases," *J. Agric. Food Chem.*, vol. 69, no. 48, pp. 14358–14371, Dec. 2021, doi: 10.1021/acs.jafc.1c04581.
[277] P. Kumar, T. Saha, S. Behera, S. Gupta, S. Das, and K. Mukhopadhyay, "Enhanced efficacy of a Cu2+ complex of curcumin against Gram-positive and Gram-negative bacteria: Attributes of complex formation," *J. Inorg. Biochem.*, vol. 222, p. 111494, 2021, doi: https://doi.org/10.1016/j.jinorgbio.2021.111494.
[278] H. F. Etefa, D. J. Nemera, and F. B. Dejene, "Green Synthesis of Nickel Oxide NPs Incorporating Carbon Dots for Antimicrobial Activities," *ACS Omega*, vol. 8, no. 41, pp. 38418–38425, Oct. 2023, doi: 10.1021/acsomega.3c05204.
[279] V. Haritha, S. Gowri, B. Janarthanan, Md. Faiyazuddin, C. Karthikeyan, and S. Sharmila, "Biogenic synthesis of nickel oxide nanoparticles using Averrhoa bilimbi and investigation of its antibacterial, antidiabetic and cytotoxic properties," *Inorg. Chem. Commun.*, vol. 144, p. 109930, 2022, doi: https://doi.org/10.1016/j.inoche.2022.109930.
[280] C. Tiloke, K. Anand, R. M. Gengan, and A. A. Chuturgoon, "Moringa oleifera and their phytonanoparticles: Potential antiproliferative agents against cancer," *Biomed. Pharmacother.*, vol. 108, pp. 457–466, 2018, doi: https://doi.org/10.1016/j.biopha.2018.09.060.
[281] G. Félix, C. A. Soto-Robles, E. Nava, and E. Lugo-Medina, "Principal Metabolites in Extracts of Different Plants Responsible for Antibacterial Effects," *Chem. Res. Toxicol.*, vol. 34, no. 9, pp. 1970–1983, Sep. 2021, doi: 10.1021/acs.chemrestox.1c00161.
[282] M. Haripriyaa and K. Suthindhiran, "Pharmacokinetics of nanoparticles: current knowledge, future directions and its implications in drug delivery," *Future J. Pharm. Sci.*, vol. 9, no. 1, p. 113, 2023, doi: 10.1186/s43094-023-00569-y.

[283] T. J. Quirk, “Sample Size, Mean, Standard Deviation, and Standard Error of the Mean BT - Excel 2016 in Applied Statistics for High School Students: A Guide to Solving Practical Problems,” T. J. Quirk, Ed., Cham: Springer International Publishing, 2018, pp. 1–22. doi: 10.1007/978-3-319-89993-0_1.
[284] M. B. Mobarak, M. D. F. Sikder, K. S. Muntaha, S. Islam, S. M. F. Rabbi, and F. Chowdhury, “Plant extract-mediated green-synthesized CuO nanoparticles for environmental and microbial remediation: a review covering basic understandings to mechanistic study,” *Nanoscale Adv.*, vol. 7, no. 9, pp. 2418–2445, 2025, doi: 10.1039/D5NA00035A.
[285] D. K. Singaravelu, D. N. Binjawhar, F. Ameen, and A. Veerappan, “Lectin-Fortified Cationic Copper Sulfide Nanoparticles Gain Dual Targeting Capabilities to Treat Carbapenem-Resistant Acinetobacter baumannii Infection,” *ACS Omega*, vol. 7, no. 48, pp. 43934–43944, Dec. 2022, doi: 10.1021/acsomega.2c05252.
[286] N. M. Al-Enazi, K. Alsamhary, and F. Ameen, “Evaluation of citrus pectin capped copper sulfide nanoparticles against Candidiasis causing Candida biofilms,” *Environ. Res.*, vol. 225, p. 115599, 2023, doi: https://doi.org/10.1016/j.envres.2023.115599.
[287] S. Liu *et al.*, “Antibacterial activity of graphite, graphite oxide, graphene oxide, and reduced graphene oxide: membrane and oxidative stress.,” *ACS Nano*, vol. 5 9, pp. 6971–6980, 2011, [Online]. Available: https://api.semanticscholar.org/CorpusID:11779481
[288] G. Eka Putri, Y. Rilda, S. Syukri, A. Labanni, and S. Arief, “Highly antimicrobial activity of cerium oxide nanoparticles synthesized using Moringa oleifera leaf extract by a rapid green precipitation method,” *J. Mater. Res. Technol.*, vol. 15, pp. 2355–2364, 2021, doi: https://doi.org/10.1016/j.jmrt.2021.09.075.
[289] S. Riahi *et al.*, “Bactericidal activity of ZnO nanoparticles against multidrug-resistant bacteria,” *J. Mol. Liq.*, vol. 387, p. 122596, 2023, doi: https://doi.org/10.1016/j.molliq.2023.122596.
[290] G. Vasiliev *et al.*, “Synergistic antibacterial effect of copper and silver nanoparticles and their mechanism of action,” *Sci. Rep.*, vol. 13, no. 1, p. 9202, Jun. 2023, doi: 10.1038/s41598-023-36460-2.
[291] A. Chiș *et al.*, “Bioactive Compounds in Moringa oleifera: Mechanisms of Action, Focus on Their Anti-Inflammatory Properties,” *Plants*, vol. 13, no. 1, 2024, doi: 10.3390/plants13010020.
[292] A. Semwal, K. Gautam, M. Bhatt, R. Yadav, S. Barthwal, and H. Singh, “Green synthesis and application of metal nanoparticles (MNPs): A sustainable strategy for protecting wood from fungal and termite decay,” *Mater.*, vol. 9, p. 100962, Oct. 2025, doi: 10.1016/j.nxmate.2025.100962.
[293] M. Devaraji, P. V. Thanikachalam, and K. Elumalai, “The potential of copper oxide nanoparticles in nanomedicine: A comprehensive review,” *Biotechnol. Notes*, vol. 5, pp. 80–99, Jan. 2024, doi: 10.1016/j.biotno.2024.06.001.
[294] S. Prabhu and E. K. Poulose, “Silver nanoparticles: mechanism of antimicrobial action, synthesis, medical applications, and toxicity effects,” *Int. Nano Lett.*, vol. 2, no. 1, p. 32, 2012, doi: 10.1186/2228-5326-2-32.
[295] X. Ma, S. Zhou, X. Xu, and Q. Du, “Copper-containing nanoparticles: Mechanism of antimicrobial effect and application in dentistry-a narrative review,” *Front. Surg.*, vol. 9, 2022, [Online]. Available: https://www.frontiersin.org/journals/surgery/articles/10.3389/fsurg.2022.905892
[296] A. Labanni, Z. Zulhadjri, D. Handayani, Y. Ohya, and S. Arief, “The effect of monoethanolamine as stabilizing agent in Uncaria gambir Roxb. mediated synthesis of silver nanoparticles and its antibacterial activity,” *J. Dispers. Sci. Technol.*, vol. 41, no. 10, pp. 1480–1487, Aug. 2020, doi: 10.1080/01932691.2019.1626249.
[297] L. M. Estes *et al.*, “Characterization of a nitric oxide (NO) donor molecule and cerium oxide nanoparticle (CNP) interactions and their synergistic antimicrobial potential for biomedical applications,” *J. Colloid Interface Sci.*, vol. 586, pp. 163–177, 2021, doi: https://doi.org/10.1016/j.jcis.2020.10.081.

[298] S. M. Dizaj, F. Lotfipour, M. Barzegar-Jalali, M. H. Zarrintan, and K. Adibkia, "Antimicrobial activity of the metals and metal oxide nanoparticles," *Mater. Sci. Eng. C*, vol. 44, pp. 278–284, Nov. 2014, doi: 10.1016/j.msec.2014.08.031.
[299] M. Raffi *et al.*, "Investigations into the antibacterial behavior of copper nanoparticles against Escherichia coli," *Ann. Microbiol.*, vol. 60, no. 1, pp. 75–80, 2010, doi: 10.1007/s13213-010-0015-6.
[300] Y. N. Slavin, J. Asnis, U. O. Häfeli, and H. Bach, "Metal nanoparticles: understanding the mechanisms behind antibacterial activity," *J. Nanobiotechnology*, vol. 15, no. 1, p. 65, Oct. 2017, doi: 10.1186/s12951-017-0308-z.
[301] N. S. Wigginton *et al.*, "Binding of Silver Nanoparticles to Bacterial Proteins Depends on Surface Modifications and Inhibits Enzymatic Activity," *Environ. Sci. Technol.*, vol. 44, no. 6, pp. 2163–2168, Mar. 2010, doi: 10.1021/es903187s.
[302] H. Hemeg, "Nanomaterials for alternative antibacterial therapy," *Int. J. Nanomedicine*, vol. Volume 12, pp. 8211–8225, Nov. 2017, doi: 10.2147/IJN.S132163.
[303] Y. N. Slavin and H. Bach, "Mechanisms of Antifungal Properties of Metal Nanoparticles," *Nanomaterials*, vol. 12, no. 24, 2022, doi: 10.3390/nano12244470.
[304] S. H. S. Dananjaya, R. S. Kumar, M. Yang, C. Nikapitiya, J. Lee, and M. De Zoysa, "Synthesis, characterization of ZnO-chitosan nanocomposites and evaluation of its antifungal activity against pathogenic Candida albicans," *Int. J. Biol. Macromol.*, vol. 108, pp. 1281–1288, Mar. 2018, doi: 10.1016/j.ijbiomac.2017.11.046.
[305] D. Y. Kim *et al.*, "Bioinspired silver nanoparticle-based nanocomposites for effective control of plant pathogens: A review," *Sci. Total Environ.*, vol. 908, Jan. 2024, doi: 10.1016/j.scitotenv.2023.168318.
[306] F. A. Bezza, S. M. Tichapondwa, and E. M. N. Chirwa, "Fabrication of monodispersed copper oxide nanoparticles with potential application as antimicrobial agents," *Sci. Rep.*, vol. 10, no. 1, p. 16680, 2020, doi: 10.1038/s41598-020-73497-z.
[307] J. Ramos-Zúñiga, N. Bruna, and J. M. Pérez-Donoso, "Toxicity Mechanisms of Copper Nanoparticles and Copper Surfaces on Bacterial Cells and Viruses," *Int. J. Mol. Sci.*, vol. 24, no. 13, p. 10503, Jun. 2023, doi: 10.3390/ijms241310503.
[308] Y.-W. Baek and Y.-J. An, "Microbial toxicity of metal oxide nanoparticles (CuO, NiO, ZnO, and Sb2O3) to Escherichia coli, Bacillus subtilis, and Streptococcus aureus," *Sci. Total Environ.*, vol. 409, no. 8, pp. 1603–1608, 2011, doi: https://doi.org/10.1016/j.scitotenv.2011.01.014.
[309] M. Godoy-Gallardo *et al.*, "Antibacterial approaches in tissue engineering using metal ions and nanoparticles: From mechanisms to applications," *Bioact. Mater.*, vol. 6, no. 12, pp. 4470–4490, 2021, doi: https://doi.org/10.1016/j.bioactmat.2021.04.033.
[310] A. Menichetti, A. Mavridi-Printezi, D. Mordini, and M. Montalti, "Effect of Size, Shape and Surface Functionalization on the Antibacterial Activity of Silver Nanoparticles," *J. Funct. Biomater.*, vol. 14, no. 5, 2023, doi: 10.3390/jfb14050244.
[311] K. Neethidevan *et al.*, "Wattakaka volubilis powered green synthesized CuO, NiO and ZnO nanoparticles for cost-effective biomedical applications," *Biomass Convers. Biorefinery*, 2023, doi: 10.1007/s13399-023-04949-5.
[312] M. E. Elshobary *et al.*, "Combating antibiotic resistance: Mechanisms, multidrug-resistant pathogens, and novel therapeutic approaches: An updated review," *Pharmaceuticals*, vol. 18, no. 3, p. 402, 2025.
[313] M. D. Lenardon, C. A. Munro, and N. A. Gow, "Chitin synthesis and fungal pathogenesis," *Host–Microbe Interact. FungiParasitesViruses*, vol. 13, no. 4, pp. 416–423, Aug. 2010, doi: 10.1016/j.mib.2010.05.002.
[314] J. B. Parsons and C. O. Rock, "Bacterial lipids: Metabolism and membrane homeostasis," *Prog. Lipid Res.*, vol. 52, no. 3, pp. 249–276, Jul. 2013, doi: 10.1016/j.plipres.2013.02.002.
[315] C. A. Munro and N. A. R. Gow, "Chitin synthesis in human pathogenic fungi," *Med. Mycol.*, vol. 39, no. 1, pp. 41–53, Jan. 2001, doi: 10.1080/mmy.39.1.41.53.
[316] S. W. White, J. Zheng, Y.-M. Zhang, and C. O. Rock, "THE STRUCTURAL BIOLOGY OF TYPE II FATTY ACID BIOSYNTHESIS," *Annual Review of*

Biochemistry, vol. 74, no. Volume 74, 2005. Annual Reviews, pp. 791–831, 2005. doi: https://doi.org/10.1146/annurev.biochem.74.082803.133524.
[317] M. Alam, "Photocatalytic activity of biogenic zinc oxide nanoparticles: In vitro antimicrobial, biocompatibility, and molecular docking studies," vol. 10, no. 1, pp. 1079–1091, 2021, doi: doi:10.1515/ntrev-2021-0069.
[318] E. Hamdy *et al.*, "Copper oxide nanoparticles-mediated Heliotropium bacciferum leaf extract: Antifungal activity and molecular docking assays against strawberry pathogens," vol. 22, no. 1, 2024, doi: doi:10.1515/chem-2024-0028.
[319] P. K. Tyagi, R. Mishra, F. Khan, D. Gupta, and D. Gola, "Antifungal effects of silver nanoparticles against various plant pathogenic fungi and its safety evaluation on Drosophila melanogaster," *Biointerface Res Appl Chem*, vol. 10, pp. 6587–6596, 2020.
[320] C. Migliorini, E. Porciatti, M. Luczkowski, and D. Valensin, "Structural characterization of Cu2+, Ni2+ and Zn2+ binding sites of model peptides associated with neurodegenerative diseases," *Eur. Group Thermodyn. Met. Complexes*, vol. 256, no. 1, pp. 352–368, Jan. 2012, doi: 10.1016/j.ccr.2011.07.004.
[321] J. Yao and C. O. Rock, "Exogenous fatty acid metabolism in bacteria," *Microbe Host Lipids Gerli Meet.*, vol. 141, pp. 30–39, Oct. 2017, doi: 10.1016/j.biochi.2017.06.015.
[322] M. J. Hajipour *et al.*, "Antibacterial properties of nanoparticles," *Trends Biotechnol.*, vol. 30, no. 10, pp. 499–511, Oct. 2012, doi: 10.1016/j.tibtech.2012.06.004.
[323] E. Sánchez-López *et al.*, "Metal-Based Nanoparticles as Antimicrobial Agents: An Overview," *Nanomaterials*, vol. 10, no. 2, 2020, doi: 10.3390/nano10020292.
[324] T. J. Boram *et al.*, "Activity of Fatty Acid Biosynthesis Initiating Ketosynthase FabH with Acetyl/Malonyl-oxa/aza(dethia)CoAs," *ACS Chem. Biol.*, vol. 18, no. 1, pp. 49–58, Jan. 2023, doi: 10.1021/acschembio.2c00667.
[325] C. Cai, Y. Huang, L. Zhang, and L. Zhang, "The Molecular Basis of the β-Ketoacyl-ACP Synthase FabH in Catalyzing C–C Bond Formation of Acetoacetyl-ACP," *ACS Catal.*, vol. 15, no. 6, pp. 5028–5038, Mar. 2025, doi: 10.1021/acscatal.5c01167.
[326] Z. Yao, R. M. Davis, R. Kishony, D. Kahne, and N. Ruiz, "Regulation of cell size in response to nutrient availability by fatty acid biosynthesis in Escherichia coli," *Proc. Natl. Acad. Sci.*, vol. 109, no. 38, pp. E2561–E2568, Sep. 2012, doi: 10.1073/pnas.1209742109.
[327] C. Roncero, "The genetic complexity of chitin synthesis in fungi," *Curr. Genet.*, vol. 41, no. 6, pp. 367–378, Sep. 2002, doi: 10.1007/s00294-002-0318-7.
[328] L. Barthel *et al.*, "Breaking down barriers: comprehensive functional analysis of the Aspergillus niger chitin synthase repertoire," *Fungal Biol. Biotechnol.*, vol. 11, no. 1, p. 3, Mar. 2024, doi: 10.1186/s40694-024-00172-7.
[329] S. M. Bowman and S. J. Free, "The structure and synthesis of the fungal cell wall," *BioEssays*, vol. 28, no. 8, pp. 799–808, Aug. 2006, doi: 10.1002/bies.20441.

List of Publications and Attended Conferences

List of publications arising directly from thesis

1. **Yadav S.**, Singh A., Choubey A.K. (2023). Composition dependent variation in structural, morphological, optical and magnetic properties of biogenic CuO/NiO mixed oxide nanoparticles. *Journal of alloys and compounds*, 979, (117):173422.

2. **Yadav S.**, Srivastava P.K., Choubey A.K. (2025). Optimizing growth performance of *Abelmoschus esculentus (L.)* via synergistic effects of biogenic Cu/Ni/Co oxide nanoparticles in conjunction with rice straw and pressmud based vermicompost. *Pedosphere.* https://doi.org/10.1016/j.pedsph.2025.08.009.

3. **Yadav S.**, Singh A., Rana D., Choubey A.K., Srivastava P.K. Evaluation of broad-spectrum antimicrobial efficacy of biogenic NiO/CuO nanocomposite: *In vitro, in silico,* and molecular docking approach.

List of attended conferences

1. "International Conference on Biotechnology for Sustainable Development Goals (ICBSDG-2025)", April 2025, Sharda University, Greater Noida, India. **(BEST POSTER AWARD)**

2. "18th International Congress on Thermal Analysis and Calorimetry (ICTAC-2024)", September 2024, IIT Madras, India. (Oral presentation)

3. "Conference on Innovations in Material Science (IMAT-24)", April 2024, Institute Instrumentation Centre, IIT Roorkee, India. (Poster presentation)

4. "International Conference on Advanced Materials for Emerging Technologies (ICAMET-2023)", May 2023, Department of Physics, Netaji Subhas University of Technology, Delhi, India. (Oral presentation)

5. "International Hybrid Conference on Nano Structured Materials and Polymers (ICNP-2023)", May 2023, Mahatma Gandhi University, Kottayam, Kerala, India. (Oral presentation)

6. "Energy, environment and advanced materials for a sustainable future (ICEEAMSF-2021)", December 2021, Kongu Engineering College, Tamil Nādu, India. (Oral presentation)

7. "Recent Trends in Energy Science and Engineering (ICRTESE-2021)", October 2021, Rajiv Gandhi Institute of Petroleum Technology, Jais, Uttar-Pradesh, India. (Volunteered)

8. “Recent Advances and Applications of Conducting Polymer Nanostructures and Nanocomposites”, June 2021, IIT-Mandi, India. (Oral presentation)

List of attended workshops

1. “Nine-Day Online Workshop on Molecular Docking”, May 2024, SAIS Research Forum.

2. “Two-Week Online Workshop on Rietveld Refinement”, February 2024, SIAS Research Forum.

3. “Skill Development Program on Synthesis and In Vitro Toxicity Evaluation of Silver Nanoparticles”, December 2023, CSIR-Indian Institute of Toxicological Research, Lucknow, India.

4. “Skill Development Program on Industrial Catalysis (SDP_NCL31_22-23)”, November-December 2022, CSIR-National Chemical Laboratory, Pune, India.